Powder-based additive manufacturing for space

From granular rheology in varying gravitational environment to the development of a gravity-independent powder handling method

From the Faculty of Georesources and Materials Engineering of the
RWTH Aachen University

Submitted by

Olfa Lopez D'Angelo

M.Sc. M.B.A.

from Paris, France

in respect of the academic degree of

Doctor of Engineering

Approved thesis

Advisors Priv.-Doz. Dr. rer. nat. Jürgen Brillo
Univ.-Prof. Dr.-Ing. Dr. h. c. Dieter Georg Senk
Prof. Dr. rer. nat. Andreas Meyer

Date of the oral examination: Tuesday 18th May, 2021

This thesis is available in electronic format on the university library's website.

Abstract

As human reach into space expands, need arises for versatile technologies, working under extreme conditions – notably, in absence of gravity. In-Space Manufacturing (ISM) would allow payload optimisation by enabling on-demand production of tools, spare parts or building elements, increasing self-sufficiency of long-endurance missions. While powder-based three dimensional (3D) printing processes offer high printing quality and adaptability to multiple raw materials, for all techniques available today, constrains remain on feedstock flow properties and recyclability of base-material.

The work presented here proposes a new method for handling and additively manufacturing granular materials, independently of the gravitational environment, and emancipating from requirements on powder-feedstock flow properties.

Technical evolutions go hand in hand with an understanding of the physical phenomena that underlie them. The development of a powder-based Additive Manufacturing (AM) process was hence preceded by a study of the factors influencing granular rheological response. To be used as demonstrator, a spherical polystyrene (PS) powder was modified to increase its surface roughness, resulting in two powders similar in all respects but their surface state. The link between physical and rheological properties of powders was explored, through typical rheometry tests (flow start-up and stationary flow curves, powder-bed tensile strength), but also through phenomenological testing methods found in industrial applications (notably the *flow energy* test). Observing and quantifying essential differences in flow-behaviour emerging from this modification of the frictional interactions between particles, allowed to approach the ill-defined concept of *powder flowability*, to propose a definition which encompasses not only the inherent powder physical properties, but also the environmental factors surrounding the material.

To query the influence of such environmental factors, the same powder was used to study the effect of gravity (and absence thereof) on piston-probing of granular material. Using parabolic flight as a microgravity platform, this experiment revealed that, in absence of the secondary force field provided by gravity, powder flow deteriorates and packing fraction at jamming lowers, with dramatic consequences for powder handling in reduced gravity.

Results from this first experimental campaign led to the design of the mentioned AM process. To deposit the granular base-material, this process uses solely driving mechanisms independent of gravity (namely shear and shaking). To allow versatility in feedstock material's flow-behaviour, adaptability of the process printing parameters was implemented through a control loop fed by *in-situ* probing during powder handling. The material deposition method was first validated through Discrete Element Method (DEM) simulation, showing no dependence of the process efficiency on the gravitational environment, nor on the increased interparticle cohesive forces. Experimental demonstration was also provided, through the construction of

two prototype 3D printers, used on-ground and on parabolic flights to manufacture parts from the two powders mentioned above: PS powders of high and mediocre flowability.

The successful manufacturing of parts under gravity as well as in weightlessness, from both powders, regardless of their flow properties, represents the main achievement of this work. X-ray computed tomography (CT) analysis of the sintered parts showed no systematic change in porosity between the samples manufactured under different gravitational environments, with near-perfect density and isotropic porosities. Parts were also produced directly from recycled material (under $1g$), obtained by closed-loop recycling of former 3D printed parts; an achievement that no commercially available additive manufacturing process to date could realise, and that will be a critical asset for increasing the self-sustainability of space exploration missions.

The work presented lead to filing a patent in September 2020, endorsed by the German Aerospace Center, under the application number 10 2020 123 753.7 for an "Apparatus and Method for Additive Manufacturing of Components in Environments with Various Gravitation-levels and with Materials of Different Flowability".

Zusammenfassung

Mit dem zunehmenden Drang der Menschheit in den Weltraum entsteht ein Bedarf für vielseitig einsetzbare Technologien, die unter extremen Bedingungen – besonders in Abwesenheit der Schwerkraft – einsetzbar sind. Fertigung direkt im Weltraum [In-Space Manufacturing (ISM)] würde es ermöglichen, Nutzlasten zu optimieren, indem durch Produktion von Werkzeugen, Ersatzteilen oder Bauteilen auf Abruf die Autarkie von langandauernden Missionen erhöht würde. Während pulverbasierte 3D-Druckverfahren hohe Druckqualität und Flexibilität bezüglich der Rohmaterialien ermöglichen, so bleiben dennoch alle derzeit verfügbaren Realisierungen dieser Technik im Hinblick auf die Fließeigenschaften des Pulvers sowie auf die Recycling-Fähigkeit eingeschränkt.

Die vorliegende Arbeit stellt eine neue Methode der Handhabung und der additiven Fertigung granularer Materialien vor, die unabhängig von der Schwerkraft ist, und die sich von den Zwängen wohlbestimmter Fließeigenschaften des granularen Rohmaterials befreit.

Technische Evolution erfolgt Hand in Hand mit einem verbesserten Verständnis der physikalischen Phänomene, die der jeweiligen Technik zugrunde liegen. Der Entwicklung einer pulverbasierten additiven Fertigungsmethode wurde hier deshalb eine ausgedehnte Studie der Faktoren, die die rheologischen Eigenschaften granularer Materialien beeinflussen, vorangestellt. Sphärische Polystyrol (PS)-Pulver mit einer gezielten Modifikation der Oberflächenrauigkeit der Teilchen wurden als exemplarische Materialien benutzt, um zwei Pulver zu erzeugen, die in allen Belangen ähnlich sind, bis auf die Oberflächen der Granulatteilchen. Die Verbindung zwischen physikalischen und rheologischen Eigenschaften dieser Pulver wurde untersucht: zum einen durch typische rheologische Messungen (Einschalt-Vorgänge, stationäre Fließkurven, sowie Zugfestigkeitstests im Pulver-Bett), zum anderen durch phänomenologische Tests aus der industriellen Anwendung (insbesondere der Fließenergie-Test zur Ermittlung der *flow energy*). Durch die Beobachtung und Quantifizierung wesentlicher Unterschiede im Fließverhalten der Pulver, die allein auf die Modifikation der Reibungswechselwirkung zwischen den Granulatteilchen zurückgehen, konnte das bislang nur schlecht definierte Konzept der Pulverfließfägkeit [*powder flowability*] neu betrachtet werden, um eine Definition zu geben, die nicht nur genuine Pulvereigenschaften des Materials, sondern auch die Umgebungsbedingungen einbezieht.

Der Einfluss solcher Umgebungsbedingungen wurde hier insbesondere betrachtet, indem die Auswirkung der Gravitationskraft (oder die ihrer Abwesenheit) auf Kolben-Kompressionstests des granularen Materials untersucht wurde. Durch Experimente in Schwerelosigkeit im Rahmen einer Parabelflugkampagne konnte hier gezeigt werden, dass in Abwesenheit eines durch die Gravitationskraft bereitgestellten sekundären Kraftfeldes sich das Fließen des Pulvers verschlechtert und sich die Packungsdichte, bei der das Pulver blockiert, verringert. Dies hat dramatische Konsequenzen für die Handhabung von Pulvern in verringerter Schwerkraft.

Die Ergebnisse dieser ersten Experimentkampagne führten zur Entwicklung des genannten additiven Fertigungsprozesses. Dieser Prozess verwendet ausschließlich Antriebsmechanismen zur Schichtung des granularen Basismaterials, welche unabhängig von Schwerkrafteinflüssen sind (insbesondere Scherung und Vibration). Der Prozess erlaubt eine Anpassung an unterschiedliche Fliesseigenschaften des Basismaterials, indem die Prozessparameter über einen Regelkreis, der auf *in-situ*-Messungen rheologischer Eigenschaften des Pulvers zugreifen kann, während des Drucks verändert werden können. Die Pulverauftragsmethode wurde zunächst durch Diskrete-Elemente-Simulationen validiert; die Simulationen bestätigen, dass die Wirksamkeit des Prozesses weder von der Schwerkraftumgebung abhängt, noch von Variationen in den kohäsiven Wechselwirkungen der Granulatteilchen. Eine experimentelle Bestätigung des vorgeschlagenen Prozesses wurde ebenso realisiert: zwei Prototypen von 3D-Druckern wurden hergestellt und sowohl am Boden als auch im Rahmen zweier Parabelflugkampagnen verwendet, um Teile aus den beiden oben genannten PS-Pulvern mit hoher und mäßiger Fließfähigkeit herzustellen.

Die erfolgreiche Herstellung dieser Teile sowohl unter gewöhnlicher Schwerkraft als auch unter Schwerelosigkeit, sowohl auf der Basis gut fliessfähiger als auch auf der Basis schlecht fließfähiger Granulate, stellt die Haupterrungenschaft der vorliegenden Arbeit dar. Die auf diese Weise gesinterten Proben wurden mit Hilfe von Röntgentcomputertomographie untersucht. Es zeigt sich keinerlei systematischer Unterschied in der Porosität zwischen den Proben, die unter verschiedenen Schwerkraftbedingungen hergestellt wurden: die Proben sind von nahezu perfekt hoher Dichte und isotrop. Es war mit den Prototypen ebenso möglich, (am Boden) Teile direkt aus Recyclingmaterial herzustellen; dazu wurde das Basismaterial direkt aus einem vorher 3D-gedruckten Teil durch Zermahlen gewonnen. Dies stellt einen Fortschritt für das Recycling im geschlossenen Kreislauf im Bereich der pulverbasierten additiven Fertigung dar, der bislang in keinem kommerziell erhältlichen Fertigungsprozess umgesetzt werden konnte, und der einen wesentlichen Beitrag zur Erhöhung der Selbstversorgungsfähigkeit zukünftiger Weltraummissionen liefert.

Die vorliegende Arbeit führte im September 2020 zur Einreichung eines Patents, unterstützt durch das Deutsche Zentrum für Luft- und Raumfahrt e.V. (DLR), unter der Patentantragsnummber 10 2020 123 753.7 mit dem Titel “Vorrichtung und Verfahren zur additiven Fertigung von Bauteilen in Umgebungen mit unterschiedlicher Gravitation und mit Material unterschiedlicher Fließfähigkeit [Apparatus and Method for Additive Manufacturing of Components in Environments with Various Gravitation-levels and with Materials of Different Flowability]”.

Résumé

La curiosité humaine tend à toujours repousser les frontières de la connaissance, y compris en explorant de plus en plus loin dans l'espace. Cette recherche n'est viable que si elle est soutenue par l'élaboration de nouvelles technologies, plus polyvalentes et plus robustes – notamment fonctionnant en absence de gravité. L'optimisation de la charge utile est une problématique majeure de l'exploration spatiale, faisant de la possibilité de fabriquer directement sur place outils, pièces de rechanges et éléments structuraux, un atout vital à l'autosuffisance de futures missions. Les méthodes d'impression 3D à base de matériaux pulvérulents offrent une haute qualité d'impression et un large choix de matières premières. Cependant, les techniques disponibles à ce jour sont basées sur l'utilisation du champ gravitationnel terrestre, et sur la haute capacité d'écoulement des poudres utilisées. Ces contraintes obligent à l'utilisation de matériaux produits spécifiquement, ce qui rend impossible l'utilisation de matériaux recyclés.

L'objet du présent travail est le développement d'un procédé visant au contrôle de l'écoulement de matériaux granulaires pour la fabrication additive. Ce procédé vise à s'affranchir du champ de force gravitationnel, et des limitations quant aux propriétés rhéologiques des matières premières, proposant ainsi une alternative fonctionnant indépendamment de ces contraintes.

Les évolutions techniques allant de pair avec la compréhension des phénomènes physiques qui les sous-tendent, une étude des facteurs influençant le comportement rhéologique des poudres précède le développement de ce procédé. Une poudre composée de grains de polystyrène, sphériques et lisses, est modifée pour en augmenter la rugosité. On crée ainsi deux poudres similaires en tous points, excepté leur état de surface. Le lien entre les propriétés physiques et rhéologiques des matériaux granulaires est exploré à travers des tests rhéologiques typiques: démarrage de l'écoulement (*flow start-up*), courbe de débit à l'état stationnaire (*flow-curve*) et résistance du lit de poudre en traction par fluidisation. Cette étude est complétée par des tests phénoménologiques courants dans l'industrie, comme "l'energie d'écoulement" ou *flow energy*. La friction de surface modifiée entre ces deux matériaux donne lieu a des différences essentielles, qualitatives et quantitatives, dans le type d'écoulement observé. Le concept de *fluidité* ou *coulabilité* des poudres, souffrant de l'absence de description claire, est ainsi examiné, de manière à en proposer une définition, prenant en compte non seulement les propriétés physiques intrinsèques du matériau pulvérulent, mais aussi l'environment dans lequel il est évolue – y compris gravitationnel.

Questionnant l'influence de tels facteurs environnementaux, cette même poudre est utilisée lors d'une experience en vol parabolique visant à déterminer l'effet de la gravité sur la mise en mouvement d'une poudre par un piston compressant le matériau. Cette experience révèle qu'en l'absence d'un champ de force secondaire (comme celui produit par l'attraction terrestre), la poudre s'écoule avec plus de difficultés. D'autre part, le blocage entrainant l'arrêt de l'écoulement (ou *jamming*) se produit à plus basse densité en apesanteur que sur Terre, avec

les conséquences dramatiques qu'on imagine.

Les résultats de cette première experience guident la mise au point du procédé d'impression 3D mentionné ci-dessus. Pour le transport du matériau de base, les mécanismes de transmission de force mis en œuvre sont sélectionnés pour leur indépendance à la gravité – notamment, cisaillement et vibration. Pour permettre une plus grande polyvalence dans les matériaux de base, adaptativité des paramètres d'impression est assurée par une boucle de contrôle et de régulation: deux dispositifs de sondage *in-situ* indiquent la réponse rhéologique de la poudre pendant qu'elle est en train d'être déposée.

La méthode employée pour contrôler le transport du matériau granulaire est d'abord validée par modélisation par éléments discrets. Une fois son efficacité demontrée pour différents environnements gravitationnels ($-1g$, $0g$ et $1g$), la cohésion entre les grains est considérablement augmentée pour simuler une poudre de très mauvaise coulabilité. Ce nouveau défi relevé avec succès, la prochaine étape se concrétise par une démonstration expérimentale du procédé d'impression 3D.

Deux prototypes construits dans ce cadre sont utilisés en vols paraboliques pour parvenir à cette démonstration. Le transport de poudre et la production de pièces en fabrication additive, indépendamment de leur comportement rhéologique et du milieu gravitationnel, demontrés par l'utilisation des deux matériaux présentés ci-dessus (de coulabilité haute et médiocre), représentent un acquis majeur de ces recherches. L'analyse tomodensitométrique des pièces frittées ne montre aucun changement systématique en terme de porosité entre les pièces imprimées sous différents environments gravitationnels, dénotant même une densité proche de la valeur idéale attendue, et une haute isotropie. Des pièces sont aussi produites directement à partir de matériaux issus de recyclage en circuit fermé d'objets antérieurement imprimés; une performance qu'aucune autre technologie disponible aujourd'hui n'avait atteinte, et qui représente pourtant un atout de taille pour l'exploration spatiale.

Ce travail a permis le dépôt d'un brevet en septembre 2020, sous l'égide du Centre Aérospatial Allemand (DLR), référencé 10 2020 123 753.7, pour un "Appareil et [une] Méthode de Fabrication Additive de Composants dans des Environments à Gravité Variable et avec des Matériaux de Multiples Coulabilités [Apparatus and Method for Additive Manufacturing of Components in Environments with Various Gravitation-levels and with Materials of Different Flowability]".

Acknowledgements

The work presented here was made possible by the financial support of the ESA NPI contract 4000122340 on "Physical Properties of Powder-Based 3D-Printing in Space and On-Ground", and of the DLR/DAAD Research Fellowship 91647576, as well as the ESA Education Fly Your Thesis! 2019 flight opportunity and sponsoring through the GrainPower project: thank you for believing in this project; in doing so, *you* made it happen.

I would like to express my deepest appreciation to my committee, in the hope to raise their interest and foster insightful scientific discussions. Particularly, my most sincere acknowledgements go to Prof. Dr. Andreas Meyer for his renewed support, and for the freedom and trust he gave me throughout my doctoral research. I am also grateful to Priv.-Doz. Dr. Jürgen Brillo for his assistance, displayed at all times with calm and kindness. Lastly, thank you to Prof. Dr. Dieter Senk, whose encouraging words and scientific interest came at exactly the right moment.

The work presented here (as well as its author) would not have been the same if it was not for the countless discussions with Prof. Dr. Thomas Voigtmann. His intelligent advice, scientific excellence and encouragement have been essential in this work, and enabled me to push the ideas always one step further. Thank you for being the best discussion partner. I would like to extend my gratitude to Dr. Till Kranz, who has followed my work since its infancy, always being able to make me see our work in a brighter light; his help has been truly empowering. It is also important for me to mention here my ESA/EAC tutor, Dr. Aidan Cowley, whose motivating words and brilliant ideas have been a source of inspiration since my time as a Master student. The team of Fly Your Thesis! 2019 from ESA/ESTEC, and particularly Dr. Nigel Savage, has also taken a large part in the success of this project, by closely following the evolution of the engineering work during prototypes construction, remaining kind, caring and supportive in the bright moments but also through the difficult times. Special thanks to Dr. Andrew Barnes and the entire team of ESA/ECSAT (particularly Dr. Martina Meisnar) and STFC/ITAC (particularly Dr. Joe Bennett and Chantal Fowler) for their warm welcome in the ESA/ECSAT centre and their scientific help. Thank you to Dr. Raphael Widely for his help and patience with the tomography of my samples. I cannot leave DLR without mentioning the Granular group as a whole, and in particular Dr. Philip Born for his very good lectures on granular materials and many times pointing out excellent readings. I would also like to acknowledge the DLR-MP workshop and in particular Horst Esser – Herzlichen Dank für Deine Unterstützung. Finally, the entire Novespace team has by far deserved to be cited for their (sometimes) friendly assistance, and in particular Thomas Villatte for his forbearance, put to the test a few times.

I also want to express how grateful I am to the students I had the luck to work with and/or tutor. I cannot express the gratitude I have for Felix Kuthe, with who we built the RheoPrint prototype 3D printers, our babies *Barbie* and *Lafayette*. He is the one and only person to

whom I will say: I would not have made it without you. More generally, the entire GrainPower team has been a breath of fresh air in the most stressful times: Merve Seçkin, Abeba Birhane and Tolga Bastürk, thank you a thousand times – and let's do it again! Anabelle Horb was a great student and I cannot thank her enough for all the moments shared. The realisation of the piston-probing PFC experiment was fully carried out with her (in the context of her Master diploma thesis); it would not have happened if it was not for her careful work and determination. The simulation work was conducted with Szu-Jia Liu, within the framework of a three months Bachelor internship, selected and financed by DAAD as part of the RISE 2019 program under the grant number 57467143 for the project "Characterising powder flow in a prototype microgravity powder-based 3D printer". She has been a very promising student; her serious work and reliability make her someone I hope to work with again. Lastly, I am glad that I had the chance to work with Joshua Kiefer, and hope we will have the opportunity to continue our research on the rheology of Lunar regolith and its simulants.

Indeed, my friends and colleagues deserve to be acknowledged. Dr. Luis Fernando Elizondo-Aguilera, Laura André-Boyet and Antoine Micallef, Dr. Christian Neumann, Dr. Alexandre Meurisse, Dr. Jan Haeberle, Dr. Sebastian Pitikaris, Dr. Mitja Beckers, Thomas Werner and all the others: thank you for finding the perfect balance between enlightening discussions and delightful company. Thank you to Jonas D'Angelo for sharing my life, and to Fanny and Claire Schaepelynck for being the most amazing sisters I ever had. All my love goes to Samia Kachkachi and Carlos Lopez for their infallible support and instilling in me the belief that one decides who they are for themselves; not once and for all, but at each and every instant.

Contents

Abstract

Acknowledgements

Introduction **1**

I Granular rheology under varying gravitational environment **5**

1 Granular matter – from discrete elements to continuum description **7**
1.1 Long range force transmission in dense packings . . . 7
1.1.1 Force-chain network . . . 8
1.1.2 Stress redistribution in a contained granulate . . . 9
1.1.3 The jamming transition from flowing to static matter . . . 12
1.2 Powder rheology: the study of flowing granulate . . . 13
1.2.1 From measuring flow curves to identifying rheological regimes . . . 13
1.2.2 Rheometry: granular media under shear . . . 14
1.2.3 Flow inhomogeneity, hysteresis and their microscopic grounds . . . 15
1.3 Dilute and fluidised states of granular matter . . . 16
1.3.1 Granular gas . . . 16
1.3.2 Fluidised granular bed . . . 17
1.3.3 Granular temperature . . . 17
1.4 Towards a theoretical description of powder flow? . . . 18
1.4.1 Challenges preventing large scale predictions . . . 18
1.4.2 The mode coupling theory applied to granular flows . . . 19
1.4.3 Validation of granular mode coupling theory: experimental results . . . 21
1.5 Conclusion . . . 24

2 Granular rheology **25**
2.1 Material: introducing the main characters . . . 25
2.2 Phenomenological definitions of flowability . . . 28
2.2.1 Defining *powder flowability* . . . 28
2.2.2 Process-relevant measurements of powder flowability . . . 29
2.2.3 Standardised test procedure: the *flow energy* measurement . . . 31
2.2.4 Flowability-probing procedures: grandeur and decadence . . . 36
2.3 Tensile strength of the granular packing . . . 37
2.4 Rheological properties of granular media . . . 39
2.4.1 Rheometry installation . . . 39
2.4.2 Start-up curves . . . 40

2.4.3 Flow curves . . . 42
2.5 Discussion & conclusion . . . 44
2.5.1 What relevant parameters influence granular rheology? . . . 44
2.5.2 Conclusion . . . 46

3 Handling granular matter in microgravity 49
3.1 Change in relative force contributions as a function of g-level . . . 49
3.1.1 Cohesive forces between grains *versus* gravitational force . . . 49
3.1.2 Granular Bond number . . . 53
3.2 Triggering powder flow in microgravity . . . 54
3.2.1 Microgravity experiment: piston-probing of granular packing . . . 54
3.2.2 Results: granular response to piston-probing in $0g$ *vs.* $1g$ . . . 56
3.2.3 Discussion: influence of the gravity on granular flow . . . 63
3.3 Conclusion: controlling powder flow in microgravity . . . 66

II Powder-based additive manufacturing for space 69

4 State of the Art 71
4.1 A brief overview of AM technologies . . . 72
4.1.1 Early development of additive manufacturing . . . 72
4.1.2 Technologies available today . . . 73
4.2 In-space manufacturing . . . 73
4.2.1 Extrusion-based AM: the *one* available technology . . . 73
4.2.2 Directed energy deposition: promises and reality . . . 77
4.2.3 Powder-bed stabilisation for low- and microgravity . . . 79
4.3 Recycling in space . . . 82
4.4 Process *in-situ* monitoring for quality assurance . . . 83
4.5 The future of in-space manufacturing . . . 84
4.5.1 Bioprinting in space . . . 84
4.5.2 A fully integrated FabLab in space? . . . 84
4.5.3 In-space manufacturing of large structures . . . 85
4.6 Conclusion: technological gap . . . 86

5 The RheoPrint additive manufacturing process 87
5.1 Challenges . . . 87
5.1.1 Variability in behaviour & environment dependency . . . 87
5.1.2 Force transmission & reorientation . . . 88
5.1.3 Tendency to jam . . . 88
5.1.4 Restricted type of stimuli for enforcing flow . . . 89
5.2 Description of the RheoPrint process . . . 89
5.2.1 Confinement: a new approach to powder-based manufacturing . . . 90
5.2.2 Desired powder movement . . . 91
5.2.3 3D printing procedure . . . 95
5.2.4 *In-situ* monitoring: towards autonomous manufacturing . . . 96
5.3 Limitations . . . 97
5.3.1 Limitations in material properties . . . 97
5.3.2 Limiting factors in size . . . 99
5.4 Conclusion . . . 101

6 Simulation of powder flow **103**
6.1 Motivations . . . 103
6.2 Principle of study . . . 103
6.2.1 Simulation principle . . . 103
6.2.2 Methodology for data analysis . . . 110
6.3 Results & discussion . . . 112
6.3.1 Rotation speed of the movements . . . 112
6.3.2 Simulating consecutive steps . . . 114
6.3.3 Influence of gravity . . . 115
6.3.4 Impact of cohesive forces between grains . . . 118
6.4 Conclusion . . . 121

7 Design & construction of RheoPrint prototypes **123**
7.1 Motivations & scientific objectives . . . 123
7.2 Microgravity platform . . . 124
7.2.1 Existing experimental microgravity platforms . . . 124
7.2.2 Technology demonstration . . . 124
7.3 Prototypes development . . . 125
7.3.1 Hardware . . . 126
7.3.2 Printing procedure . . . 134
7.3.3 Controls & electronics . . . 136
7.3.4 Solidification system . . . 142
7.3.5 Solidification window . . . 147
7.3.6 Implementation of live-monitoring . . . 150
7.4 Experimental methodology . . . 151
7.4.1 Parabolic flight environment . . . 151
7.4.2 Material . . . 153
7.4.3 Experimental plan & procedure . . . 154
7.5 Conclusion: obtaining a proof of concept . . . 156

III Evaluation of the RheoPrint process **157**

8 Results: analysis of 3D printed samples **159**
8.1 Characterisation methods employed . . . 159
8.1.1 *In-situ* monitoring of layers homogeneity . . . 159
8.1.2 Live rheological probing of feedstock . . . 161
8.1.3 Calculation of the energy transferred for powder deposition . . . 165
8.1.4 Introducing a *flowability* dimensionless number . . . 165
8.1.5 Post-manufacture characterisation: X-ray tomography . . . 166
8.1.6 Samples density homogeneity in bulk & pore size distribution . . . 167
8.2 Manufacturing from powders of high to mediocre flowability . . . 169
8.2.1 Reliability of torque as *in-situ* rheological characterisation . . . 169
8.2.2 Dependence of homogenisation time on powder nature . . . 173
8.2.3 Density of parts manufactured on-ground & porosity size distribution . . . 174
8.3 A gravity-independent process? . . . 176
8.3.1 Torque recorded in-flight during material deposition . . . 177
8.3.2 In-flight data: powder layer homogenisation time . . . 181
8.3.3 Density & pore size distribution for parts manufactured in microgravity . 181

8.4 3D printing recycled material . . . 188
8.4.1 Recycled powder: physical & rheological characterisation . . . 188
8.4.2 Samples 3D printed from closed-loop recycling . . . 190
8.4.3 *In-situ* probing of recycled material during manufacturing . . . 191
8.5 Conclusion: a process tailored for space applications . . . 193

Conclusion **199**

List of acronyms **i**

List of Figures **iii**

List of Tables **xiv**

Appendices **xvi**

A Observing force chains formation **xviii**

B Simulation **xx**
B.1 Command script . . . xx
B.2 Snapshots of simulation results . . . xxv

C Electronic hardware specifications **xxx**
C.1 Inner tube . . . xxx
C.2 Closing disc . . . xxxi
C.3 Outer tube . . . xxxi
C.4 Vibrating disc . . . xxxii
C.5 Infrared lamp . . . xxxii

D Printed circuit boards **xxxiv**

E Cognitive science project **xxxvi**

F Curriculum vitae **xxxviii**

Introduction

The possibility to explore space has fascinated humankind since long. The myth of the unknown territory aside, scientific, technological, economical and ecological challenges make the prospect of leaving Earth manifold and fascinating.

Space exploration missions are severely constrained by payload capacity. For long-endurance missions, such as long-term human presence on the Moon, a lunar orbiter or a journey to Mars – and back? – the crew cannot rely on material support from Earth [1]. Functional parts, replacement items and multi-purpose tools need to be manufactured directly in space. Instead of launching entire sets of spare parts, fully equipped toolboxes and contingency payload at high environmental and financial costs – around $25 000 per kilo in 2018 using the Falcon 9 and Dragon cargo capsule to resupply the International Space Station (ISS) [2] – sending to space a machine to create parts from raw material and a virtual database would drastically increase self-sufficiency of crewed and robotic missions [3–5].

Additive Manufacturing (AM) technologies are the future of sustainable parts production, since only the quantity of material needed for creating the part is consumed [6, 7]. Space is a hostile, unforgiving environment, where adaptability is a matter of survival; allowing on-demand part production directly in space, In-Space Manufacturing (ISM) would increase missions' self-sustainability by allowing to independently solve unexpected issues. Payload optimisation leads to the need for adaptable technologies, able to handle recycled materials. To this day, only filament-based three dimensional (3D) printing is used as a permanent utility in space [8, 9]. Yet, mere *functioning* in microgravity is a necessary, but not sufficient condition for a technology to be viable for space applications, and filament-based AM processes suffer inherent limitations. Powder-based technologies allow for higher precision than any filament-based process [10], and easier recycling if the process is based on a single raw material, without binder or processing fluids. Developing a powder-based AM technique for space applications would provide a more versatile technology, adaptable to multiple raw materials – notably, materials with heterogeneous flow-properties like recycled material or regolith, the highly abrasive material abundant on planetary surfaces and main *in-situ* resource for planetary exploration [11]. Yet, all commercially available powder-based processes crucially rely on gravity and on high-flowability powder feedstock for material deposition. The outlines of a technological gap appear: instead of adapting existing powder-handling processes to reduced gravity, and continuing to especially manufacture powders to conform to the available techniques, the desired powder-based AM process would be adaptable to the powder it is fed, and robust against varying gravitational environments.

Developing such process must go hand in hand with understanding fundamental principles of powder flow under varying gravitational environments. Granular rheology, the study of flowing granular media, is a wide field of research which includes many unknown territories,

even on-ground [12, 13]. Dense granular flows are difficult to model, as the force transmission between particles happens simultaneously on two scales: on the local scale, direct interactions between the grains transmit force and momentum by friction; on the scale of the packing, a network of force chains carries long-ranged forces. Hitherto, in absence of a constitutive law governing granular flows, the development of powder-based processes has been largely empirical. A radical environmental change – e.g. a change in gravitational field – challenges our conception of powder rheological behaviour, forcing us to invent new methods to trigger and control powder flow independently of gravity.

The approach taken in this work is to study in parallel powder rheology under different gravitational fields and develop a powder-handling method that emerges from it, towards the invention of a gravity-independent method to additively manufacture objects regardless of the flow-properties of the feedstock material.

This thesis is structured in three parts, from granular rheology on-ground and in microgravity (Part I) to the development of a novel process for handling and 3D printing powders, tailored for space applications (Part II), and finally the assessment of this process (Part III). In this last segment, we will link back the rheology of the feedstock material to the quality of the printed samples, thereby evaluating the adaptability of the process, through its printing parameters, to changes in base-material and in gravitational environment. Specifically, this entails the following points:

- After making acquaintance with the wonders of granular materials, the rheological concepts that will be used throughout this work will be defined in Chapter 1.
- A series of rheological measurements, conducted by the author and presented at the end of Chapter 1, provide new experimental data that are in remarkably good agreement with recent predictions of a microscopic theory proposed by Kranz *et al.* [14], hence confirming the appearance of three qualitatively different rheological regimes in agitated granular materials under shear.
- Two granular materials, composed of polystyrene (PS) grains differing solely by their surface state (smooth *versus* rough) will be used as model systems in the different stages of this work. First, their flow-behaviour will be characterised through four state-of-the-art rheological tests in Chapter 2, showing how the combined effect of particle roughness and packing density result in a rich and complex rheology.
- After having presented rheological measurements on-ground in Chapter 2, we will turn to microgravity in Chapter 3. Theoretical analysis of the force-balance change as a function of the gravitational environment will be followed by the results of a parabolic flight experiment that flew on the 31st DLR Parabolic Flight Campaign (PFC) in March 2018, aiming to understand how to trigger and control powder flow through boundary forces in microgravity.
- Concomitantly, the parabolic flight experiment presented in Chapter 3 will provide experimental proof of the gravity-dependence of the jamming packing fraction.
- From the findings of Chapters 2 and 3, we will extract stable ways of driving powder flow, robust against changes in powder nature and gravitational environment. After a brief overview of available AM techniques and their limitations in Chapter 4, in Chapter 5, the previous finding will be implemented into a novel powder handling method, operational for powders of high to mediocre flowability and regardless of the gravitational environment,

in the perspective of powder-based additive manufacturing for space.

- This powder handling method has been tested through Discrete Element Method (DEM) simulations presented in Chapter 6, and experimentally on PFC. During the the 34^{th} DLR PFC in September 2019, and the 72^{nd} ESA PFC, in November 2019, a proof of concept in microgravity was obtained for this method for powders of good to mediocre flowability.
- In Chapter 7, the reader will be taken through the design and construction of the two prototype 3D printers used to demonstrate the feasibility of this method on-ground, then on parabolic flights to access microgravity conditions.
- Through the analysis of samples 3D printed under different gravitational fields and from the smooth and rough powers characterised in Chapter 2, the viability of this material deposition technique for powder-based additive manufacturing for space applications will be assessed in Chapter 8.
- Finally, the applicability of this AM process for closed-loop recycling will be tested, as discussed in Chapter 8, by printing from recycled powder obtained from grinding former printed objects.

Part I

Granular rheology under varying gravitational environment

Chapter 1

Granular matter – from discrete elements to continuum description

A granular medium is a discrete material formed by a conglomerate of particles *big enough* not to be subject to thermal motion, but small enough such that on the scales of interest in the application context, continuous material properties emerge. The idea of *big enough* seems loosely defined, because granular materials are "defined by their behaviour": the lower limit in size of grains at which a particulate solid is called a granular material is defined by the fact that its particles cannot be moved by diffusion (thermal motion), in times *relatable* to human timescales [15]. Applying this definition gives particles larger than 1 µm [15, 16]; although this is a general indication rather than a strict rule, it explains that the particles forming granular matter can be qualified as *mesoscopic*, etymologically: large enough to be examined with the naked eye, but small enough that the whole can be examined as a single entity.

The constitutive elements of a granular material interact through dissipative contacts: inelastic collisions and friction dissipate energy as particles collide or slide against each other [12]. In absence of energy input, a granular ensemble will hence sediment, eventually reaching a state of rest. The study of granular media (the term powder will be used synonymously) is therefore one of materials inherently out of equilibrium.

Coupled with negligible thermal agitation, this dissipative nature implies that unlike a gas, a granular material does not expand to the entire volume available. Therefore, it is subject to local phenomena: heterogeneous packing density can give rise to jamming [17], clustering, stick-slip behaviour under deformation or shear banding [13]. Those are some of the peculiar phenomena prominent in granular solids that are addressed in this chapter.

1.1 Long range force transmission in dense packings

Inside a granular packing, force transmission happens on the particle-particle level, by direct contact between grains, but also through a long-range network of contact chains spanning through dense packings under load. A multi-scale approach is hence necessary to understand force transmission in granular packing [18].

1.1.1 Force-chain network

Forces are carried within dense packings through the network of contacts between grains, forming force chains, defined as a subset of grains carrying an amount of force *much larger* than the average force [17, 19]. They appear when the medium is transmitting load, may it be when externally compressed or sheared (see Figure 1.1) or simply under its own weight (see Figure 1.2). Majmudar and Behringer [20] report that the force chains form in a sheared sample in the direction of shear (see Figure 1.1a), while under isotropic compression a six-fold symmetry appears (see Figure 1.1b); generally, force chains align with the major principal stress axis [21]. In static experiments, force chains spanning up to 10^2 grains were reported [22, 23]. Such observations with bare eyes were made possible using photoelastic particles, made of a material whose degree of birefringence varies with the local stress level, and placed between two cross-polarising filters [24]. Using this technique, a two dimensional (2D) packing can show the appearance of force chains [17, 19, 25, 26] (see Appendix A) and their magnitude can be measured [20, 27].

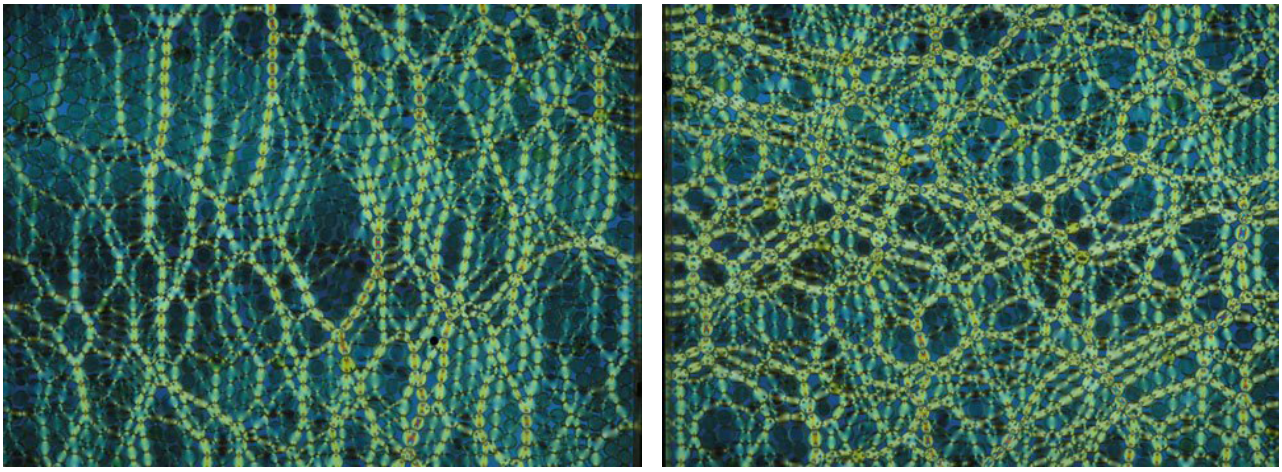

(a) Shear **(b)** Compression

Figure 1.1: Force chains appearing (a) during shear and (b) in isotropic compression, made visible using stress-birefringent photo-elastic 2D particles. Images from Ref. [28], reproduced with permission of Springer.

Force chains and redistribution of forces in a static packing. Force transmission through force chains among a discrete solid leads to a redistribution of the direction of application of those forces. Edwards and Mounfield [29–31] showed from geometrical arguments that in a pile of granular beads, regardless of the beads' shape, the force that one particle applies to the supporting beads below is deflected from its original direction by the mere fact that it is transmitted solely through the contact points. The inhomogeneity of the granular lattice causes an uneven distribution of the weight of each particle on the particles below, creating such redistribution of the force [17, 32]. The force on every grain is the sum of the forces transmitted through contact with the neighbouring grains, inducing large variations in the carried force from one grain to another.

Within a heap of granulate, this deflection repeated at each layer of particles implies the appearance of an arch of force chains that holds most of the weight. As an ogival arch in Gothic architecture, it is reinforced by holding the pressure coming from above, and leaves an inner volume full of particles holding nothing but their own weight. This phenomenon is responsible

for a stress dip observed under a heap of granular matter [33, 34]. The angle at which the forces are deviated is called the internal angle of repose [35]. This is illustrated by the image of a large granular pile under its own weight presented in Figure 1.2, obtained through Discrete Element Method (DEM) simulation by Nadukuru and Michalowski [36].

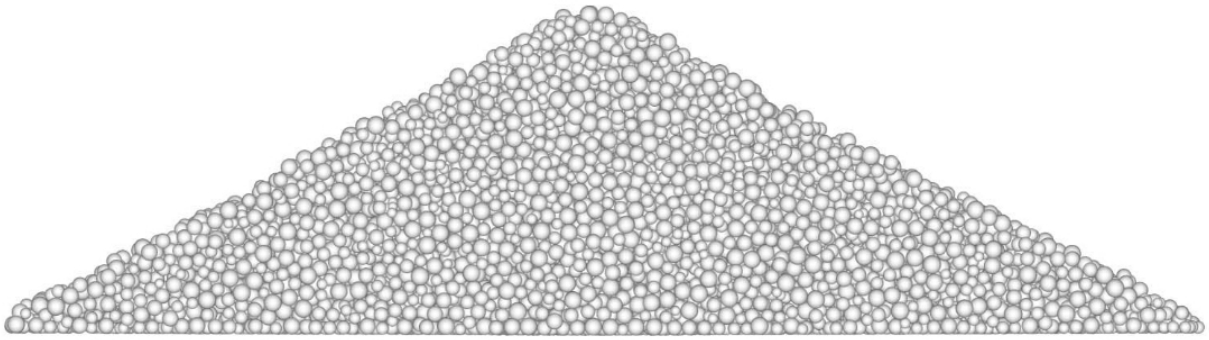

(a) Granular particles simulated

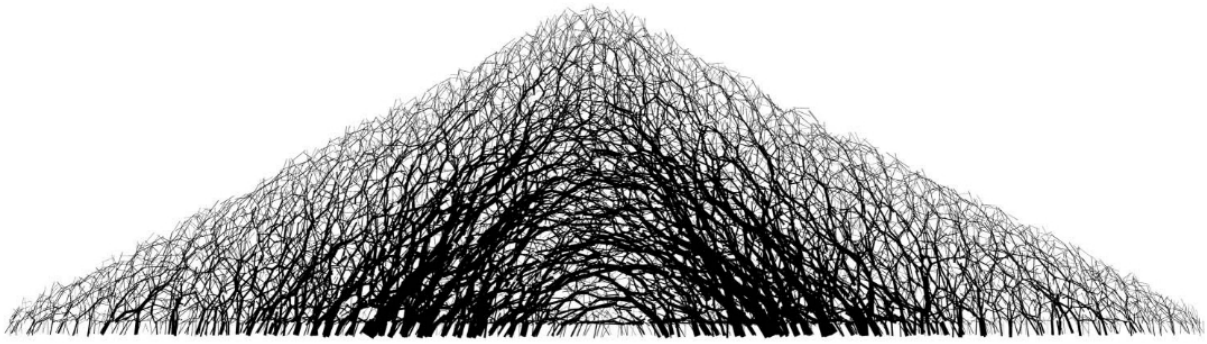

(b) Force chains

Figure 1.2: On a large pile of granular material under its own weight, the force chains arch, inducing an heterogeneous repartition of the weight of the heap. The thickness of the black lines indicates the relative strength of the forces. Image obtained with DEM simulation by Nadukuru and Michalowski – image reproduced from Ref. [36] with permission from ASCE.

If the redistribution of the load among particle derives from geometrical considerations, the average angle at which the forces are redirected depends on the configuration in which each grain rests on the grains underneath, which is set by the physical characteristics of the granular material, including shape, distribution or surface friction of the particles. This dependence of the deviation angle on the structural arrangement of the packing is illustrated by Figure 1.3.

1.1.2 Stress redistribution in a contained granulate

This redistribution of the load through granular media finds implications in a well-known engineering problem: the design of silos. As an interesting back and forth between continuum approach and discrete description, it was first demonstrated through a continuum-mechanics treatment of enclosed granular media by Janssen [37], in 1895, before the idea of force chains was even conceived. The key idea that allows the model proposed by Janssen to be still used today is his intuition that a vertical pressure applied on granular media will be partially transmitted horizontally. This is transcribed by using the ratio of horizontal to vertical stress k to describe

(a) **(b)**

Figure 1.3: Different configurations of the granular packing, as illustrated by configurations (a) and (b), imply different reorientation and redistribution of the force $\vec{F}$ from layer n to layer $n+1$ and then $n+2$. While this is purely geometrical, the angle of reorientation itself depends on the properties of the granular media. Freely adapted from Refs. [29–31].

the stress transfer in granular media:

$$k = \frac{\sigma_h}{\sigma_v}, \tag{1.1}$$

where σ_h is the horizontal pressure and σ_v the vertical pressure in the silo. k takes values between zero and unity; it is the stress-related equivalent to Poisson's ratio, and is sometimes called "Janssen coefficient" or "coefficient of lateral Earth pressure" in soil mechanics.

Let's follow Janssen in his demonstration. We consider a container of height h, cross-section A, and perimeter P, as the one represented in Figure 1.4, and take a slice of height dz from the material contained inside. This material, considered here as a continuum, has a density of ρ^*, corresponding to the apparent density of the granular media: the density of the grains' material in bulk multiplied by its packing fraction. The packing fraction or packing density φ of a granular material is the ratio between the space filled by its constitutive grains and the total space it occupies. Once made the hypothesis that the horizontal stress σ_h is constant per slice, we can assess the force balance on this slice of material.

From above is applied the force $A\,\sigma_v$, due to the weight of material above and potentially an external force $A\,\sigma_v^0$ applied on the top of the pile. The slice itself has a weight of $g\,\rho^* A\,dz$. From below, the force $(\sigma_v + d\sigma_v)\,A$ acts to fulfil force continuity. Finally, static friction between the wall and the material causes an upward tangential force on the entire perimeter of the container: $\sigma_w\,P\,dz$. Equilibrium of forces in the z-direction gives:

$$A\sigma_v + \rho^* g A\,dz = A(\sigma_v + d\sigma_v) + \sigma_w P\,dz. \tag{1.2}$$

Assuming that the friction force is proportional to the normal force through the coefficient of friction of a material, by defining μ as the friction coefficient between the walls and the granular material, we have:

$$\sigma_w = \mu\,\sigma_h = k\,\mu\,\sigma_v. \tag{1.3}$$

Hence a differential equation for the vertical stress σ_v can be obtained:

$$\frac{d\sigma_v}{dz} + \sigma_v \frac{k\mu P}{A} = \rho^* g. \tag{1.4}$$

Equation 1.4 can be solved analytically. For a boundary condition of $\sigma_v = \sigma_v^0$ at $z = 0$, we get the well known Janssen equation, in its general form as we don't assume σ_v^0 null:

$$\sigma_v(z) = \rho^*\,g\,\frac{A}{P\,k\,\mu}\left[1 - \exp\left(-\frac{P\,k\,\mu}{A}z\right)\right] + \sigma_v^0\,\exp\left(-\frac{P\,k\,\mu}{A}z\right). \tag{1.5}$$

σ_h and σ_w can then be deduced by substitution in Equation 1.5, respectively from Equation 1.1 and 1.3.

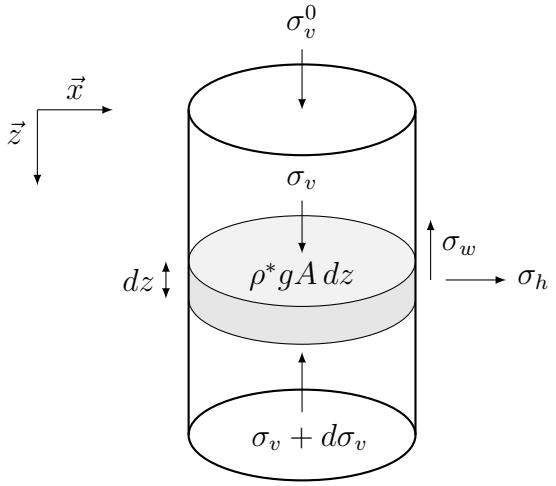

Figure 1.4: Schematic of a cylindrical container full of granular material considered a continuum material. The force balance is assessed along the z-direction on a slice of matter of height dz and of weight $\rho^* g A\, dz$.

This solution is graphically represented in Figure 1.5 for the two cases: σ_v^0 nonzero and null. For the case where no pressure is applied on the top surface ($\sigma_v^0 = 0$), at shallow depth close to the surface ($z \ll {}^{A}/_{Pk\mu}$), the vertical pressure almost shows the same evolution as the hydrostatic pressure in a liquid, with $\sigma_v \approx \rho^* g z$. After the characteristic length ${}^{A}/_{Pk\mu}$, the pressure tends exponentially towards a saturation value at $\sigma_v^{sat} = \rho^* g \frac{A}{Pk\mu}$. For the case $\sigma_v^0 \neq 0$, the term depending on σ_v^0 tends towards zero exponentially; meanwhile the other term becomes predominant and tends towards the saturation value σ_v^{sat}.

The remarkable consequence of this model is that from the intuition of a redistribution of part of the vertical forces spanning across a granular media into horizontal forces, it predicts the appearance of a vertical saturation pressure in the container, hence that for a sufficiently high pile, the pressure at the bottom of the granular packings does not depend on the filling height nor on the pressure applied at the surface.

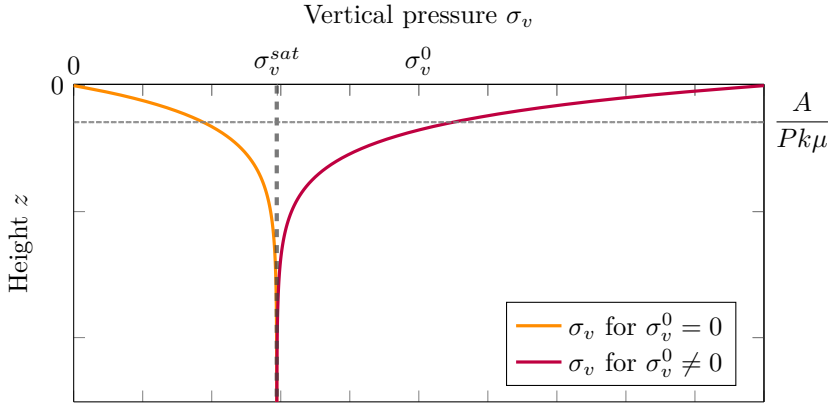

Figure 1.5: Graphical representation of the solution proposed by Janssen, presented in Equation 1.5. The height z in ordinate corresponds to the container height as presented in Figure 1.4: $z = 0$ is the open top surface of the powder bed and the ordinate increases downward.

Physically, the vertical forces are redirected towards the sides through force chains, creating a normal pressure on the walls of the container; this normal pressure towards the frictional walls generates a proportional frictional force (see Equation 1.3), that carries part of the weight of each slice of material. As we see the material as a continuum, the same portion of its weight is carried at each section, which explains the appearance of a saturation pressure. If a pressure is added on the top surface, it will also be transmitted towards the walls in the same proportion, hence decaying exponentially as we go deeper in the material.

Misjudgement of this effect has caused dramatic failure in industrial-scale silos, as imperfections on the inner wall of the container can cause local convergence of normal stress on the walls. It also shows that an increase in radius of the container increases the saturation pressure inside the container, while increasing height does not increase pressure at the bottom of the silo; hence, unlike a water container that should be of large radius and small height to restrain the pressure inside, to increase capacity of grain silos they should be long and thin. This filling-height independent pressure is also responsible for hour-glasses being filled with sand and not with liquids, as time should indeed pass at the same rate, independently of the filling height of the top part of the hour-glass.

1.1.3 The jamming transition from flowing to static matter

As a dense granular packing is deformed, force chains intermittently form and break. This spatiotemporal phenomenon entails self-reorganisation of the granular fabric: the load-bearing network forms a *granular skeleton*, surrounded by the other grains, which in contrast play a minor role in force transmission. This skeleton is defined as *fragile* by Cates *et al.* [38, 39] as it only remains existing as long as the force keeps its same direction of application (on the particles' scale). The slightest change in direction of application will impose a torque on the particles and provoke self-rearrangement of the packing, hence breaking of the force network, that can then reform in a new metastable configuration.

The *jamming transition* describes the changeover between this "flowing state", in which the granular fabric undergoes plastic deformation, and the formation of a resistant, stable contact network that can withstand a high amount of stress without reorganisations [40, 41]. If the packing enters this jammed state, it becomes stiff, undergoing an increase in apparent viscosity to enter a "solid-like state": like an amorphous solid, it is in dynamical arrest and retains its shape under a certain amount of external load. The force chains span throughout the system, transmitting the force to its boundaries instead of triggering flow.

The appearance of a jammed region in a larger packing can be a calamity in industrial processes, as it can draw entire production lines to a halt; it is generally an undesirable phenomenon. Nevertheless, it can also be used to our advantage: Brown *et al.* [42] proposed to use this peculiar property to create a gripper that is able to grab and handle complex-shaped objects by dint of this transition from soft to stiff texture: a granular material is contained into an elastic container; by applying vacuum to this packing, it jams, hence hardening and contracting by approximately 0.5% in volume, ergo securing its hold on the given object without requiring sensory feedback.

1.2 Powder rheology: the study of flowing granulate

Granular rheology is the study of how a granular material flows: it explores the deformation of the granular fabric under load.

1.2.1 From measuring flow curves to identifying rheological regimes

The flow behaviour of a material is established by its flow curve, i.e. the relation between stress and deformation rate. To capture comparable material behaviour, rheological tests often try to isolate a specific type of stimuli. Particularly, in shear tests, the dependence of the shear stress σ applied to the material *versus* its corresponding shear rate $\dot{\gamma}$ can be defined as an effective viscosity η (although it must be noted that we are in the case of an out-of-equilibrium particulate solid):

$$\eta = \frac{\sigma(\dot{\gamma})}{\dot{\gamma}}. \tag{1.6}$$

The material response to shear defines typical rheological behaviours:

- **Newtonian**: the viscosity η is independent of the shear rate $\dot{\gamma}$.
- **Shear-thickening**: the viscosity η increases with increasing shear rate $\dot{\gamma}$. If the viscosity increases over time at constant shear rate, the material is called rheopectic.
- **Shear-thinning**: the viscosity η decreases with increasing shear rate $\dot{\gamma}$. Time-dependent shear-thinning at constant shear rate is called thixotropy.

A granular medium under shear can, given certain conditions of agitation and packing density, exhibit a rheological response akin to a Newtonian, shear-thinning or shear-thickening fluid depending on its packing density and shear rate [14], as will be shown through theoretical prediction and corresponding experiment in Section 1.4. Premises of those different flow regimes in sheared granular media were found through the early rheology experiments of Bagnold [43]. In particular, he showed that a granular material sheared at high shear rate (in his experiment suspended in a Newtonian fluid) can manifest a shear-thickening behaviour later referred to as Bagnold regime, where the shear stress increases quadratically with shear rate:

$$\sigma = B\,\dot{\gamma}^2 \tag{1.7}$$

where B is the so-called Bagnold coefficient.

As mentioned, those typical flow responses are identified by subjecting materials to shear testing, which can be done at fixed shear rate or stress. In the common case of fixed shear rate, the material first undergoes a transient state corresponding to the on-set of flow and illustrated by start-up curves, equivalent to the engineering stress-strain curves in solids. These curves showing stress as a function of time (or strain, as the deformation is imposed at fixed rate) can already provide substantial information about the material. At low strain, the stress increases linearly with time $\sigma = G\,\dot{\gamma}\,t$; the shear modulus G corresponds to the slope of this stress-strain curve. At this point, the structural components of the material remain close to their initial position, and the material is in its elastic region. An overshoot of the stress before reaching its steady-state value can sometimes be observed, displaying the yield stress of the material. More generally, plotting the evolution of stress over time can provide access to irregularities in the flow like stick-slip behaviour, which finds its root in the microscopic interaction between the material's discrete components. For an example of such use, the reader can refer to Section

2.4, where the impact of surface state on rheological response of polymer powders is analysed through start-up curves.

After this initial transient, a plateau is reached, that gives the steady-state stress and hence the effective viscosity of the material at the given shear rate, on which flow curves are based. A typical flow curve of an ordinary fluid is monotonic and positively sloped: stresses increase with increasing flow rate, which is compatible with bulk mechanical stability of the sample. Non-monotonic flow curves show the appearance of flow inhomogeneities [44].

1.2.2 Rheometry: granular media under shear

Certain experimental geometries used more than a century ago remain the base of state-of-the-art machines today. Among them, the set-up referred to as Taylor-Couette or Couette type shear-cell [45–47] consists of two concentric cylinders separated by a gap, inside which the granular sample is placed. One of the cylinders is rotated while the other is static, shearing the material at constant pressure normal to the shear direction (see Figure 1.6 for a simplified top-view). The sample can then be confined by placing a disc closing the gap and applying pressure onto it, or left with an open surface. In a Couette cell, the stress field is inhomogeneous (the shear stress decays over the radius as $1/r^2$) [44, 48]. Despite this being known, the flow profile $v(r)$ is often approximated as linear, such that the shear rate is constant; therefore, the gap between the concentric cylinders ($r_e - r_i$) should generally be small to minimise the error due to this approximation (around ten particle diameters of the largest particles tested) [49, 50]. A larger gap is also prone to provoke the appearance of inhomogeneous flows [44, 48] (*cf.* Section 2.4).

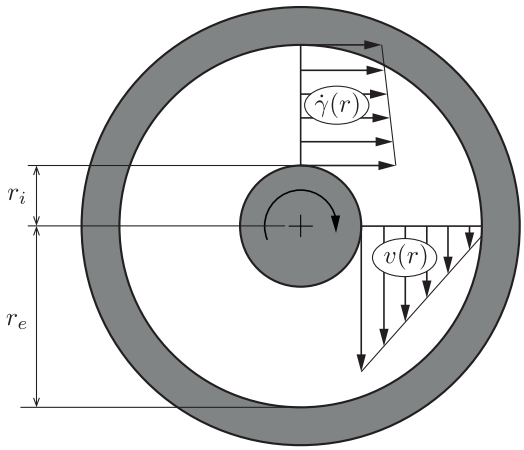

Figure 1.6: Schematic representation of a Couette-Taylor shear-cell seen from above. In this particular example, the inner cylinder is rotated and the outer one is static. The material in the gap is sheared at a rate $\dot{\gamma}$. Image freely adapted from Ref. [50].

The strategies deployed in rheometers to impose a given effort on a sample and measure its resistance to flow are discussed below, as they will be applied in Chapters 5 and 7 to design and construct a machine to probe and handle granular materials in a way that adapts to their flow behaviour.

Control parameters. A rheometer enabling to conduct shear tests can conventionally be velocity-controlled or stress-controlled. It is commanded through the current rotating the rotor, which is varied to adapt to the fixed parameter. The velocity-controlled system is schematised in Figure 1.7. This loop control can be responsible for slight oscillations around the measured value.

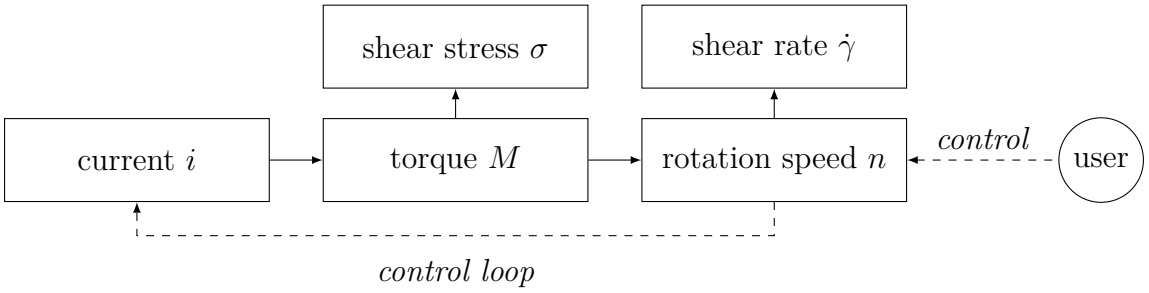

Figure 1.7: Diagram of the control loop of a stress-controlled system. Such system can be deployed even if the variable fixed by the user is the rotation speed of the rotating part of the rheometer, leading to an indirect stress controlled system.

Representative rheological parameters. As featured in Figure 1.7, the variables recorded by the rheometer during a shear test are the revolution per time unit of the inner cylinder n and the torque M developed for the rotation. From those values the shear rate $\dot{\gamma}$ and the shear stress σ are calculated, as shown respectively in Equations 1.8 and 1.9. The same strategy of simultaneous probe and control of the material will be deployed in Part II of the present work, in the development of a powder-handling method for varying gravitational environments.

As previously stated, a linear shear profile is assumed. Consequently, the shear rate $\dot{\gamma}$ is calculated as the ratio of variation in speed over difference in radius throughout the gap between the coaxial cylinders:

$$\dot{\gamma} = \frac{\Delta v}{\Delta r} = \frac{\omega\, r_i}{r_e - r_i} = \frac{r_i}{(r_e - r_i)}\, 2\pi\, n \tag{1.8}$$

where $v = \omega\, r$ is the circumferential velocity at radius r, and ω the angular velocity.

Regarding the shear stress σ, it results from the torque M applied through the rotor. As the direction of application of the force and the lever arm are perpendicular, it is given by:

$$\sigma = \frac{F}{A} = \frac{M}{2\pi\, L\, r_i^2} \tag{1.9}$$

where A is the inner cylinder surface, L its height and r_i its diameter.

1.2.3 Flow inhomogeneity, hysteresis and their microscopic grounds

In granular rheology, the material probed is generally conceived as a continuum; the parameters $\dot{\gamma}$ and σ as previously established are based on this continuum description. However, some microscopic phenomena, reminiscent of the discrete nature of the material, are responsible for inhomogeneities in the flow [44].

Stick-slip. One such manifestation is the *stick-slip* behaviour exhibited by granular materials under shear, defined as periods of slow loading followed by rapid failure [51]. In fixed-velocity

shear tests, stick-slip becomes apparent through the strong oscillations in the stress recorded; each oscillation encompasses a linear phase of elastic loading, followed by plastic creep accompanied by dilatation of the packing, and finally brittle failure [52]. Cain *et al.* [52] also show that an increase in the cohesive force between the grains (in this case, capillary forces) entails an increase of magnitude in the stick-slip response. This is explained by an increased stability of force chains for higher adhesion between particles.

Shear banding. Like many other complex fluids, granular materials can also exhibit *shear banding* [44, 53]. Shear banding qualifies the localisation of the flow in a narrow zone of high particle mobility and lower density. The energy input through shear is dissipated by friction in this zone. Such instability can be identified by flow decaying very rapidly away from the inner cylinder in Couette-type shear cell [48], and in the appearance of non-monotonic flow curves [44].

Hysteresis. Powders keep memory of their previous packing state: the behavior of a granular packing depends on the spatial organisation of the grains, which is engendered by the stress history of the packing; moreover, surface forces between grains are also influenced by the stress history [18]. Therefore, granular media are subject to hysteresis effects, which increases the complexity of both their theoretical modelisation and their experimental manipulation.

1.3 Dilute and fluidised states of granular matter

1.3.1 Granular gas

A granular gas is defined as the dilute state of granular material where the mean free path of each particle is substantially larger than its diameter [54]. Given the inherent athermal and dissipative nature of granulates, this can only be achieved by a regular energy input into the system [55]. Moreover, to avoid sedimentation, the gaseous state of granular material is best achieved in absence of gravity [56–59].

Whereas difficult to access through experiment, this regime has been favourable to theoretical descriptions. The kinetic theory of molecular gases was extended to granular gases [60, 61]. The two regimes of granular gases, namely driven gas (kinetic energy is kept constant by external input) and cooling (the system is undisturbed, hence progressively reaching a state or rest), have been accurately described (see respectively Refs. [62] and [59, 63]).

Dynamical clustering. The dissipative nature of the interactions between grains in a dilute system leads to *clustering*, defined by McNamara and Young [64] as the spontaneous non-uniformity in the packing density that appears for coefficient of restitution inferior to unity. The coefficient of restitution of a particle is the ratio of its outgoing velocity after collision to its incoming velocity before collision; it represents a measure of energy dissipation in the granular material. Studies of the formation of particle clusters starting from a low-density state have been conducted through experiments [65] and simulation [66–69]. In particular, Opsomer *et al.* [67, 68] propose to use dynamical clustering to gather and handle granular material in microgravity. An important result is the linear transport of granular material through asymmetrical driving. This transport strategy through dynamical clustering is exploited in Chapter 5 to transport granular material by horizontal vibration and to homogenise the packing density in microgravity.

1.3.2 Fluidised granular bed

Fluidisation is a physical phenomenon observed when, under certain conditions, a granular medium transitions from a static solid-like state to a dynamic fluid-like state. A granular medium can be fluidised by shaking, or by flow of either a liquid or a gas [70].

In a gas-fluidised granular bed, the gas flows upward through the granular medium into the interstices between the particles. At low gas velocity, the aerodynamic drag on each single particle is low, hence they are not displaced by the air flow and stay static. As the gas velocity is increased, the aerodynamic drag begins to counteract the gravitational force acting on each particle. The bed expands, as the fluid streams between the particles. A threshold is reached when the upward drag forces and downward gravitational forces compensate each other; this tipping point is called the *point of minimum fluidisation gas flow*. Then, once the drag of the fluid also overcomes the frictional attractive interactions within the packing, the packing has passed its *fluidisation point*: the granular bed is fluidised. From this point on, the particles are suspended within the fluid, and the fluidised bed shows the characteristics of a fluid – for example, it conforms to the shape of its container, and keeps a surface normal to the direction of gravity. Once the bed is fluidised, its packing fraction continually decreases as the air velocity increases. Bubbles eventually appear in the fluidised bed as the air velocity is further increased (this step is generally refereed to as *bubbling fluidisation*). The medium becomes unsteady as the bubbles create local density gradients. Then emerges *turbulent fluidisation*, as the medium becomes completely inhomogeneous. Finally, if the air velocity is yet increased, the particles no longer form a granular bed as they are conveyed by the gas flow.

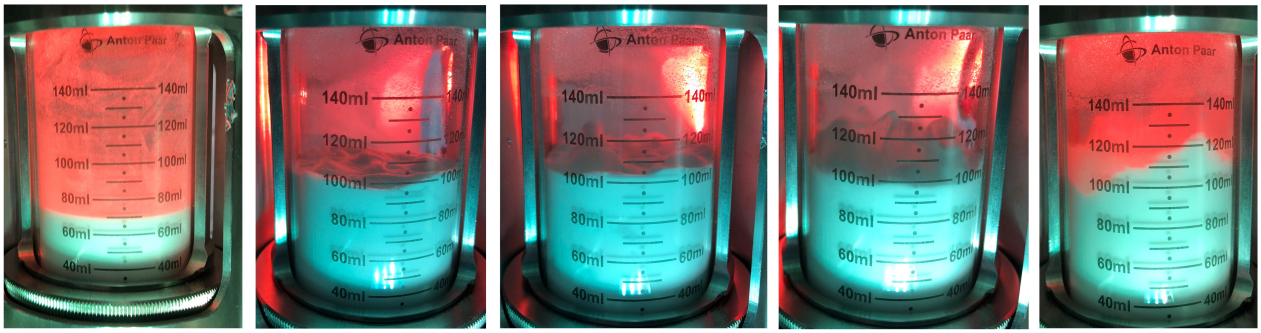

(a) (b) (c) (d) (e)

Figure 1.8: The type of fluidisation observed in the granular bed shifts as the gas velocity u (or flow rate Q) is increased, from (a) no fluidisation to (e) turbulent fluidisation, for the same powder sample.

1.3.3 Granular temperature

As previously explained, temperature in its thermodynamical sense is not a relevant parameter in the study of granular media. However, a quantity measuring the *agitation* (or *velocity fluctuations*) of grains resulting from the fact that they are in motion (and regardless of *how* they are put in motion, e.g. through shaking, fluidisation, magnetic or electrostatic field…) have been proposed: the granular temperature T_{gr}. Particularly relevant for granular gases and fluidised granular beds as in those two cases the particles are externally agitated, it is defined in a space of D dimensions as the average kinetic energy of particles of mass m moving at speed v:

$$T_{gr} = \frac{1}{D} m \langle v^2 \rangle. \tag{1.10}$$

Despite being derived from the kinetic theory for granular gas, the concept of *granular temperature* applies in principle to agitated granular material at high packing density [71] and also enters in theoretical modelling beyond granular gases [14].

1.4 Towards a theoretical description of powder flow?

1.4.1 Challenges preventing large scale predictions

A reliable continuum description of granular flows is desirable for safety [72] and efficiency [73] of human constructions, on Earth and in space [74]. But the coexistence of multiple regimes, sometimes within one granular system [13, 44], multiple modes of interaction among particles through a wide range of length-scales [17, 75] and hysteresis [18] make dense granular systems difficult to encompass under a unified description. The lack of coherence in existing models was highlighted in 2006 by Aranson and Tsimring [76], who point out that "the theoretical description of granular systems remains largely a plethora of different, often contradictory concepts and approaches."

In the solid-like regime, identified by lasting contacts among particles and little grain mobility, the statistical nature of the repartition of forces incites to propose statistical models of force transmission in dense granular packings [17, 18]. In the gas-like regime, kinetic theory has been derived for collisional rapid flows [77]. For dense granular flows, only recently have systematic experiments, simulations and theory begun to merge into a coherent picture of granular rheology; it emerges from such studies that granular rheology depends sensitively on confinement pressure [78]. The $\mu(I)$ rheology proposes an empirical approach based on relating the dimensionless inertial number I to the internal friction $\mu = {}^{\sigma}/_{p}$ [79]. I, as the ratio of intrinsic to external time scales, quantifies the importance of inertial over shear forces, and μ is the friction parameter linking the vertical pressure applied to the packing boundary to the internal friction forces. Yet, to date, no continuum model of granular materials as a whole is widely accepted. While particle-interactions based simulations are commonly used in academia and industrial applications [80, 81], they show significant inaccuracies and necessitate experimental validation. The simplified interaction models used in simulation need to be carefully checked against the much more complex realistic systems, as the picture they propose can deviate from the reality of relevant granular materials [82]. Moreover, granular systems being prone to develop inhomogeneous response to external driving, system-size effects in particle-based simulations can be cumbersome to check. (The reader is referred to Chapter 6 for a complete description of the principle of Discrete Element Method (DEM) simulation and its application to powder transport in varying gravitational environment.)

Recently, Kranz *et al.* [14, 83–87] proposed a novel approach to the theoretical description of granular flows: by applying the Mode Coupling Theory (MCT) to shear flow of driven granular fluids, they provide a dynamical theory to predict the viscosity of such material at high density and finite shear rate. If this model would be proven to reflect reality faithfully, it would represent a meaningful progress in understanding granular flows. Rheological measurements were conducted in the framework of the present work to provide experimental proof of this theoretical description.

1.4.2 The mode coupling theory applied to granular flows

Kranz *et al.* propose to describe granular dynamics through MCT. MCT was originally developed by Götze and coworkers [88, 89] to describe the complex behaviour of glass forming materials. Glasses are solid materials that show an absence of structural order on large scales, reminiscent of the structure of liquids, and *infinite* viscosity η (i.e. relaxation time beyond human-relatable time-scales) [90]. They are challenging to model theoretically, and a strict distinction between liquid- and (amorphous) solid-state is necessary of dynamic origin.

Mode coupling theory: from glassy materials to granulates. MCT distinguishes itself from other glassy dynamics theories by relying only on first principles, hence detaching from phenomenological assumptions (albeit also making *ad hoc* approximations). In other words, MCT requires as inputs solely signature constants of the system (like density and temperature) and the average microscopic structure of the material, providing information on the nature of particle interaction. The latter is provided through the static structure factor $S(k)$. As output, after suitable approximations, it aims to provide the complete picture of relaxation dynamics through the average movement of the elements in the system, hence predicting the state of matter in amorphous systems. Precisely, the relaxation dynamics are characterised by the density correlation function $F(k,t)$, which measures the statistical *similarity* in the system from its state at a given instant to its state t later, at a length-scale $1/k$. For a solid, $F(k,t)$ fails to decay to zero at long times. The long-time limit (i.e. $t \to \infty$) of $F(k,t)$ thus provides a precise prediction of the critical point at which the transition to glassy solid-state takes place; such prediction represents one important success of MCT. A clear description of MCT applied to glassy materials and its recent developments can be found in Ref. [91].

MCT is actually a formalisation of the *cage effect*, a mechanism proposed to be behind vitrification dynamics. The cage effect refers to the particles each being "trapped" in cages formed by the surrounding particles, which restrains particle motion in the system. This caging phenomenon explains the transition from liquid (with long-range, almost unrestrained particle movement) to supercooled liquid (the particles can *eventually* escape the cage formed by surrounding particles), and finally to glass (the particles are restrained from long-range motion by trapping, and being trapped, by the neighbouring elements).

The transposition of MCT to granular materials proposed by Kranz *et al.* [83–85] must account for the fact that MCT is inherently based on thermally agitated particles. Hence, it is valid under the condition that an external energy source be added to compensate the dissipative nature of granular particles. A way to realise such system experimentally is to use driven granular media, fluidised by an air flow or by vibration [92]. In the model they propose, random particles kicks are therefore introduced, through a collision frequency ω_c. The granular system can thus be described by its granular temperature T_{gr}, which summarises the balance between the driving power P used to agitate the material, and the energy loss due to inelastic collisions at the given granular density φ. Dissipation is introduced through the coefficient of normal restitution ε – a detailed description of the coefficient ε is found in Section 6.2.

Generalisation to granular shear flow. To obtain a generalisation of MCT to far from equilibrium stationary sheared granular fluids, Kranz *et al.* [14, 86, 87] combine granular MCT with the Integration Through Transients (ITT) formalism. The latter relates macroscopic stress to a microscopic quantity known as the dynamical shear modulus $G(t,t')$ [93], which gives the stress evolution at a given shear rate between two times t and t'. The dynamical shear modulus

$G(t, t')$ is approximated through the density correlation function $F(k, t - t')$ found by MCT.

The predicted rheology can be summarised by the competition between two effects. On the one hand, the density correlation function decays increasingly slowly with increasing packing fraction: the system being denser and denser, movements of the particles are blocked by their neighbours – this is the cage effect predicted through MCT. Shear on the other hand distorts the granular fabric, hence disrupting the cages, and inputs energy in the system, thereby increasing particle mobility. The result of those competing effects is the prediction of different *flow regimes* as a function of the density φ and shear rate $\dot{\gamma}$.

More specifically, Kranz *et al.* predict that a driven granular material under shear will exhibit two regimes: a fluidisation-dominated regime for $\sigma\dot{\gamma} \ll nP$, and a shear-dominated regime for $nP \ll \sigma\dot{\gamma}$ (n being the number density of particles in the granular fluid). In the fluidisation-dominated regime, the granular temperature T_{gr} is independent of the shear rate $\dot{\gamma}$. If the shear rate is low enough, also the viscosity $\eta = \sigma/\dot{\gamma}$ is constant, entailing a *Newtonian regime*. If shear becomes predominant, two situations arise. At intermediate shear rates, *shear thinning* reflects a shear rate faster than the intrinsic relaxation rate of the granular fluid: σ remains constant independently of the increase of $\dot{\gamma}$. At high shear rates, the granular fluid undergoes a strong shear heating, *shear thickening* is predicted as $\sigma \propto T_{gr} \propto \dot{\gamma}^2$, ultimately showing Bagnold scaling. The predicted flow regimes mapped as a function of packing fraction φ and shear rate $\dot{\gamma}$ (scaled by the collision frequency ω_c to give the relevant time-scale of the system) are summarised in Figure 1.9.

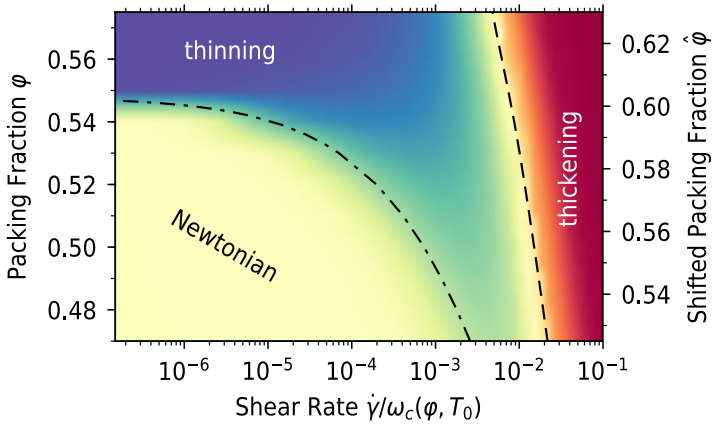

Figure 1.9: Theoretical state diagram of the driven granular fluid under shear. The modelling is conducted for a granular fluid of coefficient of restitution $\varepsilon = 0.5$, at varying packing fraction (with $\hat{\varphi} = \varphi + 5.5\%$) and shear rate $\dot{\gamma}$. The shift in packing fraction is meant to facilitate comparison to experiment, as the MCT is known to underestimate the density at glass transition for elastic hard spheres; however, as the magnitude of this underestimation is not known, it is arbitrarily proposed as 5.5% [14, and references therein]. Image from Ref. [14], licensed under the Creative Commons Attribution 4.0 International.

To conclude, Kranz *et al.* [14, 86] propose a theory to derive the stress σ arising in a sheared granular fluid at high packing fraction φ and finite shear rate $\dot{\gamma}$, based on intrinsic properties of the system; they predict the appearance of various flow regimes. These predictions were subjected to a first test against experiments that have been performed as part of the present work. A direct comparison of predicted and measured flow curves appears very promising and is presented below; this is the first experimental result of the present work.

1.4.3 Validation of granular mode coupling theory: experimental results

Material & procedure. The experimental set-up used consists of an Anton-Paar Modular Compact Rheometer 102 large gap Taylor-Couette type shear-cell, within which the granular sample can be fluidised. This rheological set-up is precisely described in Section 2.4. The granular material used is composed of glass beads of diameter 150 to 200 µm (average diameter of $d = 175\,\mu\text{m}$), for a sample mass of 170 g.

The experimental procedure applied to obtain steady-state flow curves $\sigma(\dot{\gamma})$ consists of measuring startup curves $\sigma(t)$ at fixed rotation velocity, i.e. fixed shear rate $\dot{\gamma}$, for rotation velocities from $5 \cdot 10^{-3}$ min^{-1} to $8 \cdot 10^{2}$ min^{-1}, for different magnitudes of fluidisation (i.e. modifying the flow rate Q of the gas stream fluidising the powder bed). The modification of the fluidisation magnitude also entails a different number density n (or packing fraction $\varphi = n\,\pi d^3/6$), as the volume occupied by the powder bed increases with the air stream flow rate Q, implying in first-order approximation $Q \propto 1/\varphi$. The sweep in shear rate is done first for increasing shear rates, then for decreasing shear rates, in order to ensure reproducibility of the measured data.

Startup flow curves are obtained, setting a shear rate $\dot{\gamma}$ and waiting until reaching a steady state. The necessary time until reaching steady state is generally around one hundred rotations for the inner rotating cylinder[1], which represents, depending on the shear rate, up to approx. 30 h. Then, the measurement is continued for a minimum of one hundred rotations again. The median value of the shear stress σ is taken for each shear rate $\dot{\gamma}$, at all packing fraction φ, representing each one point of the final flow curves; the standard deviation over shear stress values are used to set error bars per point. Results obtained are shown in Figure 1.10; experimental measurements are represented by points, while theoretical predictions appear as solid lines.

Approximations and fitting parameters. To proceed to the comparison proposed in Figure 1.10, certain hypotheses are made. Particularly, to calculate the shear rate from the experimental rotation velocity, a linear shear profile is assumed, considering the flow to be homogeneous; hence, Eq. 1.8 can be used. As previously stated, MCT underestimates packing densities. Therefore, a mapping of packing fractions is adjusted to achieve best accordance in behaviour between experimental and theoretical flow curves. The comparison between matching experimental and theoretical packing fractions (respectively φ_{exp} and φ_{th}) is shown in the inset of Figure 1.10. Theoretical predictions are also shown for all packing fractions φ_{th} between 0.46 and 0.56 at intervals of 0.01 (thin, faded solid lines), giving an indication on the predicted evolution of material rheology *vs.* packing density. Furthermore, it should be noted that the experimental data set of packing fraction $\varphi_{\text{exp}} = 0.607$ (circular purple marks in Figure 1.10) should be considered carefully, as the material has not yet reached its fluidisation point: therefore the granular fluid is not provided with sufficient agitation to be in the state hypothesised by granular MCT.

Theoretical calculations are made for a coefficient of restitution $\varepsilon = 0.5$. Fitting parameters to be determined for the present granular system are the collision frequency ω_c and energy density of the system without shear $n\,T_{gr}^0$, where T_{gr}^0 is the granular temperature solely due to fluidisation. The collision frequency $\omega_c(\varphi,\, T_{gr})$ increases with density and granular temperature

[1] As such duration is unusually long for transient shear flows, the startup curves obtained in the present rheological setup are further discussed in Chapter 2.

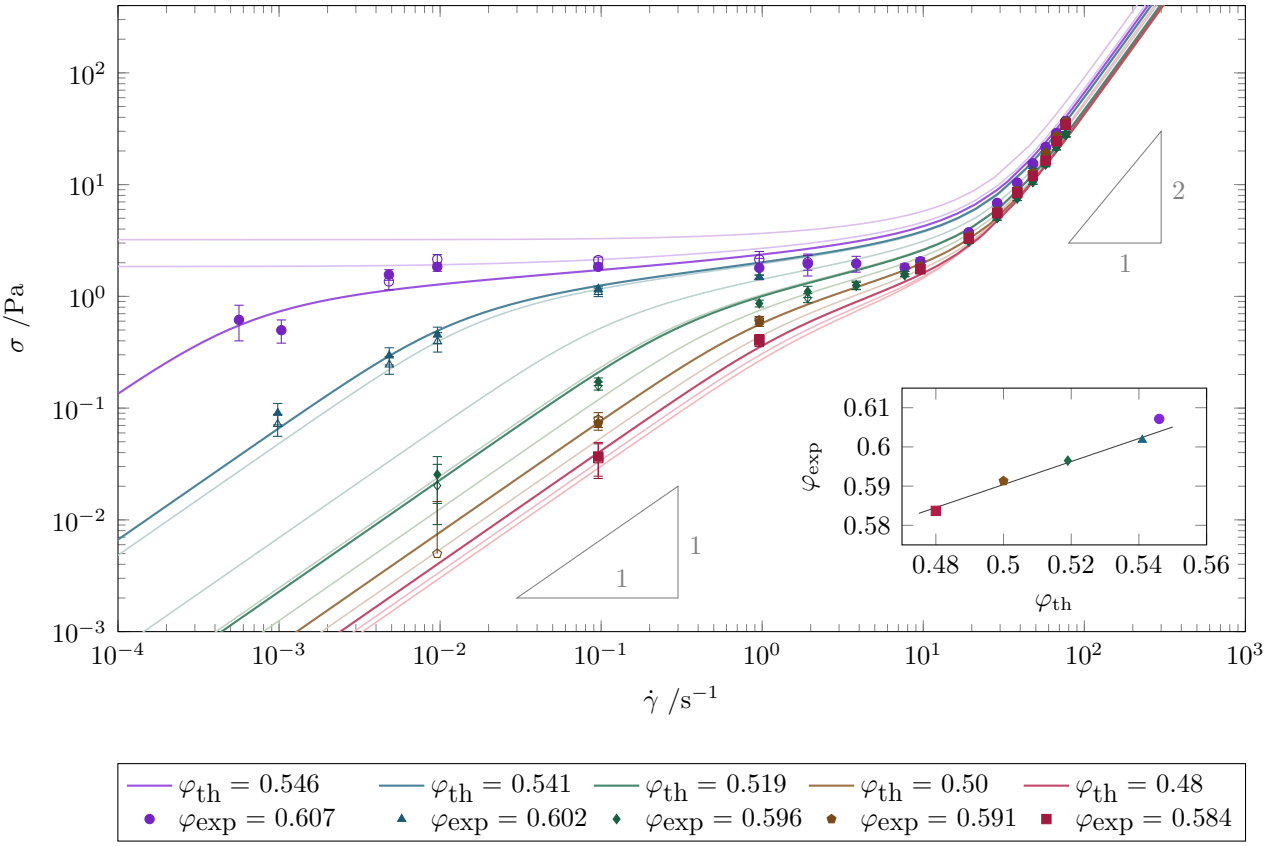

Figure 1.10: Comparison between theoretical prediction proposed by Kranz *et al.* [14, 86] (solid, thicker lines) and experimental data from the present work (marks: full for upward sweep, empty for downward sweep of the shear rate). Error bars on the experimental data points represent the standard deviation on each data set measured per shear rate, at fixed packing fraction. Theoretical predictions are also shown for all φ_{th} between 0.46 and 0.56, at intervals of 0.01, as thin, faded solid lines. Comparison between matching experimental and theoretical packing fractions (respectively φ_{exp} and φ_{th}) is shown in the inset. Fitting parameters (namely the collision frequency ω_c and energy density of the system without shear $n\,T_{gr}^0$) are discussed in the body of the text.

as $\omega_c \propto \chi(\varphi)\,\varphi\,\sqrt{T_{gr}}$ (where $\chi(\varphi)$ is the pair correlation function at contact) [14, and references therein]. Given that $\varphi_{\text{th}} \in [0.48, 0.546]$ is within a small interval, the relation between packing fraction φ_{th} and collision frequency ω_c is assumed to be best approximated linearly in this range (see Figure 1.11).

The linear relation is obtained by fitting the experimental curves to the theoretical predictions; a linear regression made on the five available data points for $\omega_c = f(\varphi_{\text{th}})$ enables to predict collision frequency values for the remaining packing fractions $\varphi_{\text{th}} \in [0.46, 0.56]$ and is presented in Figure 1.11a.

The second fitting parameter is the quantity $n\,T_{gr}^0$. As the number of particles remains constant (within acceptable approximation), but the powder bed volume increases, the number density $n \propto \varphi$. The granular temperature solely due to fluidisation, T_{gr}^0, represents the energy balance of the system, excluding the shear-induced energy; therefore T_{gr}^0 increases with the amount of energy input into the system through the fluidisation gas flow rate Q, and hence is inversely proportional to the packing density φ. Therefore, determining the evolution of $n\,T_{gr}^0$ (which provides the system's shear-independent energy density) with increasing φ amounts to comparing the steepness in increase of T_{gr}^0 and n *vs.* φ. This can be done be comparing

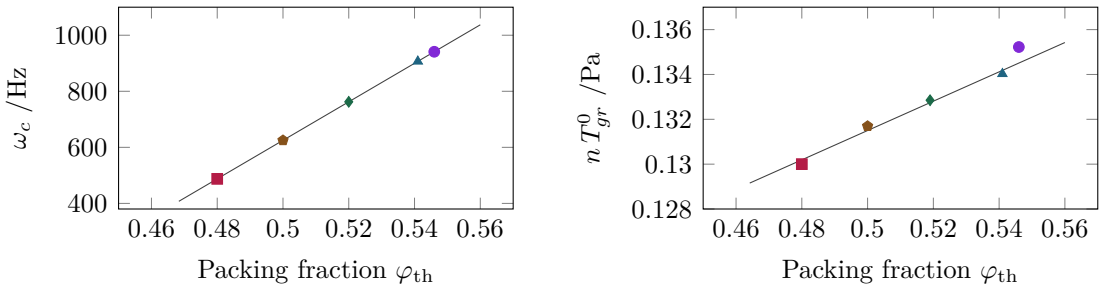

(a) **(b)**

Figure 1.11: Evolution of fitting parameters (a) ω_c and (b) $n\,T^0_{gr}$ as a function of packing fraction φ_{th} used in calculating all theoretical flow curves presented above.

the evolution of those two parameters as compared to $\omega_c(T^0_{gr}) = \omega^0_c$, the shear-independent collision frequency. On the one hand, $n \propto \varphi \propto \omega^0_c$. On the other hand, $\omega_c \propto \sqrt{T_{gr}}$, which remains valid at T^0_{gr}. Hence it is assumed that $n\,T^0_{gr}$ increases with increasing packing fraction. Values are determined by fitting to the experimental data sets; the linear regression thus found is presented in Figure 1.11b, and used to produce the supplementary theoretical flow curves shown in Figure 1.10.

Preliminary observations. Figure 1.10 summarises the comparison obtained between theoretical calculation and experimental measurements. Foremost, the shear regimes predicted by Kranz *et al.* [14] are indeed observed experimentally:

- At low shear rate and packing fraction, where the fluidisation dominates, a *Newtonian regime* is observed as $\sigma \sim \dot{\gamma}$.
- For high shear rates ($\dot{\gamma} > 2 \cdot 10^1$ s^{-1}, roughly independent of packing fraction), shear heating dominates: a quadratic increase $\sigma \propto \dot{\gamma}^2$ is observed, corresponding to a particular type of shear-thickening: the *Bagnold regime*.
- Between those two regimes, σ is almost constant as $\dot{\gamma}$ increases in a window that strongly depends on φ and extends as φ increases: a *shear-thinning regime* becomes apparent.

In the shear thinning regime, measured flow curves recede from the theoretical predictions. At high packing fraction especially, the experimental flow curve shows a more pronounced plateau and a slightly non-monotonic behaviour. This discrepancy could be due to inhomogeneous flow: in the large-gap rheometer used, shear banding is likely to appear, implying two distinct zones at different shear rates could coexist in the system. In such case, the plateau could be a zone of instability of the system. More generally, all experimental curves converge as they enter the Bagnold regime. If a convergence at high shear rates is indeed predicted, the shear thinning regime observed experimentally is restricted to a shorter period, as the system enters the shear thickening regime at shear rate $\dot{\gamma} > 2 \times 10^1$ s^{-1}, regardless of its packing fraction. The accuracy of the prediction in this regime is hence subject to further experiment. Besides, the comparison between experimental and theoretical packing fractions shows a linear dependence rather than a shift in value. The comparison between experimental and theoretical packing fractions shows a linear dependence, $\varphi_{\text{exp}} \simeq a\,\varphi_{\text{th}} + b$ with $a \approx 0.29$ and $b \approx 0.44$, instead of the *ad hoc* shift that was assumed in Ref. [14] (see Figure 1.9). The fitted linear dependence found here is in line with expectations from MCT [88].

1.5 Conclusion

Regardless of their prevalence in industrial and natural disasters, the wealth of complex, multi-variable physical phenomena that govern granular flows is yet to be fully understood.

Reliable and widely applicable constitutive equations describing granular flow would open the possibility to forecast geophysical phenomena like avalanches and landslides, increase efficiency in handling of granular material in industrial processes, or else enable predictions necessary to develop new technologies for sandy, remote and difficult to access environments, among which planetary surfaces. Yet, as granular media are found in multiple states – sometimes coexisting within one system [13, 44] – with various interaction modes and relevant spatial and temporal scales [17, 18, 75], no global description exist therein to enable such predictions. Only relatively recently have systematic experiments, simulations and theory begun to merge into a coherent picture of granular rheology through the $\mu(I)$ approach [79]. The model proposed by Kranz *et al.* for agitated granular media, of which a first direct experimental test was provided as part of the present work, also provides hope that appreciable progress is improving our understanding of granular flows.

In the next chapter, we will see how the flow behaviour of non-fluidised granular materials can be qualified and quantified through different rheological measurements, before focusing on the influence of gravity – or absence thereof – on granular media in Chapter 3.

Chapter 2

Granular rheology

The term *ubiquitous* is hackneyed for qualifying granular materials, as it perfectly outlines their plural nature: they can exhibit, depending on their environment, qualities that reminds us of a *solid*, of a *liquid* or even of a *gas* [13]. Granular rheology, as the study of the flow of granular media, handles them as a continuous material, as we have discussed in the preceding chapter. Yet, microscopic changes in the grain's physical properties generate large changes in the flow behaviour of the powder.

In this chapter, the reader is introduced to the two powders used throughout this work as models for the influence of the changes due to microscopic grain properties on powder flowability. The two powders are composed of grains that share all mechanical and physical properties but their surface state. The rheological characterisation of those two powders is used to propose a comparative study of three state-of-the-art characterisation techniques to access *powder flowability*. In doing so, the following questions will be addressed:

- What is behind the concept of *powder flowability*?
- What are the state-of-the-art techniques to characterise the flow behaviour of a granular material?
- Can the results given by different measurement techniques be compared, and do they let us obtain a coherent characterisation of the material?

2.1 Material: introducing the main characters

The rheology of an ensemble of particles is determined by the properties of the discrete elements, as the grain-scale interactions modify the macroscopic behaviour of the ensemble [75]. To tweak the granular material's rheological properties while preserving the density and mechanical properties of the grains, a strategy consists in modifying the surface of the particles.

The material used throughout the present work is a polystyrene (PS) powder produced by the company Microbeads under the name Dynoseeds. The powders comprise spherical particles of main diameters 40, 80, 140, 250 µm within ±5%. The physical and mechanical properties of the PS bulk-material as given by the manufacturer are summarised in Table 2.1. The powder as-received from the manufacturer is dry-coated with a sub-micron size dust of diameter $\sim 0.01\,\mu m$, as shown in Figures 2.1c and 2.1d as well as 2.2. This powder is called

Rough Surface (*RS*) in the subsequent text. This coating is removed by wet-sieving the powder batch and subjecting it to ultrasound at a frequency of 20 kHz for a duration of 8 hours per batch. The resulting particle surface state is shown in Figure 2.1a and 2.1b: the asperities have been removed, leaving exposed the smooth surface of the spherical particles. This powder is named *Smooth Surface* (*SS*) in the subsequent text.

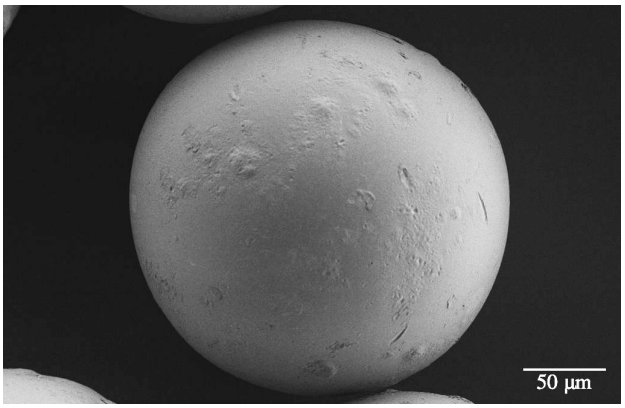

(a) Smooth surface grain

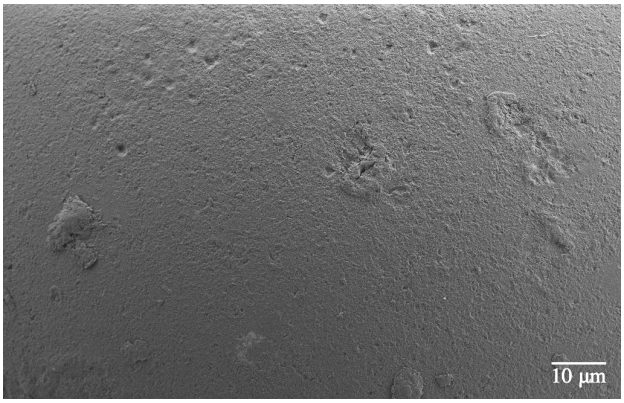

(b) Close-up on the smooth surface

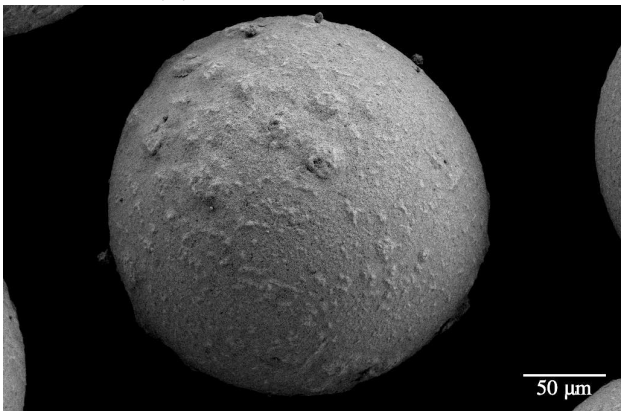

(c) Rough surface grain

(d) Close-up on the rough surface

Figure 2.1: Scanning Electron Microscopy (SEM) images of the PS powder used as raw material (the microscopies are done for particles of diameter 250 µm), (a) for powder with smooth surface state, at the scale of a particle and (b) at the scale of its surface; (c) for powder with rough surface state, at the scale of a particle and (d) at the scale if its surface. The imaging was done using low voltage (1 keV) SEM.

The powders are expected to show more resistance to flow when dry-coated with sub-micron size particles, as the coating creates a rough layer fully covering all the particles' surface [94]. The mechanisms involved are, on the one hand, mechanical locking between the asperities, which thereby decrease the ease of grains to flow past one-another [95]. On the other hand, increase in the van der Waals attractive forces between particles. Maradudin and Mazur [96, 97] show that for a large surface coverage and non-mobile particles, despite the van der Waals interactions between small particles being weaker than between large particles, the global interaction between the two surfaces is larger because each small particles interacts with multiple others.

It should be noted that the addition of small diameter, even angular powders, can be used as flow enhancer under certain conditions [70, 98, 99]. The guest particles, which are mobile and roll on the surface of the large particles, should comply to a certain ratio in size as compared

to the large particles (predictions are given by the Rumpf model [100]; for experimental proof see Ref. [101]). The mechanism involved is the diminution of the cohesive van der Waals forces between particles, and is thoughtfully described in Refs. [70, 99].

In the case of the PS particles presented here, before undergoing rheological characterisation to verify the influence of the dry-coating on their flow behaviour, the resistance to wear of the rough coating was tested to ensure that the long duration shear tests performed do not remove (or wear off) the coating. The particles were subjected to a long duration test consisting of a 20 hours long shear test with 2 minutes of fluidisation before and after at flow rate of $5\,\mathrm{L\,min^{-1}}$; Figure 2.2 presents before-and-after close-ups of the rough surface particles.

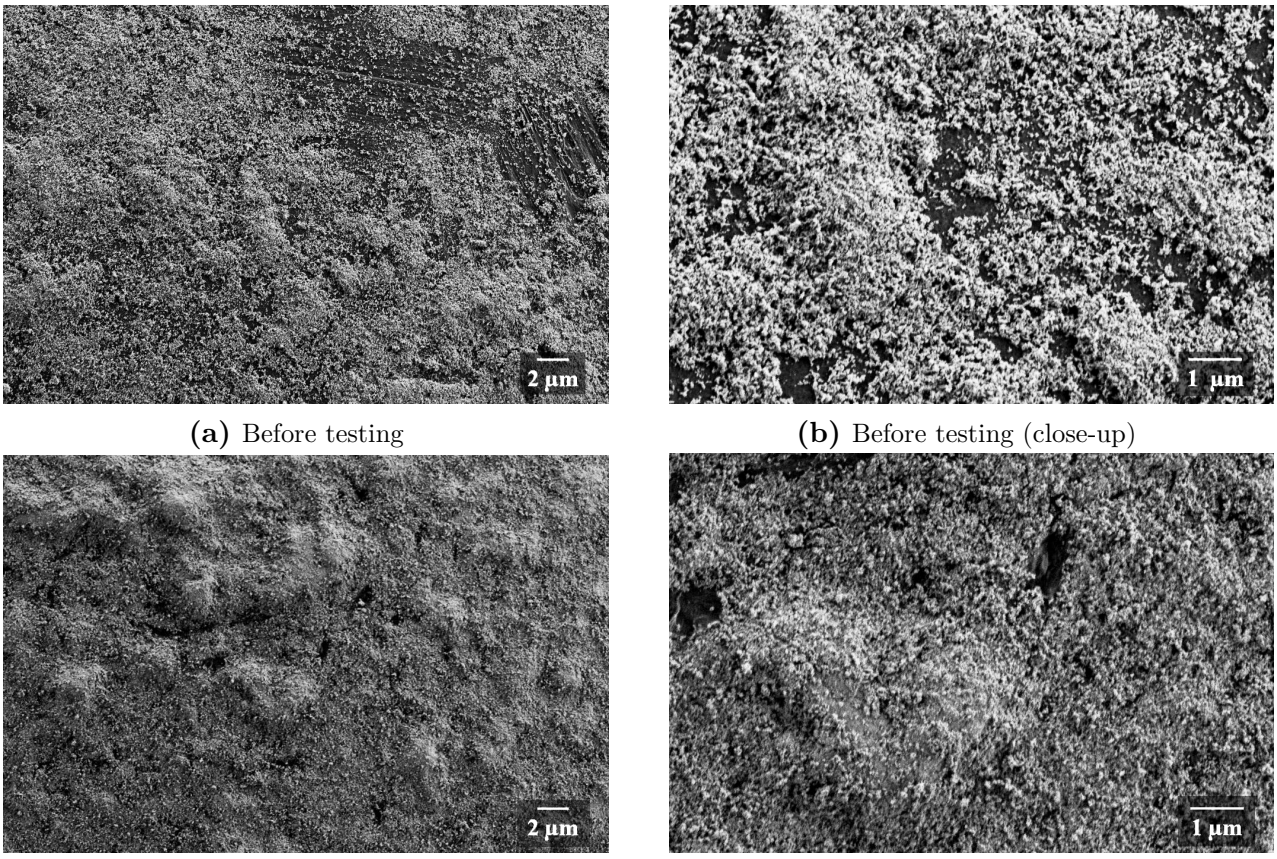

(a) Before testing

(b) Before testing (close-up)

(c) After testing

(d) After testing (close-up)

Figure 2.2: SEM images of the rough surface PS powder used as raw material (a) before and (b) after a 20 hours long shear test with 2 minutes of fluidisation before and after at flow rate of $5\,\mathrm{L\,min^{-1}}$. The imaging was done using low voltage (1 keV) SEM.

It is visible on those images that the surface state is not modified by the long term testing: the coverage is still distributed on the entire particle surface, and the small particles show the same average size of clusters ($\sim 0.01\,\mu\mathrm{m}$) that form the surface roughness. We conclude that the dry-coating can withstand testing without being removed.

The resistance to wear of the dry-coating being verified, the flow properties of both powders are compared. The following state-of-the-art rheological characterisation techniques are employed:

- The *flow energy* test [102, 103] proposed by Freeman Technology [104] on the Freeman Technology 4 Powder Rheometer (FT4) rheometer.

- The *tensile strength* test proposed by Valverde *et al.* [70, 105].
- High precision rheological testing is used to obtain the *flow start-up curves* for both materials, as well as their *flow curves* at steady-state, using the Modular Compact Rheometer (MCR) from Anton Paar [106].

Table 2.1: Physical properties of the bulk-polymer composing the grains of the powder used as raw material. The mechanical and physical properties are given by the manufacturer; the glass transition temperature is from Ref. [107].

Physical property	**Nominal value**	**SI units**	**Test method**
Density of bulk material (at 20 °C)	1.05	$\mathrm{g\,cm^{-3}}$	ASTM D1505
Flexural modulus (Young's modulus)	3000 – 3600	MPa	ASTM D790
Tensile Strength at Break	46 – 60	MPa	ASTM D638
Vicat Softening Point	~ 90	°C	ASTM D1525
Glass transition temperature	~ 100	°C	from [107]
Peak Melting Point	~ 270	°C	ASTM D3418

There are currently two instruments commercially available for dynamic powder rheometry that allow to fluidise the powder before or during testing:

- The MCR from Anton Paar (Austria).
- The FT4 from Freeman Technology (United Kingdom).

The two apparatus have been used to propose a full rheological description of the materials used and to compare the different strategies deployed to attempt reaching a valid characterisation of *powder flowability*. While both propose dynamical testing of non-confined powder samples, they rely on different standardised tests and technical specifications; their comparative assessment is provided in Table 2.2.

Details on the FT4 will be given in Section 2.2; details on the MCR can be found in Section 2.4.

2.2 Phenomenological definitions of flowability

2.2.1 Defining *powder flowability*

The concept of *powder flowability* does not rely on a normalised measurement method; it is not defined by a physical quantity with international system units. In that sense, it does not qualify as a characterisation of the rheological behaviour of powders. However, whereas being an ill-defined concept, it is nevertheless useful, in particular for industrial applications where the "process-ability" of a given material in a given system needs to be quantified.

A powder is defined as *flowable* if it tends to plastically deform (i.e. flow like a liquid) under a certain stimulus, which may simply be its own weight, entailed by the particles' mass under Earth gravitational field [108]. In contrast, a *non-flowable* powder resists flowing and tends to maintain its shape akin to a solid. If it is forced to flow, for example due to an external stress applied at a boundary of the packing, it will do so in large chunks of material themselves preserving their shape, in an erratic manner and generally showing higher tendency to block

Table 2.2: Comparative assessment of the possibilities offered by the rheometers MCR from Anton Paar (Austria) and FT4 from Freeman Technology (United Kingdom). The specifications listed here are only valid for the powder-testing version of the rheometers.

	AP MCR-102	**FT4**
Standard tests available		
Rotational shear test	✓	✗
Oscillatory shear test	✓	✗
Confined shear test	✗	✓
Specifications		
Powder fluidisation	✓	✓
Temperature control	✗	✗
Sealed powder bed	✓	✗
Performances		
Minimum - maximum torque	$5 \cdot 10^{-9}$ to 200 mN m	$2 \cdot 10^{-2}$ to 900 mN m
Torque resolution	$5 \cdot 10^{-10}$ mN m	$2 \cdot 10^{-2}$ mN m
Minimum - maximum normal force	$1 \cdot 10^{-2}$ to 50 N	$1 \cdot 10^{-4}$ to 50 N
Normal force resolution	$1 \cdot 10^{-3}$ N	$1 \cdot 10^{-4}$ N
Maximum rotational speed	3000 rpm = 314 rad s^{-1}	129 rpm = 12 rad s^{-1}

the flow by forming stable aggregates (jammed regions) that can withstand a finite amount of stress before yielding. In other words, contacts between grains tend to be more enduring [70]. The terms of *high*, *mediocre* and *low flowability* are used throughout the present work following this phenomenological definition.

Powder flowability hence depends on many physical phenomena that can be attributed to the grains themselves (e.g. surface state and van der Waals interactions), but also to external factors, like ambient humidity, which might create water bridges between grains, ergo increasing capillary forces [70, 109]. Beyond humidity or temperature, as the grains pass each other, tribocharging can happen, creating electrostatic charges between particles. The evolution of those cohesive interactions with varying particles size and distance between grains will be further studied in Chapter 3. All those factors and more (e.g. setup geometry compared to particles size, gravitational environment or stress history of the packing) combine and interact in a complex manner to sum-up into the global *powder flowability*. It is hitherto an open question whether the desired measurement quantifying powder flowability should encompass all those phenomena, since they influence the powder flow behaviour; or on the contrary if it should emancipate from them to propose a material-specific quantity, independent of the testing conditions.

In absence of a universal definition, different phenomenological measurements have been proposed to provide *one* number supposedly characteristic of a powder's flowability.

2.2.2 Process-relevant measurements of powder flowability

To characterise or anticipate the behaviour of a granular material in a given process, specific measurements have been designed that mimic a particular property of the material, relevant in that case.

Measuring the ability to pack. In powder-bed based additive manufacturing – a topic further addressed in Part II of the present thesis – like in many other industrial areas, the packing-ability of the powder bed is an essential parameter. It defines the minimum porosity that can be reached by the final printed part [110]. In this instance, a measurement of the packing-ability of a material is a useful indication of the effective increase in packing density that can be reached despite intrinsic powder properties.

In such case, the Hausner ratio HR can be used [111]. It is defined as the ratio of the tapped density ρ_{tapped} (sample packing fraction after densification by tapping for a fixed duration and frequency), over the so called bulk density ρ_{bulk}, which in this case is defined as the the packing density of the sample as is when poured into the container, compacted only under its own weight:

$$HR = \frac{\rho_{\text{tapped}}}{\rho_{\text{bulk}}}. \tag{2.1}$$

The higher the difference between packing density of the material settled freely under its own weight and having been packed by tapping (or by compression in the case of the Carr index [112], a measurement otherwise similar), the lower the "intrinsic ability to pack densely" of the powder, therefore lower flowability. The rationale behind this measurement is that for a cohesive powder, grains are less mobile in regard to each other: they tend to naturally pack in a less dense state.

Measuring the angle of a heap. Another example is the so called *static angle of repose* measurement, defined as the metastable slope of an unconstrained pile of grains with the horizontal [113]. As heaps of granular material are relevant in industrial processes and frequently encountered in nature, they provide a good probe-system for many-body theoretical descriptions [114] and have been extensively used as an empirical parameter reflecting the material's cohesion [115].

It is however questionable whether the angle formed by the heap with the horizontal can be used as an intrinsic granular material property measurement. Despite profusion of different standards proposing "normalised" procedures to implement the angle of repose measurement[1], it can be difficult to implement experimentally with reasonable precision, especially for small samples and materials with high cohesion, and the values produced are hardly reproducible in different setups [70]. This lack of reproducibility can be explained on theoretical grounds: from the Mohr-Coulomb failure analysis, the angle at which a heap of granular material forms is shown to depend not only on the powder intrinsic cohesion but also on the height of the heap (see Ref. [109, Chap. 6] for full demonstration). Besides, Topić *et al.* [35] showed that for a large enough pile of material, the heap does not form one angle to the horizontal but two different ones, due to the arch of forces chains present in the middle of the pile and creating a zone of high material packing density, surrounded by an area of lower density that piles at a lower angle to horizontal (see Section 1.1). Those well documented evidences question the significance of the static angle of repose to characterise powder flowability.

Measuring the dynamical fall angle in a rotating drum. The *dynamic angle of repose* corresponds to the avalanche angle of a granular sample partially filling a rotating drum [116].

[1] Among which: ASTM C1444-05, Standard test method for measuring the angle of repose of free-flowing mold powders – ASTM D6393-14, Standard Test Method for bulk solids characterization by Carr indices – ISO 902:1976, Aluminium oxide primarily used for the production of aluminium: Measurement of the angle of repose – ISO 4324:1977, Surface active agents: Powders and granules, measurement of the angle of repose – ISO 8398:1989, Solid fertilizers: Measurement of static angle of repose.

Generally, under Earth gravity, higher avalanche angles are obtained for powders composed of smaller diameter grains and rough surface particles [95]. This is explained by higher contact surface and interlocking asperities, which increase the stability domain of the angle formed by rough particles, before gravity overcomes the interparticle frictional and/or cohesive interactions.

Brucks *et al.* [117] studied the change in dynamic angle of repose of a powder under hypergravity ($1g$ to $25g$) on a centrifuge. They propose to account for the relative importance of gravitational *versus* shear effects in terms of the Froude number: $Fr = {\omega^2 r}/{g_{eff}}$ where ω is the angular frequency of the rotating drum, r its radius, and g_{eff} effective gravity acting on the powder. They find that the Froude number can be used to scale shallow flows under various gravitational accelerations. Earlier experiments in the regime of $0.1g$ to $1.8g$ were performed by Klein and White [118, 119] on parabolic flight, and these data appears compatible with the Froude number scaling. Nevertheless, reproducing this experiment more recently on parabolic flight under $0.1g$, $0.38g$ and $1g$, results reported by Kleinhans *et al.* [115] do not correlate with those observations. They report that the dynamic angle of repose does not obey the Froude number scaling and undergoes a decrease in reduced gravity of approximately 10 degrees for all materials. The explanation proposed by Kleinhans *et al.* is that under low gravity, the granular system is subject to a reduction of the pressure applied on the grains due to their own weight: as the frictional and/or cohesive forces are not activated, the balance between the attractive forces holding the packing together and the mass-induced downwards acceleration of the grains shifts towards a smaller avalanche angle.

In conclusion, such measurements clearly indicate *something* about a given powder: when comparing two materials in the exact same setup, the results can enable to estimate or compare the process-ability of a material in a given installation. However, large-scale predictions cannot be based on the results of such measurement, as they do not provide a universal nor intrinsic characterisation of the material: a specific measurement accounts for a given property, and the threshold is a process-related empirical result. No property independent from the measuring setup can be extracted, hence no generalisation can be made, making such measurement dependent on complementary empirical trial-and-error experimental campaigns.

2.2.3 Standardised test procedure: the *flow energy* measurement

To propose a measurement that is not specifically tied to one particular phenomenon or property, but still offers an easily implemented and understood solution to characterise powder flow behaviour, rheometer manufacturers have proposed ready-made solutions to satisfy their industrial customers. Such measurement procedures are meant to provide a turnkey solution to summarise complex granular flows in a single number.

An example of such procedure is the so called *flow energy* measurement [102, 103] available on the FT4. This rheometer, shown in Figure 2.3a, is composed of an open powder-bed of diameter 25 or 50 mm and proposes multiple types of measuring systems and tests, including one presented by the manufacturer as a way to assess the "dynamic flow properties" of the powder: the *flow energy* measurement.

The measurement procedure is summarised by Figure 2.3b; it determines the *flow energy*, quantity further defined below, and is based on the repeated penetration of the powder bed by the helix shown in Figure 2.3c. The procedure itself consists of the following sequence of measurements and data processing:

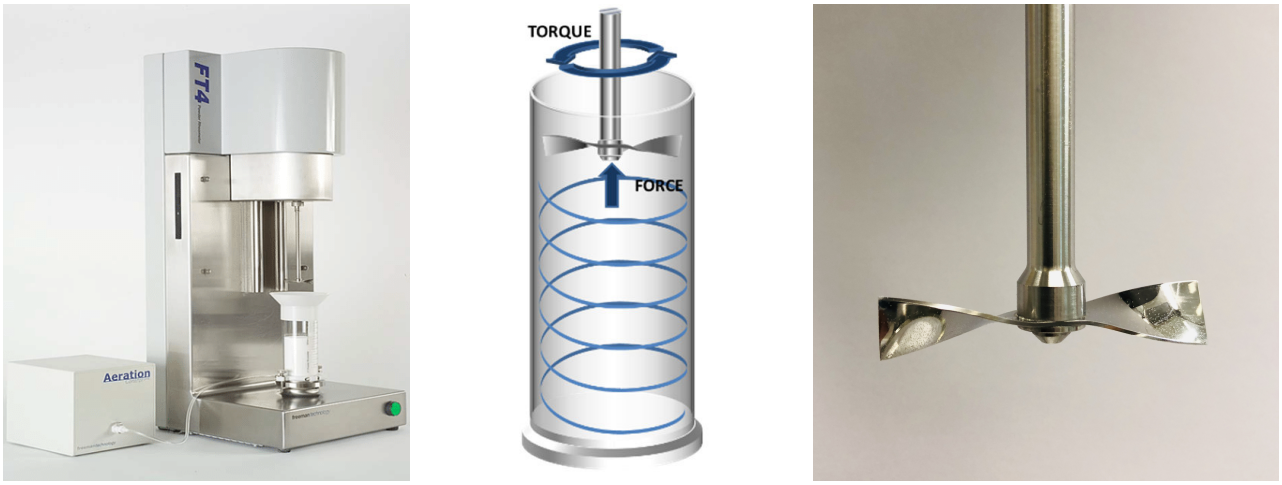

(a) **(b)** **(c)**

Figure 2.3: (a) Freeman Technology 4 Powder Rheometer (FT4). (b) Schematic of the flowability measurement method proposed by the FT4 rheometer. Images (a) and (b) from [104], reproduced with authorisation from Freeman Technology. (c) Helix used as measuring system in the FT4 rheometer *flow energy* measurement, of radius $r = 24\,\mathrm{mm}$.

1. *Conditioning* – As discussed in Chapter 1, a powder can keep memory of its previous stress state. To ensure reproducibility, a conditioning phase is necessary to "erase" the stress history of the sample and create a fixed starting state. The FT4 preset conditioning procedure consist of inserting the helix in the sample twice at a rotation speed $\omega = 2.5\,\mathrm{s}^{-1}$ (i.e. tangential speed at the helix's tip $60\,\mathrm{mm\,s}^{-1}$) to achieve a consistent state of compression of the powder bed.

2. *Measurement* – The torque and normal force needed for the blade to move upwards within the powder are recorded. Powder bed height and penetration velocity of the helix are fixed at the beginning of the experiment. Therefore, the torque and force recorded can be presented as a function of the height of the helix within the powder bed (from h_2 at its bottom to h_1 at the surface).

3. *Data processing* – The next step aims to derive from the torque and normal force one quantity that would be representative of the "global resistance of the powder" against the blade's penetration. The *total flow energy* E is introduced, defined as the work deployed for the helix to move through the powder:

$$E = \int_{h_1}^{h_2} \left(\frac{M(h)}{r \tan \alpha} + F(h) \right) dh \tag{2.2}$$

   where r is the radius of the helix, α the helix angle, M the torque and F the normal force recorded along the height h of the powder bed.

4. *Sequence of measurements* – The standard dynamic test consists of repeating the same procedure (including conditioning and measurement) seven times to assess the stability of the *total flow energy* E obtained. The change in flow-resistance of the powder as a function of applied turning rate is evaluated by varying the rotation speed of the helix for four more measurements. This procedure is summarised in Figure 2.4a. To probe the effect of this preset conditioning step, we propose another measurement routine: the conditioning is done by fluidising the sample for two minutes, and for each penetration speed the

measurement is repeated five times. This procedure is summarised in Figure 2.4b.

5. *Analysis by comparison* – Different numbers and comparative ratios can be extracted from this sequence of tests. The manufacturer puts forward some such comparisons, among which: the "basic flowability energy" (E for the stability test №7); the "specific energy" (E for the blade moving upward instead of downward); the "stability index" (ratio of the *flow energy* of test №7 over test №1); or else the "flow rate index" (ratio of E for test №11, done at low rotation speed, over test №8, done at high rotation speed). The change in behaviour can then be mapped to rheological definitions. In the present work, the evolution of the *total flow energy* E for increasing rotation speed (tests №8 to №11) will be used as a characteristic number representing the energy input necessary to make the powder flow (in other words, evolving inversely to the powder flowability).

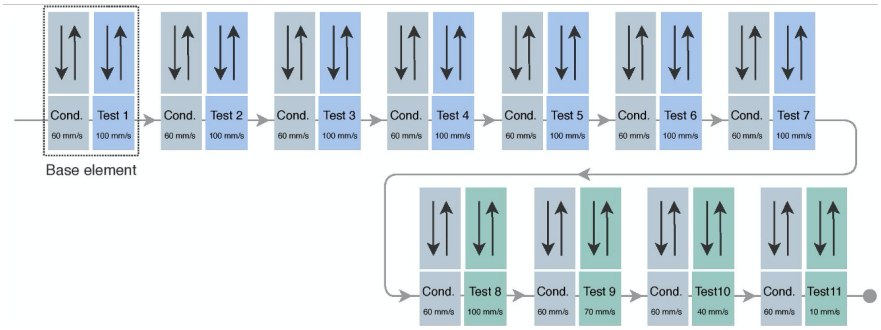

(a) Preset conditioning and measurement procedure

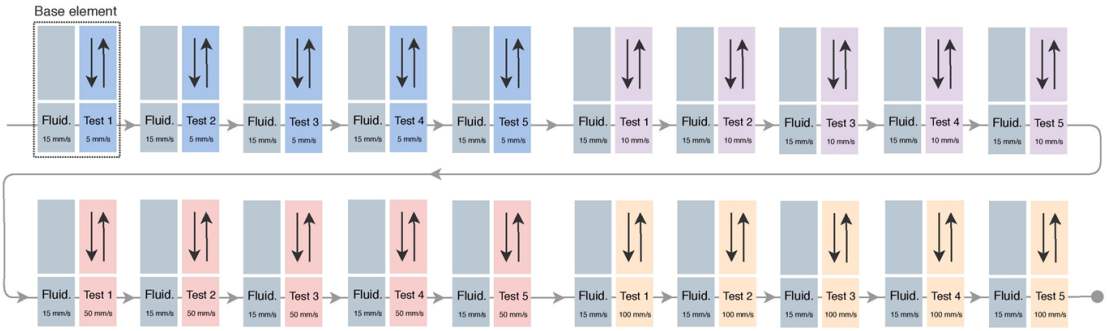

(b) Proposed conditioning (by fluidisation) and measurement procedure

Figure 2.4: (a) Sequence of measurements proposed by the preset FT4 dynamic test. The first sequence (in blue) corresponds to the stability test, and the second sequence (in green) is the "variable rotation rate" test. (b) Sequence of measurements proposed in the present work to test the influence of the helix penetrating the sample. The preset conditioning is replaced by two minutes of fluidisation, and each measurement is repeated five times. For both schematics: a conditioning and measurement cycle form a base element. One conditioning step (in grey) is done prior to each measurement (in colour). The rotation speeds are given as the velocity of the tip of the helical blade, for a blade of radius 24 mm.

Normalisation of the *flow energy*. The torque and normal force needed for the helix to go through the sample depend on the volume of the sample and on the density of the material. Hence, comparison of measurements done on materials of different density or with powder beds of different diameters would not be valid. This dependency of the *total flow energy* on the quantity of material sampled is shown in Figure 2.5a for the same material sampled five times with different total sample mass. To avoid this dependency, a normalisation of the *flow energy*

E is proposed. Following Nan *et al.* [120, 121], a dimensionless *flow energy*, E^* is introduced by normalising the *flow energy* by the potential energy of the sample:

$$E^* = \frac{E}{m_s \, H_s \, g} \tag{2.3}$$

where m_s is the total mass of the sample, g is the gravitational acceleration and H_s is the height of the powder bed. In Figure 2.5 the same data is plotted using the *total flow energy* (Figure 2.5a) and its normalised counterpart, the *specific flow energy* (Figure 2.5b). For the same material, the *specific flow energy* is equal within experimental error, and the trend followed as the rotation velocity is increased remains the same.

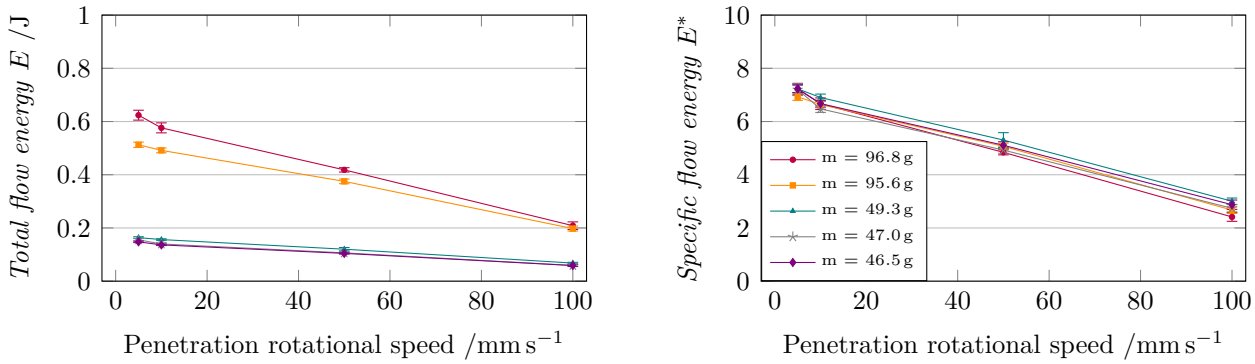

Figure 2.5: Five measurements, for samples of varying mass (thence varying filling height), plotted (a) as the *total flow energy* E and (b) as the *specific flow energy* E^*, at four increasing penetration speeds. The experimental procedure follows the measurements sequence presented in Figure 2.4b (fluidisation as conditioning). The measurements were conducted on samples of PS powder of diameter 40 µm; the error bars correspond to the maximum and minimum values out of five repetition of each measurement.

Aiming to probe the ability of this phenomenological measurement to provide information on the flow properties of a given powder, the PS powders presented in Section 2.1 are tested. Three variables are studied:

- Particle size (40, 80, 140 and 250 µm diameter particles).
- Surface state (smooth surface and rough dry-coated particles).
- Effect of the conditioning step: preset conditioning done by mechanical compression by the helix (consolidation), and proposed conditioning consisting of two minutes of fluidisation before each test. The conditioning modifies the packing density of the granular bed during the test, lower after fluidisation than after consolidation.

Effect of particle size. Figure 2.6 compares the *specific flow energy* for PS powders of diameter 40, 80, 140 and 250 µm with smooth surface. For consolidated powder, the packing fraction at the beginning of the experiment was measured $\varphi_0 \approx 0.59$ (Figure 2.6a). The *specific flow energy* E^* increases with decreasing particle size, which shows a lower flowability (i.e. higher energy needed to induce flow) for a powder constituted of smaller grains. This is the expected effect, as van der Waals interactions are higher for smaller particles (see Section 3.1), inducing higher cohesive forces among particles, thus a less flowable granular material.

On the other hand, if the sample is conditioned by fluidisation, the helix-penetration test starts at lower packing fraction: $\varphi_0 \approx 0.56$ (Figure 2.6b). In this case, no clear correlation exists between the particles size and the *specific flow energy*. Furthermore, the powder composed of 40 µm diameter particles spans across the other larger diameter powders, and the 250 µm powder shows non-monotonic behaviour, showing a slight decrease in *specific flow energy* at $10\,\mathrm{mm\,s^{-1}}$ in an otherwise constant curve. However, a clear tendency can be noted: all *specific flow energy* values, regardless of the particles diameter, are lower for low packing density than for the consolidated sample.

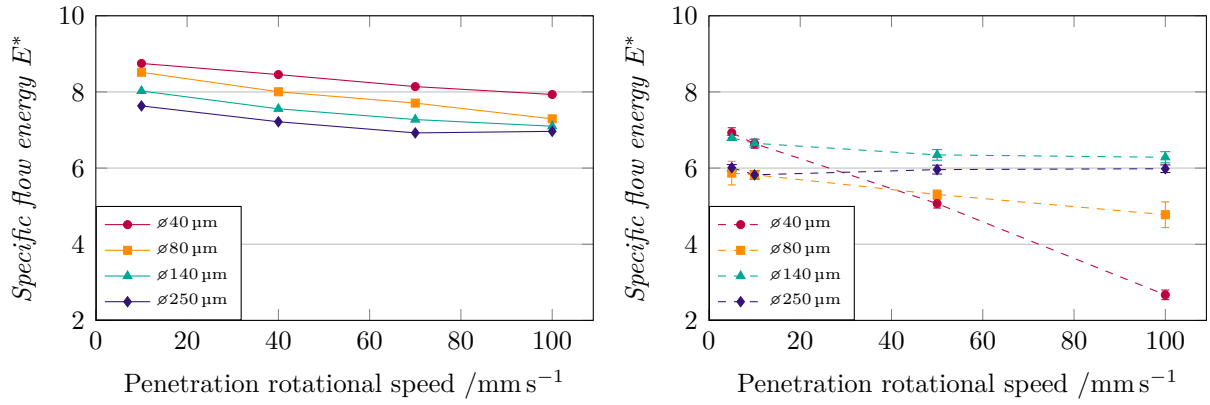

(a) Consolidation as conditioning ($\varphi_0 \approx 0.59$) **(b)** Fluidisation as conditioning ($\varphi_0 \approx 0.56$)

Figure 2.6: Dimensionless *specific flow energy* E^* as a function of the helix penetration speed, for PS powder of diameters 40, 80, 140, 250 µm. Error bars represent the standard deviation in five subsequent measurements. (a) Conditioning step realised mechanically by the helix penetrating the powder bed twice before the measurement. Error bars are smaller than the symbol size. (b) Conditioning through powder-bed fluidisation.

Effect of surface state. The same test is repeated for the PS powder composed of particles of diameter 80 µm, with smooth and rough surface. Results are presented in Figure 2.7. For consolidated powder at packing fraction $\varphi_0 \approx 0.59$, the effect of surface state is obvious in the measured *specific flow energy*: the rough surface powder necessitate more energy to flow, entailing a *flow energy* steadily higher by approx. 15% at every penetration speed.

In contrast, for the less packed powder conditioned by fluidisation, the *specific flow energy* is the same within experimental error on the entire range of penetration speed available. Here again, at all penetration speeds the force needed to penetrate the packing is largely higher for densely packed powder than for low density granular material.

Effect of packing density on *flow energy* for different surface roughness. The conditioning procedure chosen determines the packing density of the material at the beginning of the helix-traverse test: consolidation increases the packing fraction by mechanical compression, whereas fluidisation breaks the granular fabric by expanding and agitating the entire granular sample, leaving it in a more dilute state at the end of conditioning. Typical packing fraction observed vary from $\varphi_0 \approx 0.59$ after consolidation *versus* $\varphi_0 \approx 0.56$ after fluidisation.

Comparing Figures 2.6 and 2.7, the "flowability test" proposed by the FT4 strongly depends on the granular sample's packing density. If the preset conditioning is used, the sample is consolidated mechanically, and the higher packing fraction implies that the difference in cohesive

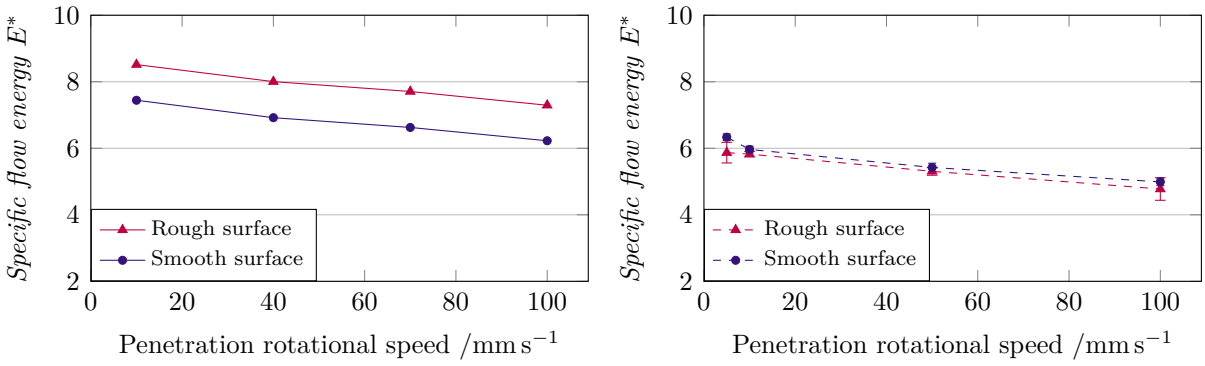

(a) Consolidation as conditioning ($\varphi_0 \approx 0.59$) **(b)** Fluidisation as conditioning ($\varphi_0 \approx 0.56$)

Figure 2.7: Dimensionless *specific flow energy* E^* as a function of the helix penetration rate, for the two PS powder *RS* (rough surface state) and *SS* (smooth surface state) of diameter $\varnothing$ 80 µm. (a) The conditioning step is realised mechanically by the helix penetrating the powder bed twice before the actual measurement taking place. (b) The conditioning step is the fluidisation of the powder bed.

forces and friction are clearly visible in the measured *specific flow energy*. If the conditioning step is modified, the results show a trend that is not obviously linked to the microscopic interactions on the particles surface: the two powder differing only by their surface state show the same tendency. A change in surface roughness is reflected in the *flow energy* measurement only if the powder is at high enough packing density; otherwise, the frictional contacts between the particles are not activated and the two powders show the same response to the helix penetration. Moreover, the torque and force recorded are generally lower for the powder packed at lower density: the quantity of matter to displace for the helix to move through the sample is lower, and the interparticle forces are less strong as the grains are further away from each other (see Section 3.1 for a more detailed list of such forces).

2.2.4 Flowability-probing procedures: grandeur and decadence

The *flow energy* measurement procedure and its proposed variant, the *specific flow energy*, provide a characterisation procedure resulting in one number, that can be simply implemented, give highly reproducible results and does not appear to necessitate a full understanding of granular rheology to be used. If the sample is consolidated before undergoing the measurement procedure, as recommended by the preset testing procedure, the interparticle interactions are enforced and their influence is reflected in the measurement of torque and normal force needed for the helix to rotate and ascend within the powder bed.

While such measurement gives no information on the powder nature, as it does not provide a universal rheological powder characterisation nor an intrinsic property of the granular material, it gives a base for comparative study of different powders in one specific density state. As with the process-related measurement above-mentioned, this comparison can be useful for determining if the flow behaviour of a powder will allow for its processing in a given setup. Despite the fact that information is blurred by summarising a complex, multi-variable phenomenon into a single number, phenomenological flowability measurements undoubtedly capture *something* about the powder rheological behaviour. In other words, phenomenological measurements succeed brilliantly in the industrial market by failing to render the complexity in flow-behaviour of granular materials.

2.3 Tensile strength of the granular packing

Valverde *et al.* [105] propose a method, based on the fluidisation of a granular bed, to access the intrinsic cohesion of the granular material, i.e. the attractive forces between grains in a granular sample.

Pressure drop measurement during powder fluidisation. The pressure drop measurement is a typical test method related to granular fluidisation; it consists in measuring the pressure drop through the fluidised bed *versus* increasing flow rate (directly proportional to gas velocity). The pressure drop across the bed (or equally, the drag force exerted on the particles) increases linearly with increasing the flow rate as long as the bed is not fluidised. At this stage, the pressure drop across the bed, described by Darcy's law [122], is due to frictional interactions with the powder as the air flow crosses the static powder bed like a porous material.

Eventually, the pressure reaches a threshold, when the pressure drop across the powder bed equals the weight per unit area of the powder sample. Nevertheless, the bed is not yet fluidised: no increase in the volume of the bed is observed. Indeed, the drag force holds the weight of the powder but the interparticle forces are now holding the bed in its static form. The gas velocity is further increased; the pressure drop will concomitantly increase until it reaches a maximum Δp_{max}. Once the interparticular forces are overcome, a sudden decrease of the pressure drop occurs, until reaching a steady value at the weight per unit area of the powder $p = {}^{mg}/_{A}$, where m is the mass of the sample, g the gravitational acceleration and A the section area of the bed. Valverde *et al.* [105] propose to qualify the overshoot of the pressure drop beyond the weight per area of the powder bed as the tensile strength of the powder [70, 105]:

$$\sigma_t = \Delta p_{max} - \frac{mg}{A} \tag{2.4}$$

where σ_t is the tensile strength of the powder, Δp_{max} the maximum pressure drop, m the mass of the granular sample, g the gravitational acceleration, A the section area of the bed.

The point of minimum fluidisation gas flow is reached when the pressure drop across the powder bed balances the weight per unit area of the sample, which occurs at a stable pressure for a given sample; a powder where the cohesive interparticle forces are nonexistent would become fluidised at this point. In reality, no such powder exists, but the amplitude of the cohesive forces can be tuned (for example by changing the initial consolidation state of the packing, see Refs. [70, 105]), which shifts the fluidisation point, hence the tensile strength of the powder.

This method is applied here to the two PS powders of particles' diameter 80 µm with different surface state: *SS* and *RS*. Results are given in Figure 2.8. The measurement starts at high gas flow velocity ($u = 0.04$ m s^{-1}, hence with a fluidised sample) to decrease towards $u = 0$ m s^{-1}. At high gas flow velocity, the packing fraction is approximately $\varphi \approx 0.53$. In order to apply the procedure proposed to find the intrinsic tensile strength due to material cohesion, a reproducible baseline, corresponding to the pressure drop across the porous substrate below the powder bed, must be obtained. In the analysis presented, this baseline is not measured but estimated indirectly from the pressure drop measurements, presented in the insets in Figure 2.8, in order to increase the reproducibility of the measurements presented. When experimentally measured, the pressure inside the experiment cell without sample shifts by up to 10% from the start of the measurement (at high u, decreasing) and its end (back to high u, after having spanned through the full spectrum of u available). As such measurement should not be subject

to hysteresis, this shift in pressure at a given gas flow velocity u is attributed to a lag of the pressure sensor due to lack of precision at relatively low pressure.

Following Darcy's law, it is expected that the pressure drop evolves linearly with increasing gas flow velocity [122]. Thence, to obtain this theoretical baseline, a linear regression is applied to the second part of the pressure recorded (corresponding to the fluidised sample), as the slope is similar for the powder bed once fluidised and for the uncharged bed, i.e. due to the porous substrate under the powder sample. The intercept is the pressure at null gas flow ($u = 0\,\mathrm{m\,s^{-1}}$). The baseline obtained is presented as a dotted line in the insets of Figure 2.8.

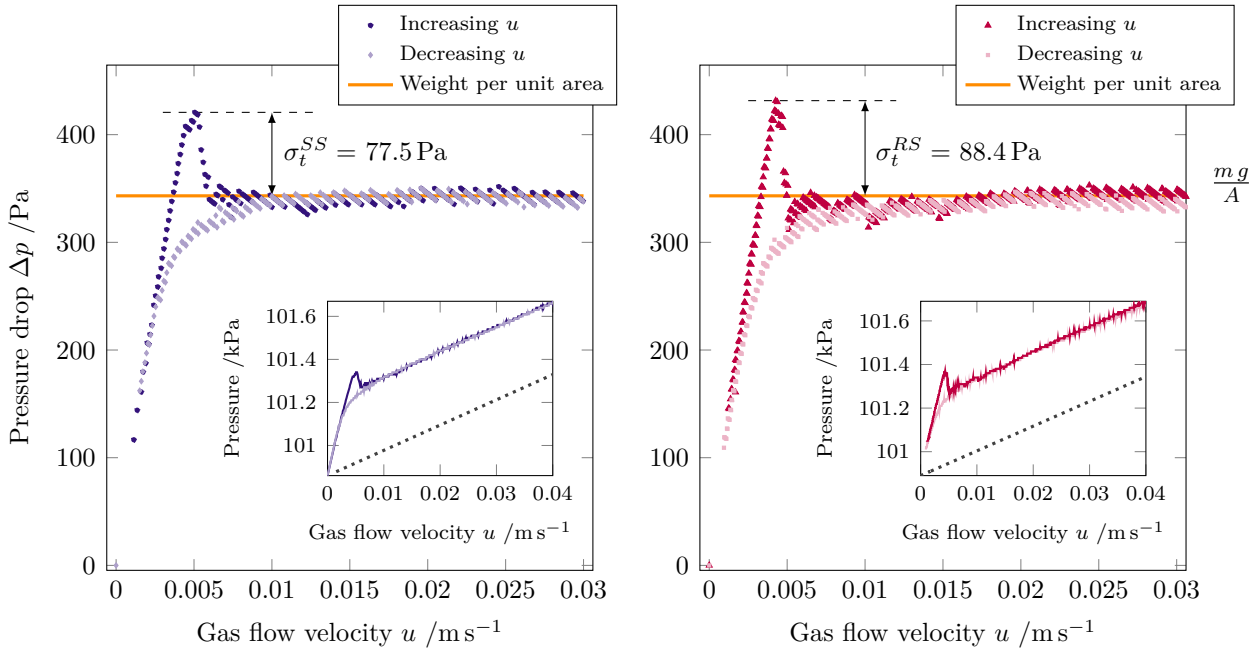

(a) Smooth surface powder

(b) Rough surface powder

Figure 2.8: Pressure drop across the powder bed for (a) smooth surface PS powder, and (b) rough surface PS powder. The powder bed has a diameter $d_b = 50.5\,\mathrm{mm}$ and the sample mass is $m = 70\,\mathrm{g}$. The insets are the measured pressure drop across the powder bed before removing the baseline (dotted line in the insets) due to the pressure drop across the porous substrate.

The tensile strength is $\sigma_t^{SS} = 77.5\,\mathrm{Pa}$ for smooth surface powder against $\sigma_t^{RS} = 88.4\,\mathrm{Pa}$ for rough surface power, which represents an increase of 14% for the *RS* powder. This increase indicates that higher cohesive strength links the particles together within the *RS* packing, which tends to imply a lower flowability. This difference in σ_t persists although the samples are at low packing fraction ($\varphi \approx 0.53$). Contrary to the *flow energy* measurement, the tensile strength test captures a difference between the two powders *RS* and *SS*, even at low packing fraction, bespeaking the high sensitivity of this measurement technique. However, the difference between the two measurements represents only 3% of the pressure due to the weight of the samples: at this low packing fraction, the two powders show relatively similar cohesion. For rough surface powder, the mechanisms expected to be responsible for an increase of the interparticle attractive behaviour are higher cohesive forces and increased frictional contacts. Surface friction and mechanical locking among grains, which depend on the density of sample, are linked to the normal pressure it is subjected to. The higher tensile strength of the rough surface powder shows that this change in surface state slightly increases the cohesion of the material, even at the very low packing fraction reached right before fluidising the sample.

2.4 Rheological properties of granular media

Rheometry, as the quantitative study of soft materials' rheological properties, aims to link a specific stimulus to its response. This is done through careful measurement of the relationship between a stress applied and the deformation it entails in a material. Whereas the concept of *flowability* was meant to encompass the rheological response of a material into one single measurement or parameter, the goal of rheological measurements is to capture material behaviours that hold true independently of the set-up; this is done by isolating the type of stimulus applied through precise technical installations.

2.4.1 Rheometry installation

All the experiments presented in the following sections are performed on the Anton Paar MCR 102, equipped with a powder cell and including a fluidisation set. This set-up is shown in Figure 2.9a; the measuring system (inner rotating part) is the "profiled cylinder" shown in Figure 2.9b. The powder is sheared by rotating the measuring system in an open-surface powder bed. The profiling of the inner cylinder, by carrying powder in its entrenchments, offers predominant powder-powder contact near the rotating inner surface during the shear test.

(a) **(b)** **(c)**

Figure 2.9: Experimental set-up: (a) rheometer MCR 102 equipped with powder cell. Image reproduced with permission from Anton Paar, from Ref. [106]. (b) Measuring system: "profiled cylinder". (c) Schematic representation of the Couette-type large gap rheometer used (cross-section). Image freely inspired from Ref. [50]. In the experimental setup used the inner rotating cylinder has a radius of $r_i = 12\,\text{mm}$ and the external static cup of $r_e = 25.25\,\text{mm}$.

Live monitoring of the packing fraction is made possible by recording an image of the height of the granular fluidised bed throughout each measurement (see Figure 2.10). The images taken are analysed to obtain the volume of the fluidised bed; after removing the volume increase due to the measuring system, the packing fraction φ is calculated according to $\varphi = {}^{m}/_{\rho V}$, where m is the mass of the granular sample, ρ the density of the particles in bulk, and V the volume occupied by the fluidised sample.

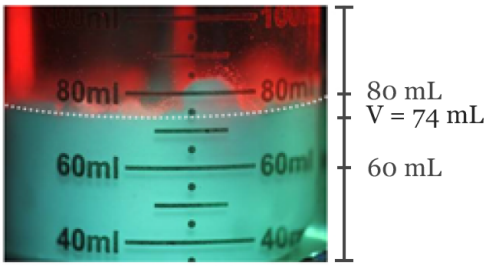

Figure 2.10: Image capture of live-monitoring of the sample's volume, to obtain *in fine* the packing fraction.

The flow rate of the air streaming through the powder bed is controlled by a Mass Flow Controller (MFC) from Bürkert. The rheometer described was customised to widen the span of flow rates available: for high precision at low flow rate (up to $15\,\mathrm{L\,min^{-1}}$), the Bürkert MFC-8712 is used; for reaching flow rates up to $120\,\mathrm{L\,min^{-1}}$, the Bürkert MFC-8626 takes over.

The experimental procedure is illustrated in Figure 2.11. The rheometer is calibrated before each series of measurements; the calibration consists of a dry run on the empty machine to measure the stress due to the weight and inertia of the measuring system, and is meant to find the baseline per rotation speed due to the inner cylinder in rotation. Besides, to obtain a reproducible initial state despite known hysteresis in granular materials, the sample is fluidised for six minutes at high flow velocity ($u = 0.02\,\mathrm{m\,s^{-1}}$) before each measurement.

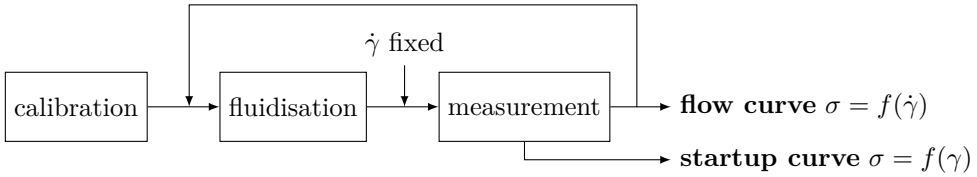

Figure 2.11: Diagram illustrating the experimental procedure used to obtain the rheological measurements presented below.

2.4.2 Start-up curves

In startup experiments, one applies a fixed shear rate $\dot{\gamma}$ and records the resulting macroscopic stress σ from $t = 0\,\mathrm{s}$, corresponding to zero deformation, as a function of shear strain $\gamma = \dot{\gamma}\,t$. A selection of startup curves – e.g. stress-strain curves for flow onset – is presented in Figure 2.12, for 80 µm PS powder with smooth (2.12a) and rough (2.12b) surface state. The shear strain γ in a Couette-type shear cell is calculated under the same approximations leading to the expression for shear rate in the Couette cell (Eq. 1.8):

$$\gamma = \frac{\theta\, r_i}{r_e - r_i} = \frac{2\pi\, N_t\, r_i}{r_e - r_i} \tag{2.5}$$

where θ is the rotated angle, r_e and r_i respectively the external and internal cylinder radii, and N_t the number of turns rotated by the inner cylinder. In Figure 2.12, at high shear rate $\dot{\gamma} > 10\,\mathrm{s^{-1}}$, the curves show strong oscillations in stress. Their period reflects the rotation frequency of the inner cylinder of the rheometer; therefore those oscillations are considered an artefact of the machine, due to the inertia of the rotating measuring system and possibly a slight misalignment, exacerbated by the high precision of the machine and the low density of the material tested.

Typically, startup curves for amorphous materials display three regimes: at very low strain, a linear increase $\sigma = G\,\gamma$, representative of the nearly elastic response of the material, with G being the elastic shear modulus. At intermediate strain, a stress overshoot might be observed, which can be seen as defining the material's yield strain. Finally, once a strain-independent (but shear rate dependent) plateau is reached, the system is considered to be in stationary state. Stationary state is expected to be reached at strain around $\gamma \sim 0.5$ to 1, which can be explained through the "cage effect" described in Section 1.4: the particles – may they be grains, colloidal particles or atoms, as in the framework of the hard-sphere analogy those entities are comparable – are trapped by their neighbouring particles, forming *cages* around

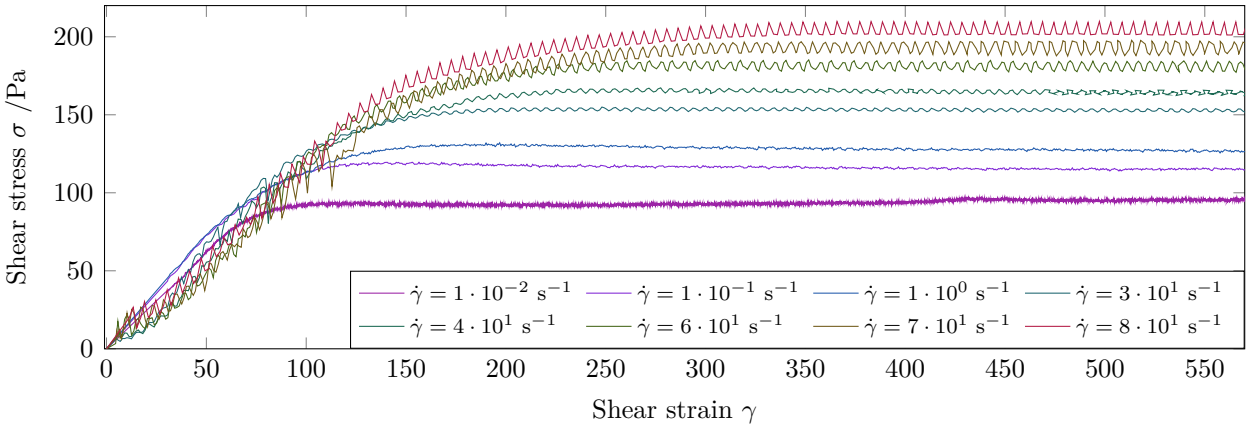

(a) Smooth surface

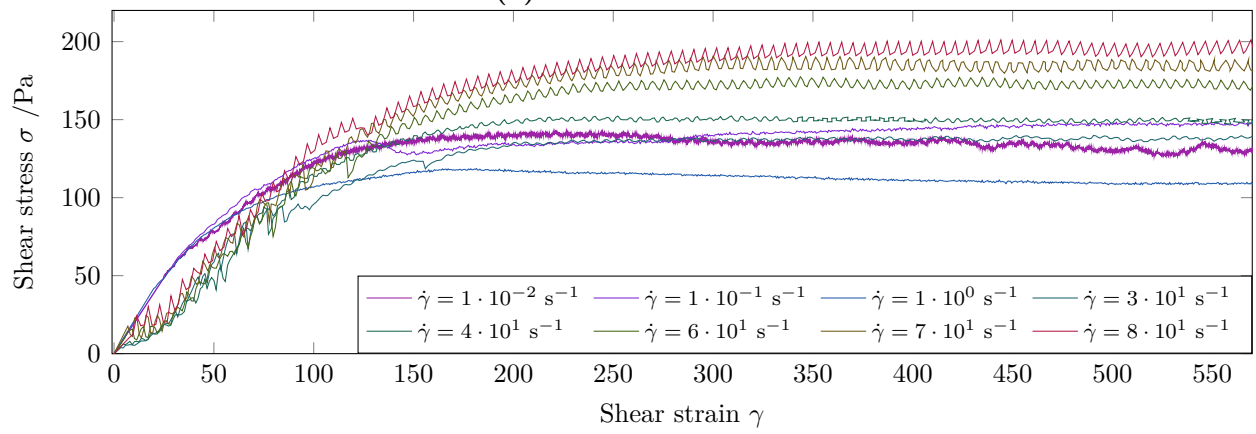

(b) Rough surface

Figure 2.12: Startup curves for PS powder of grain diameter 80 µm, at shear rates $\dot{\gamma} \in [10^{-2}, 8 \cdot 10^{1}]$, for (a) smooth and (b) rough surface state. Samples' mass is 80 g. The first one hundred full rotations of the inner cylinder are presented, corresponding to a shear strain up to $\gamma \approx 550$, in order to show the transition between transient and stationary flow; however, each experiment was run for up to approx. 5000 turns.

each other. Shear deforms those cages, and once the lattice has been deformed sufficiently to reach a strain of approximately 0.5, the particles have already been displaced away from their original position sufficiently for their initial state not to be relevant anymore in the description of the their present sate. In other words, the transient state following flow onset should be over around $\gamma \sim 0.5$ as the so-called cages should then have already been destroyed by shear [123].

In the system that has our attention, as can be seen in Figure 2.12, regardless of the surface state of the material, a stationary state is only reached at a shear strain $\gamma \approx 100$ to 200, which corresponds to one hundred times more than the expected time necessary to reach stationary flow. This surprisingly large strain could be explained by the appearance of slowly growing large shear bands (as discussed further below), or from an agglomeration of the grains into large clusters that are broken under shear (as has been discussed for strongly attractive colloidal particles, see Refs. [124, 125]).

Besides, in Figures 2.12a and 2.12b, two typical behaviours can be clearly distinguished: in the initial regime, at low shear rate $\dot{\gamma} \leq 40\,\mathrm{s}^{-1}$, the stress undergoes a steep, linear increase with strain, while at high shear rate, it shows a sigmoid (S-shaped) increase. (As the initial

linear regime is not reversible, one shall refrain from referring to it as an *elastic* regime.) If at higher shear rate the behaviour is similar for both types of surface states, at low shear rates, the initial rise in stress (representing approx. the first ten rotations, i.e. up to $\gamma \approx 50$) is steeper for the rough surface power, with an equivalent shear modulus $G^{RS} = 1.81\,\mathrm{Pa}$ *vs.* $G^{SS} = 1.39\,\mathrm{Pa}$ (see Table 2.3). The higher shear modulus, i.e. higher initial resistance to shear, of the rough surface powder compared to the smooth surface powder, can be explained by the fact that the geometrical degrees of freedom of the grains in regard to the neighbouring particles are reduced for rough surface powder: the interparticle contacts, may they be through rolling, sliding of twisting, require higher stress when they happen between rough surfaces prone to friction and mechanical locking.

This phenomenon is strong at low shear rate; however, when the shear-heating becomes predominant, the characteristics of the system become less relevant to describe its mechanical response: the granular flow asymptotically approaches a regime dominated by shear, where inertia of the particles becomes the dominant effect. It appears here that $\sigma \propto \gamma^2$, akin to the Bagnold scaling in stationary state flow curves. High grains' velocity, imposed by shear, does not allow reorganisation of the granular fabric through frictional contacts. Instead, particles interact through *instantaneous* collisions, relatively impervious to surface roughness. Hence, the *ease* of the particles to reorder into a new configuration under shear, is relevant in our system at low shear rate on the order of $\dot{\gamma} = 10\,\mathrm{s}^{-1}$ but not at higher shear rates. It should be noted, that this claim is made solely for systems under *no confining pressure*. In such "open surface" system, the volume and thus the packing fraction are not fixed, leaving the system free to dilate, hence reducing the significance of frictional interparticle contacts.

Table 2.3: Shear moduli G at low shear rate $\dot{\gamma} < 1$ for smooth and rough surface state powder. G is the average slope of the linear part ($\gamma < 40$) of the stress-strain curves, for shear rates $\dot{\gamma} \in [10^{-2}, 1]$.

	G /Pa	Stdv. /Pa
Smooth surface	1.39	0.117
Rough surface	1.81	0.118

2.4.3 Flow curves

The comparison between the two powders can be extended through comparing their flow curves, presented in Figure 2.13. The solid line linking full marks represents the first upward sweep, while the dotted line and empty marks represent the downward sweep directly following.

The first obvious observation is a shift in stress: values recorded during the downward sweep show, for shear rates $\dot{\gamma} \leq 40\,\mathrm{s}^{-1}$, the same trend but a decrease of approx. 20 Pa in magnitude. This shift is an artefact of the apparatus: at high rotation speed, the machine records very high stresses due to the inertia of the measuring system, which is relatively heavy ($\sim$100 g) compared to the sample mass of 80 g (i.e. relatively small density of PS, as the volume of the powder bed is fixed within a certain range). The resulting high stress tends to de-calibrate the machine for experiments lasting multiple hours. Hence, while the trend of the flow curves remains accurate, the stresses recorded after the series of high shear rates tend to be underestimated by the machine.

More generally, the flow curves again show two distinct trends between high and low shear rate. At high shear rate $\dot{\gamma} > 20\,\mathrm{s}^{-1}$, the behaviour of both powders is quite similar: the flow

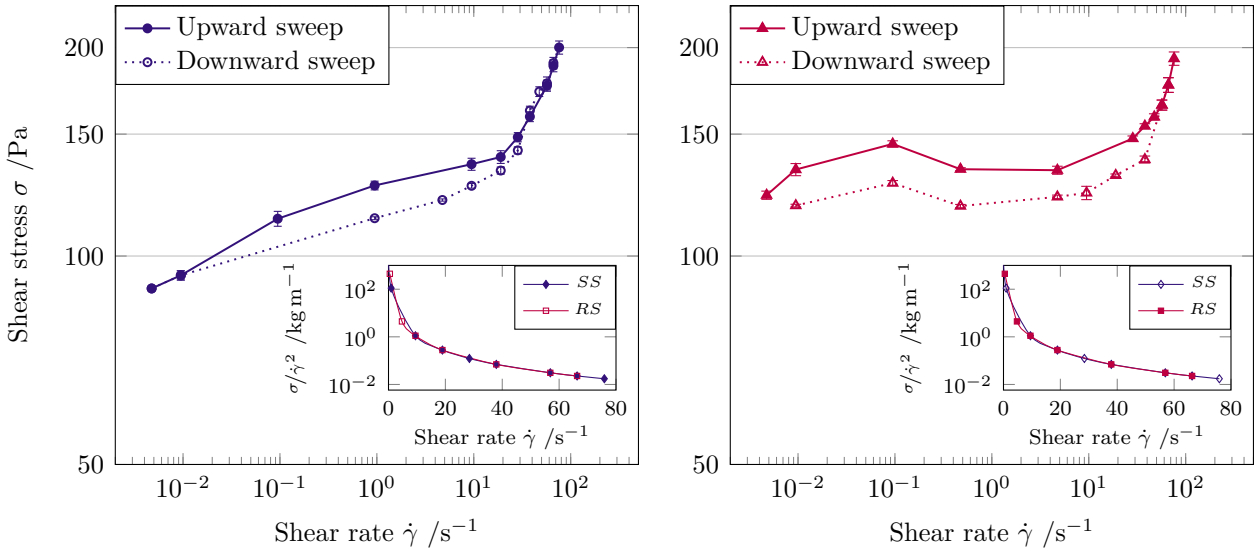

(a) Smooth surface **(b)** Rough surface

Figure 2.13: Flow curves for shear experiments performed in a Couette-type shear-cell on the PS powder of diameter 80 µm, for powder with (a) smooth and (b) rough surface state. The solid line and full marks represents the upward sweep (experiment run for increasing shear rates $\dot{\gamma}$), while the dotted line and empty marks represents downward sweep. Error bars represent standard deviation in stress values recorded in stationary state. The inset represents the evolution of $\sigma/\dot{\gamma}^2$ with increasing $\dot{\gamma}$ in order to probe if the system has reached the Bagnold regime, where $\sigma/\dot{\gamma}^2 = B$ should be constant.

curve monotonically increases and the stress values are similar within experimental error. The steepness of the flow curves drastically increases, indicating that a shear thickening regime is entered. To probe if the Bagnold scaling is observed (see Section 1.4), the evolution of the ratio $\sigma/\dot{\gamma}^2$ with increasing $\dot{\gamma}$ is plotted in the insets of Figures 2.13a and 2.13b. A constant $B = \sigma/\dot{\gamma}^2$ would show that the system is indeed in the specific shear thickening regime predicted by Bagnold [43]. The evolution of this ratio for both materials shows that B is not yet constant: although it seems that the system is approaching this regime, it would be reached for shear rates slightly higher than the ones accessible in the present set-up. In the shear thickening regime observed here, the roughness of the particles seems to be irrelevant as both systems show similar behaviour. In other words, the effect of high surface friction is predominant until the system becomes dominated by fast shear, thence entering the Bagnold regime. We estimate $B \approx 1 \cdot 10^{-2}$ kg m^{-1}; the shear rate $\dot{\gamma}$ where Bagnold scaling is reached appears similar for the RS and SS materials, identifying the regime where both show the same rheological response.

At low shear rate $\dot{\gamma} \leq 10\,\mathrm{s}^{-1}$, flow-behaviour becomes dependent on the surface state. The macroscopic stress σ is always higher for rough surface powder at fixed $\dot{\gamma}$. Moreover, the flow curve for rough surface particles is non-monotonic, indicating the appearance of a shear band in the rough material [44, 126]. Previous experimental work [127] has linked interparticle friction to the appearance of non-monotonic flow-curves. The appearance of flow instabilities can hence be linked to particles' roughness: what we observe might be the formation of a stationary shear band for shear rates under $\dot{\gamma} = 10\,\mathrm{s}^{-1}$, or a transient shear band whose size varies with shear rate. In the large gap rheometer used, the sheared region is sufficiently wide for the system to develop such discontinuous shear. The appearance of a shear band could also explain the remarkably long duration of transient flow observed during startup experiment (see Figure 2.12), as during flow onset the size of the shear band might be unstable and slowly increase

until finding its most stable position. Only at this point does the stress become constant over time, placing the system in steady state after a relatively long transient regime.

Observation of the flow curves for our two PS powders clearly indicate that roughness in granular material has an impact on its rheology, as at low shear rate $\dot{\gamma} < 10\,\mathrm{s}^{-1}$ it requires higher stress and undoubtably triggers the appearance of flow heterogeneities. However, this dependence on particles roughness seems to be regime-dependent, as it is linked not only to the material's packing density φ and boundary condition (i.e. confined or within variable volume), as we have seen in Section 2.2, but also to the rate of deformation it is submitted to.

2.5 Discussion & conclusion

2.5.1 What relevant parameters influence granular rheology?

Two granular materials differing only by their surface state (smooth and roughened through dry-coating of an angular sub-micron powder), namely PS powders of diameter 80 µm, were characterised through four different rheological tests:

- The flowability measurement proposed by the FT4 under the name of *flow energy* measurement. This quantity was modified to become the *specific flow energy*, to enable direct comparison between measurements done on samples composed of powders of different material density in bulk ρ and sample size.
- The tensile strength test proposed by Valverde *et al.* [70, 105], enabling to quantify interparticle cohesion regardless of its origin.
- Flow startup experiments $\sigma = f(\gamma)$ at shear rates $\dot{\gamma} \in [10^{-2}, 10^{2}]$, providing the effective shear elastic modulus for both powders at low $\dot{\gamma}$ and the duration of transient flow before reaching stationary state.
- Flow curves $\sigma = f(\dot{\gamma})$ at steady-state, spanning on different flow regimes to provide ground for comparison of the two powders on a broad spectrum of shear rates.

Through testing the effect of surface roughness at various packing density and rate of motion, for different types of imposed driving, our results show the difficulty to isolate the influence of a single parameter on powder flow-behaviour. Dense granular flows show a rich rheology, resulting from interactions among particles, but also with their surroundings and their stress history, and ultimately arising from the complex interplay between those multiple parameters.

On the influence of surface roughness. Surface roughness was the parameters at the heart of this study. The direct influence of increased rugosity at the surface of granular beads depends on the pressure pushing the grains together: following the Coulomb friction law, the friction force F_f is evaluated as $F_f \leq \mu F_N$, hence showing dependency on the materials in contact through the friction coefficient μ, and the normal pressure F_N exerted by the surfaces in contact on each other [128, 129]. Therefore, the frictional contacts between particles are activated once the pressure between grains is sufficiently high, which is particularly true for material confined inside a fixed volume at high packing fraction. Surface roughness herewith influences the ability of the packing to reorganise through frictional contacts, increasing the stiffness of the granular network. The degrees of freedom of the particles to slide, twist, and roll into new configurations are reduced as the stress needed to overcome friction is higher.

Besides, mechanical locking affects the ability of the particles to be set apart from one another, as surface asperities and/or the particles themselves become hooked. Cohesive forces also tend to force the particles to remain together once they have entered in the close vicinity of one another, and can be modified by changes in the surface's geometrical features.

In Section 2.3, we have used the tensile strength test proposed by Valverde *et al.* [70, 105] to measure the pressure overshoot needed to set apart the particles by subjecting them to an air flow passing through the packing until fluidising it. The tensile strength found for rough surface powder, $\sigma_t^{RS} = 88.4\,\text{Pa}$, is 12% higher than that of the SS powder, $\sigma_t^{SS} = 77.5\,\text{Pa}$, showing that higher stress is needed to set the particles apart, even at very low packing fraction (in this case $\varphi \approx 0.53$). This result enforces the fact that besides the known effect of surface roughness in an enclosed granular medium, asperities also have an influence on the force needed to set the particles apart, possibly through mechanical locking among grains.

On the influence of boundary conditions. As we have seen, granular density plays a key role, in particular through the activation of frictional rheology. Therefore, a first distinction must be made between confined and unconfined powder. In the case of an unconfined granular material under stress, the density state of the material is not fixed: the material can dilate without causing a pressure rise within the packing. Dilatancy being a well-known feature of granular materials under shear (the interlocked grains need to expand in volume in order to gain motion freedom [130]), the absence of a volume constraint can make the difference between flowing and jamming [131].

On the influence of packing fraction. The natural next parameter to evoke is the density of the packing. Indeed, packing fraction φ generally undergoes local variations. For unconfined powder, it should be noted that φ can largely vary, as the total volume is not fixed. The different experimental methods discussed here to probe the rheology of granular materials all work with an unconfined medium. The results hence obtained can be divided between two density regimes: the distinction is made between *high* packing fraction $\varphi \approx 0.59$ and *low* packing fraction $\varphi \approx 0.56$.

The *specific flow energy* E^* (see Figure 2.7), measured at low packing fraction, shows no variation with surface roughness, regardless of the helix penetration speed (which is used in this case as a proxy for the shear rate). On the contrary, when the penetration is performed at high packing fraction, the *specific flow energy* E^* undergoes an increase of 20% for rough surface powder, corresponding to a decrease in flowability. We can conclude from this fundamental difference that for the experiment run at low packing fraction, friction plays a minimal role in the rheology, as frictional contacts are not activated.

On the influence of shear rate. For confined powder, i.e. at fixed volume, conclusion made by Mari *et al.* [132] through simulation, later confirmed experimentally by Royer *et al.* [133], show that at low shear rates $\dot{\gamma} \to 0$, the friction between grains is almost absent, rendering it an irrelevant parameter; at high shear rates, it becomes an essential property that determines the material's rheological response (as well as its critical packing density at jamming).

For unconfined granulates at high packing fraction $\varphi \geq 0.59$, we find through shear flow startup experiments (Figure 2.12) that the behaviour of the stress-strain curves show a strong dependence on shear rate. At low shear rate $\dot{\gamma} \leq 1\,\text{s}^{-1}$, the initial elastic response of the material varies with its surface state, with an equivalent shear modulus $G_{\text{eff}}^{RS} = 1.81\,\text{Pa}$ higher by 30% for

rough surface powder than $G_{\text{eff}}^{SS} = 1.39\,\text{Pa}$ for smooth surface powder (see Table 2.3). On the other hand, at high shear rate $\dot{\gamma} > 40\,\text{s}^{-1}$, both powders show the same behaviour, identifying a regime independent of the material's rheological response.

Similarly, the stationary-state flow curves measured on both powders (see Figure 2.13) also show the same trend at high shear rate, and strong dependence on the surface state at low shear rates. The quantitative limit between those two regimes is found on the order of $\dot{\gamma} = 10\,\text{s}^{-1}$. The powder with high surface rugosity produces a non-monotonic flow curve, clearly indicating the appearance of a shear band. The smooth surface powder produces a monotonic flow curve; if shear-band formation cannot be excluded, the flow is presumably more stable as the stress rises steadily with rising shear rate. Moreover, the macroscopic stress recorded in the SS powder is lower than in the RS powder for all corresponding shear rates $\dot{\gamma} \in [5 \cdot 10^{-3},\, 40]\ \text{s}^{-1}$.

At low shear rate $\dot{\gamma} \leq 10\,\text{s}^{-1}$, the particles' interactions dominate the rheology, hence causing a strong dependence on their properties. At high shear rate $\dot{\gamma} \leq 60\,\text{s}^{-1}$, the material is entering Bagnold regime, and the interparticular contacts become too short-lived for surface friction to play a role.

2.5.2 Conclusion

Under the ill-defined concept of *powder flowability* one summarises the resultant of all the parameters, may they be essential or environmental, that influence the manner in which a granular material flows. Concretely, the tendency of the grains to remain together (due to cohesive forces or to mechanical locking), the fact that they require higher stress to be set in motion, and the reduced degrees of freedom for particles motion due to friction among particles are important factors lowering the flowability of rough surface powders.

Supporting the idea of a pressure-dependent rheology as put forward by the $\mu(I)$ rheology [78, 79], Wyart and Cates [134] propose a model for shear thickening based on stress-induced frictional interparticle contacts. At low packing density, the rheology is essentially frictionless, as the normal stress is too low to activate interparticle friction. At high packing density, the pressure is high enough to activate interparticular friction, which henceforth takes an important role in the rheology. The experimental results presented in this chapter are in accordance with this model, and continue the inherently multi-variable vision of granular rheology by showing a shear-rate dependence of the influence of surface friction. Rheometry reveals the nuanced influence of surface roughness on rheological properties: at low shear rate, the granular friction strongly influences the granular flows; at high shear rate, the regime becomes collisional and the interparticle friction becomes less relevant in the description of the material's rheology.

Despite a large industrial and academic interest, granular rheology is yet to be encompassed into a globalised theory. To predict powder behaviour in new, peculiar situations – e.g. under low- or microgravity – the absence of general theoretical description forces one to come back to relying on empirical observation and adaptability to predict and control dense granular flows. Looking at the results examined in this chapter in an engineering perspective, they provide essential indication on the most favourable regime to probe the final flowability of a granular material, resulting from the interplay of the multiple, inter-dependant parameters evoked. More explicitly, on-demand probing of the material would enable to create adaptable systems: instead of trying to maintain perfect control over the physical properties of the granular materials and of their surrounding environment, such system could probe the material to obtain live-information on the material exactly in its current state. But to function, such system would need to be

designed to probe the granular material in a regime where their rheological response reflects their characteristics, hence categorising them with accuracy. The tests presented in this chapter enabled to determine that such regime, optimal for obtaining information on the flow-behaviour of a granular material, is at high packing density φ and low shear rate $\dot{\gamma}$.

In the next chapter, we will probe the influence of a new parameter: gravity. Putting this parameter in the framework of our present understanding of granular rheology, we will question how and why it influences powder flow, in order to propose, in Part II, a process to handle granular materials regardless of their flow properties, but also under variable gravitational conditions, through probing their rheological properties and adapting the process parameters accordingly.

Chapter 3

Handling granular matter in microgravity

Whereas gravity can be considered a weak force in many areas of materials physics dealing with ordinary solids, liquids, and gases, the same does not hold true for the study of granular materials. These particulate systems are by definition composed of macroscopic grains [15, 16]; on-ground, such grains are henceforth large enough for gravitational forces on each of them not to be negligible in comparison to the other forces in presence. The flow behaviour of granular matter can thus change dramatically with a change in gravitational environment, such as the one affecting a body relocated from Earth to foreign planetary surface, or subjected to microgravity conditions.

In this chapter, we will study the change in rheology of granular dense flows as the gravitational environment changes from Earth gravity to microgravity, addressing the following questions:

- How does the absence or presence of gravity modify the force balance between particles?
- How are granular flows impacted and conditioned by their gravitational environment?
- How to trigger and control granular flow in microgravity?

3.1 Change in relative force contributions as a function of *g*-level

To unravel the changes in powder behaviour between gravity on-ground ($1g$) and microgravity (μg), the relative relevance of the different forces acting on granular particles is estimated.

3.1.1 Cohesive forces between grains *versus* gravitational force

The forces acting on the particles constituting a granular medium can be summarised as, on one hand, the interparticle surface interactions on the microscopic scale, and on the other hand, the flow-inducing forces impelling the collective particles motion. Let us consider the granular material presented in Chapter 2: a PS powder constituted of grains of radius r, whose surfaces are separated by a distance l. The surface roughness, which could trigger mechanical locking,

is ignored, as well as the direct elastic effects due to particles collision. As flow-inducing force, only gravity is considered. The interactions between two such particles encompass electrostatic, van der Waals and capillary forces.

Gravity-induced weight of a particle. The effect of the gravitational acceleration of magnitude g on a spherical particle of volume V, density ρ and radius r is:

$$F_g(r) = V\,\rho\,g = \frac{4\pi}{3} r^3\,\rho\,g. \tag{3.1}$$

Electrostatic interactions. Most granular particles charge through tribocharging as grains collide, by a mechanism that is to this day not fully understood [135]. Especially, in the case of insulating materials (like PS), the charges accumulate on the surface. The Coulomb law for interactions between electrically charged objects [128, 129] can be applied to two charged particles. For a pair of spherical bodies of radius r whose surfaces are at distance l, with a constant surface charge density σ, the interaction force is approximated by that of two point charges $Q = 4\pi r^2\sigma$ separated by $(2r + l)$, hence:

$$|F_e(r,l)| = \frac{k_e\,Q^2}{\varepsilon_r\,(2r+l)^2} = \frac{4\pi\,\sigma^2 r^4}{\varepsilon_0\,\varepsilon_r\,(2r+l)^2}. \tag{3.2}$$

Here, k_e is the Coulomb constant with $k_e = {}^1\!/_{4\pi\varepsilon_0}$, σ the surface charge density, ε_r the dielectric constant of the embedding medium and ε_0 is the vacuum permittivity. Electrostatic forces can be attractive for opposed sign charges ($F_e < 0$) or repulsive for same sign charges ($F_e > 0$).

Capillary forces. In the presence of small amounts of interstitial liquid, unsaturated granular particles can be linked by liquid bridges. The surface tension γ of the liquid brings the particles together in an effort to reduce the free surface of the liquid meniscus, entailing capillary forces that can be expressed as the Laplace pressure between two curved surfaces:

$$F_c(r,l) = -2\pi \frac{\gamma\,\cos\theta}{(1 + {}^l\!/_d)}\,r, \quad \text{with} \quad d = r\,(1-\cos\phi). \tag{3.3}$$

The two particles of radius r are linked by a liquid bridge on a (small) aperture angle ϕ; the contact angle between the liquid meniscus (of surface tension γ) and solid particle is θ [136].

The forces exerted by the liquid bridges are dependent on the bridge volume: for a small amount of liquid, the moisture is only bridging the asperities on the particles' surface. As the liquid quantity increases, the interparticle capillary forces reach a maximum for a liquid bridge radius larger than the size of the asperities, but lower than the particles' radii [136, 137] – this is the case considered here. When the particles are effectively immersed, the capillary force disappears and the liquid can serve as a lubricant, causing a steep increase in flow properties at high liquid content.

Van der Waals interactions. The van der Waals interactions summarise various surface energy forces inherent to material boundaries [119]. Resulting from electron density shifts creating polarities on the molecular or atomic level [136, 138], they are very short-ranged, but become significant between macroscopic bodies in close vicinity ($\sim$ nanometer-scale), scaling up with their contact area. For particles of the same material, they are necessarily attractive [139].

For two macroscopic spheres of radii r_1 and r_2 whose surfaces are separated by a length l, the force derivation proposed by Hamaker [139] and simplified by Israelachvili [138] gives:

$$F_{VdW}(r, l) = -\frac{A}{6\,l^2}\frac{r_1\,r_2}{(r_1 + r_2)} \tag{3.4}$$

where A is the Hamaker constant, an empirical constant related to the body's surface energy [139]. It was mentioned in Section 2.1 that an addition of small particles could enhance granular flow by reducing the van der Waals interactions. This mechanism is explicitly expressed by Equation 3.4: for $r_1 \ll r_2$, the term $r_1\,r_2/(r_1+r_2)$ is smaller than if $r_1 = r_2$. In other words, adding small guest particles in a host powder of larger particles can reduce the van der Waals attractive interactions between those large particles [70, 98, 99], thereby enhancing the flow properties of the granular material. However, as shown by the multiple rheological experiments reported in Chapter 2, this mechanism depends on many more factors, among which the confining pressure (i.e. packing density) at which the granular flow takes place: if the particles are confined and undergo lasting frictional contact, a sub-micron scale dry coating can create a rough surface on the particles, enhancing mechanical locking and forcing the particles in close contact regardless of the guest particles (especially if they cannot roll on the large particles' surface), thereby decreasing the flow properties of the material. On the other hand, if the particles do not undergo a large confining pressure, the reduction in van der Waals forces can reduce the cohesion within the packing and in the end enhance flow.

For the (ideal) case of smooth particles of same radii $r = r_1 = r_2$, the van der Waals attractive forces are [138]:

$$F_{VdW}(r, l) = -\frac{A}{12}\,\frac{r}{l^2}. \tag{3.5}$$

The van der Waals interactions hence scale linearly with particle size, and inversely proportional to the square of the distance l between the particles. This underlines the importance of the confining pressure in granular material properties, as it tweaks the packing fraction, which modifies the typical interparticular distance and thereby the magnitude of cohesive forces between grains.

Relative effect of gravity on powder cohesion. Figure 3.1 shows the evolution of the magnitude of the various interparticle forces versus gravitational acceleration as a function of the two particles separation distance (Figure 3.1a) and as a function of their radius (Figure 3.1b).

As a body force, the gravitational pull F_g scales with particles' volume, i.e. $\sim r^3$, whereas interparticle forces only scale quadratically ($F_e \sim r^2$) or linearly (F_c and $F_{VdW} \sim r$, unless $r \approx l$), hence increasing less strongly than F_g with increasing particle size. The relative effect of gravity depends on the particle size: for very small particles, the cohesive forces (van der Waals and capillary forces, electrostatic in the case of oppositely charged particles) between a particle and its neighbour are by far dominant over the gravitational force pulling each of them downwards. (It should also be noted that the interactions represented here are for a pair of particles, whereas in a granular medium multiple neighbours surround each particle, accordingly increasing the cohesive interactions.) Powders composed of smaller particles, in the size range of 100 µm and smaller, behave more cohesively, both on-ground and under lower gravitational acceleration: when sufficiently close, they tend to stick to one another rather than flow under gravity. Yet, particles under 100 µm are very relevant for low-gravity applications: they are found on planetary surface [140] and used for space-relevant technologies [141]. In this regime, a change in

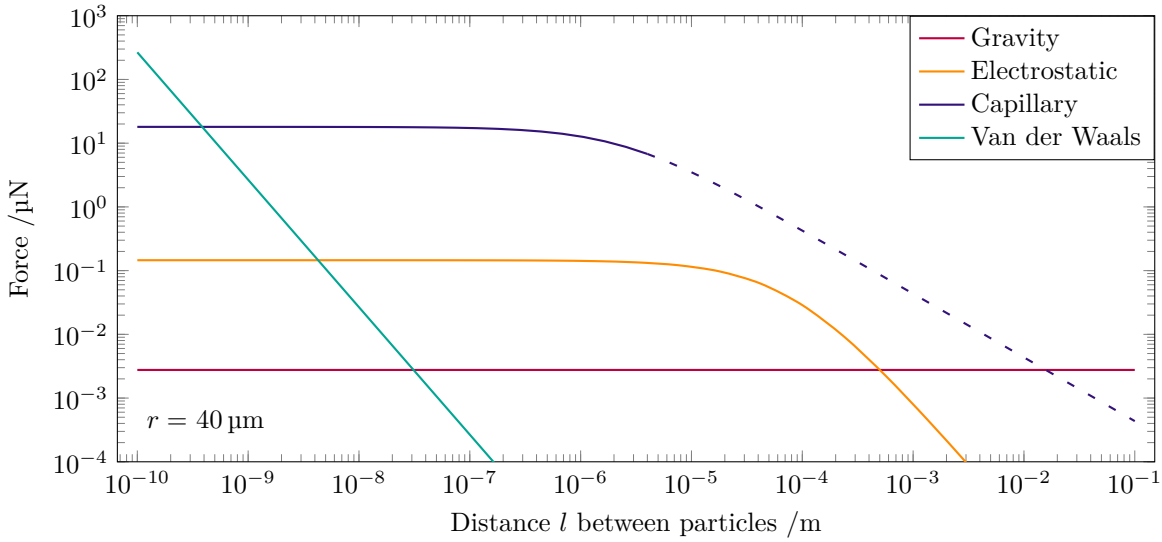

(a) Interparticle force magnitude *versus* interparticular distance

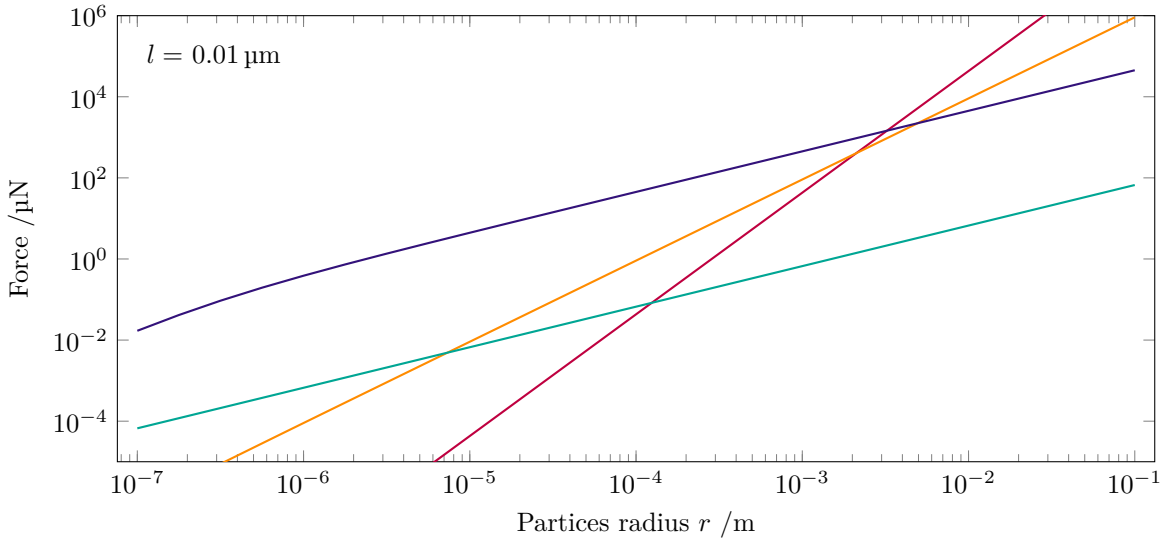

(b) Interparticle force magnitude *versus* particles radii

Figure 3.1: Evolution of the relevant interaction forces on the microscopic scale between two particles (a) as a function of length l separating the particles' surfaces, for particles of 80 µm diameter, and (b) as a function particles' radius r for spheres separated by 0.01 µm. As water bridges of more than a few percent of particle diameter are geometrically impossible, the capillary force for an interparticular distance larger than $0.1\,r$ is represented by a dashed line. For the evaluation of the forces, the following material parameters were used, corresponding to polystyrene particles in air: mass density $\rho_m = 1050\,\mathrm{kg\,m^{-2}}$ dielectric constant $\varepsilon_r = 1$, surface tension $\gamma = 72\,\mathrm{mN\,m^{-1}}$, contact angle $\theta = 5°$, aperture angle of capillary liquid bridges $\phi = 20°$, Hamaker constant $A = 8 \times 10^{-19}$ J, surface charge density $\sigma = 1.6 \times 10^{-5}\ \mathrm{C\,m^{-2}}$. Freely adapted from Ref. [99].

gravitational environment is expected to shift the force balance significantly, as all the force contributions can be of comparable orders of magnitude.

Under reduced gravity, the cohesive interactions are indeed not of higher magnitude, but become predominant: on account of the shift in predominant force acting on each particle, the material as an ensemble is dominated by the interparticle forces (generally attractive), in place of the weight of its constitutive grains. Experimental observations report exactly this

behaviour: powders in microgravity tend to agglomerate and form stable aggregates [142–145]. One consequence from this observation is that space-relevant technologies based on powder-handling have to be adaptable to highly cohesive granulates.

3.1.2 Granular Bond number

To a certain extent, granular flowability is determined by the ratio between forces impelling flow and the interparticular cohesive forces. Zimmermann *et al.* [99] proposed to conceive the flowability of a powder as the ratio between the gravitational pull acting on the particles, which (in the gravity-driven case) makes the powder flow, and the cohesive interactions between grains that hold the packing together. This is done *via* the dimensionless granular Bond number [70, 98, 146]. In fluid dynamics, the Bond number Bo (or Eötvös number Eo) measures the ratio of gravitational force over surface tension forces (attractive forces among the liquid molecules) to determine the shape of a droplet [147]. In a similar vein but defined inversely, the granular Bond number Bo_g is the ratio between attractive interparticular forces and competing force that spur the material to flow:

$$Bo_g = \frac{F_{\text{cohesive}}}{F_{\text{flow}}}. \tag{3.6}$$

Two categories of materials appear:

- For $Bo_g > 1$, cohesive materials where the grains stick together rather than flowing. As Bo_g increases, the powder is considered less and less flowable, as the forces holding the packing together become predominant.
- For $Bo_g < 1$, the material subjected to the given force F_{flow} will flow. For low Bo_g the powder is considered highly flowable.

The granular Bond number is often calculated as the ratio of cohesive forces between a pair of grains over the weight of a grain: $Bo_g = {}^{F_c}/_{m\,g}$. Whereas this definition is valid for gravity-driven flows, it becomes irrelevant if the main flow-driving force is not gravity. The definition of the granular Bond number proposed in Equation 3.6 offers the advantage of being sufficiently broad to encompass any flow-driving force.

The Bond number as a characterisation for powder flowability has the advantage to make this granular property clearly situation-dependent: it qualifies a ratio of forces acting in a specific context instead of pretending to transform a phenomenological measurement into a universal material property. However, this approach implies that the interparticle forces are known *a priori* – which can be the case in simulation, but hardly in experiment – and that the flow-driving forces are the same throughout the packing – which is only true if the flow-driving forces are solely body-forces.

On this last point particularly: as a microscopic approach (the force balance is done on one pair of particles), Bo_g is then extended to the entire granular packing, assuming that the force(s) impelling flow are the same on all particles. This is true in certain cases, in particular with body forces (e.g. for gravity-driven flows, for centrifugal forces at constant radius or hydrodynamic drag at constant velocity). However, for boundary forces, as discussed in Section 1.1, force transmission in a granular medium is heterogeneous as the packing redirects the forces through force chains, under the condition that a contact network exists among the particles. If the flow should be triggered by shear force or normal pressure applied on the system's boundary, localised variations of the flow-impelling force produce a varying Bo_g number throughout the packing.

Moreover, it would result in heterogeneous packing density, so that part of the granular system might be completely untouched by the boundary force. It is therefore necessary to ensure that such boundary flow-impelling stimulus be transmitted throughout the packing (particularly in microgravity), and assert that similar causes would produce similar effects in microgravity as on-ground.

3.2 Triggering powder flow in microgravity

On ground, granular flows can be triggered through their potential energy in gravity-driven flows. In microgravity, by definition the gravitational acceleration g is close to zero; the grains will not fall towards the minimum-height position available, but cluster into floating aggregates [142–145], as the interparticle cohesive forces become the predominant interactions.

Moreover, if no force field sediments the packing, particles of clusters of particles are not necessarily in contact with their neighbours [148], nor with the instrument of force transmission (in the case of boundary forces). Forces chains cannot appear unless a contact network is established, which challenges the use of boundary forces, as they might not be transmitted throughout the medium. Densifying the packing to ensure lasting interparticle contacts is therefore a necessary step if boundary forces should be used to control powder flow in microgravity.

3.2.1 Microgravity experiment: piston-probing of granular packing

To study how to trigger and control powder flow in microgravity, and observe the variations in powder response to external stimuli between $1g$ and μg, a piston-probing experiment was conducted on parabolic flight[1]. This experiment, designed and built by the author, flew on the 31st DLR Parabolic Flight Campaign (PFC) in March 2018.

Piston-probing experimental setup. A schematic view of the experiment is shown in Figure 3.2a. Piston-probing consists in applying a finite amount of normal pressure to the packing in a confined space, as a piston rises in a container filled with powder. A lateral space is left on the sides of the piston's platform, leaving the possibility for the packing to yield and flow downwards, around the platform.

The experimental equipment is presented in Figure 3.2b. The set-up consists of a transparent PMMA tube of diameter 48 mm and height 54 mm, inside which a piston of diameter 36 mm (two thirds of the tube section) can rise incrementally. The material used for this experiment is the PS powder presented in Chapter 2, of diameter 80 µm and smooth surface state. Inside the container, the mass of granular material inserted determines an overall packing fraction of $\varphi_0 = 0.55$. The piston is moved by a direct-current (DC) motor, regulated through a velocity-controlled closed-control loop. The torque developed in doing so is recorded, proportional to the apparent change in viscosity of the material as it is compressed. One important nuance is that the direct-current (DC) motor pulling up the piston alternates between an *active* and a *passive* state:

- In its active state, it receives a binary command, given by the user: it is either supposed to be rising at constant speed or to remain immobile in its position. The motor develops

[1]The principle and specificities of parabolic flights as a microgravity experimental platform are detailed in Chapter 7.

a torque in both states, as keeping the motor motionless also represents an effort.

- While the piston is in its active "rising" state, the motor is pulling it up. However, its rising-speed is slowed down by the densification of the packing above its platform, either until the granular packing flows around the piston's platform to fill the freed volume under it, or until reaching a jammed state that would drive the piston to a complete stop.

An optical measurement of the piston height provides an indirect assessment of its position, thus of its *true* rising speed. The concomitant decrease in rising speed and increase in torque developed (as the DC motor struggles to maintain the programmed velocity) are used as proxies to capture the increase in packing density, which entails an increase in apparent viscosity of the granular sample.

The changes in distribution of the granular material in regard to the piston are monitored. Pressure sensors are placed inside the tube, on the lateral walls, and record the pressure evolution as the piston compresses the granular sample. One sensor is placed on the upper part of the container ($h \approx 45\,\text{mm}$), and another one on the bottom part ($h \approx 15\,\text{mm}$). The sensitive area of the pressure sensors measures $200\,\text{mm}^2$, which represents approx. 30 000 particles. The pressure sensors are calibrated in-house, so the pressure recorded corresponds to the pressure difference due to the powder contained in the cell. A camera below the transparent container enables to observe the set-up from below. At the beginning of the experiment, the piston is generally at its lowest position, i.e. the platform touches the bottom of the closed tube; it is then programmed to rise by step-by-step, each step being activated by the user after approximately 20 s. In some experiments the platform is placed in the middle of the box, at its median position in height. The technical specifications of the hardware used are given in Table 3.1.

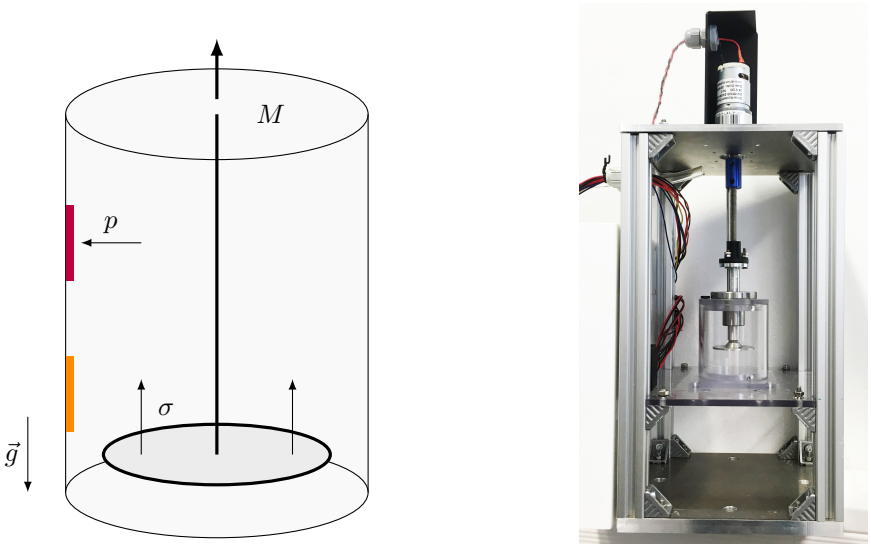

(a) **(b)**

Figure 3.2: Experimental setup. (a) Piston-probing principle: a piston rises incrementally in a closed container, filled with powder, applying a normal stress σ on the contained packing corresponding to the torque M generated by a DC motor. The pressure p transmitted through the packing is recorded by two pressure sensors placed on the lateral walls of the container. (b) PFC setup, showing the container in its support structure.

Table 3.1: References for hardware used on the piston-probing experimental setup.

Hardware	**Model**
DC motor	DSMP 320-24-0189-BF (max. torque 0.69 N m)
Current sensor	Pololu ACS7174
Pressure sensor	SingleTact capacitive pressure sensor
Camera	YI 4K Plus Action Camera (resolution 3840×2160 pixels)

3.2.2 Results: granular response to piston-probing in $0g$ *vs.* $1g$

The piston-probing experiment is conducted in microgravity and reproduced on-ground for comparison. Generally, the granular sample undergoes the following steps:

1. Densification of the granular medium: the packing density increases on top of the piston, leaving an empty volume under it.
2. The granular medium reaches a critical packing fraction over the piston: it jams.
3. Under $1g$, the packing eventually yields and flows into the empty space below the piston's platform. In μg, the piston is blocked by the jammed packing; it remains in this state until the piston is moved down.

It is noteworthy that the pressure p recorded by the sensors is normalised by the pressure p_0, recorded by each sensor at the instant we label as t_0. In-flight (μg-experiments), t_0 corresponds to the start of the microgravity period. On-ground ($1g$experiments), it corresponds to the instant right before the start of the piston-rise for each step. Ultimately, the pressure variation p/p_0 is used to observe the transitions in density-regime: *loose*, *dense* or *jammed* packing.

Densification of the packing. Data from the first step up of the piston, measured on the upper half of the container, on-ground and in microgravity, is presented in Figure 3.3. At first and until approximately 6 s, the piston is rising but the pressure does not undergo any change. For both experiments, it is only then that the pressure starts increasing. This first step is the densification of the packing: as the initial packing fraction is $\varphi_0 = 0.55$, which for a monodispersed granulate is lower than random close packing ($\varphi_{rcp} = 0.64$ [149, 150]), the packing still has enough space and mobility to reorganise into a denser configuration.

The pressure recorded on the container's upper lateral wall then increases, as the packing has reached a state of high density and continues to be compressed by the rising piston. From this point on, the flow-behaviour of the packing depends on its gravitational environment.

Under $1g$, the powder placed on top of the piston's platform is collectively moved upward until it occupies all the free volume available in the container above the piston. At $t^{1g} \approx 6$ s, the network of contacts formed in the packing spans from the top of the platform to the upper wall of the container. The pressure recorded by the top sensor starts increasing. The packing undergoes a first large-scale reorganisation at $t^{1g} \approx 10.5$ s – labelled point (c) in Figure 3.3 – which temporarily releases pressure on the sensor, but with almost no powder flowing under the platform (see Figures 3.3c and 3.3d). The jamming packing fraction φ_J^{1g} is reached at $t_J^{1g} = 12.5$ s. The position of the piston in height correlates with the pressure measured on the wall of the container: the piston is blocked and stops rising when a peak in pressure is reached. This shows a flow-regime change as the critical jamming density is reached inside the container. The piston is stopped for a few seconds; then, at $t^{1g} \approx 18$ s, a yielding point is reached and the

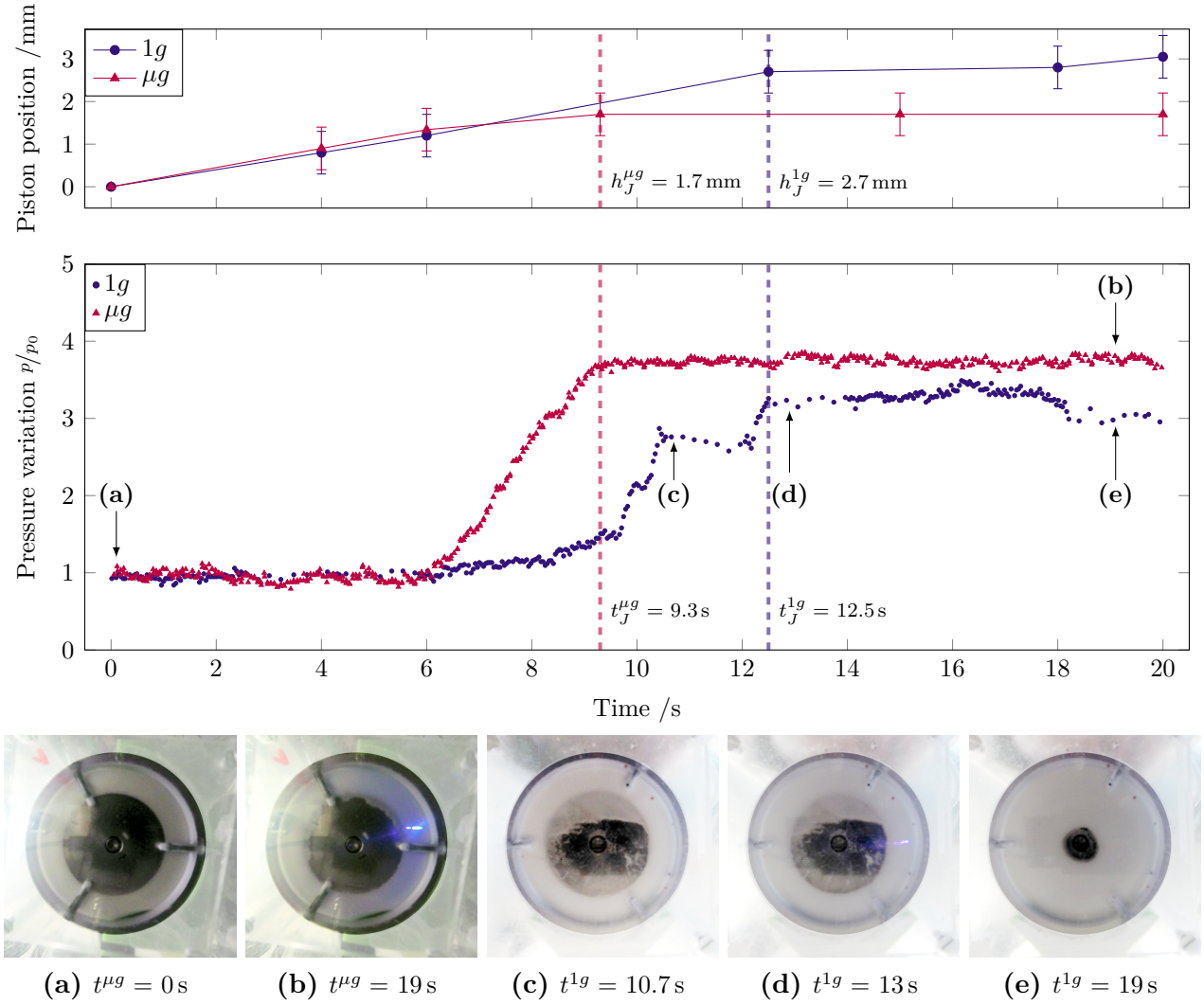

(a) $t^{\mu g} = 0\,\mathrm{s}$ **(b)** $t^{\mu g} = 19\,\mathrm{s}$ **(c)** $t^{1g} = 10.7\,\mathrm{s}$ **(d)** $t^{1g} = 13\,\mathrm{s}$ **(e)** $t^{1g} = 19\,\mathrm{s}$

Figure 3.3: (Top graph) Piston position in height as a function of time. Error bars represent the experimental precision in optical measurement. (Bottom graph) Pressure recorded by the top sensor during the first step up of the piston, on-ground (blue dots, labelled $1g$) and in microgravity (red triangles, labelled μg). The critical jamming time are marked, as well as five points of interest that correspond to images (a) to (e): (a) and (b) are images from the bottom of the experiment cell looking up in microgravity, and (c), (d) and (e) on-ground; the piston's platform is black and the PS powder white.

packing flows under the platform, releasing the pressure on the container wall (see position (e) on Figure 3.3).

To determine experimentally the packing fraction at jamming, the powder density is calculated as a function of the *new* piston height, at the instant when it is driven to arrest by the packing, because it is considered that at this instant the entire packing above the piston is jammed. For the $1g$ experiment shown in Figure 3.3 we obtain thus a jamming packing fraction of $\varphi_J^{1g} = 0.579$.

In μg, the granular behaviour is quite different. First, the packing undergoes a localised densification right on top of the platform, as only the grains directly or indirectly in contact with the rising platform are subjected to its movement. Approximately at the same time as for the ground experiment ($t^{\mu g} \approx 6\,\mathrm{s}$), the pressure rises on the sensor; however it is not jerky as under

$1g$, but a smooth and relatively steep increase towards its saturation pressure. This pressure is reached earlier than on-ground: at $t_J^{\mu g} = 9.3\,\mathrm{s}$, the piston stops because the jammed granular packing prevents its further motion. The measured position and the absence of material covering the bottom of the platform suggests a critical packing fraction of $\varphi_J^{\mu g} = 0.567$. It should also be noted that at this instant – point labelled (b) in Figure 3.3 – despite the platform having risen by 1.7 mm, almost no powder has flown under the platform: only the fringe of the platform is slightly covered by less than 1 mm, which is attributed to gravity-jitter in the horizontal plane, common on parabolic flight [151].

Critical packing fraction at the jamming point. In fact, the height at which the packing jams in microgravity was repeatedly measured to be lower than on-ground. A transcript of the corresponding critical packing fraction calculated from the height at which the piston is stopped (blocked by the granular packing), is presented in Figure 3.4 for four repetitions of the experiment, each for the first step up of the piston in the experiment sequence, in order to capture the densification phenomenon; and before yielding for the $1g$ experiment, and before observing any powder covering the bottom of the piston's platform.

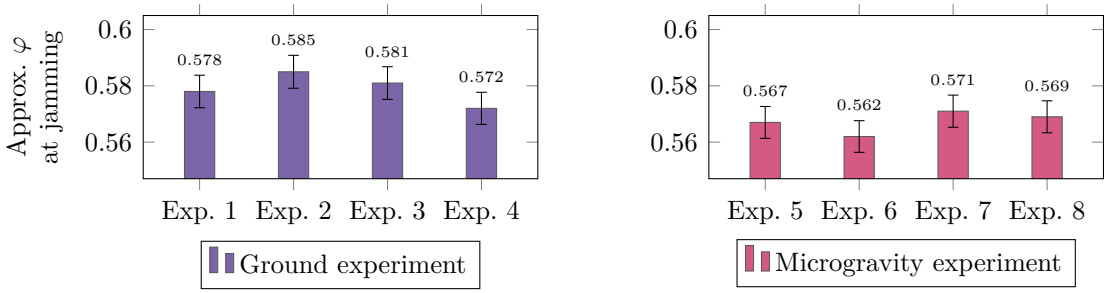

Figure 3.4: Critical packing fraction at jamming, estimated from the height at which the piston is driven to a halt by the resistance of the jammed packing, (left) on-ground and (right) in microgravity.

The critical packing fraction at which jamming occurs is lower in microgravity than on-ground for each repetition; in average (over the four experimental recurrences available), it is of $\varphi_J^{1g} = 0.579$ on-ground against $\varphi_J^{\mu g} = 0.567$ in microgravity.

Qualitative flow and force redirection. On-ground, once reaching a certain packing fraction, the packing yields and flows under the pressure applied by the piston; in microgravity, it jams at lower packing density into a stable configuration that then remains until the piston is lowered. This happens regardless of the repeated periods of hypergravity that occur in between microgravity periods on parabolic flight. This qualitative difference was observed on all repetitions of the experiment; some are visualised in Figures 3.5 and 3.6. Mechanisms explaining this difference in behaviour are proposed below.

On-ground, the packing is first pushed upward by the rising piston; once the top of the granular sample has reached the top wall of its container, the packing is compressed and the pressure on the lateral walls starts increasing. This first step is visible in Figure 3.3. Then, the piston continues rising; so does the pressure on the lateral walls as the packing is now under compression. Eventually, φ_J^{1g} is reached and the piston stops, blocked by the jammed packing. But unlike in microgravity, the gravitational pull creates a secondary downward force field. As the piston continues to push, the stress level in the packing eventually reaches a threshold; the powder collapses and flows under the piston's platform. (This transition is visible between Figures 3.3d and 3.3e.) The piston is then free to rise again until the end of the step. After this

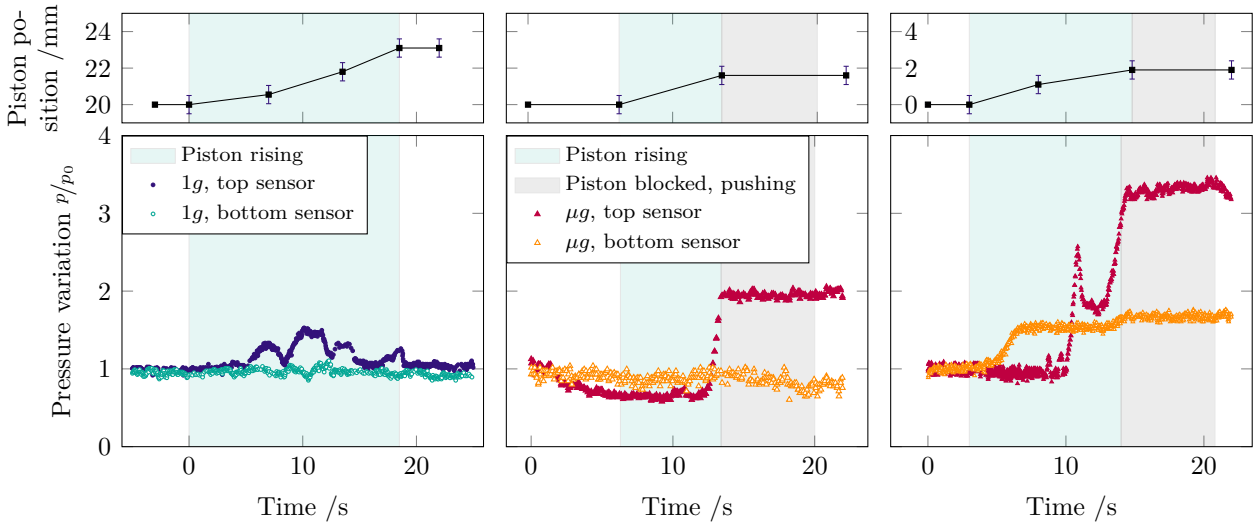

(a) On-ground **(b)** In microgravity **(c)** In microgravity

Figure 3.5: Typical pressure evolution per step up of the piston, (a) on-ground and (b), (c) in microgravity. The pressure variation p/p_0 (bottom graphs) correspond the pressure changes recorded by sensors in two positions: on the top part of the cell (filled marks, 1$g$in blue and μg in red) and on the bottom part of the cell (open marks, 1g in green and μg in orange). On (a) and (b), the piston starts in the middle of the cell (position $h = 20\,\text{mm}$), while on (c) it starts at the bottom of the cell ($h = 0\,\text{mm}$), which means that on (a) and (b) the pressure sensors are distributed one above the piston's platform and one below, while on (c) both are above the platform. On (b) and (c), $t = 0\,\text{s}$ represents the start of the microgravity phase; on (a) it represents the start of piston rise.

first step, the piston rise is stopped, and can be started again for a further step up. Figure 3.5a shows a step up of the piston in 1g after having previously travelled up to half of the container. During this step, alternating phases of pressure build-up and collapse show that the packing flows intermittently under the platform, in a manner reminiscent of stick-slip events [51, 52]. The pressure on the bottom part of the cell is also shown in Figure 3.5a. In this experiment, as at $t^{1g} = 0\,\text{s}$ the piston is in the middle of the cell, the top sensor records the pressure above the piston and the bottom sensor that under it. As periods of increase and steep decrease of the pressure alternate on the top part of the cell, the bottom one remains relatively undisturbed. Slight variations corresponding to the largest pressure drops on the upper part of the cell can be linked to an event of collapse of the granulate around the piston: as it flows around the platform, the bottom lateral pressure rises; then, as it flows down into the free volume under the piston, the bottom lateral pressure decreases again, going back to its original state.

In microgravity, the densification is localised directly on top of the piston. As it rises, the area in indirect[2] contact with the piston expands, until a network of contact spans from the piston to the container's top wall. Then the pressure on the lateral walls starts rising, as visible in Figure 3.3, until reaching a critical packing fraction where the packing jams and the piston is stopped. This behaviour is observed repeatedly in all microgravity experiments. Two examples of pressure evolution on the top and bottom part of the cell are given in Figures 3.5b and 3.5c.

In Figure 3.5b, at $t^{\mu g} = 0\,\text{s}$ the piston is in the middle of the cell. (It is its initial position in

[2] *Indirect* contact qualifies here the grains in contact with grains in contact with the piston; in other words, the zone of influence of the piston.

this experiment.) Hence the bottom sensor records the pressure under the piston and the top one the one over the piston. On the top part of the cell, after a mild pressure decrease when entering microgravity, the piston rises for approx. 5 s before the pressure undergoes a steep increase, which lasts approx. 3 s, similar to the pressure increase in μg shown in Figure 3.3. At this point, the piston is pushing but does not move: it is blocked by the jammed packing. Meanwhile, no change is recorded on the bottom sensor, showing that the powder already on the bottom half of the cell remains there but no powder is transmitted from the top to the bottom half. Without gravitational field to offer a secondary flow directed downwards, the powder remains in its initial half of the container.

In Figure 3.5c, the piston starts at position $h = 0\,\text{mm}$ (at the bottom of the cell). The densification reaches first the bottom pressure sensor, which records a first increase; then it reaches the top sensor which also undergoes a steep pressure increase. The pressure upsurge lasts here approx. 4 s, interrupted by a reorganisation of the packing that triggers a pressure drop at $t^{\mu g} \approx 11\,\text{s}$. Once the piston is stopped by the jammed packing, the pressure recorded at the bottom is subjected to another rise, and the pressure on the entire cell saturates.

Stability of the jammed state. The stability of the jammed packing can be assessed by observing the evolution of the pressure for a longer duration after the first step of densification leading to jamming of the packing. Such experiment is presented in Figure 3.6.

On-ground (see Figure 3.6a), the repeated steps lead to multiple repetitions of the same phenomenon, with pressure build-up and collapse creating oscillations of period around 5 s at each step. The inset corresponds to the detail of the third step up of the piston.

One surprising phenomenon is observed in microgravity: as shown in Figure 3.6b, once the packing is jammed, neither the next attempt of the piston to rise, nor the alternating periods of hypergravity and microgravity make the packing flow. The pressure applied on the top sensor is high ($\approx 15\,\text{kPa}$) and remains constant until the piston descends. In order to verify that this is not due to malfunction of the pressure sensors, on a different flight-day the pressure is recorded during ten parabolas without any motion of the piston: the result is presented in the inset of Figure 3.6b. The pressure variations due to change in gravitational acceleration is clearly visible, and corresponds to the temporal structure of the parabolic flight.

Torque developed to rise the piston. The torque developed to rise the piston in the different gravitational environments is presented for one step up of the piston in Figure 3.7. On-ground (see Figure 3.7a), the holding torque is on average $4 \cdot 10^{-2}\,\text{N m}$; as the piston starts rising, the torque developed slightly increases up to $6 \cdot 10^{-2}\,\text{N m}$. The packing jams at $h_J^{1g} = 2.1\,\text{mm}$ (corresponding to a packing density of $\varphi_J^{1g} = 0.572$), triggering a torque increase up to $2.5 \cdot 10^{-1}\,\text{N m}$. After 4.7 s, the powder yields and flows around the piston, causing the rise of the piston to start again and the torque thereby developed to drop to its previous value.

In hypergravity (Figure 3.7b, dark diamonds), the average holding torque is $1.4 \cdot 10^{-1}\,\text{N m}$, because under $1.8g$ the piston holds the doubled weight of the powder sample resting on it (and the weight of the piston itself). Once reaching microgravity (Figure 3.7b, red triangles), the holding torque drops; at $t = 5.6\,\text{s}$, the piston starts rising. After rising up to $h_J^{\mu g} = 1.78\,\text{mm}$, the packing jams and the piston is blocked (at $\varphi_J^{\mu g} = 0.569$). At this point, the torque rises to $3.5 \cdot 10^{-1}\,\text{N m}$ and only decreases once the piston is stopped.

The same behaviour is observed on all the steps where the piston rises, as presented in

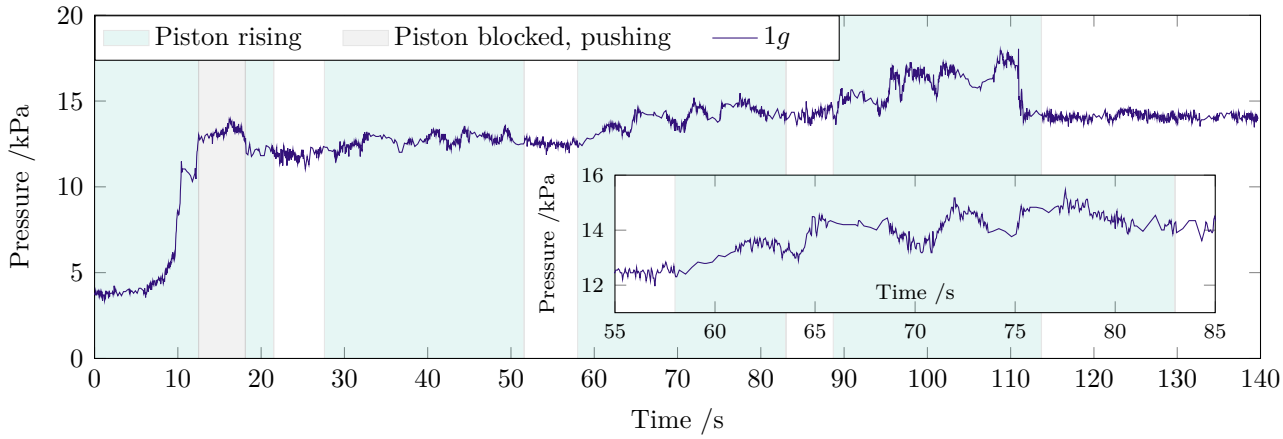

(a) On-ground

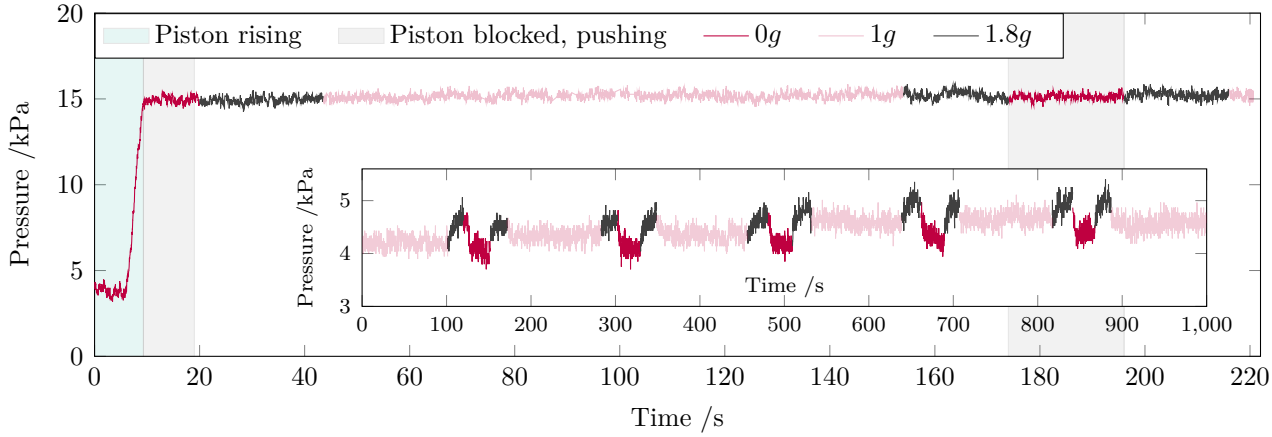

(b) Microgravity

Figure 3.6: Pressure recorded by the top sensor inside the powder container, (a) on-ground and (b) in microgravity, for a longer duration after the initial densification step leading to a jamming transition. The inset of graph (a) is a close-up of the pressure evolution during the second step up of the piston. The inset of graph (b) is the evolution of pressure inside a cell filled with powder but where the piston does not move: the pressure changes are solely due to changes in gravitational acceleration during the parabolic flight manoeuvres.

Figure 3.8 for sixteen repetitions in microgravity and on-ground.

The peak torque developed is in average 0.615 N m for the steps taken in microgravity, against 0.312 N m on-ground, which represents an increase of 49% in microgravity. Moreover, on almost all steps in microgravity where the piston should rise, it is blocked and remains at constant position while the torque shoots up to almost the motor's maximum (0.69 N m). The critical packing fraction at which the powder on top of the piston jams is reached at the first step ($h_J^{\mu g} = 2.0\,\text{mm}$, thus $\varphi_J^{\mu g} = 0.571$). After this first jamming event, all the steps up of the piston are blocked and it moves only within a small magnitude slightly, up to $h^{\mu g} < 3$ mm at the end of sixteen attempted steps in microgravity.

For the experiment conducted on-ground, the peak torque developed per step to move the piston are lower. As powder flows under the platform, the maximum rising magnitude of the piston is higher than the critical height at which the granular material jams and stops the piston at its first step up (h_J^{1g} in Figure 3.3). Under $1g$, the secondary force field due to gravitational

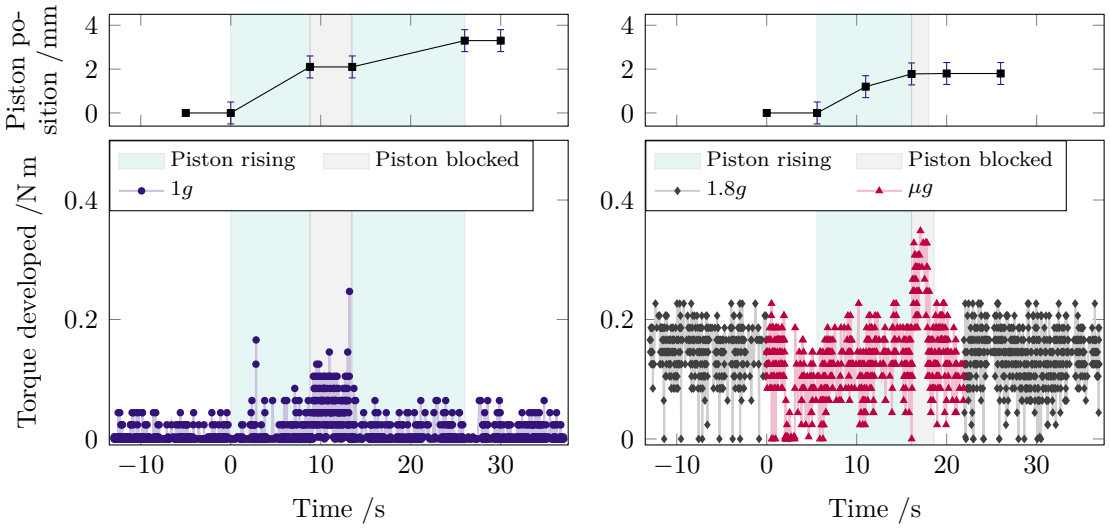

(a) On-ground **(b)** In microgravity

Figure 3.7: Torque developed for one step up of the piston, (a) on-ground and (b) in microgravity. The error bars in piston position correspond to the experimental measurement error. This measurement was conducted on (smooth surface) PS particles of diameter 140 µm.

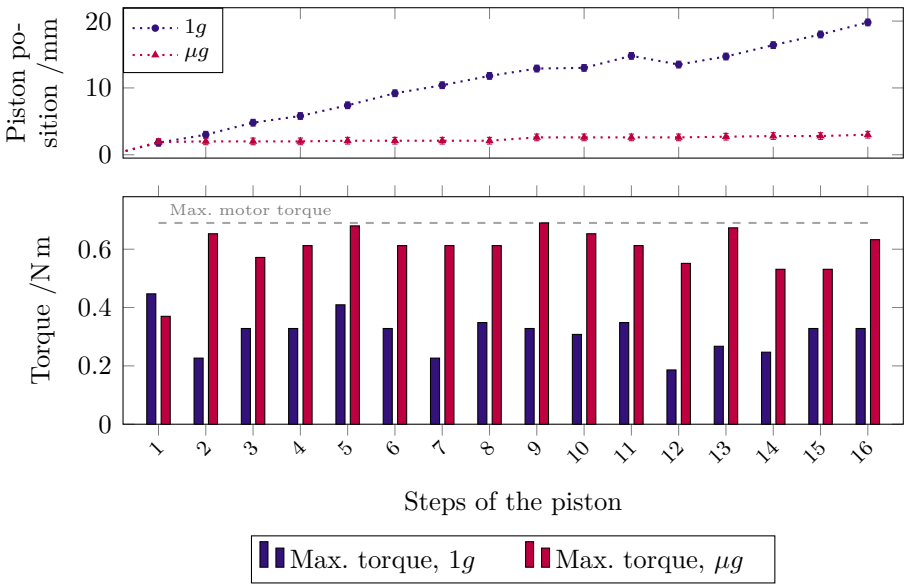

Figure 3.8: (Top) Position of the piston, estimated at the end of each step. The error bars in piston position correspond to the experimental measurement error. (Bottom) Maximum torque developed at each upward step of the piston. This measurement was conducted on PS particles of diameter 140 µm.

pull adds a downward force to the pressure applied by the piston, and triggers the fall of the material surrounding the space left empty by the piston rise. The material yields under the piston push coupled with the gravitational force, leaving free space on the upper side of the cell for the piston to continue rising.

3.2.3 Discussion: influence of the gravity on granular flow

The piston-probing experiment conducted on-ground and in microgravity shows a different granular response depending on the gravitational environment, in two main aspects:

- Under compression, jamming occurs in microgravity at lower packing fraction than on-ground.
- The packing eventually yields and flows under gravity, due to the secondary (gravitational) force field; in its absence, i.e. in microgravity, the granular material arranges into a highly stable jammed state.

This experiment was repeated for powders of diameter 140 µm and 250 µm on-ground and in microgravity; the same general behaviour is observed, and within the experimental precision limits, no notable change is identified due to the change in particle diameter.

Regions of flowing and jamming. While characterising the point of transition to jamming is still a controversial topic [152, 153], the particle-scale phenomena at its origin is generally accepted: jamming occurs if strong force chains appear along the major stress compression direction, in response to the load itself [154]. The absence or presence of a secondary gravitational force field modifies the force distribution in the different zones of the packing [155]. Hence, piston-probing creates coexisting regions in different density states. Figure 3.9 proposes a mapping of those regions: on top of the piston (region №1), the packing is jammed. The volume under the piston (region №2) is empty or partially empty. The area around the piston and surrounding this empty zone is filled with a free-floating, static packing in microgravity (region №3). Under gravitational attraction, the powder in region №3 flows down into the empty bottom space, leaving the space surrounding the piston free and thereby destabilising the jammed packing, which yields under the piston pressure and flows.

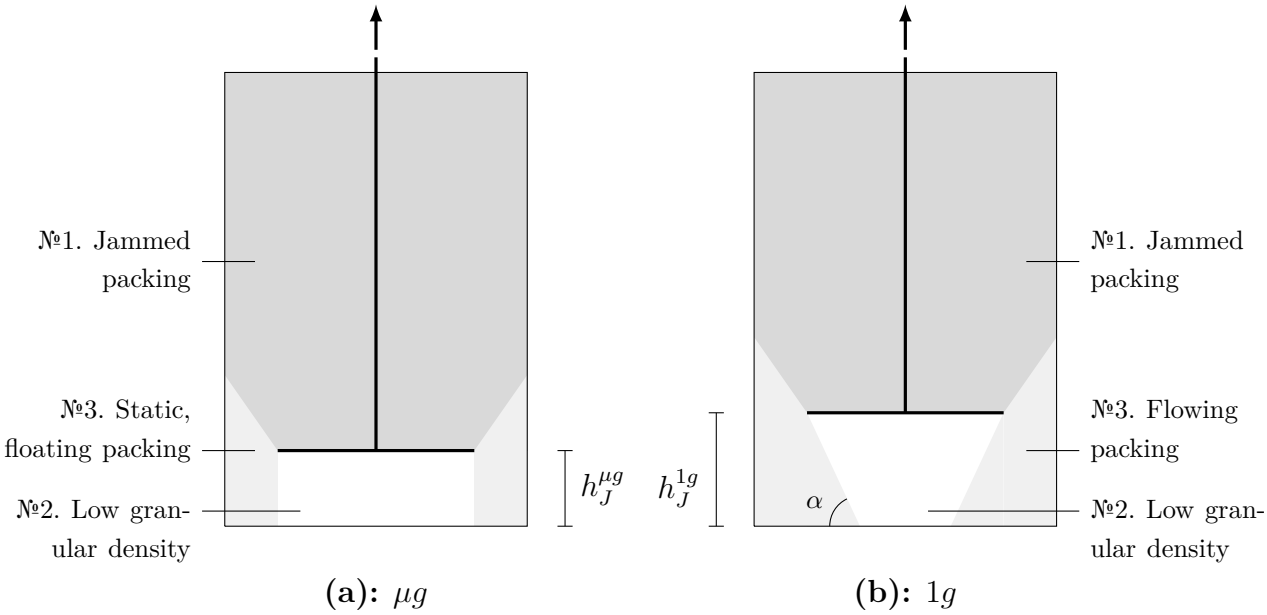

Figure 3.9: Schematic representation of the regions appearing in the experimental cell where material is confined during piston-probing, (a) in microgravity and (b) on-ground, where the powder forms a slope at its angle of repose α with the horizontal.

The stability of the jammed state that remains even under repeated hypergravity phases can be linked to the height h_J between the bottom wall of the container and the piston when this rising platform is stopped by the jammed packing. The existence of a critical height under which a heap of vertical slope remains stable under its own weight is derived theoretically from the Mohr-Coulomb failure criterion analysis (the full derivation is available in Ref. [109, Chap. 6]). The height $h_J^{\mu g}$ reached in microgravity is not sufficient, even during the hypergravity phases, for the weight of the particles from the region surrounding the empty space to overcome the frictional and cohesive particles interactions and flow down. For the experiment under $1g$, the height h_J^{1g} is high enough to allow the material to flow. The angle formed by the flowing material on-ground is known as the powder's "angle of repose" α (see Section 2.2).

A small 2D hands-on version of the experiment using photo-elastic discs allows to visualise the packing and the force chains therein; it qualitatively confirms the appearance of the three regions sketched in Figure 3.9. Results from this hands-on experiment are exhibited in Appendix A.

Shift of jamming point due to gravitational environment. Concomitantly to the maximum height reached by the piston under the different gravitational environments, the critical packing fraction at which jamming occurs under compression is found to be lower in microgravity (in average $\varphi_J^{\mu g} = 0.567$) than on-ground (in average $\varphi_J^{1g} = 0.579$). Variability in the granular density φ_J at which the jamming transition occurs, defined as the packing fraction at which the granular material or suspension undergoes a steep increase in viscosity leading to solid-like behaviour, has been widely studied [132, 134, 156]. It is linked to the change in material rheology with both varying confining pressure [78, 79] and frictional interactions between particles [132, 134]. In particular, the model proposed by Wyart and Cates [134] and supported by the experimental findings presented in Chapter 2 gives an explanation for shear-thickening based on stress-induced frictional interparticle contacts. At low packing density, the rheology is essentially frictionless, as the normal stress is too low to activate interparticle friction. At high packing density, the pressure is high enough to activate interparticular friction, which henceforth takes an important role in the rheology.

In the latter case of dense granular media (close to jamming) under high stress, Mari *et al.* [132] show that increased frictional interactions restrict the reorganisation possibilities of the packing, resulting in a higher stress needed to induce flow, as it competes with higher interparticle forces. Figure 3.10, reproduced from Ref. [132], summarises their findings. (This perception of a material's rheological behaviour as a competition between flow-inducing forces and internal attractive interparticle interactions is reminiscent of the principle of the Bond granular number Bo_g as presented in Section 3.1.) Thus, if the particles' contact number is high enough (corresponding to high stress, or high rate $\dot{\gamma} \to \infty$ in Figure 3.10), the jamming transition happens at lower packing fraction for frictional particles (i.e. with a friction coefficient $\mu \neq 0$, opposed to frictionless particles with $\mu = 0$), where the interparticle forces at contact are higher: $\varphi_J^{\mu \neq 0} < \varphi_J^{\mu=0}$. The reduction in number of collective degrees of freedom available for the granular fabric to reorganise into a denser packing under the applied stress results in a jamming transition happening at lower packing fraction [132, 134, 156]. In fact, the value found by Mari *et al.*, $\varphi_J^{\mu=0} \approx 0.56$ is in good agreement with our $\varphi_J^{\mu g} \approx 0.567$, while their $\varphi_J^{\mu=1} \approx 0.58$ numerically coincides with our $\varphi_J^{1g} \approx 0.579$. This demonstrates that the shift we observe is of similar magnitude as expected from a change in frictional parameters.

As seen in Section 3.1, the cohesive forces among particles, predominant in microgravity, create a packing where contacts among neighbouring grains are likely to remain once particles

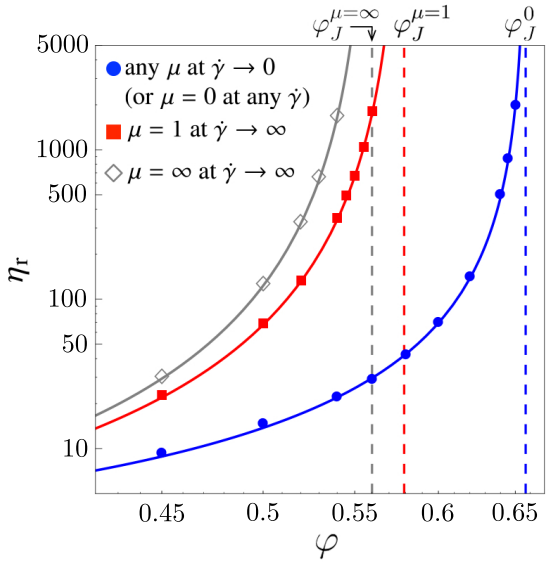

Figure 3.10: Relative viscosity η_r as a function of the packing density φ, for $\dot{\gamma} \to 0$ (blue circles) and $\dot{\gamma} \to \infty$ (red squares and white diamonds). At low stresses, the viscosity is independent of the interparticle friction coefficient μ, because the frictional interactions are not activated: the frictionless jamming volume fraction $\varphi_J^{\mu=0} \approx 0.66$. On the contrary, at high stresses, the jamming volume fraction is directly impacted by a change in friction coefficient of the particles: $\varphi_J^{\mu=1} \approx 0.58 > \varphi_J^{\mu=\infty} \approx 0.56$. Reprinted with permission from [132]. Copyright 2014, The Society of Rheology.

come into each other's vicinity. An increase in the number of lasting interparticle contacts is triggered – in the simulation performed by Mari *et al.* by increasing the shear rate $\dot{\gamma}$ (or shear stress σ), and in the piston-probing experiment reported here by the rise of the piston, i.e. pressure increase. This proliferation of contacts leads to the augmented importance of attractive interparticle interactions, frictional and/or cohesive. In turn, those enhanced cohesive interactions provoke the appearance of jamming at lower packing fraction, due to the stiffness of the granular contact network which restrains the packing from reorganising into a denser configuration. Due to steric hindrance and as magnitude of the cohesive forces is inversely proportional to the distance between grains (see Section 3.1), the relative viscosity of the system increases with increasing number of frictional contacts in a shear-thickening manner. Hence, in low gravity, cohesive forces create a stiffer granular fabric where grains loose mobility: the number of collective degrees of freedom is reduced. This reduction in grains mobility, that is responsible for a decrease in the packing fraction at jamming with increasing particles friction, explains the decrease in jamming packing fraction as the apparent granular cohesion increases due to the reduced gravitational acceleration, or absence thereof. In other words, as the relative importance of the cohesive interparticle forces increases with decreasing gravity, the ability of the packing to reorganise into a denser assembly is reduced: the jamming transition occurs at lower packing density.

This observation confirms results from one of the first rheology experiments performed in microgravity, on board the Space Shuttle [157, 158] (see Ref. [159] for theoretical considerations before launch). A startup curve was measured (i.e. the time-dependent stress after the sudden imposition of a constant shear rate) for a dense ($\varphi = 0.65$), polydisperse powder, compared under $1g$ and $0g$. The response in microgravity is jagged, and samples in $0g$ exhibit a much higher peak friction strength.

Regarding force transmission in a granular packing in low and microgravity, compression can be used, up to a limited height, to densify the material to a packing fraction close to its jamming point, yet lower. In this state, boundary forces can be transmitted through the granular fabric, instead of being limited to the grains in direct contact with the force-transmitter. However, once a certain packing density is reached, the packing, undergoing local variations, can easily jam locally; in absence of appropriate counter-measures, this state of stiffness can propagate throughout the medium, challenging the restart of flow. As a conclusion, direct granular compression can be used in microgravity to densify the packing, but not to trigger nor control powder flow: other types of stimulus must be employed, such as shear or shaking.

Shear has been experimentally studied under varying gravitational environments. By flying a Couette-type rheometer on parabolic flights, Murdoch *et al.* [155, 160] showed the appearance of shear banding in densely packed granular sample under shear in hypergravity ($1.8g$), Earth gravity ($1g$) and microgravity ($0g$). They observe that if the packing fraction is controlled, the response of a granular packing to shear is similar on-ground and in microgravity. The only difference is the secondary flow (transverse to the shear flow, in the direction of gravity), which does not appear when the latter is close to zero and seems to increase in strength in hypergravity. This gravity-dependence of the secondary flow is explained as follows: since the region close to the inner cylinder is fluidised by shear, particles motion is enhanced there. Under the action of gravity, particles are pulled downwards, which causes a secondary flow to move particles inwards on the top surface of the Couette cell. Due to particle conservation and the near-incompressibility of the system, this also implies that towards the bottom, a radially outward directed secondary flow emerges. The strength of the inward flow on the top of the sample cell scales with gravity and hence is nearly vanishing in microgravity.

Finally, predominance of cohesive forces in microgravity and the resulting tendency to cluster can also be used as an advantage. At low packing density, Noirhomme *et al.* [68] showed that granular transport can be triggered by vibration to create a collective motion in the packing; by tuning the vibration amplitude, they use this clustering effect in microgravity to trigger granular transport [66, 67, 69].

3.3 Conclusion: controlling powder flow in microgravity

The gravitational environment modifies the force balance between particles. Because gravity, as a body force, scales with the cube of the grain size, whereas interparticle cohesive surface interactions scale with the grain diameter at lower power, changes in the gravitational field can completely modify the global powder behaviour, with a strong dependence on particles size. If powder flowability is defined as the ratio of cohesive forces internally holding the packing together *versus* flow-impelling forces, as suggested by the granular Bond number Bo_g [109], then powder flowability strongly decreases in low-gravity environment for particles of diameter below approx. 100 µm. Powders composed of such small particles are of high relevance in technological applications for space [140, 141]; yet they generally appear more cohesive in microgravity than on Earth, due to this change in predominance of the cohesive surface force on the grain-scale, resulting in particles aggregating once they come into close distance to one another [145], forming stable clusters.

Moreover, in absence of a gravitational field, the packing does not sediment towards the lowest position available. Whereas on-ground this property is used to control granular flows, in microgravity the contact network between grains must be externally generated, in order for

boundary forces to be transmitted within the dense packing. The creation of a force-chain network thus relies on the densification of the granular medium to a state close to its jamming point. This underlines the importance of the densification step (going from a relatively loose packing to a dense one), which can be done through reduction of the available volume, hereby compressing the packing until a pressure increase indicates the formation of a contact network.

For triggering powder flow through boundary forces in microgravity, the working packing fraction lies on the boundary between very dense flow and the jamming transition. The dependence of the jamming volume fraction on interparticle friction has been previously studied [132, 134]. As the experiment discussed in this chapter has shown, the gravitational environment also influences the jamming point to occur at lower packing density in microgravity, setting a supplementary challenge. However, as a steep pressure increase indicates that a contact network has formed, regardless of the gravitational environment, *in-situ* monitoring of the rheological evolution of the granular medium can be used to provide a direct indication of the state of the packing within a closed container. Regarding the type of external stimuli used to control powder flow in low gravity: direct compression of powder must be avoided for triggering flow in a dense granular material, in order to lower risks of jamming the packing into a stable motionless state that would prevent further particle motion. Shear becomes the preferred type of effort to trigger particles movement, as at controlled packing fraction it shows very similar features in different gravitational environments [155, 160]. Planar vibrations can also be used to transport powder in microgravity at lower packing density [68], or to modify the material repartition in a given volume [66, 67, 69].

Those conclusions will be exploited in Part II to develop a method for handling granular material in varying gravitational environment, towards powder-based additive manufacturing for applications on-ground and in microgravity.

Part II

Powder-based additive manufacturing for space

Chapter 4

State of the Art

A vision for space industry is direct ISM and assembly of both small and large structures [3–7]. ISM has the potential to significantly enhance the self-sustainability of missions, as it could support space exploration missions by maintenance, repair and production of objects without dependence on ground-support. Long endurance missions must be able to solve unexpected problems autonomously. Relying fully upon ground-support would by large increase the risk of failure of such mission. A sustainable approach is the only valid alternative for human spaceflight to non-Low Earth Orbit (LEO): the self-reliability of missions will be a key to their success [1]. Having autonomous manufacturing capabilities in space also opens the possibility to adapt the design of structural systems to their final function in zero-gravity environment, instead of over-engineering them to resist terrestrial gravity and launch. Approximately 30% of the structural mass of payload shipped to space today could be saved if the launch load constrains could be avoided [161].

In fact, this is not an utopian vision. The International Space Station (ISS) was made possible by the assembly of large-scale structures directly in space. Strictly speaking of manufacturing, at this very moment additive manufacturing is used as a permanent tool in space: 3D printers using extrusion-based manufacturing techniques have been on-board the ISS since 2014 [8, 9, 162]. Nevertheless, we are still a long way from a large in-space manufacturing platform to use as a gateway to outer space. The desired technology (or more likely, technologies) would be able to cover the unforeseen failures and unexpected needs by manufacturing autonomously (namely, without post-processing procedures requiring user input), at a resolution on the micrometer scale to manufacture functional tools and spare parts. This high resolution also implies repeatability; implementing quality assurance feedback loops could also enhance reliability of such technology, which is essential in the context of a space mission where human lives rely on it. Naturally, it also needs to function in microgravity and possibly to be able to withstand vibrations. To optimise the amount of off-the-shelf spare parts that need to be launched, of feedstock spare material, and also to reduce the amount of "nuisance materials" (packaging, broken parts and consumable), a recycling possibility should be available. Finally, versatility and adaptability would be strong assets for in-space manufacturing capabilities, with the possibility to print from different raw-materials: mainly, metal and polymers; secondarily, multi-materials printing, and possibly bio-printing of human living cells [5, 7].

In this chapter, the additive manufacturing technologies available on-ground today will be explored, before moving our focus to space. We will see in which form AM is already used in space: what is the development stage of the technologies, and which manufacturing strategies

are most promising for the future, with particular emphasis on powder-based methods. Finally, as a technological gap emerges from this presentation, the reasons will be established for choosing powder-based additive manufacturing as a promising technology for space application, and in this realm see where the present work finds its place.

4.1 A brief overview of AM technologies

As 3D printing technologies recently became available in parallel for cutting-edge applications and to the general public, the field is rapidly developing in opposite directions, making it increasingly difficult to produce a holistic view of the existing technologies. To guide the reader into a topic that is often assessed with unreasonable expectations, we will recapitulate the early stages of the technology and give an overview of the commercially available technologies.

4.1.1 Early development of additive manufacturing

Historically, additive manufacturing was born with the necessity "to show three-dimensional shapes such as those stored in the memory of a computer or imaged in the mind" [163]. The first tentative steps of AM (at the time named *advanced holography*) took place in the 1960s, using liquid resin and laser beams. It was made possible by the advent of photopolymeric resin, and relied on intersecting two laser beams to solidify the material at their intersection, in the material bulk [164]. Based on this dual laser approach, the first "3D printing patent" was filed by Wyn Kelly Swainson in 1970 [165, 166]. Swainson soon realised that his idea of transforming a 3D object or image into an ensemble of coordinate positions in order to reproduce it as a new concrete object could be applied not only for representing 3D shapes, but also to produce new parts. Despite the fact that this work never led to a commercially available technology because no part could ever actually be manufactured, it paved the way for technologies still considered advanced today.

The first real breakthrough came with Hideo Kodama, researcher at the Nagoya Municipal Industrial Research Institute in Nagoya, Japan, who realised that the difficulty to obtain a well-defined object with the existing method was due to varying refraction of the incoming lasers when inward polymerisation took place in the bulk of the material. He proposed a way to circumvent this issue by using a platform to print onto, and possible techniques based on exposing liquid photosensitive resin to ultraviolet light (either mounted on an xy-table, or using a system of masks to selectively polymerise the resin). This way, solidification happened not in the bulk but from the surface of the liquid [163]. The parts printed by Hideo Kodama in 1981 might be the first functional parts ever 3D printed.

The field then diversified into a variety of techniques and base-materials. Selective Laser Sintering (SLS) was the first additive manufacturing technique producing objects from powder, based on fusing polymer powder layer-by-layer from a powder-bed. It appeared on the market in 1992 under the name *Soliform*. Powder Bed Fusion (PBF) techniques are now widely used. Their versatility in base material (the same process can be used on metals, ceramics and polymers with little modification) and high dimensional accuracy as compared to filament or wire-based technologies make them the most precise and adaptable AM technologies to date [10].

4.1.2 Technologies available today

The current ISO/ASTM standard on additive manufacturing terminology and general principles divides the commercially available printing processes into seven categories [167]. The classification of the mature AM technologies available today can be made based on many different grounds: the type of material of the feedstock (liquid, powder, molten material…), the nature of the base material (polymer, metal, ceramic or composite material), the type of energy input needed to form an object (infrared light, laser, electron beam, chemical bonding…). A summary of the technologies available in Table 4.1 shall give an overview of the field to the reader.

4.2 In-space manufacturing

Out of many different AM techniques, three have been considered for production of technical parts and tools for ISM: extrusion-based Fused Deposition Modeling (FDM) [4, 8, 9], directed material deposition of powder or wire [168–170], and powder-bed based techniques [141].

4.2.1 Extrusion-based AM: the *one* available technology

To this day, extrusion-based AM has been the only method for production of technical parts to make its way to space. FDM technologies are based on heating up a filament of material to a temperature slightly lower than its melting point to decrease its viscosity enough for extruding it through a nozzle onto a two-axis building platform. The deposited fused filament then binds to the layers beneath, before cooling down and hardening to create a base for the following layers to form a 3D structure. The principle is summarised in Figure 4.1. As it does not rely on the gravitational pull for any critical step, it was an obvious pick for bringing AM to space.

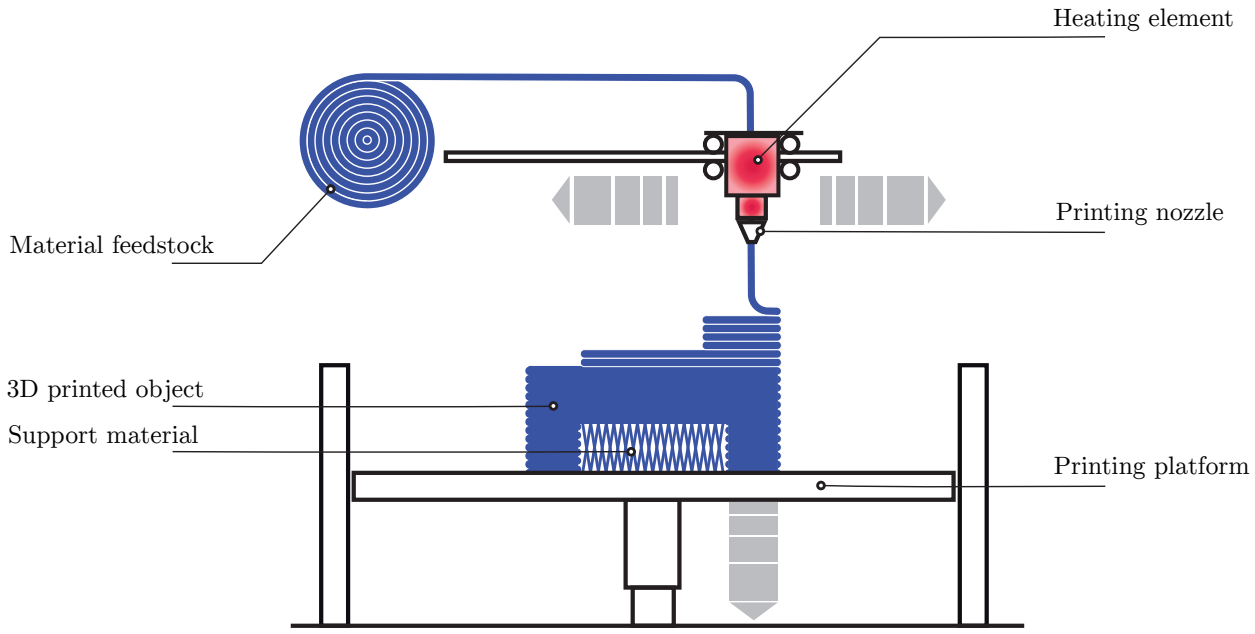

Figure 4.1: Principle schematic of extrusion-based manufacturing technique.

First stage towards in-space manufacturing: one small step for machines... The first 3D printer tested in microgravity, in 1999, was the FDM 1600, commercialised by Stratasys

Table 4.1: Overview of the different additive manufacturing technologies commercially available today, as well as the type of materials they can print from. Further information on the different AM techniques can be found in the current ISO/ASTM norm on AM terminology [167].

Process category	Basic AM principle	Type of feedstock	Type of material	Material distribution	Source of fusion or bonding
Powder Bed Fusion	Selective fusion of material in powder bed	Powder	Metal Polymer Ceramic Ceramic Composite metal-polymer (thermoplastic) Composite ceramic-polymer (thermoplastic)	Powder bed	Electron beam Thermal reaction bonding Laser
	Selective bonding (sintering) of material in powder bed	Powder		Powder bed	Thermal reaction bonding, can be followed by thermal post-processing
	Selective fusion of particles in a high density green compact	Powder and liquid suspension	Ceramic	High density green distribution	Post-processing needed: furnace sintering
Direct Energy Deposition	Selective deposition and fusion of material	Filament or wire Powder	Metal (pure, alloys, multi-materials)	Deposition nozzle	Laser Electron beam Plasma or electric arc
Material Extrusion	Extrusion of molten material	Filament or wire	Polymer (thermoplastic) Composite metal – polymer Composite ceramic - polymer	Deposition nozzle	Thermal reaction bonding
Vat Photopoly-merisation	Light reactive polymer curing	Liquid Liquid Liquid Powder	Polymer (photosensitive) Polymer (photosensitive) Composite metal or ceramic - polymer (photosensitive) Composite metal or ceramic - polymer (photosensitive)	Print head Vat Vat Vat	Chemical reaction bonding, can be followed by thermal post-processing
Binder Jetting	Reactive curing	Powder Liquid	Polymer	Powder bed Print head	Thermal reaction bonding Chemical reaction bonding
	Solvent reactive curing	Liquid	Composite metal - polymer (thermoplastic) Composite ceramic - polymer (thermoplastic)		Thermal reaction bonding, can be followed by thermal post-processing Thermal reaction bonding, can be followed by thermal post-processing
Sheet Lamination	Fusion of stacked sheets	Sheet	Metal Polymer Composite material sheets	Sheet stack	Ultrasound Chemical reaction bonding Thermal reaction bonding, can be followed by thermal post-processing
Material Jetting	Multi-jet material printing	Molten or photosensitive material	Polymer	Print head	UV light curing Thermal reaction bounding

[171, 172]. Tested on a KC-135 Reduced Gravity parabolic flights proposed by the National Aeronautics and Space Administration (NASA), it proved FDM 3D printing to be operational for fabricating objects in absence of gravity. The experiment was repeated in 2011 and 2013 by a joint initiative of the Marshall Space Flight Center, the Johnson Space Center and the Milwaukee School of Engineering. Three 3D printers were sent on several parabolic flights: the Extended Structure Additive Manufacturing Machine (ESAMM), designed by the company Made In Space Inc. especially to be gravity independent, a widely available 3D printer commercialised by MakerBot, and the more advanced Bits From Bytes BFB 3000 printer [3]. Positive results were obtained as parts were successfully printed in microgravity. The main issue reported was layer thickness variation inversely related to gravity, causing a discontinuous substrate and resulting in structural weakness of the parts. On this account, the two commercially available 3D printers were shown to be weaker regarding stability of the printed parts than the ESAMM of Made In Space Inc. as they had to undergo formatting corrections in order to be able to print outside of Earth gravity. After modification, layer thicknesses of the three devices across all gravity regimes were close enough to Earth-made samples that differences could be imputed to measurement errors, with a precision of $\pm 12\,\mu$m in layer diameter [8, 9].

A technology that made its place in space. The Zero-G 3D printer of Made In Space Inc. was launched to the ISS in 2014 by NASA [7], and printed 55 parts from acrylonitrile butadiene styrene (ABS) [4] used for testing and analysis (see Figure 4.2). The samples were tested following norms used for composite materials in order to give mechanical results dependent on the layup direction of the anisotropic parts; once again, no significant differences in physical nor mechanical properties were observed between $1g$ and μg samples [173]. Shortly after, an Italian designed and built machine for printing from biodegradable materials, the POP3D Portable On-Board Printer, was launched by European Space Agency (ESA) [174]. Both are now replaced by the so called Additive Manufacturing Facility (AMF), developed by Made In Space Inc. for NASA and patented in the USA under the name: "Manufacturing in microgravity and varying external force environment" [175].

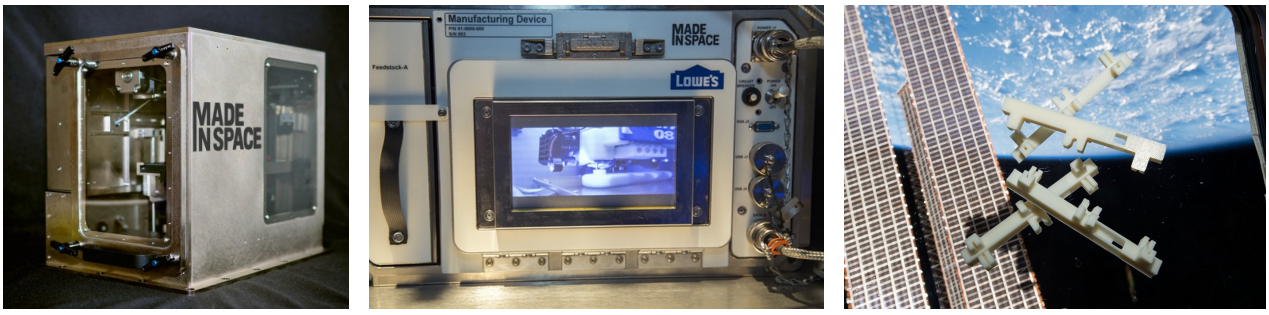

(a) **(b)** **(c)**

Figure 4.2: (a) First AM apparatus launched to space: the Zero-G 3D printer of Made In Space Inc. installed in the glove-box of the ISS. Image credit Made In Space Inc. (b) AMF, 3D printer currently on-board the ISS. Image credit Made In Space Inc. & Lowe's. (c) CubeSat rails structure, fully 3D printed on board the ISS in the AMF. Images reproduced with permission, © Made In Space Inc./NASA.

The AMF was activated in 2016, and is thought of as a permanent commercial manufacturing platform in space. It is extensively used for many scientific research projects as well as for maintenance issues: it has produced over 200 parts in orbit to this day, including spare parts and tools, hence showing that AM has its full place in space and will be a beneficial tool for

future long term space missions. The working principle of the apparatus currently on-board the ISS is that of a basic FDM 3D printer for printing low and high quality polymers (namely, ABS, high density polyethylene (HPDE) and polyetherimide (PEI) [173]). To be adapted to varying gravity, the process widely used on Earth for low quality prints had to undergo a few adaptations:

- On the apparatus used in space, the position of the extrusion nozzle relatively to the building plate and printed object must be regularly recalculated to ensure that the material is continuously deposited, unlike on Earth where the material flows towards its target. Under microgravity, the material must be actively kept from migrating or floating away before reaching its target, which is done by monitoring at all time the distance between the nozzle and the printed object and keeping this distance on sub-millimetre scale [175].
- For use in a closed space with human presence (typically, a crewed space mission), the process must be enclosed in a sealed container to avoid environment contamination, such as fumes or nanoparticles emitted by heating a polymer [176]. Crew safety must be accounted for by having special nanoparticles filtering [177].

Drawbacks of filament-based methods. Bringing additive manufacturing to space has proved to be a full success. However, FDM 3D printing suffers inherent limitations:

- Especially manufactured filaments of the raw material are necessary for feeding this process. These specific filaments have to be carried along if the process should be used in remote, inaccessible locations.
- The raw material used as feedstock must have a continuous viscosity decrease as the temperature increases, which disqualifies most metals[1] as they tend to pass directly from solid to low-viscosity melt. Thermoplastics, which continuously soften as temperature rises, are best adapted to this method. They can possibly contain metal or ceramic powder or a binder or filler of some sort [175], but using a composite material as base impedes recyclability.
- Even in the case of pure thermoplastic, the recycling process can only happen through a process harmful to the material quality: if the former parts are ground to form pellets of material, then heated up to be reformed into a filament of perfect diameter all along (otherwise the process would be blocked by variability in the feedstock filament diameter), the polymer chains are shortened and the mechanical strength of the part will undergo a steep decrease as the number of recycling cycles increases.
- Filament-based technologies have limited resolution along the z-axis, restrained by the diameter of the extruded filament. The minimum resolution in this direction is generally around 100 µm, obtained at the costs of very high printing time [8, 9].
- Typically, parts produced from FDM 3D printing are prone to delamination, and more generally are highly anisotropic in their mechanical and physical properties [8, 9].

[1] An interesting side-note is the possibility to print Bulk Metallic Glasses (BMGs) using filament-based techniques, relying on the fact that BMGs, unlike most other metals, have a continuous viscosity drop as temperature increases. Developed by Gibson *et al.* [178], such technique suffers many drawbacks (among others, low print precision, limitation in part dimensions, few base materials available…) but is worth mentioning as it relies on an intrinsic physical property of the material, and turn it into an asset for developing the best technique for shaping this material, which is an elegant way to select a manufacturing process.

Extrusion-based technology applied to polymer materials was the most evident technology to adapt for space environment as it doesn't rely on gravitational pull, and can function at relatively low energy costs and a temperature around 100 °C. However, the technique suffers too many inherent limitations, in particular in maximum precision and materials available. Therefore, it does not qualify as a viable option for manufacturing technical parts during long endurance human space flight: a more versatile technology is needed.

4.2.2 Directed energy deposition: promises and reality

The additive manufacturing techniques grouped under the category of Directed Energy Deposition (DED) consist in the localised deposition of material directly followed by its solidification by fusing through focused thermal energy [179]. Precisely, it is implemented in the form of a mechanical arm on which an energy source and a material deposition nozzle move in coordination: the material is deposited on a defined location through powder projection or metal wire deposition, and the focused energy melts the material as it is being deposited.

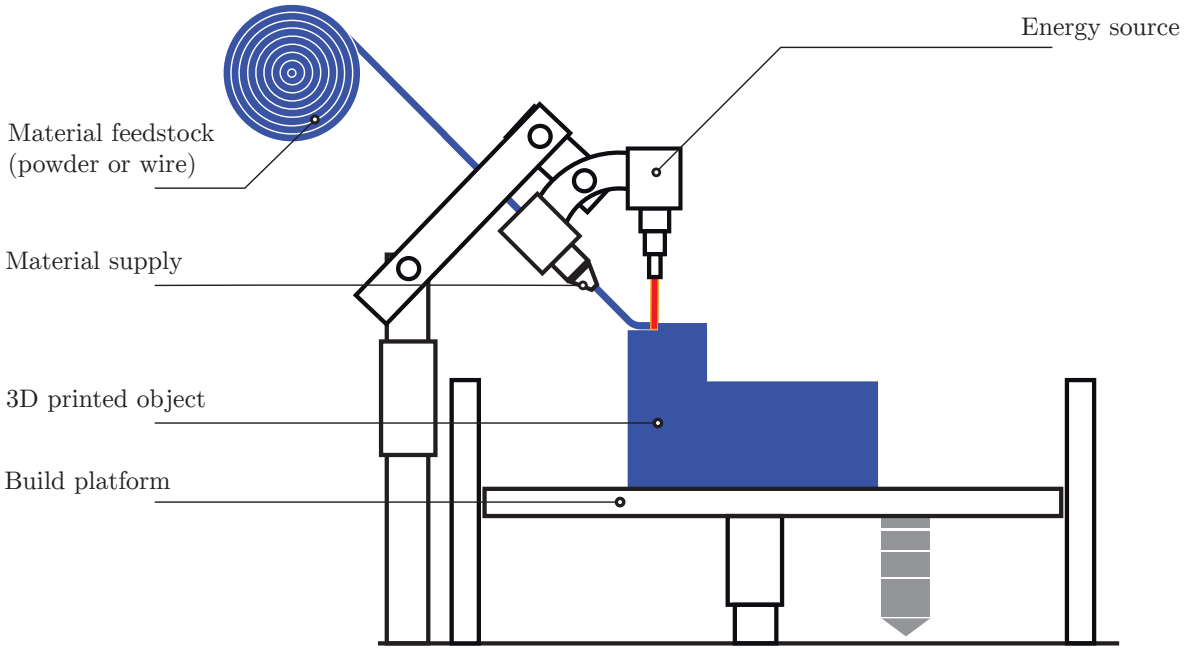

Figure 4.3: Principle schematic of the DED additive manufacturing technique (here, the wire-based method is represented; however the material feedstock can also be in the form of powder).

DED additive manufacturing has high potential for the space sector, both as a ground-manufacturing process for space applications [180] and as technology that could be implemented in space for fabrication of small to large scale objects [181, 182]. First of all, it allows for a build volume larger that the volume of the apparatus itself, unlike most techniques where the printing volume must be comprised within the volume of the apparatus. It can also be used for repair of metal parts by addition of material, and its relative versatility in implementation makes it a good candidate for hybrid manufacturing platforms combining subtractive – e.g. Computer Numerical Control (CNC) machining or laser-cutting tool – and additive technologies. The energy source used can be laser [10], electron beam [183] or plasma arc [184]; cold spraying can also be used, in which case the particles are not melted: the powder exits the nozzle at high speed, providing the kinetic energy that allows it to bond with the surface it is projected

upon [185]. It allows multi-material manufacturing, and for its powder-based form a process accuracy on the order of 10^2 µm, while the wire-based DED processes have a minimum wire diameter around 0.75 mm, which gives a process resolution of 10^3 µm only [179].

First developed by Sandia National Laboratory (New Mexico, USA) under the name of Laser Engineered Net Shaping (LENS) in the late 1990s, the original patents (now expired, see [186, 187]) used powder as base-material and laser as an energy source. This LENS technology is employed by NASA since 2019 in the context of multi-material manufacturing, with the aim to 3D print components of rocket engines [188]. Indeed, powder-based DED has aroused much interest for use in microgravity; however, as the present work emphasises, powder-based technologies are difficult to adapt to low gravity environment, and the challenging powder handling in space has hitherto been an obstacle to further development of this technique. Research is being conducted on assisting the powder deposition by a magnetic field, which would simultaneously reduce waste of powder-feedstock [182].

Currently, the wire-based method is drawing most attention, because wire feedstock enables the effective use of all the material (against up to 90% powder not reaching its target and becoming waste-material in powder-based DED [189]) and is generally easier to handle. Using an electron-beam as energy source, this welding-like method was developed by Davé [190] and taken over by NASA under the name Electron Beam Free-Form Fabrication (EBF^3) for use on-ground and in microgravity [168]. But after being tested on multiple parabolic flights in the 2000's, this DED-Electron Beam (EB) method for microgravity was eventually abandoned. Meanwhile, ESA shifted to plasma metal deposition from titanium-alloy wire. As wire-welding DED manufacturing produces only near-shape objects due to the limited spatial resolution of the method, it is coupled with subtractive techniques: a first roughly shaped metal part is 3D printed, then support structures are removed and the shapes refined to obtain the desired object. By coupling plasma metal deposition and a post-processing by CNC milling, the optical bench of the Athena mission will be the most complex functional part ever 3D printed in titanium-based alloy [170].

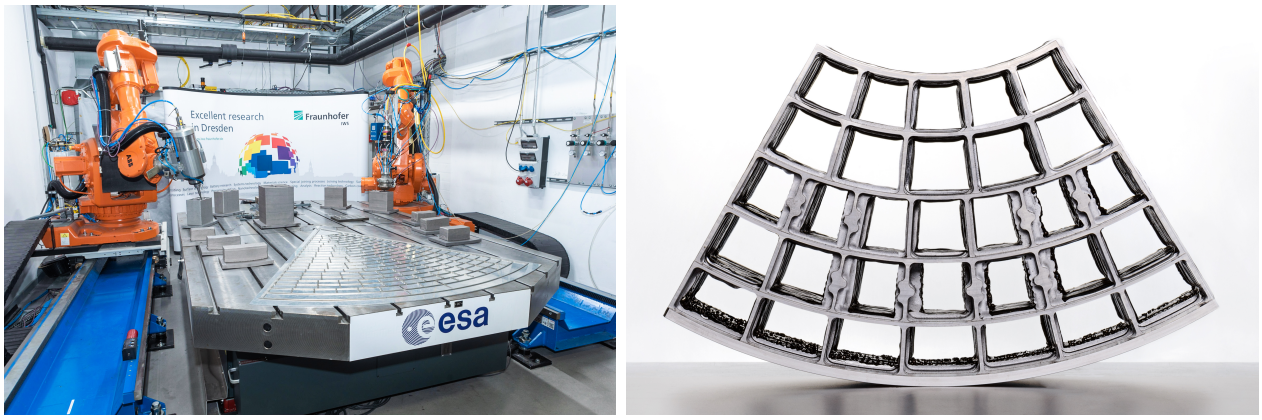

(a) **(b)**

Figure 4.4: A collaboration between ESA, RHP Technology GmbH (Austria) and the Fraunhofer Institute for Material and Beam Technology (Germany) produced a 3 m diameter optic bench for the Advanced Telescope for High-ENergy Astrophysics (Athena) mission, using the hybrid technique combining plasma metal deposition and CNC milling. The size of the machines gives an idea of the complexity to adapt such mechanism to the ISS environment. Images reproduced with permission, © RHP/SBI R. Syrovatka, from Ref. [170].

Finally, wire-based DED is also being studied for microgravity adaptation [169, 181]. ESA and the University of Birmingham have been working on a DED manufacturing process, depositing aluminium wire that is then laser-melted. In a final application, it would have to be coupled with a classical subtractive machining to produce technical parts of the correct dimensions. Tested on parabolic flight in 2016, it relies on the surface tension of the molten material to keep it in place and should result in a patented technology in the coming years [181].

DED is a technique that shows many assets and could be foreseen as the first metal-based manufacturing on the ISS. However, the difficulty of handling powders in microgravity and the lack of precision of wire-based DED have kept any functional part from being manufactured by DED fully in microgravity – to this day.

4.2.3 Powder-bed stabilisation for low- and microgravity

Selective Laser Melting (SLM) and Selective Laser Sintering (SLS) are powder-based additive manufacturing methods: flowable powder is deposited in full layers, forming a powder bed layer after layer, that are then selectively solidified from the open top surface, creating the object section-by-section within a supporting powder bed [108] (for reference patents, today expired, see [191, 192]). The process is illustrated by Figure 4.5.

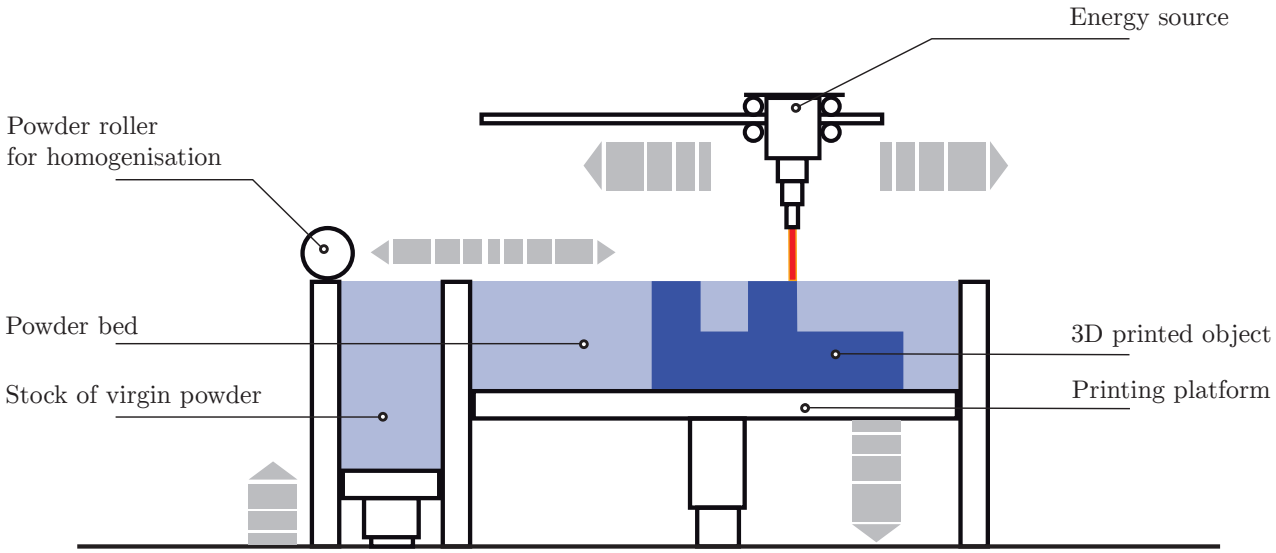

Figure 4.5: Principle schematic of the SLS or SLM additive manufacturing technique: a powder-bed is created by successive recoating, from which an object is selectively solidified section-by-section.

Powder-based techniques are versatile processes, as the deposition method relies on the macroscopic powder flow properties but can be applied to any family of materials [193–195]. Moreover, powder as base material allows for higher precision than any filament-based process, and for easier recycling if the process is based on a single raw material, without binder or processing fluids [10]. Yet, an essential prerequisite to achieve high quality of the printed parts is the perfect homogeneity of the deposited layer. In order to deposit thin and homogeneous layers of powder, all commercially available powder-bed based processes crucially rely on:

i. A powder base-material of perfect flowability.

ii. The uniform body-force of gravity.

During the deposition step, the powder is typically pushed by a roll or a blade that slides across the surface of the powder bed to push the powder into a thin, homogeneous layer. This procedure is fully relying on gravity, on one hand to distribute the powder, on the other hand for it to remain steadily on top of the powder bed; moreover, the homogeneity of this layer is ensured by the fact that the powder flows well and spreads evenly under the gravitational pull. The density of the printed parts is also set by the packing density that the powder can reach under Earth gravity [110]. If the packing density of the powder is too low, defects are more likely to appear (e.g. porosities, incomplete fusion holes, cracks) [196].

Adapting powder-bed based methods to microgravity. Powder-bed based techniques have assets that make them attractive for ISM: they can be adapted to print from polymers [193], metals [10, 194] and ceramic [195], and offer high quality prints, reducing the need for post-processing. However, the obvious difficulty to adapting them to space environment is to modify their functioning principle to operate properly in microgravity. One possibility for such adaptation has been proposed by Günster *et al.* [110, 141, 197, 198]. It consists of stabilising the powder-bed by applying a pressure difference between the bottom and the top of the powder-bed. A suction pump produces a vacuum towards the platform at the bottom of the powder bed; the particles are attracted towards the platform, which acts as a filter. The powder bed is stabilised this way, and the non-melted powder is used as a support to hold the printed parts. A schematic representation of this process reproduced from [141] is presented in Figure 4.6a. This method provides a force within the packing (the drag force due to the air flow, acting on each grain of the packing in its reach) by applying a pressure difference only from the boundary of the powder-bed. This drag force can recreate an attraction of the same order of magnitude as the gravitational pull in microgravity [141]. This method also allows for powder showing higher cohesion energy (e.g. particles of smaller diameter, which have more free-surface and therefore tend to show lower flowability) to be deposited efficiently: by increasing the effective downward force on each grain and moving the smaller grains of the packing to fill the interstices created by larger grains, the relative powder density can be increased up to $\sim 45\%$, even for powders of small diameter (in this case, a powder of average diameter of 17 µm, for which it represented an increase of 48% in relative powder density), which generally show lower ability to organise into a dense packing. Therefore, this process is also used to stabilise and densify the printing powder bed on Earth, and to circumvent the need for a support structure [110].

The powder-bed stabilisation process developed by Günster *et al.* provided the first metal powder-based additively manufactured part in microgravity. Tested on the DLR 30$^{\text{th}}$, 31$^{\text{st}}$ and 33$^{\text{rd}}$ parabolic flight campaigns between 2017 and 2019, it enabled to produce in microgravity parts from ceramic powder solidified by a binder (silicon carbide powder, see Refs. [110, 141, 198]) and metal powder (stainless steel powder printed by Laser Beam Melting (LBM), see [141, 198]). The stainless steel samples were printed by depositing 0.1 mm layers of powder in microgravity, followed by the solidification during steady flight (under $1g$). The samples that were printed show a complex microstructure typical of this material and this manufacturing technique; microgravity doesn't seem to have an obvious effect on the porosity of the printed samples, under the condition that the gas flow rate be specifically tweaked depending on the material deposited: a flow rate too low would have no effect on the powder bed, and too high cause rough layers. The main issue reported by the authors is the complexity in designing a recoating unit for powder deposition, because of the challenge of triggering and controlling powder flow in microgravity to obtain homogeneous layers with reproducibility, which has been

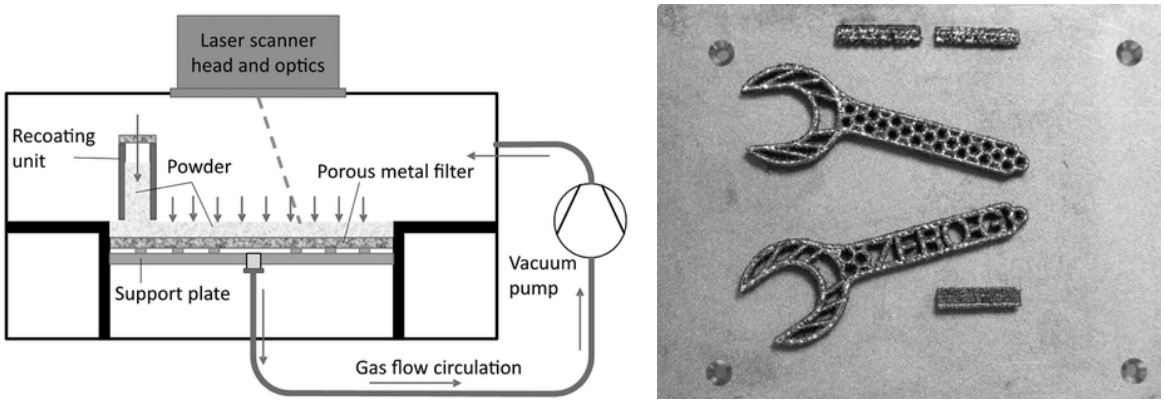

(a) Gas-flow assisted process **(b)** Parts produced

Figure 4.6: (a) Schematic of the gas flow assisted powder deposition technique for powder-bed based additive manufacturing of powder in low- and microgravity. (b) The two 12 mm wrenches presented are the first ever metal parts that were 3D printed by LBM in microgravity on parabolic flight. Images from Ref. [141], reproduced under CC BY-NC-ND 4.0 License.

discussed at length in the present work.

Specific drawbacks of gas-flow assisted powder-bed based method. The process developed by Günster *et al.* [197] suffers a specific drawback: the thickness of the vertical walls of the printed parts is limited to approximately 2 mm, because larger closed surfaces would prevent the air flow from going through the part and accessing the next deposited powder layer. Moreover, the pressure drop needed across the powder bed is constant; hence, according to Dracy's law, the flow velocity must be increased pursuant to the bed height, increasing ergo the pump power needed with the powder bed thickness. Zocca *et al.* [141] report a limiting bed thickness of 80 mm for a gas flow of 20 liters per minute, the bed areas being 28 cm^2. Obvious power and space limitation during space missions make this issue cumbersome. Finally, if the powder includes many fines (particles under ∼10 µm diameter), the filling of interstitial volume becomes too high and clogs the powder bed, annihilating the effect of the air flow [141].

Drawbacks of powder-bed based methods in general. All powder-based AM methods used on-ground and developed for reduced gravity today have a common limitation: the powder deposition step is entirely based on the flowability of the powder used as base material. This implies that:

- The powder must be specially fabricated for being used in this process, as the characteristics of a highly flowable powder imply a specific and complex production process to produce powder complying to the following physical characteristics [199]:

    1. The particles should have a smooth surface state, lacking any roughness or irregularities, to minimise friction and locking between grains.

    2. The particles should be as close to spherical as possible, to prevent mechanical locking.

    3. The distribution in diameters of the powder needs to be controlled to allow for a high packing density.

- Such specific feedstock material needs to be stored and carried along if the process shall

be used in a remote, inaccessible location. The storing conditions of the feedstock material must be strictly controlled in order to avoid corrosion, contamination, or material exchange due to extended contact between particles increasing the cohesion of the packing.

- Reusing material from a previous batch is difficult and necessitates sieving and sorting of the material, as in powder-bed based methods, particle clusters appear around the part in the powder bed [200]. Hence, the powder deposited once, including the one that was not used to manufacture parts but simply used as support structure around the parts, must be either disposed of, or go through a complicated re-qualification process in order to be reused.
- Use of recycled powder, ground from former objects, is for the same reason challenging. Heterogeneities in the deposited layer of powder would create zones of low density in the printed object, hence porosities where the desired mechanical properties of the part cannot be maintained.

The drawbacks mentioned question the superiority of additive technology over subtractive technologies, as the amount of waste material produced with such technique equals the one that would be produced with machining technologies. A technology suitable for space would combine the assets of powder-bed based AM technologies with the possibility to use powders of lower flowability, in particular recycled powders.

4.3 Recycling in space

Future space-missions will need to be conceived for being self-sustainable. This approach fosters closed-loop recycling of all payload.

A symbolic example of this change of paradigm is the Customisable Recyclable International Space Station Packaging (CRISSP) project introduced by NASA and Tethers Unlimited, Inc. [201]. It is based on the fact that hardware shipped to the ISS must be thoughtfully packed to survive the high acceleration and vibration at launch, and that the foams and packaging used to ensure objects' stability ends up as trash on the ISS, which is generally re-packed and sent to be consumed during re-entry in the atmosphere [4]. The foams and packaging are made of various polymers, and the CRISSP project developed a material and slicer to manufacture the packaging for all hardware to be sent to the ISS, replacing the padding by 3D printed foam of the exact right stiffness induced by a structure of adapted infill compactness (see Figure 4.7a). Once on board, this material can be recycled into new feedstock material and 3D printed into new objects using the "Refabricator" (see Figures 4.7b and 4.7c).

The Refabricator payload is on board the ISS since early 2019. It can currently recycle and print Ultem 9085 (a commercial mix of PEI and polycarbonate (PC) with relatively high tensile strength and heat resistance). It has the specificity to use a technique (the so-called "Positrusion") to transform the polymer back into filament that directly melts the object without prior grinding, which helps preserving the length of the polymer chains and therefore the mechanical strength of the recycled material for an increased amount of cycles [202, 203].

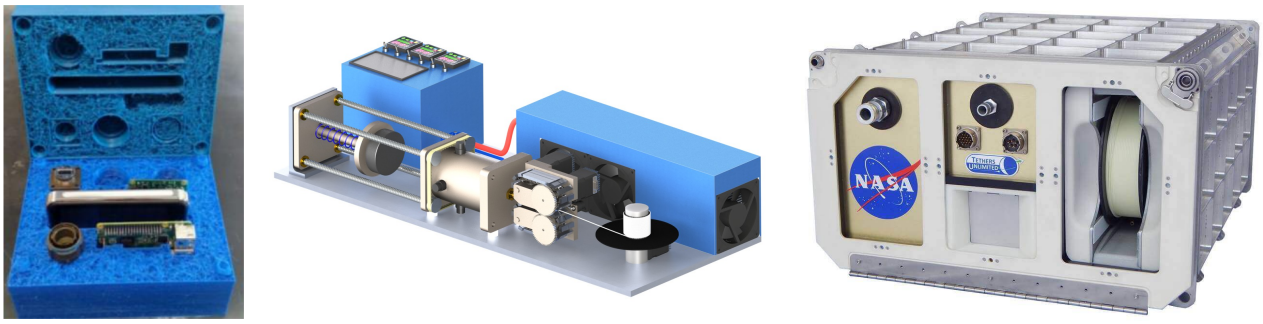

(a) **(b)** **(c)**

Figure 4.7: (a) 3D printed packaging ensuring the stability of hardware shipped to the ISS. (b) The so-called Refabricator: a small unit for transforming plastic trash into feedstock filament for FDM manufacturing. (c) Refabricator payload in its final form, as shipped to the ISS in 2019. Images reproduced with permission, © Tethers Unlimited, Inc./NASA.

This method of recycling seems specifically designed for and adapted to FDM as a printing method. Recycling of powder seems easier, and is however less obvious, due to limitations of the available powder-based printing techniques that demand high-flowability powder and are not adapted to variability in feedstock quality.

4.4 Process *in-situ* monitoring for quality assurance

A fully reliable process, which includes quality assurance, will need to allow for *in-situ* monitoring and feedback-loop control systems during the manufacturing process.

The most common type of live monitoring, especially in metal-based technologies, is through process temperature control [204]. As the appearance of certain types of microstructures can be identified by the heat profile during solidification, it is an indirect probing of the printed part's atomic structure. Such monitoring can supply real-time process control based on temperature monitoring during the process [205, 206]. AM processes can also be monitored by optical sensing, to enable recognition and localisation of defects. By extracting the process metrics, and comparing them to prior determined baseline metrics, the monitoring system can modify the laser power for the future layers to be printed [207]. Optical parameters and temperature can be monitored simultaneously [208]. Localising the position of defects can also be implemented by acoustic-wave measurements applied to the weld pool and their comparison to the "known good" parts acoustic signal [209], or by inducing a current in the part while it is printed and capturing the output impedance data [210]. Indirect assessment of defect appearance can also be done through observation of the shape of the spark plume created by the laser as it melts the raw material [211].

The existing live-monitoring systems that can be implemented during additive manufacturing do not give indication on the quality of the material deposition. They are useful for confirmation (or invalidation) of the quality of a layer, based on finding the position of defects in a part while it is manufactured, by comparison with the data corresponding to "known good" samples. Therefore, they do not prevent the appearance of defects but aim to spot, identify and localise them: the subsequent layers can possibly be modified but the one being probed is already faulty. Having this information, the user can decide to dispose of the part and start the print from scratch again, increasing the amount of waste material.

The desired technology would consist of a closed-loop feedback system that gives not only assurance of good quality of the part but also automatic real-time corrections to the layer while it is being printed.

4.5 The future of in-space manufacturing

4.5.1 Bioprinting in space

As an interesting remark, while in the context of high-strength parts manufacture, microgravity is a constraint that we must adapt to, it can also be an asset for certain applications. In particular, bioprinting could gain in emancipating from the gravitational constraint.

On Earth, bioprinting methods for depositing bioinks suffer from the fact that the extracellular matrix (generally composed of hydrophilic polymers, e.g. hydrogel) used tends to collapse under its own weight. Moreover, finding a balance between printability and biocompatibility can be challenging. New strategies must hence be implemented to achieve mechanical stability of tissues, among them dual bioprinting of a mechanically stable biomaterial and a cell-loaded bioink [212], use of "dynamic bioinks" that cross-link after deposition [213] or novel deposition methods like drop-on-demand multilayer bioprinting technique [214]. Another approach is to 3D print tissues outside of Earth's gravitational field. In 2018, the Russian laboratory for biomedical research 3D Bioprinting Solutions (Moscow, Russia) launched to the ISS the Organ.Aut, a magnetic bioprinter controlling the construction of 3D tissues using a magnetic field [215]. In 2019, another biomanufacturing payload arrived on board: the BioFabrication Facility (BFF). Developed by TechShot Inc. and nScrypt Inc. in the context of the NASA "Manufacturing Multi-material Fabrication Laboratory" initiative, it should produce cardiac-like tissue of different thicknesses using two extrusion-based techniques and one using magnetic-fields for cell positioning [4, 6, 216].

This field, deriving from additive manufacturing to create its own field of microgravity manufacturing research, thus shows an exciting perspective for a different and complementary application of additive manufacturing in microgravity.

4.5.2 A fully integrated FabLab in space?

The next step for ISM, according to NASA's guidelines, is to implement a so-called In-Space Manufacturing Multi-material Fabrication Laboratory [4, 173]. This would imply the use of hybrid techniques to manufacture additively, but also through subtractive techniques (in particular, using CNC machining) from multiple materials, including space-grade metals. Apart from increasing the number of available materials for manufacturing on-board the ISS, it aims to provide efficient end-to-end manufacturing, going toward fully autonomous manufacturing [217]. Multiple projects are currently being developed concurrently. The manufacturing techniques are based on assembling sheets of metal by ultrasonic welding (so-called Fabrisonic technique) and wire-fed welding process. Chosen for their compatibility with virtually every aerospace grade metal material available, those techniques however have low resolution (generally $\geq$1 mm), hence they must be combined with subtractive technique to post-processing the near-shape part. Composite materials with polymer matrix could also be used, 3D printed using a dual-nozzle FDM method.

Those projects are the short-term future of ISM, and show the importance of developing

multiple manufacturing tools in parallel in order to find the best combination of techniques and processes.

4.5.3 In-space manufacturing of large structures

Parallel to manufacturing small parts on board the ISS, large independent manufacturing satellites represent a long-term goal for ISM. But the idea of building large structures from simple base elements directly in space is not new.

In the 1970's, NASA associated with Grumman Aerospace Crop. (now Northrop Grumman) to build the "Beam Builder B2", a large machine assembling beams of aluminium by bending and welding them. The project was tested in underwater Extra-Vehicular Activity (EVA) but never made it to space [3]. In the early 2010s, this idea reincarnated in the SpiderFab project for on-orbit construction of large, lightweight structures. An artist's rendering of the SpiderFab is presented in Figure 4.8a. The interesting idea born from this collaboration between Tethers Unlimited, Inc. and NASA is to adapt the material extrusion technique used in FDM 3D printing, automated composite layup, and robotic assembly to manufacture simple beams in space and assemble them into large architectures [218]. Manufacturing and assembly of antennas in space [219] and harvesting and reusing valuable components from nonworking satellites already in orbit [220] are other examples of such visions.

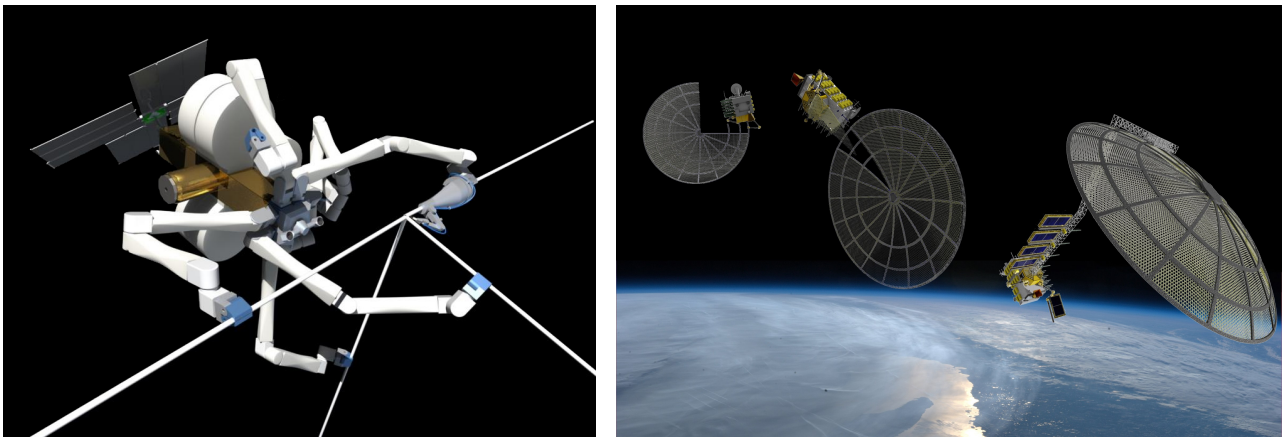

(a) **(b)**

Figure 4.8: ESAMM projects are producing a great number of artists' rendering, as the ones presented here, but no hardware has – yet – found its way to space. (a) The principle idea of the SpiderFab. Image reproduced with permission, © NASA/Tethers Unlimited, Inc. and (b) the Archinaut One creating in-orbit an antenna in three stages of evolution. Image reproduced with permission, © Made In Space, Inc./NASA.

The current implementation of this idea is the Archinaut One. Created in the realm of NASA Technology Demonstration Missions program with Made In Space Inc. (leading the project) and Northrop Grumman, the Archinaut is an automated system able to create spacecraft in space by extruding material and fabricating large structures from assembled rods. Essentially, it consists of a satellite with a large extrusion-based 3D printer and robotic arms; it is patented by Kemmer *et al.* and Made In Space Inc. under the name of *Additive Manufacturing of Extended Structures* [221, 222]. Such system and its alike go under the generic appellation of ESAMM. The Archinaut One is expected to be launched in 2022 for a technology demonstration mission, consisting of building its own operational solar array.

4.6 Conclusion: technological gap

Outer space is an unforgiving environment, where self-sustainability is a question of survival. A process with limited precision, manufacturing from only one type of material, showing relatively low mechanical properties and little recycling possibilities, combined with frequent failure in parts due to defects coming from the manufacturing technique [8, 9], is not the most adapted process for such environment. Moreover, while an additive manufacturing method adapted to space environment certainly needs to function in microgravity, this alone is not a sufficient characteristics. The method should also be adapted to the type of tasks that are needed in the context of space missions: a versatile process, able to create objects with high precision and reliability, possibly including a quality assurance and the option to use recycled materials.

To this day, powder-bed based AM technologies offer by far the most precise and versatile processes [10]. However, open powder beds as well as directed powder spraying are hardly compatible with the closed inhabited space of spaceships, where contamination of the habitat would be catastrophic. Moreover, those techniques rely on feedstock granular materials of perfect flowability, which implies a complex powder manufacturing process and storage capability, and the impossibility to reuse the same powder bed multiple times, even less powders produced by closed-loop recycling. The difference in rheological response observed with an increase in surface roughness studied in Chapter 2 offers an exemplary demonstration of the large decrease in powder flowability that can happen with a slight change in its physical properties. Furthermore, as seen in Chapter 3, handling granular materials in varying gravitational environments enhances this challenge, as granular packings flow with increased difficult in absence of gravity.

In conclusion, no method exists for handling powder with the aim to deposit it in thin homogeneous layers suitable for 3D printing that would function:

i. Independently of the powders' flowability.

ii. Functional on ground, in low gravity environment and in microgravity.

iii. Including a quality assurance system in the form of a control feedback loop.

Based on the study of the rheological response of granular materials in presence or absence of gravity presented in Part I, a method for handling powders is proposed in the following, which functions independently of the characteristics above mentioned. This process for controlling and additively manufacturing objects from powder was elaborated to function independently of the gravitational environment and to adapt to the flow behaviour of the feedstock granular material; it was fully developed as part of the present work. In the following chapter, the development of the powder handling method is described, including the detailed mechanisms used to trigger the desired powder movements. It is then probed, first through simulation (Chapter 6), then in the creation of two model 3D printers (Chapter 7) used for a technology demonstration in microgravity (Chapter 8).

Chapter 5

The RheoPrint additive manufacturing process

As we have seen, designing a powder-based additive manufacturing process adapted to space missions translates into the following tangible requirements:

i. **Flexibility in raw material.** A process tailored for space missions must be adaptable to multiple raw materials. This implies that such process should enable handling of different granular materials whose flow properties may differ dramatically.

ii. **Adaptation to low- and microgravity.** The control of powder flow should be independent of the gravitational field, in order to function on Earth, in microgravity or in low gravity environment like the Moon or Mars.

Additive manufacturing generally amounts to multiple iterations of two main steps: material deposition and material solidification. This work, focusing on the material deposition step, proposes a method for handling and creating thin, dense layers of powder, functioning independently of the flowability of the powder used as raw material and of the gravitational environment. In this chapter, we will start by reviewing the intrinsic challenges in designing powder-based processes, thus explaining why commercially available AM processes are generally not able to handle powders of mediocre flowability. Drawing consequences from those largely studied phenomena, we will propose a powder deposition method that sets itself apart from existing material deposition techniques used in AM by being designed in accordance to the requirements explicitly stated above. Finally, we will explore the possible limitations of the developed powder handling method. The experimental proof of concept of this method, in the form of powder-flow simulation and construction of two prototypes 3D printers, will be subject to independent chapters.

5.1 Challenges

5.1.1 Variability in behaviour & environment dependency

Handling granular materials is in itself challenging as small changes on the particles' scale draw large consequences that can condition powder flow (see Chapter 2). The usual approach in process engineering applied to particulate solids intends to govern powder flow by a perfect control over the material itself [199]. This can only be achieved at high costs in manufacturing

and storage; moreover, this strategy doesn't withstand a profound environmental change.

As we have seen in Chapters 2 and 3, the rheological response of a granular material is conditioned not only by the nature of the grains themselves, but also by the environment in which they are handled. A striking example of high relevance for our study is of course the gravitational environment: the exact same sample might keep its shape like a solid under hypergravity, flow like a fluid under Earth's gravity, or float undisturbed in microgravity. Because the environment modifies the force balance on each particles, the global motion of the granular fabric is inevitably altered.

5.1.2 Force transmission & reorientation

The gravitational environment is modifying the macroscopic behaviour of a granular matter through the presence or absence of a general direction of movement through an acceleration field, and of lasting contacts between particles. If a general movement is not given to the packing by a body force like gravity, it should be transmitted by a boundary force, which implies that the transmission of such force throughout the packing is a crucial issue.

In the case of a dense packing, force transmission through a network of contacts forming force chains is the predominant mechanism. But force chains can develop only if lasting contacts exist between the particles. Therefore, in order for a dense granular flow to be triggered in absence of gravity, controlling the packing fraction of the material is essential.

However, controlling the packing fraction is in itself challenging, as unlike a gas, a granular sample – even in microgravity, unlike suggested by the denomination of *granular gas* – will not expand to fill the entire space at its disposal. It could seem obvious to control the packing fraction inside of a closed container through expanding or retracting the volume of such container. However, transmitting a given motion to a granular packing by normal pressure would prove ineffective, as pressure is not transmitted straight into a powder: the force network will redirect the pressure towards the vertical walls of the container, as discussed by Janssen [37] and summarised in Chapter 1.

This defines a first specific difficulty for controlling granular flows: the packing fraction must be actively controlled, especially in microgravity, in order to ensure contact between grain and thus force transmission; this cannot be done by compacting the packings through direct normal pressure, which will only be redirected laterally by the packing.

5.1.3 Tendency to jam

The jamming transition is defined as the appearance of rigidity in a particulate matter. Setting itself apart from a crystallised state as it occurs in disordered matter, a jammed state can withstand finite amount of stresses before yielding, as a solid would [40]. (A more complete picture of jamming and its implications in granular behaviour can be found in Section 1.1.)

In the case of a process relying on powder flow, jamming of the raw material would be critical to proper functioning, as it would prevent any further movement of the packing and possibly cause damage to the machine by directly transmitting all the force applied by one part to another. This is bound to eventually happen when applying a normal pressure in the direction of desired movement of the powder, compressing it between two rigid surfaces. Such piston-compression experiment was realised for the first time in microgravity in the realm of

this work – see Section 3.2 – showing the appearance of a rigid jammed state of granular matter in microgravity, appearing independently of the friction between grains.

The network of particles transmitting the force in a dense packing is defined as a *fragile skeleton* [38], as it can elastically withstand compatible loads, whereas it plastically reorganises under incompatible loads (in this case, if the force is applied in a different direction of application) – see Chapter 1 for a more comprehensive description. This plastic deformation is desirable in our case, as it forces the grains to flow without risking to jam the entire packing.

Force chains are therefore a phenomenon with ambivalent consequences for process development. To detach from gravity-dependence, boundary forces are used to control the powder flow, which are transmitted in dense granular packings through force chains; but if those force chains become too stable, the entire system undergoes jamming and the flow is stopped. The optimal state for the present application is a system that is always on the edge of jamming, yet never does.

5.1.4 Restricted type of stimuli for enforcing flow

The granular flow should be triggered only through stimuli that can function in absence of gravity and that will not risk causing jamming of the packing.

It is the case with shaking, that can be used for unjamming [223] and homogenising a granular sample [224, 225] under Earth gravity, and can also be used to transport granular materials in microgravity [68]. But because of the dissipative nature of granular materials, if force transmission is done through collision between grains, the packing will tend to cluster [66, 67, 69] and the gradient in local packing fraction will create a highly heterogeneous packing, therefore difficult to handle.

As we have seen, applying a normal pressure to the packing in the direction of desired movement would be a strategy prone to failing (see Chapter 3). But the application of shear stress to a granular packing allows to create a primary flow in the direction of shear, and Murdoch *et al.* [155, 160] showed that this phenomenon is independent of the gravitational field. Shear stress also triggers formation of force chains, as they are the prevailing mechanism for force transmission in a densely packed granular media. But instead of forming collinear to the direction in which the force is applied, force chains due to shear stress form oblique to the direction of shear; their persistence and planar repartition will then depend on the uniformity of distribution of the packing [226].

As a conclusion, in order to trigger flow in the packing without generating jamming, the movements of the granular packing should be predominantly controlled though shear and shaking, and direct compression of the packing can be used to densify the packing but must not be used to initiate flow in the direction of the applied force.

5.2 Description of the RheoPrint process

Additive manufacturing generally equates to multiple iterations of a material deposition step and a material solidification step. In order to 3D print powders (i) independently of the rheological properties of the raw material and (ii) independently of the gravitational environment, the critical step is the powder deposition. It consists in depositing a thin and homogeneous layer of granular material for it to be selectively solidified.

5.2.1 Confinement: a new approach to powder-based manufacturing

The approach proposed here consists in confining the raw material in a closed container inside which the entire process takes place. The deposition step amounts to controlling the powder flow inside the closed space, in order to force material to the desired location. Inside the container is a platform or printing substrate on which the object will be printed upside down; the desired location for each new layer to be deposited is the horizontal space under this printing platform. At the beginning of the manufacturing process, the platform is placed at the bottom of the container. It then moves up in discrete steps, each iteration allowing one new layer of the object to be 3D printed underneath the platform and the part of the object already printed. The basic principle of the "confined" additive manufacturing method proposed is illustrated by Figure 5.1; in this schematic, the discrete rise of the platform is labelled as step I. Increment.

Handling the confined raw material is achieved by moving the container itself in a certain way that forces the material to flow towards the desired location (step II. Deposition). The powder displacement can be divided into two types of movement: the vertical, downward powder transport and the horizontal, planar movement to create homogeneous layers under the platform (labeled 1 and 2 in Figure 5.1). Compression of the newly deposited layer follows to increase material density before solidification (movement II.3. in Figure 5.1).

Once deposited, the powder can be selectively solidified (step III. Solidification in Figure 5.1). The solidification also takes place inside the container: an energy input is provided from outside to the material inside the container through the bottom wall of the container. This bottom wall is a "window": it is transparent to the type of energy used to solidify the raw material.

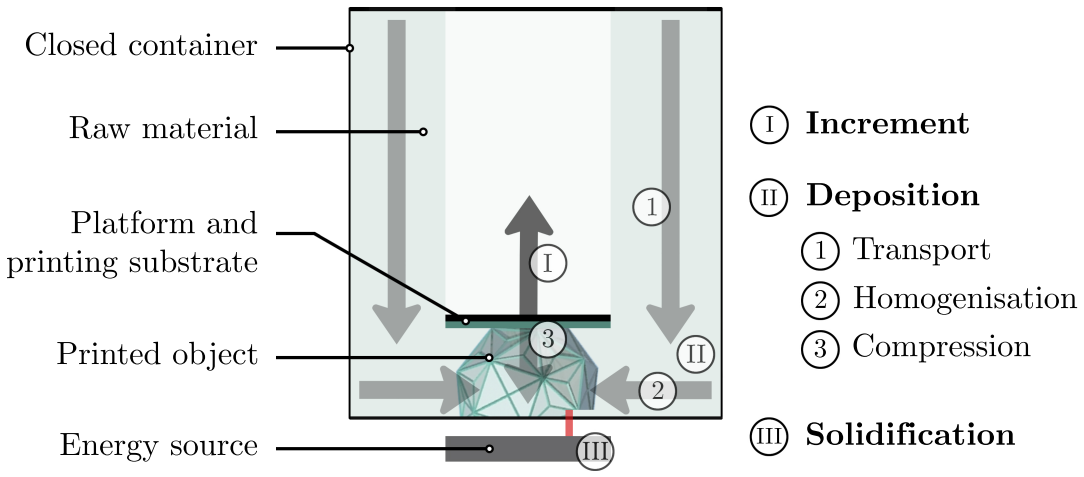

Figure 5.1: Principle of the additive manufacturing method proposed. The approach consists in confining the raw granular material in a closed container inside which the entire process takes place. The steps of the process, executed repeatedly until the part is fully formed, can be summarised as: I. Incremental upward movement of the platform, on which is mounted the printing substrate, II. Powder deposition. III. Selective solidification of the newly deposited layer. The powder deposition step consists of the following desired powder movements: 1. Vertical downward transport towards the bottom of the container. 2. Horizontal homogenisation to create a homogeneous layer under the platform. 3. Compression of the newly deposited layer.

5.2.2 Desired powder movement

The challenge lies in controlling the powder flow within the container exclusively by movements of the container itself, i.e. only by boundary forces and thus independently from body forces such as gravity. This is achieved through two basic types of stimuli: shear and shaking. The container is cylindrical and hence axially symmetrical about the axis along which the platform rises. On the one hand, the different parts of this container rotate with respect to each other to create a shearing movement dragging down the powder inside: downward granular transport is achieved through shearing the powder. On the other hand, the bottom part of the container vibrates horizontally in order to produce planar shaking and homogenise the powder layer.

Taking the entire process from top to bottom, we will go through each movement imposed to the powder to highlight their role in the process and their theoretical rationale. The reader can support their mental representation of the process by schematics proposed in Figures 5.2 and 5.3.

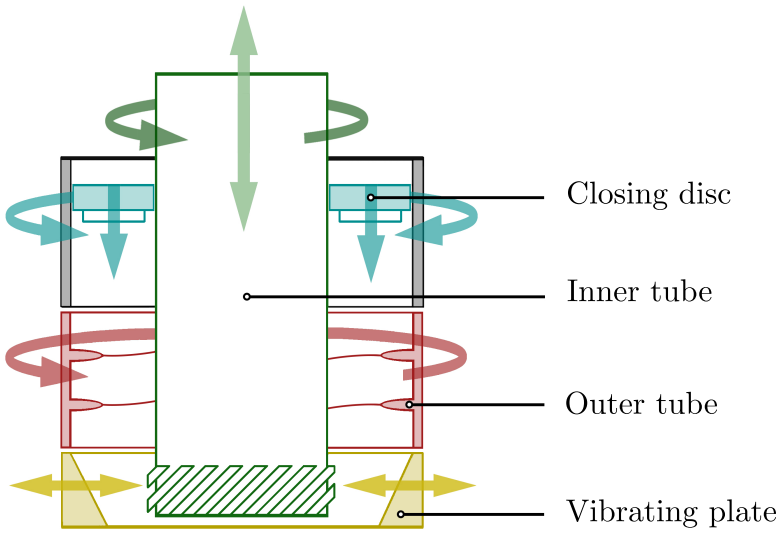

Figure 5.2: Schematic representation of the movements of the different parts composing the RheoPrint powder deposition process. Each arrow represents one type of movement, and the arrows of same colour refer to movements of the same part, also represented in the given colour.

Direct compression of the packing, or what to avoid. In the RheoPrint process, to avoid direct compression of the powder, the printing platform moving through the container is not a platform but a tube. This way, no powder is stuck between the platform and the upper wall of the container as the platform moves upward to give space to the printed part. This rising tube on which the printing substrate is installed is named the *inner tube*.

Feedstock area: a tool for volume compensation. The rise of the inner tube at each new iteration of the process increases the volume available for the powder under the printing platform, but also in the container in general. This would imply a decrease of the global packing fraction, which shall remain constant throughout the process, firstly to ensure homogeneity of the printed part and secondly because a lower packing fraction might create "empty" zones where the continuity of force transmission would be broken. In order to ensure a relative

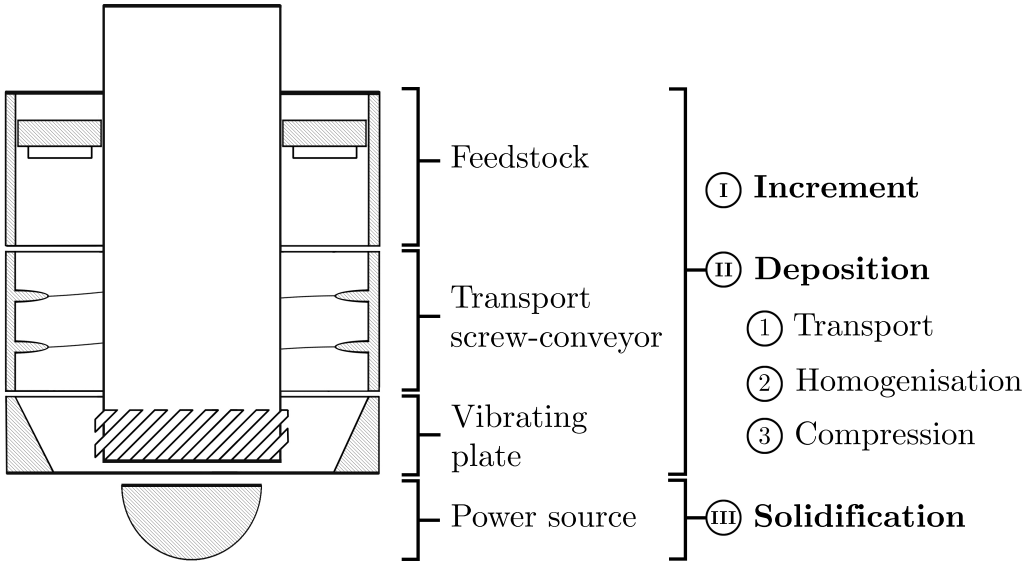

Figure 5.3: Schematic representation of the different stages of the RheoPrint additive manufacturing process, including the corresponding step of the process. The apparatus can be divided in four stages: the powder feedstock, the material transport through a screw conveyor system, the homogenisation by a vibrating plate and the power source (or energy source).

consistency of the packing fraction within the container, the volume gain due to the rise of the inner tube must hence be compensated.

The part closing the container on its upper section, linking the outer wall of the container to the inner tube, is called the *closing disc*. It is this part that is used to counteract the volume gain due to incremental rise of the inner tube, doing so by going down as the inner tube goes up by the right height to cover a similar volume. However, if the closing disc would simply push the material down, the material would be under direct compression, creating a perfect situation for jamming to appear. In order to prevent it, the closing disc is oscillating while it is descending. Equipped with paddles going into the packing, it rotates and changes its rotation direction at a frequency on the order of 1 Hz. This way, the *fragile skeleton* [38, 39] formed by the force chains supporting the pressure is forced to reorganise frequently while the closing disc is going down, so that at each reorganisation, the particle are pushed to a position of (temporary) stability lower along the z-axis than their previous one. In this manner, it is ensured that the material held in the stock is periodically pushed downwards and enters the next step of the powder handling system: the transport area.

Downward powder transport. As seen in Chapter 3, transmitting motion to a granular ensemble by normal pressure is the most effective way to jam the packing. Moreover, in the case of a granular material enclosed in a container at high packing density, a normal pressure on one end of the packing will not be transmitted straight by the powder, but reoriented towards the vertical container walls. So the question arises, of how to transport downward a granular material contained in a sealed box without relying on gravity. As shear stress applied to a granular packing creates a primary flow that is independent of the gravitational field [155, 160], shear will be the preferred type of flow to trigger controlled motion within the RheoPrint process.

The means used to drive the granular packing are carefully chosen, with the aim to ensure that force chains forming are intermittently destroyed, constantly imposing plastic deformation to the granular packing to shape it to our convenience, without risking to create a jammed phase that would render any motion impossible. This is achieved by superposition of different driving mechanisms. Firstly, the downward motion is ensured by a screw conveyor system: the rotating outer container (named *outer tube*) is equipped with helical blades. During granular shear, force chains form oblique to the direction of shear [226]. At the same time, the inner tube rotates to superimpose a supplementary motion, orthogonal to the first one, at the end of the force chains created by the screw conveyor rotation, in contact with the inner tube. Imposing a torque on the particles touching the surface of the inner tube is a way to forestall and defuse the jamming phenomena. If an array of particles should settle into a configuration stable enough to support a high force instead of reorganising to contribute to the general powder flow, the "last" particles of the chains (in contact with the inner tube from which the secondary force is transmitted) will start rolling, destabilising the entire network of force by rolling out of the main stress direction [38, 227]. In other words, the force chain is "elongated" by the secondary motion. This disruption of the force chains by rotation of their end-constituents out of place, forces new configurations to emerge in response, as a secondary force field is created in a direction different from the one imposed by the screw conveyor. It is noteworthy, that if surface friction increases stability of the force chains, both mechanisms used in the superposition of orthogonal drives are enhanced by such surface friction increase, as it also renders contacts between particles and container's surface more stable. A schematic illustration of this mechanism is proposed in Figure 5.4; similar principle has been described in previous work as Orthogonal Superimposed Perturbation (OSP) to tune jamming in dense shear thickening suspensions [228].

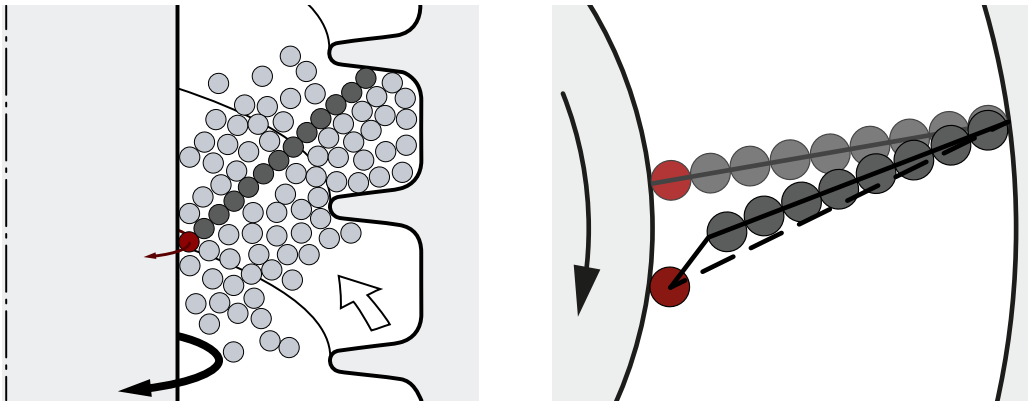

(a) Side view **(b)** Top view

Figure 5.4: Illustration of the superimposition of force chains (in dark grey) imposed by the screw conveyor motion (white arrow), and motion created by rotation of the inner tube (black arrow), disrupting the end-components of those force chains (small arrow, in red) in the idea of OSP, viewed from (a) side (xz-plan) and (b) top (xy-plan).

The main downward motion is imposed by the rotation of a screw conveyor. Screw conveyors, also known as auger conveyors, have been used for transporting and mixing highly cohesive materials for many years [229]. Working on the same principle as extruders, they do not rely on breaking the granular fabric (or penetrating through the viscous material), but instead push the material along as the screw is rotating. Consequently, such type of material-conveying also function for highly cohesive granular material, fine powders, and powders with very irregular distribution in shape and size.

As using screw conveyor systems in microgravity is an unexplored field of research, the exact mechanism behind optimal transport of the material in this environment is yet to be described theoretically. The mechanism proposed here, illustrated by Figure 5.5, relies on having a dense packing inside the container. As they enter the screw conveyor area, the particles are being pushed down all-together by the rotation of the outer tube, following the inclination of the blades. The advancing screw blade surface shears the particles as it pushes them downwards. The entire container is filled with powder, hence steric hindrance keeps the particles from being individually taken along by the screw; instead they are collectively pushed down.

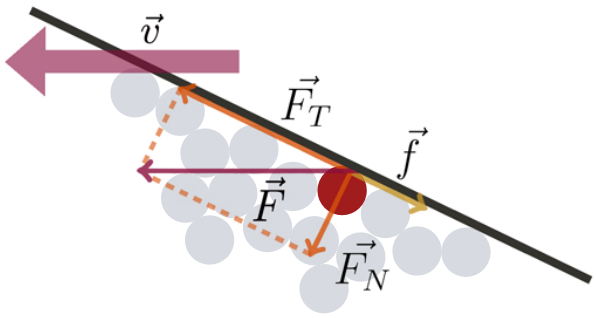

Figure 5.5: Transport mechanism using screw conveyor blades: the blade, moving at velocity $\vec{v}$ transmits the force $\vec{F}$ to a given particle, composed of a normal component, $\vec{F_N}$, that pushes the whole packing downwards, and a tangential component, $\vec{F_T}$, that imposes a rotation on the particles touching the blades, as they are kept from moving along with the blade by their neighbours. $\vec{f}$ is the friction force acting between the blade and our particle of interest. The size of the arrows are not representative of the magnitude of each force, and the force acting from one particle to its neighbours and reciprocally are represented only through steric hindrance of the surrounding particles.

As a consequence, force chains are formed and destroyed over and over, while the packing is generally pushed down through the inclined blades, each reorganisation imposing a generally lower position. The secondary force field, in a different direction as the primary one, imposes constant reformation of the force chains network. None of those mechanisms rely on the powder's ease to flow. The packing is never straightforwardly broken by a normal force, but it is into constant reorganisation: it is flowing. Finally, the particles get out of the screw conveying system into the last part of the powder deposition process.

Homogenisation by planar shaking. Once the grains have been brought to the bottom of the container, the powder needs to be spread on the entire bottom surface. There, the challenge lies not only in shifting the powder to the centre position, but also in forming a layer that is homogeneous, thin and of high density.

The first response to this difficulty is to rise the inner tube not by only one layer-height increment, but by more, in order to leave a volume under the printing platform that is higher than the one of a layer. From this point on, at the bottom of the container, an empty space is created under the platform. So while the rest of the container is densely packed, the new layer at its bottom starts by being empty of powder, and will be slowly filled, hence going from a zero packing fraction towards a high filling by the implementation of an homogenisation strategy.

The homogenisation strategy consists in applying horizontal shaking to the bottom of the container. Homogenisation by planar shaking is a well-know effect on Earth [224, 225]. In

microgravity, it has been shown in experiment [65, 69, 230] and simulation [66–68] that shaking a confined granular sample leads to clustering. Opsomer *et al.* showed that in such conditions, cluster formation depends on the packing fraction, the volume accessible to the powder and the amplitude of the vibrations; for high packing fractions like the ones inside the printing area, we can extrapolate from their work that shaking the bottom plate will lead to a large cluster bouncing around the middle position of the axis along which shaking is applied.

As our aim is to transport powder towards the centre of the container, we use shaking to form a cluster in the middle of the bottom layer. This powder aggregate will grow regularly as more material is added to it, coming from the sides, as the quantity of powder reaching the lower part of the container increases. The shaking continues until powder fills completely the bottom layer. As we will see below, the duration needed to reach this state is live-monitored throughout the process in order to ensure that the entire surface be filled with powder.

Final compression. After having been transported down and homogeneously distributed into a layer, the newly deposited powder undergoes compression. In order to increase this powder density to print compact objects, the printing platform descends on the newly deposited layer, hence pushing on the layer of powder that lies under and densifying it. By compressing the powder between the previously solidified layer and the bottom wall, the powder density is increased on the entire surface of the new layer, going up to random close packing ($\varphi = 0.64$ for monodisperse spheres, higher for polydisperse packings). Moreover, reinforced contacts between grains accelerate the material exchange that will take place during the solidification of the part, hence quickening the densification of the powder into a solid object.

5.2.3 3D printing procedure

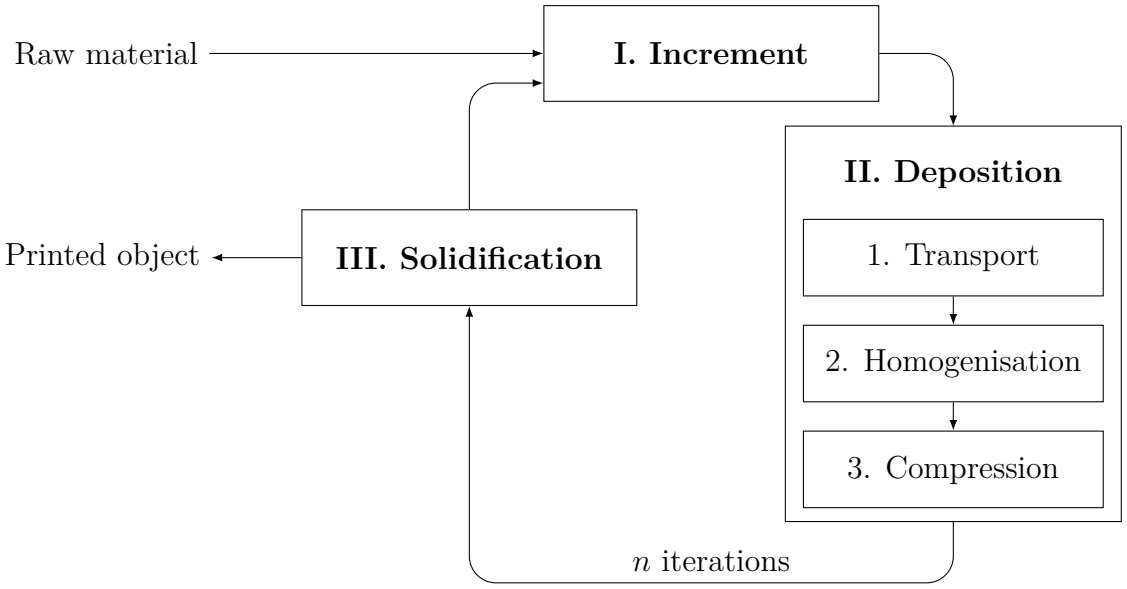

Figure 5.6: Overview of the step-wise additive manufacturing method proposed: one iteration of the process consists in this sequence of actions, repeated n times until the object is fully manufactured.

An overview of the manufacturing method, as represented in Figure 5.6, consist of the iterative repetition of the following steps:

I. **Increment** – Incremental rise of the platform to create space under it for the next layer to be deposited.

II. **Deposition** – Material deposition step, which consists in depositing a thin and homogeneous layer of granular material under the printing platform. The powder deposition is achieved through three stages:

    1. **Transport** – Vertical transport of the raw material towards the bottom of the container, applied by shearing the material.

    2. **Homogenisation** – Horizontal shaking of the bottom of the container, shifting material from the external diameter towards the centre, hence homogenising the powder on the space created by the rise of the platform.

    3. **Compression** – Compression of the newly deposited powder layer by the descend of the printing platform, increasing material density on the entire surface.

III. **Solidification** – The newly deposited layer of raw material is selectively sintered or melted through the bottom "window". It is followed by active cooling, if necessary.

5.2.4 *In-situ* monitoring: towards autonomous manufacturing

Tapia and Elwany [204] point "quality and repeatability" as the Achilles hill of additive manufacturing today. Existing for all commercially available technologies, the problem of defects appearing regularly in printed parts constitutes a major obstacle for industrial applications. Indeed, layer-wise material deposition increases the risk of defects appearance; yet it also enables a direct insight into the bulk while the object is manufactured. Therefore, *in-situ* monitoring of additive manufacturing process is a key element for the development of 3D printing in general, as it would enable to spot and hinder the appearance of defects in printed parts [231, 232]. Live-monitoring the homogeneity of the structure (or microstructure) of the parts being printed during their fabrication could widen the possible applications of additive manufacturing by increasing the reliability of the processes.

In the described process, the downwards transport of material happens at fixed rate, as the screw conveyor turns at fixed speed, through adaptation of the torque provided by the driving motor. Therefore, the duration of the powder transport remains fixed. On the other hand, the duration of the homogenisation step is automatically monitored. While rotating its inner tube, outer cylinders, and closing disc, the 3D printer functions like a rheometer and records the current that each motor consumes to perform the rotation of one of the parts. Thus the torque exerted by each motor, and from this the shear stress applied to the granular packing are calculated; as the rotation speed is fixed, the apparent resistance to flow of the granular medium is obtained. This defines the flowability of a powder: the ease with which a powder can flow in a given geometry, i.e. with which it can be moved and occupy the space given to it as a fluid would. In other words, by running its usual procedure of deposition, the machine automatically probes the flowability of the raw material it contains; it can then adapt its deposition and homogenisation parameters to the material that is fed to it as raw construction material.

Adding a system to probe the raw material in order to adapt the deposition parameters (namely, transport and homogenisation time) to the flow behaviour of the material fed to the printer is a step toward autonomous manufacturing, as the machine's deposition system can

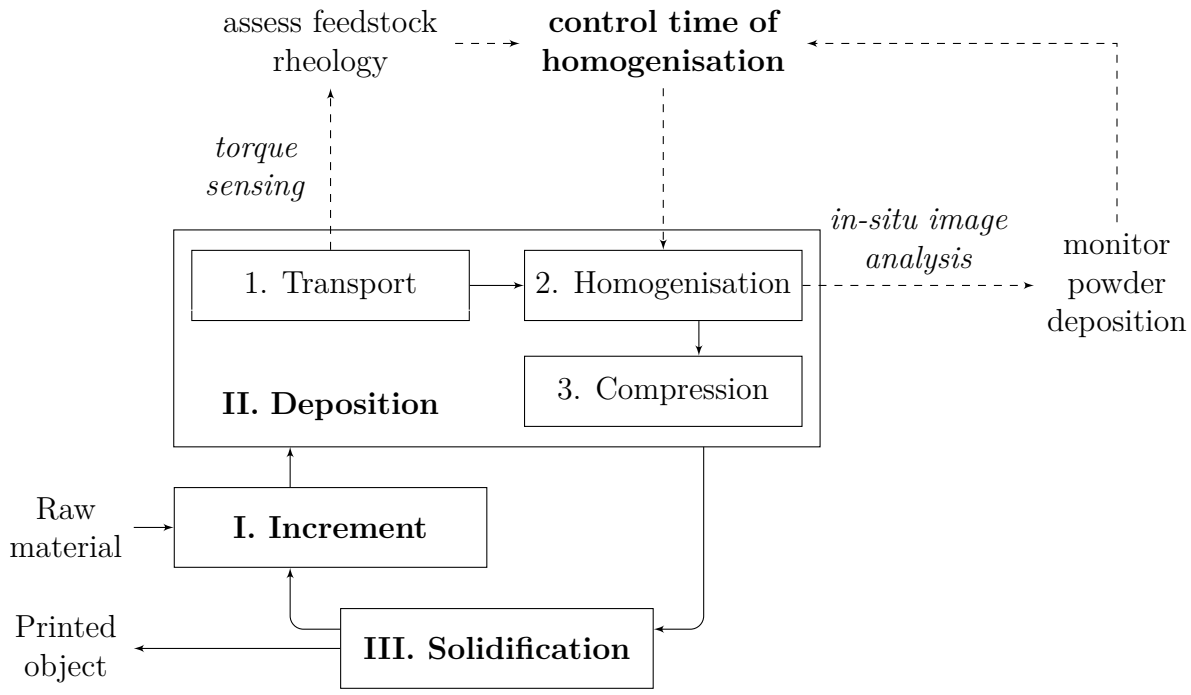

Figure 5.7: Principle of the double control loop implemented on the RheoPrint process: the raw material flow properties is probed upstream .

fully automatically adapt to the raw material's flowability.

Finally, a quality assurance system is implemented during the powder deposition step. The "solidification window", through which an energy input solidifies the material, is made to be transparent not only to this energy source but also to visible light; hence live video can be captured of the advancement of the powder homogenisation. This provides a further possibility to adapt the homogenisation times to the raw material, as well as traceability of the homogeneity of all layers deposited, giving a guarantee that all layers deposited were defect-free, hence, in the end, manufactured parts of constant and reliable quality.

5.3 Limitations

5.3.1 Limitations in material properties

While no obvious limitation exists in the flowability of the raw material used as raw material in the RheoPrint 3D printing process, two materials' characteristics would risk to damage the machine and force cessation of the process: highly abrasive materials and too soft powders.

Abrasive materials. As shear is the main type of stimuli used to set the powder in motion, repeated use of highly abrasive materials, constantly rubbed against the surface of the conveying screw, would progressively scrape the metal surface of the machine away.

Two-body wear occurs when matter is scratched away from a surface by abrasion, in our case abrasion from a granular material. Abrasiveness is a material characteristic that encompasses both the mechanical properties of the bulk (e.g. hardness, toughness) and the physical characteristics of the grains (e.g. sharpness of the particles, roughness of the surface, contact geometry) [233]. Therefore, drawing a boundary line of materials *too abrasive* for use in the

RheoPrint process is not straightforward. Besides, there is no such thing as *too abrasive* in itself; the relevant question is the comparison between the material forming the 3D printer inner surfaces and the raw material it is fed. In order to use powders composed of hard and sharp materials, the entire inner surface of the screw conveyor could be coated with a material exhibiting a combination of low friction coefficient and high hardness. For example, carbon-based coatings, and in particular doped diamond-like carbon coating, show low friction coefficients (generally 0.01 to 0.5) as well as high wear resistance, in particular when paired with steel counter-faces [234, 235]. Often used to increase the hardness of subtractive manufacturing tools, they could also be used to coat the inner surface of 3D printers in needed cases.

This is an important feature to point out, as a possible application of the RheoPrint process would be in the context of a Moon-mission. Lunar regolith is a highly abrasive material, because it is composed of nanometer-scale chunks of sharp minerals that would scratch away most materials [140]. In the case of lunar regolith-based manufacturing, the apparatus should be engineered taking into account the need for a screw conveyor made of a material or coated to be resistant to wear and abrasion.

Soft materials. The consecutive appearance and breakage of force chains, which is the phenomenon assumed to be behind the granular flow in this process, happens regardless of the friction at contact between particles (increased by a rough surface and asperities), and of the shape or "roundness"of the material. However, if the bulk material composing the particles is soft and undergoes large deformation in the stress range that is applied to the material in the process, the particles will deform and deformation will allow transverse loads on the force chains without breaking them (see Figure 5.8). The force chains will remain stable as the axis of application of the force rotates, increasing the risk of jamming [38, 39]. This would be catas-

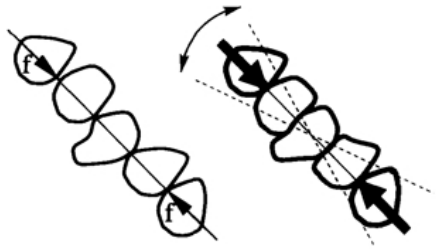

Figure 5.8: A jammed force chain (left) will break if the load varies from its straight angle of application to a transverse load, unless soft particles change shape to adapt to the new angle of application of the force (right). Reprinted from Ref. [38] with permission from Elsevier.

trophic for the powder flow, because as the powder would loose its core powder characteristics and instead become a paste-like highly viscous fluid, the process, adapted to granular materials, would undergo systemic jamming and cease to be operational.

A numerical estimation of the minimum elastic modulus acceptable for avoiding process malfunction can be provided. Typical stress inside industrial scale screw conveyors is on the order of 10^{-2} MPa [236, 237]. In order to have linear elastic deformation inferior to 1% at a stress of 10^{-2} MPa or higher, Hooke's law gives an elastic modulus of 1 MPa. Ergo, a Young's modulus of 1 MPa is the lower acceptable stiffness limit. It corresponds to a material exhibiting low stiffness: typically, expanded polystyrene foam shows an elastic modulus of approximately 5 MPa in linear compression [238]. Even including the necessary security margins

not to jeopardise the powder deposition process, the range of materials processable includes hard polymers, metals and ceramics.

5.3.2 Limiting factors in size

Screw-conveying system. Screw conveyors have been used since Ancient Egypt to transport water, and are widely used today in industrial plants to transport material over very large distances, for granular materials among other materials [229]. There is no obvious limitation in the length of such screw conveying system, which are generally found in length of 1 m to 10 m. In applied engineering literature, for screw conveyors of 5 m and more, the possible deflection angle is a critical parameter. More generally, the limitation in length of screw conveyors is due to a limitation in power required to activate the rotation of the screw [229]. In our case, for a screw conveyor moving material downward in microgravity with the mechanism abovementioned, increasing the transport zone could be done with the same limitations in length as for the same technology used on-ground: finding the best balance between length and power consumption for rotating the screw and keeping a low deflection angle.

Feedstock area. However, in order for the screw conveying to function properly, the material needs to be fed into the transport zone of the process, which must be achieved through a normal downward powder flow. As we have seen, transmitting normal pressure within a granular media is not a trivial issue. It is important that a downward movement be applied to the particles throughout the entire feedstock area, because although not resulting only from normal pressure, this downward movement is necessary for the particles to enter the screw conveying zone and to keep the packing fraction similar between the top and the bottom of the feedstock.

The derivation proposed by Janssen [37] and previously addressed in Chapter 1, can help us estimate the length at which we can ensure that at least some of the pressure applied to the top of the container will be transmitted to the entrance of the powder transport area. Janssen derived from mechanical considerations a way to estimate the repartition of pressure in a container filled with granular material; he showed that the vertical pressure on each section of the material tends towards a saturation value, σ_v^{sat}, which is independent of the height of the container – contrary to hydrostatic pressure in a liquid – and of the pressure applied on top.

This arises because the pressure due to the weight of the material inside and the pressure applied on top of the granular pile is not transmitted straight-forwardly in this media. Instead, the force is partially transmitted to the lateral walls of the container, which hold part of the weight of the material through friction. The vertical pressure can therefore be described by Equation 1.4, reproduced here:

$$\sigma_v = \underbrace{\rho^* g \frac{A}{Pk\mu}\left[1 - \exp\Big(-\frac{kP\mu}{A}z\Big)\right]}_{(1)} + \underbrace{\sigma_v^0 \exp\Big(-\frac{kP\mu}{A}z\Big)}_{(2)}$$

where ρ^* is the density of the granular material, equal to the packing fraction multiplied by the density of the material in bulk, g the gravitational constant, P the perimeter of the section of the cylindrical container and A its area; k is defined by Janssen as the ratio of the horizontal pressure over the vertical pressure in the granular media, μ is the static coefficient of friction and z the height within the container, taken from the top where $z = 0$, where a pressure σ_v^0 is applied. Term (1) represents the pressure evolution due to material weight under gravity, while term (2) is the decay of the pressure σ_v^0 applied from the top.

Which leads us to wonder: how would such pressure repartition evolve in microgravity? Following this train of thoughts, let us observe what would happen if the gravitational acceleration g would tend towards zero.

In the case where no pressure is applied to the top of the granular packing, it is clear: the saturation pressure σ_v^{sat} drops to zero for a gravitational acceleration of zero. If the grains are not held together by any cohesive force, which would be the case in this thought experiment, they simply float around each other with no reason to come to contact and no force to transmit. On the other hand, in the case where pressure is applied on top of the packing, this pressure is transmitted within the granular media until reaching the same pivot point in height as under Earth gravity. After which, as the saturation pressure tends towards zero, the packing stays virtually untouched by the pressure applied at its top surface. In absence of gravity, in order to transmit downward pressure to the bottom of the feedstock area, the height of this zone must not exceed $z = {}^{A}/_{Pk\mu}$.

Following Janssen's prediction, the vertical pressure from the top of a container (corresponding to $z = 0$) downwards (z increasing) for our system can be calculated. The graphical representation is given in Figure 5.9. The numerical parameters used are listed in Table 5.1. We find that with those parameters, the limiting height for sufficient downward pressure (approximately one third) of to be transmitted to the bottom of the feedstock area is $z = 0.25\,\mathrm{m}$.

Table 5.1: Numerical parameters corresponding to our system simplified as a horizontal cylinder: a PS powder in an aluminium container. Plethora of ways are available to access numerically the Janssen coefficient, that must be in the between 0 and 1; the one proposed here follows recommendations given in [113]. The PS properties are taken from the powder manufacturer data-sheet.

	Parameter	Unit	Value
ρ_b	Density in bulk	$\mathrm{kg\,m^{-3}}$	1050
φ	Packing fraction	–	0.64
$\rho*$	Density	$\mathrm{kg\,m^{-3}}$	672
g	Gravitational constant	$\mathrm{m^2\,s^{-1}}$	9.81
σ_v^0	Top pressure	Pa	10000
μ	Static friction coefficient	–	0.3
P	Perimeter	m	$3.77 \cdot 10^{-1}$
A	Area	$\mathrm{m^2}$	$1.13 \cdot 10^{-2}$
k	Janssen coefficient	–	0.4

This development shows a counter intuitive behaviour of force transmission in granular materials: as the forces are reoriented towards the walls of the container, the vertical pressure cannot be directly transmitted through a granular packing. The feedstock area in the RheoPrint process can be used as buffer zone to compact the packing and ensure that material is being fed into the conveyor, with the condition that this feedstock zone remains of height inferior or equal to $h = {}^{A}/_{P\,k\,\mu}$. This value is a relevant parameter to consider, should the process be up-scaled from laboratory prototype to the next technological readiness level.

Maximum radius of the apparatus. The pressure evolution description proposed by Janssen takes as a base hypothesis that the pressure be equal on each section of the cylinder, hence only dependent on the z-coordinate until reaching its saturation pressure. Therefore, it doesn't indicate any limitation in radius size regarding force transmission in the packing.

Likewise, the last part of the powder deposition process or powder homogenisation by planar

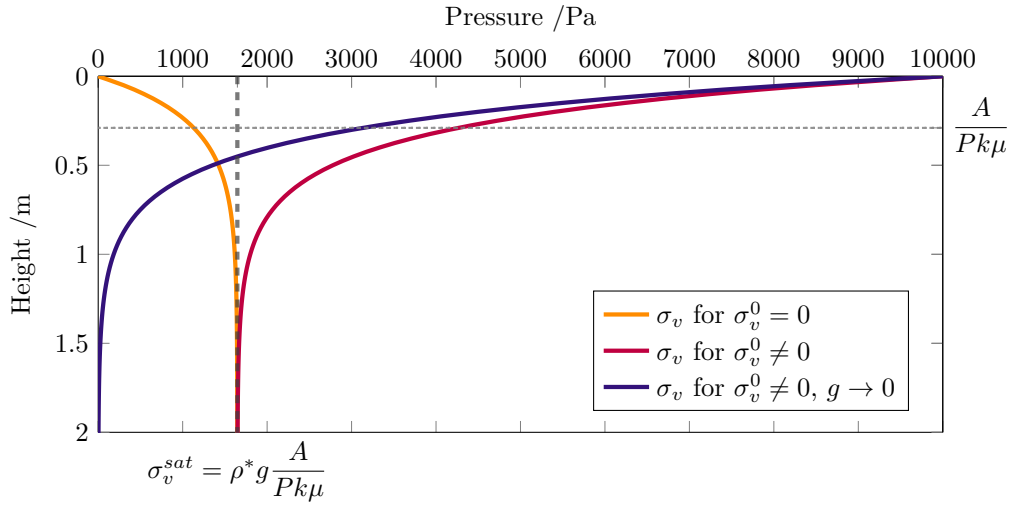

Figure 5.9: Evolution of the vertical pressure inside a cylindrical container as as a function of the height of this container (here represented on the abscissa axis). The height or z-coordinate starts from the top of the container, where $z = 0$.

shaking doesn't give us an indication of a maximum possible radius: for transport of powder through shaking in microgravity, no clear boundary is given regarding the maximum length on which the particles could be transported in microgravity [67, 68].

5.4 Conclusion

A method is proposed for handling and additive manufacturing of granular materials, adapted to space applications:

i. The process can function with materials independently of their flowability. The only restriction in base material is that the particles must have a stiffness larger than 1 MPa, which comprises most hard polymers (e.g. PS, PC, HPDE...), metals and ceramics. Besides, surface interface between the powder and the machine should be adapted to the particles' abrasiveness.

ii. The process functions independently of the gravitational pull. Therefore it is expected to function in microgravity (for example on a lunar or terrestrial satellite or on a space travel) as well as under lower gravitational force field, e.g. on the Moon or Mars.

This is achieved by using exclusively core features of granular flow that do not rely on the ease to flow nor on the gravitational pull for handling powder, which allows us to create the desired powder movements through boundary forces exclusively.

The powder handling method for additive manufacturing that was described in this chapter will be implemented, first numerically though numerical simulation of the powder flow (Chapter 6), then experimentally, providing a proof of concept on-ground and in microgravity (Chapters 7 and 8).

Chapter 6

Simulation of powder flow

6.1 Motivations

Numerical simulations are a powerful tool for reproducing environments or situations that are difficult to access through experiment – among them, absence of gravity. Based on a mathematical model associated to the phenomena studied, it uses the computational power to solve such model over a wide range of values.

The use of computer simulation has been growing parallel to the increase in computational power, and is nowadays an essential part of industrial and academic research [80]. It can be used in the design of new processes, as a complementary tool to experiments. In our case, simulation is used for the following purposes:

- Simulation of the powder flow inside the RheoPrint process offers a first principle validation of the powder deposition method.
- The robustness of the process against the following factors can be probed:
    i. Increasing the magnitude of the interparticle cohesive forces, hence testing the deposition process for powder of mediocre flowability.
    ii. Against a change in the gravitational force field. In preparation of an experimental testing campaign in microgravity, the printing parameters related to powder deposition can be tested under variable gravitational level at incomparably lower cost than any experimental platform enabling to tweak the gravitational parameter.
- The effects of modifying the printing parameters and the environment can be studied on the microscopic level, giving precise insight on the particle interactions impossible to obtain experimentally.

6.2 Principle of study

6.2.1 Simulation principle

A continuum approach to powder flow would enable precise predictions at lower computational costs; but as discussed previously, there is to this day no theoretical model that would reliably encompass the relevant aspects of granular flow. Therefore, Molecular Dynamics (MD)

simulation is used to reproduce the powder flow during the deposition process.

MD simulation is a type of algorithm developed to model particle movements, based on the iterative calculation of each interaction at each time step. In particular, DEM simulations propose to reproduce the interactions between deformable particles and describe the evolution of their position and velocity in time. Such iterative calculation can generate high computational needs; therefore, the number of particles and available time scale are generally limited. Moreover, the particle interactions are approximated through models, which can in certain cases fail to produce realistic results. Thus, the need arises to accompany results and interpretation of simulation with a clear description of the model and parameters used to obtain such results.

The principle of DEM simulation is represented in Figure 6.1; the preliminary step to this description is the choice of a number of particles and of a time step dt, parameters that will determine the time needed for the algorithm to be completed, and the precision of the results. An initial state can then be implemented, consisting of the position $\vec{x_i}(t_0)$ and velocity $\vec{v_i}(t_0)$ of each particles within the given volume. Then starts the iterative loop: first, the contacts among particles or between particles and other surfaces are detected. From the overlap resulting of those contacts, the forces acting on each particle $\vec{F_i}$ are computed. Following Newton's second law, by integration of those forces the velocity of each particle is obtained, and finally their path and new position; this gives a new state $\big(\vec{x_i}(t), \vec{v_i}(t)\big)$. This same procedure is repeated for each particle and each time-step.

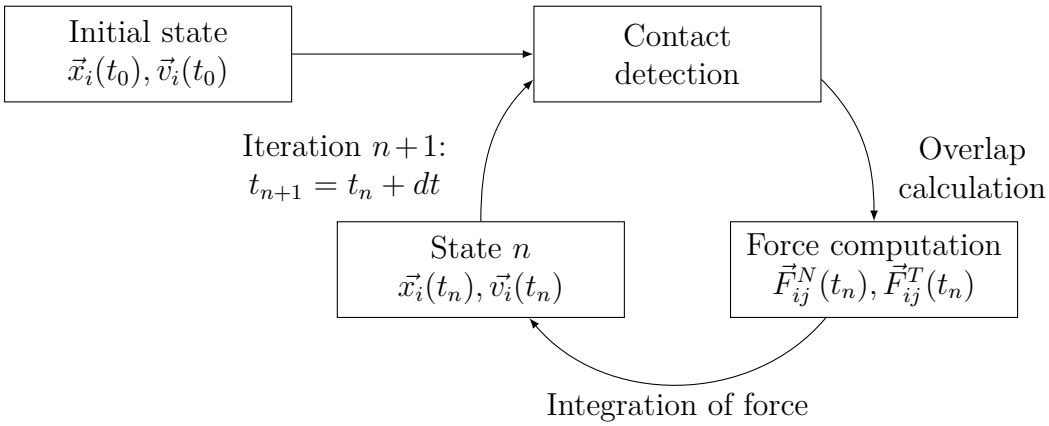

Figure 6.1: Principle diagram of DEM simulation with contact detection.

The simulation software used for this study is LIGGGHTS, which stands for LAMMPS Improved for General Granular and Granular Heat Transfer Simulations (in version 3.8.0), a classic open source DEM code widely used for granular simulations in 3D [239]. The complete command script can be found in Appendix B.1; in this script, the following command line defines the model on which all particles interactions are based: `pair_style gran model hertz/stiffness tangential history cohesion sjkr rolling_friction epsd2`. Each pair of keywords represents a specific command associated to the model or to a modification of the model, which is described in the following.

Interparticle force calculation. The dissipative collisions between particles are modelled through viscoelastic contact interaction forces, estimated as a function of the relative velocity and distance between the particles. Assuming that the particles undergo deformations small compared to their diameter, those interactions between grains are calculated based on the

Hertz-Mindlin model, which divides the force resulting from a collision into elastic overlap forces and viscous friction forces [240, 241].

Ultimately, the interaction force $\vec{F}_{ij}$ between point-particles i and j at a given time-step is computed through Equation 6.1:

$$\vec{F}_{ij} = \underbrace{\left(k_N\,\delta_{N\,ij}^{3/2}\,\vec{n}_{ij} - \gamma_N\,v_{N\,ij}\,\delta_{N\,ij}^{1/4}\,\vec{n}_{ij}\right)}_{\vec{F}_{ij}^{N}} + \underbrace{\left(k_T\,\delta_{T\,ij}\,\delta_{N\,ij}^{1/2}\,\vec{t}_{ij} - \gamma_T\,v_{T\,ij}\,\delta_{N\,ij}^{1/4}\,\vec{t}_{ij}\right)}_{\vec{F}_{ij}^{T}} - \underbrace{\kappa\,A_{ij}\,\vec{n}_{ij}}_{\vec{F}_{ij}^{sjkr}} \quad (6.1)$$

where the variable terms are δ_{ij}, the overlap between particles as illustrated in Figure 6.2 (along normal or tangential direction, respectively $\delta_{N\,ij}$ and $\delta_{T\,ij}$), as well as v_N and v_T, the normal and tangential relative velocities of the particles. $\vec{n}_{ij}$ and $\vec{t}_{ij}$ are the normal and tangential unit vectors; their direction is defined by the vector separating the particles centres. The two first components of the equation, $\vec{F}_{ij}^{N}$ and $\vec{F}_{ij}^{T}$, represent the normal force and tangential force according to the Hertz-Mindlin model. The third force component, $\vec{F}_{ij}^{sjkr}$, corresponds to an additional friction cohesive force proportional to the contact area A_{ij} and the cohesion energy κ of the two particles.

Hertz-Mindlin model for viscoelastic interaction. The base model used to compute the interparticle forces is the Hertz-Mindlin model [242–244], a non-linear model widely used to reproduce elastic and viscoelastic granular interactions. In LIGGGHTS it is called by the keywords `pair_style gran model hertz/stiffness`.

The pair interaction force is divided into a normal and a tangential component, the tangential direction being determined by the relative velocity of the particles while the normal direction links the particles' centres. They both depend on the overlap between the particles, which is recalculated for each interaction, as well as the particles' velocities. Those variable terms of Equation 6.1 are listed in Table 6.1.

δ	overlap between two spherical particles
δ_N	overlap distance projected along the normal unit vector
δ_T	tangential overlap, defined as $\delta_T(t) = \int_{t_c}^{t} \vec{v}_T(t') \cdot \vec{t}_{ij}(t')dt'$ for two particles that came into contact at $t_c < t$; this time-dependent definition is activated by the command `tangential history` (see Ref. [241] for details)
v_N	normal component of the relative velocity of the two particles
v_T	tangential component of the relative velocity of the two particles; the tangential direction depends on the relative velocity at the contact point

Table 6.1: Notation used for the variables δ and v in the Hertz-Mindlin contact model.

Normal and tangential forces $\vec{F}_{ij}^{N,T}$ are each composed of an elastic component and a viscous component. The elastic terms are nonlinear and governed by stiffness coefficients $k_{N,T}$; they have a positive value, representing a "repulsive" force that pushes the particle away after the collision. On the other hand, the damping coefficients $\gamma_{N,T}$ are responsible for viscoelastic damping, where energy is absorbed by the collision, proportionally to the arriving speed of the particle v_{ij}; this term lowers the force with which the particle is thrown back after the collision. The stiffness and damping coefficients find their respective descriptions in Table 6.2.

In order to account for frictional interactions between particles, the tangential force magnitude F_{ij}^T is truncated to obey the friction law $|F_{ij}^T| \leq \mu |F_{ij}^N|$, where μ is the Coulomb friction coefficient. Rolling friction is also implemented through the command `rolling friction epsd2` that provides an additional torque to the particles [245].

k_N	elastic coefficient for normal contact
k_T	elastic coefficient for tangential contact
γ_N	viscoelastic damping coefficient for normal contact
γ_T	viscoelastic damping coefficient for tangential contact

Table 6.2: Notation used for the coefficients $k_{N,T}$ and $\gamma_{N,T}$ in the Hertz-Mindlin contact model. The coefficients are specific to this model, i.e. $k_{N,T}$ are not Hooke's elastic constants.

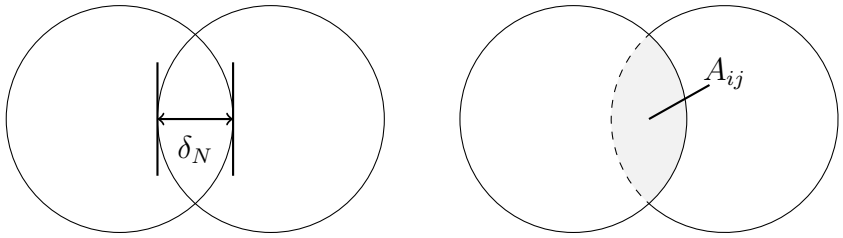

(a) (b)

Figure 6.2: Schematic representation of (a) the overlap distance δ between two particles - in this case, the normal overlap δ_N is represented; and (b) the contact area between two spherical particles when they collide, defined as the disc of surface A_{ij}. The particles are in three dimensions, hence the area A_{ij} is the projection of the "double-lens shape" on the tangential plane.

The input coefficients of the Hertz-Mindlin contact model are linked to the material's properties by Equations 6.2 and 6.3:

$$k_N = \frac{4}{3} E^* \sqrt{R^*}, \qquad k_T = 8 G^* \sqrt{R^*}, \tag{6.2}$$

$$\gamma_N = -\beta \sqrt{5 m^* k_N} \geq 0, \qquad \gamma_T = -\beta \sqrt{\frac{10}{3} m^* k_T} \geq 0. \tag{6.3}$$

Those coefficients represent the material-specific aspects and are therefore related to the mechanical properties of the grains' materials: Young's modulus E, Poisson ratio ν, coefficient of restitution ε of the material in bulk for particles i and j. This is implemented through the following equations:

$$\frac{1}{E^*} = \frac{(1-\nu_i^2)}{E_i} + \frac{(1-\nu_j^2)}{E_j}, \qquad \frac{1}{G^*} = \frac{2(2-\nu_i)(1+\nu_i)}{E_i} + \frac{2(2-\nu_j)(1+\nu_j)}{E_j},$$

$$\frac{1}{R^*} = \frac{1}{R_i} + \frac{1}{R_j}, \qquad \frac{1}{m^*} = \frac{1}{m_i} + \frac{1}{m_j}, \qquad \beta = \frac{\ln(\varepsilon)}{\sqrt{\ln^2(\varepsilon) + \pi^2}},$$

where R_i and R_j are the radii of the two particles in contact, of corresponding masses m_i and m_j. It can be noted that the coefficient β is directly related to the coefficient of restitution ε, so that while ε spans between 0 for perfectly inelastic collisions (the normal component of the kinetic energy is dissipated) and 1 for perfectly elastic collisions (no kinetic energy is dissipated, the particles' velocity is preserved), we have $\beta \in]-1, 0]$ which means that for perfectly elastic collisions, the damping coefficients become null, while they increase in absolute value as the material's coefficient of restitution decreases towards zero.

Adding frictional cohesive interaction. In dense granular flows like the one in the RheoPrint process, frictional interactions between particles are predominant; moreover, in microgravity the cohesive interactions that are usually considered weak (e.g. electrostatic force and van der Waals interactions) take a more important role, as we have seen previously (*cf.* Chapter 3 and in particular Section 3.1).

Therefore, as we have seen in Equation 6.1, an extra cohesive component is added to the force calculation, in the form of the so-called Simplified Johnson-Kendall-Roberts (SJKR) model [246]. Called by the pair of keywords `cohesion sjkr` in LIGGGHTS, it consists of appending an additional attractive normal force contribution to the force calculation at each collision: as two particles enter into contact, this force F_{ij}^{sjkr} tends to maintain the contact proportionally to the contact area, calculated from the overlap:

$$F_{ij}^{sjkr} = -\kappa\, A_{ij} \tag{6.4}$$

where A_{ij} is the disc shaped contact area between spherical particles i and j (see Figure 6.2b), and κ the cohesion energy density.

The cohesion energy density κ is a parameter that is highly relevant in a simulation. It represents all the non-mechanical cohesive forces between the particles, due to the reduction in surface free energy when particles are in contact. As it encompasses many possible mechanisms responsible for cohesion in a granular material, it is difficult to access experimentally.

Based on a simple test simulation consisting of vertical shaking of a dozen of particles, we found that the qualitative behaviour of particles can be tuned by modifying the value of cohesion energy density as follows: for a cohesion energy density of $\kappa = 2.5 \cdot 10^4 \,\mathrm{J\,m^{-3}}$, particles are moderately attracted towards each other, with some aggregate forming. Increasing this value to $\kappa = 1.0 \cdot 10^5 \,\mathrm{J\,m^{-3}}$, particles show a strong tendency to cluster as they almost never part after a collision: their cohesion energy is on the same order of magnitude as the repulsive force between them. On the other end of the spectrum, with a cohesion energy density as low as $\kappa = 1.0 \cdot 10^{-4} \,\mathrm{J\,m^{-3}}$, particles show elastic behaviour. To test the robustness of the RheoPrint process to the cohesion of the granular raw material, multiple values between those boundary ones were tested in the final simulation; unless mentioned explicitly, simulations were performed for $\kappa = 1.0 \cdot 10^5 \,\mathrm{J\,m^{-3}}$.

Numerical parameters. The physical and mechanical properties of the materials used in the present study are listed in Table 6.3 for both the particles (polystyrene, mechanical properties from Ref. [247]) and the container (aluminium, mechanical properties from Ref. [248]).

The coefficients $k_{N,T}$ and $\gamma_{N,T}$ were first calculated based on Equations 6.2 and 6.3. For particles in the range of 100 µm, this implies $k_{N,T} \sim 10^7$ N m$^{-3/2}$ and $\gamma_{N,T} \sim 10^{-1/2}$ kg m$^{-1/4}$ s^{-1} for inelastic particles ($\varepsilon = 0$).

	Parameter	**Polystyrene**	**Aluminium**
E	Young's modulus [GPa]	3.2	68.3
υ	Poisson ratio	0.325	0.340
ϵ	Coefficient of restitution	0.87	0.35
ρ	Density [kg m^{-3}]	1050	2690

Table 6.3: Material properties of polystyrene [247] and aluminium [248].

Regarding the values of elasticity coefficients $k_{N,T}$, which represent the stiffness of the material, a notable effect of the simulation principle must be taken into account. During the integration of force to obtain velocity, minimising the steepness of the force evolution as a function of time enables to use larger time steps without risking to create a large error due to the integration. To decrease the steepness of the force versus time function, it is customary to perform simulations with values for $k_{N,T}$ at the lower end of the permissible spectrum that still reproduces the expected large-scale dynamical properties, in order to reduce numerical effort. In other words, the softness of the particles can be increased, hence allowing a larger time step and therefore more reasonable computation time. For this reason, stiffness coefficients much lower than 10^8 are advised [249].

The effect of varying the simulation parameters over orders of magnitude has been studied [250] and their value must be adapted by qualitative judgement until finding an adequate representation of the real system. The considerations that need to be made in order to fix the model's coefficients value are generally not so-much related to the material's properties, but to the simulation technique itself on one hand, and to the qualitative *reasonable expectation* of the system's behaviour on the other hand, relying when possible on simple tests with well-known results or on probing the effect of changing a specific coefficient on the simulated phenomenon or process.

In order to examine the reliability of the simulation coefficients, the simulation was run for elasticity coefficients $k_{N,T}$ of 10^3 to 10^9 to investigate their effect. It was found that modifying the stiffness coefficients k_N and k_T has little to no impact on the general behaviour of the system. In the light of previous considerations on computing time and following the recommendations of Malone and Xu [249], the stiffness is kept relatively low ($k_{N,T} \sim 10^5$ N m$^{-3/2}$).

In order to produce realistic effects, as in reality, during a collision, most of the energy should be dissipated by viscous damping or through friction between the particles. We expect that the over-damped regime is obtained once $\gamma_{N,T} \gg \sqrt{k_{N,T} m}$. The absorption of the PS particles should be high enough for the particles not to be considered bouncy, which is by far the case with $\gamma_{N,T} \sim 10^8$ kg m$^{-1/2}$ s^{-1}.

Finally, to probe those parameters in a well-known situation, a simple model was constructed to simulate the particles behaviour: on an aluminium plate placed horizontally on the xy-plane, ten PS particles were dropped from random positions of 20 mm to 40 mm above the plate, and the height of the first rebound as well as the decay in height after multiple bounces were observed. This basic experiment showed that using simulation coefficients as calculated directly from the material's mechanical properties ($k_{N,T} \sim 10^7$ N m$^{-3/2}$ and $\gamma_{N,T} \sim 10^{-1/2}$ kg m$^{-1/2}$ s^{-1}) caused particles to behave extremely stiff and to show unrealistic bounciness.

However, it was also found that modifying the values of $\gamma_{N,T}$ has a strong influence on the particles' bounciness: the damping coefficients must be high enough for the particles to undergo truly dissipative collisions. Moreover, as the simulation test proposed is made to optimise the parameters and verify the workability of the powder deposition process, we want to make a *worst case* test. This means, for our simulation scenario, that the powder should be as cohesive as possible, hence reluctant to flowing and bouncing around in the container. This speaks for damping coefficients much higher than the elasticity coefficients.

The final parameters selected are presented in Table 6.4. They correspond to extremely "sticky" particles with a high damping coefficient compared to their elastic coefficient: the granular material will show a more cohesive behaviour as the particles' velocity will be reduced at each collision.

Coef.	Unit	**PS-PS**	**PS-aluminium**
k_n	N $m^{-3/2}$	$1.52 \cdot 10^6$	$4.10 \cdot 10^6$
k_t	N $m^{-3/2}$	$2.04 \cdot 10^5$	$5.51 \cdot 10^5$
γ_n	kg $m^{-1/4}$ s^{-1}	$4.56 \cdot 10^8$	$8.92 \cdot 10^8$
γ_t	kg $m^{-1/4}$ s^{-1}	$4.10 \cdot 10^8$	$8.01 \cdot 10^8$

Table 6.4: Simulation parameters $k_{N,T}$ and $\gamma_{N,T}$ for the two type of interactions present in our model: PS-PS and PS-aluminium.

Boundary surface & motion. The contact surfaces used as boundary condition in the simulation follow the stepwise powder deposition process described in Chapter 5, as represented in Figure 6.3. The consecutive motions of each of those parts are listed in Table 6.6. Apart from the initialisation (Move 0), the moves implemented in the simulation correspond to the steps of the RheoPrint process outlined in Figure 5.1: I Increment (Move 1), II.1 Transport (Moves 2 to 5), II.2 Homogenisation (Moves 6 and 7), II.3 Compression (Move 8); step III Solidification is emulated differently in the simulation (see below).

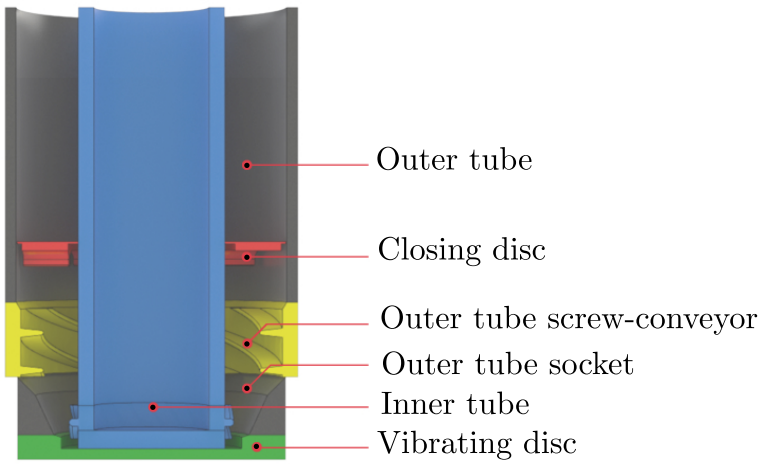

Figure 6.3: Section view of the assembled model used as mesh, labeled with names of the parts. Coloured parts are the moving parts. The movements of each part at each step of the powder deposition are given in Table 6.5.

Move 0	Particles are inserted and dropped down into the container
Move 1	Inner tube rises by two increments
Move 2	Inner tube rotation & closing disc compression
Move 3	Closing disc counterclockwise rotation
Move 4	Closing disc clockwise rotation
Move 5	Outer tube screw-conveyor rotation
Move 6	Vibrating disc shaking in x-direction
Move 7	Vibrating disc shaking in y-direction
Move 8	Inner tube compression downwards by one increment

Table 6.5: Description of the movements of the different parts of the mesh as the simulation progresses through an entire powder deposition step.

Simulation framework. In order to create a virtual system as close as possible to the experimental one, yet giving results in reasonable computational time, the size and number of particles input into the system are critical parameters, as well as the time step and total simulated time.

The time step used is $5 \cdot 10^{-7}$ s. The duration of each step of the simulation in terms of part movement are given in Table 6.6. Regarding the simulated particles, a monodisperse powder is used because the geometrical and rheological features of such packing are well-known. Moreover, the maximum packing fraction of such packing is lower than that of pluridispersed powders, giving a chance to challenge the process in a disadvantageous situation. The particles employed during the experimental campaign are monodispersed PS particles of diameter 80 µm. The number of particles is calculated to fill the volume of the experimental container of $3.4 \cdot 10^{-4}$ m^3 at a packing fraction of 0.64, corresponding to the random packing fraction of a monodispersed packing. Faithful reproduction of the experimental conditions would represent a simulation of more than 125 million particles. Limited by the available computational power and time, 76000 particles with a diameter corresponding to 2 mm were used in the final simulation, which gives a global packing fraction of 0.6, allowing for more interactions between the discrete elements and therefore more impact of the surface movements in the powder flow.

The insertion of the particles inside the complex geometry is done through free fall of the particles from a cylinder on top of the set-up, which corresponds to "Move 0" in Table 6.5. The height of the outer tube has been adapted to allow the implementation of this filling strategy (see Figure 6.3), functioning despite the complex geometry of the container. Once the particles are randomly placed in the experimental volume, and the closing disc inserted to seal the printing bed, the simulation can start.

Snapshots of the visualisation of an exemplary simulation run are available in Appendix B.2.

6.2.2 Methodology for data analysis

The purpose of this simulation study is to analyse the efficiency of the RheoPrint process for the deposition of powder in thin, dense and homogeneously distributed layers. The region that is critical for the process is the bottom layer, where the object will be selectively solidified from the powder deposited; this layer has a thickness of five particle diameters. To base this

study on quantitative data, a procedure for analysis of particle distribution within this region of interest is established.

The results of the simulation are stored in the form of the Cartesian coordinates of each particle per time step. The algorithm written to analyse this data pursues the following path:

1. The particle within the region of interest are detected and selected; their Cartesian coordinates are converted into cylindrical coordinates, which includes their radial position and height.

2. The region of interest, which is a thin cylinder, is divided in sections along different radii, creating equally spaced concentric cylindric rings, as shown in Figure 6.4. The particles inside each ring are counted to obtain n_p. Then, the volume ratio of particles within each section is calculated from the position of their centres, as illustrated in Figure 6.5.

3. The volume occupied by the particles ($n_p \frac{4}{3}\pi r_p^3$), is divided by the volume of each ring V_r. This volume ratio defines the packing fraction per ring, $\varphi(r)$. The volume ratio occupied by particles can be given as a function of the distance from the centre of the printing area.

4. This information can be represented in different ways, emphasising different aspects of the deposition:

    - The average volume ratio of particles can be calculated over the entire bottom volume at the end of each step to give one representative number characterising the effect of each step. This is used in Figures 6.6 and 6.12.

    - The average volume ratio per disc of given boundary radii after the last step of the process can be used to compare the efficiency of the complete process in different environments, as in Figures 6.7 and 6.10.

    - The packing fraction per radius and per movement allows to assess the progression of the deposition throughout the process. 3D plots give precise information on the effect of each step on the progression of powder from the external diameter towards the centre of the printing area – see Figures 6.8 and 6.11.

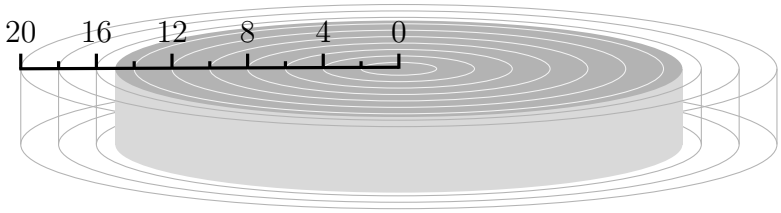

Figure 6.4: To visualise the simulation results, the bottom layer of the powder bed is divided in multiple concentric rings, each equally spaced by two particle diameters. The height of this region is five particle diameters after the compression step. The printing region is only the middle cylinder, represented in grey on the diagram, which corresponds to the diameter of the printing substrate.

The simple formula employed to obtain the volume ratio occupied by the particles is given as Equation 6.5. The number of particles' centres found per region is multiplied by the volume occupied by one particle; then, this particles volume is divided by the total volume of the disc:

$$\varphi = \frac{n_p \frac{4}{3}\pi r^3}{V_r} \tag{6.5}$$

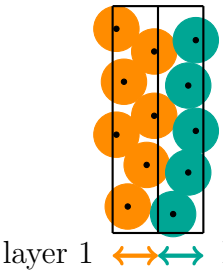

Figure 6.5: Diagram showing a possible packing of the particles. Both layers have similar packing fractions, but the number of particles counted within each region is different.

where φ is the packing fraction or volume ratio occupied by the particles, n_p the number of particles of radius r included in the region and V_r the total volume of the region.

This may cause inaccurate results, as shown in Figure 6.5: although layer 1 and layer 2 have similar packing fractions, the number of particles counted in each region is different. While layer 1 contains seven particle centres, layer 2 only holds five. Therefore, despite their volume ratio being similar, our calculation would give a high filling of layer 1 and low filling of layer 2. This approximation is smoothed by using regions separated by two particle diameters instead of one.

Furthermore, this manner of obtaining the packing fraction from the position of the centre of each particle would work for perfectly hard particles. However, we use deformable particles, which is modelled by the overlap between elements. This overlap can be large in the case of a dense packing where steric hindrance forces the particles together. In our case, this gives very high volume ratios. Any volume ratio higher than 74% for a monodispersed packing should rise the reader's concern; the volume ratio we present, particularly after compressing the packing in the last step of the simulation, go up to approx. 110%. This is explained by the fact that large overlaps between particles lead to some particles' volumes being taken into account twice in our calculation. As an example, a volume ratio of particles of 100% in simulation corresponds to an overlap of approximately 10 to 15% in diameter. Therefore, the evolution of the volume ratio, even though it gives unrealistic numbers in terms of packing fraction, still provides reliable information about the powder distribution, and any very large packing should be taken as a sign that elastic particles are deforming under compression of the dense packing.

6.3 Results & discussion

6.3.1 Rotation speed of the movements

Preparation of the experimental test campaign of the RheoPrint process consists primarily in assessing the influence of the process parameters on the quality of the powder deposition. Regarding the powder flow, the printing parameters are:

- The rotation speed of the inner tube.
- The rotation speed of the outer tube.
- The speed at which the vibrating plate is moving, both along x and y direction.

In Table 6.6, the sequence of movements that composes the simulated RheoPrint process, as

well as the part embodying each movement and the velocity at which the displacement happens are referenced. If instead of a fixed speed a range is listed, this parameter is variable and will be tested.

Number of time steps	Move number	Part	Movement	Speeds: slow param. set	Speeds: fast param. set
1 000 000	Move 0	Closing disc	Linear movement in $-z$ direction, to close printing bed	$0.23\,\mathrm{m\,s^{-1}}$	$0.23\,\mathrm{m\,s^{-1}}$
200 000	Move 1	Inner tube	Linear movement in $+z$ direction: incremental rise of the inner tube by two layer height	$0.20\,\mathrm{m\,s^{-1}}$	$0.20\,\mathrm{m\,s^{-1}}$
400 000 (slow) 200 000 (fast)	Move 2.a	Inner tube	Clockwise rotation about z-axis	Period 0.05 s	Period 0.025 s
	Move 2.b	Closing disc	Linear movement in $-z$ direction	$0.025\,\mathrm{m\,s^{-1}}$	$0.05\,\mathrm{m\,s^{-1}}$
200 000	Move 3	Closing disc	Counterclockwise rotation about z-axis	Period 0.05 s	Period 0.05 s
200 000	Move 4	Closing disc	Clockwise rotation about z-axis	Period 0.05 s	Period 0.05 s
400 000 (slow) 200 000 (fast)	Move 5	Outer tube	Clockwise rotation about z-axis	Period 0.05 s	Period 0.025 s
800 000 (slow) 400 000 (fast)	Move 6	Vibrating disc	Shaking along x direction	Period 0.1 s	Period 0.05 s
800 000 (slow) 400 000 (fast)	Move 7	Vibrating disc	Shaking along y direction	Period 0.1 s	Period 0.05 s
200 000	Move 8	Inner tube	Linear movement in $-z$ direction	$0.1\,\mathrm{m\,s^{-1}}$	$0.1\,\mathrm{m\,s^{-1}}$

Table 6.6: Description of boundary movements in the simulation. Move 2.a and 2.b happen simultaneously, and moves 2 to 5, which represent the powder transport, are grouped into one simulation step of 200 000 time steps. Between Moves 0 and 1, there are 200 000 steps left for settling of the material; it is after this point that the gravitational-level is modified. The two parameter sets in speed correspond to the "fast" and "slow" motions in Figure 6.6.

The deposition is tested for two different sets of parameters: the "slow" ones corresponds to the lowest values of speed presented in Table 6.6 and the "fast" ones, at the other end of the ranges. Essentially, at constant deposition time, the rotation speeds of the inner and outer tubes are doubled, as well as the moving speed of the vibrating disc (affecting Moves 2.a and 2.b, 5, 6 and 7). The full simulation "time" is either $3.2 \cdot 10^6$ steps (for the fast parameter set described below) or $4.4 \cdot 10^6$ steps (for the slow one).

During the transport stages (moves 2 to 5), the packing fraction varies strongly along the bottom layer, because those steps bring the powder down in the container, creating a large powder density on the outer diameter but bringing no powder in the centre, on the printing area. The homogenisation (moves 6 and 7) then brings this powder accumulated on the external diameter towards the centre, increasing the mean packing fraction and homogenising it on the entire bottom volume. Finally the compression step (move 8) increases largely the powder density, creating a full layer of powder constrained between the platform and the bottom wall. Surprisingly, the volume occupied by particles within the space of the new layer to deposit is

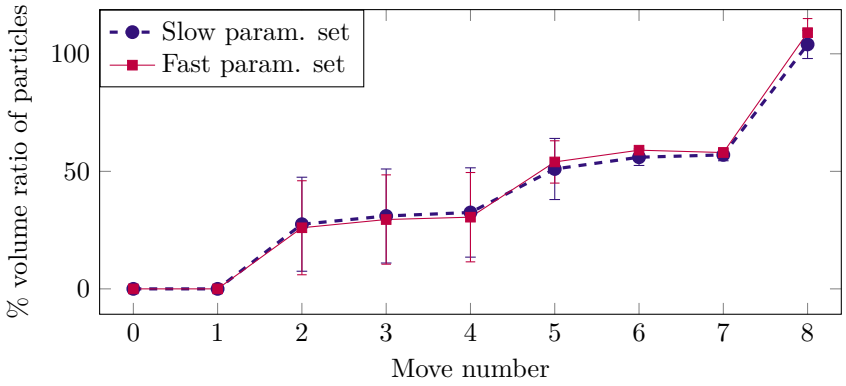

Figure 6.6: Evolution of the average volume ratio occupied by the particles on the entire bottom volume, as the process is taking place, at the end of movements 0 to 8 as described in Table 6.5, for the two sets of speed parameters tested. The set of parameters chosen, corresponding to the "fast" parameters set, is represented by a solid line (square marks), while the "slow" parameter set is represented by the dashed line (round marks). The error bars represent the standard deviation in the packing fraction over the entire bottom volume.

not affected by the speed at which the different movements in question are realised. In the range of speeds available, modifying the velocity of the parts seems to have no influence on the quality of the deposition. The set of parameters used in the following simulation runs as well as in the experimental implementation is the one with faster rotation speeds.

6.3.2 Simulating consecutive steps

In order to validate the feasibility of continuous printing, we want to determine if the repetition of the deposition process multiple times has an influence on the quality of the deposition. To simulate consecutive steps instead of only the very first layer printed, the algorithm has to be tricked into simulating the solidification step. We used a cap of the diameter of the inner tube to encapsulate the particles at the printing layer after their deposition, thus simulating their solidification after the first series of mesh movements, and then repeated steps 1 to 8 for the deposition of the next printing layer. The same procedure was then repeated another time, hence simulating the deposition and sintering of three consecutive layers. Results are shown in Figure 6.7 as the evolution of the percent of volume occupied by the particles as a function of the distance from the centre of the printing surface at the end each layer deposition procedure, before our "solidification step".

Figure 6.7a presents the packing density at the end of the process for three layers deposited with the same deposition duration. The quality of the deposition seems to decrease slightly at each new layer deposited. To improve the performance of the deposition for consecutive layers, the rotation time of the outer and inner tubes are doubled for the second layer deposited and tripled for the third. As shown in Figure 6.7b, the powder deposition quality for Layers 2 and 3 improved after the modification of this process parameter.

This test points out that during the deposition of multiple consecutive layers, it is possible that the deposition becomes less and less effective. This result should be confirmed or invalidated experimentally (see Chapter 8), as it could very well be an artefact from the simulation: as the particles interactions are generally more elastic in the simulation than in reality, the influence of the rotation of the inner tube could be overestimated in simulation. In reality,

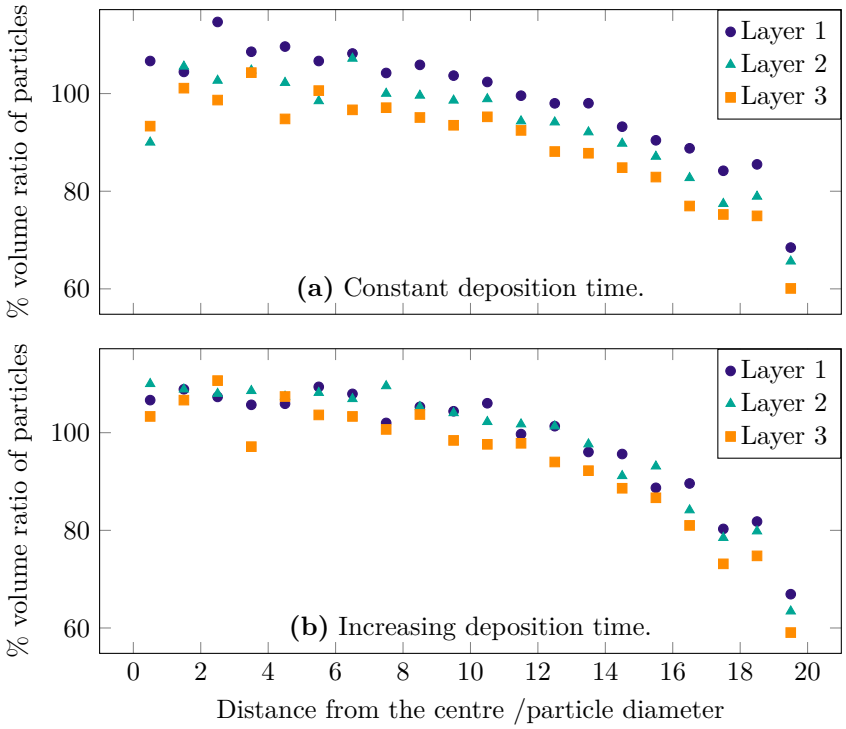

Figure 6.7: Evolution of volume occupied by particles for the simulated deposition of three consecutive layers, including solidification steps in between each powder deposition. The deposition time is constant for all layers in (a) and increased for each new layer in (b).

this movement is mostly present for probing the raw material's flow property. However, in the simulation it seems to help moving some particles toward the bottom of the printing bed. As more layers are being printed, the paddles on the inner tube go further away from the printing platform, affecting negatively the rapidity of the deposition process.

If this effect persisted in experiment, it could nonetheless be stymied by increasing the deposition time throughout the printing process, or by printing blades on the outside of the printing volume, removable structures present only to ensure constant quality of the deposition process from bottom to top of the printed object.

6.3.3 Influence of gravity

To evaluate the influence of gravity on each step of the RheoPrint process, it is simulated under gravitational fields of $1g$, μg and $-1g$. Under microgravity, no mass-dependent external force field is applied. The particle movements are only induced by the boundary movements and the forces transmitted through other particles. On the contrary, the $1g$ environment promotes the fall of particles toward the bottom of the process container, whereas the $-1g$ condition tends to pull the particles towards the top of the process, working against our desired flow direction.

Figure 6.8 presents the evolution of powder density throughout the nine steps of the process (moves 0 to 8), along the radii of the concentric discs that divide the printing volume of one layer. To ease the comparison between $1g$ and $0g$, Figure 6.9 shows the normalised difference in packing fraction:

$$\frac{\varphi(1g) - \varphi(0g)}{\varphi(1g)} \tag{6.6}$$

after moves 2 to 5, where the difference is obvious, and for comparison, after move 8 (at the end of the powder deposition), where the process has equalised the powder density. The concentric discs radii go from 20 particles' diameters, the most external radius, to 0, the center point of the layer volume; the printing zone is actually limited to the circle of radius 15 particles diameters, representing the size of the printing platform (see Figure 6.4).

Move 1 consists of the rise by 10 particles' diameters of the inner tube on which the printing platform is placed, leaving the volume underneath empty. As we are dealing with a granular solid, that by definition doesn't have an inner pressure, the space left empty is not directly filled by material: regardless of the gravitation environment (Figure 6.8) or particles' properties (Figure 6.12), at the end of Move 1 the bottom layer is never filled with powder.

Then the powder downward transport takes place. In moves 2, 3 and 4, powder is being pushed down by the closing disc descending and rotating at the same time, and rotation of the inner tube imposes a general downward flow. During those movements, under $1g$, the powder being pushed down doesn't simply accumulate by the side of printing platform: it forms a slope going towards the centre of the printing volume. This can be observed in Figure 6.8a for moves 2, 3 and 4 close to the centre, region represented in red to dark orange. The slope of the half-pile formed would correspond to the angle of repose of the sample. Although it is discussed that the angle of repose under different levels of gravity might be the same for the same sample of material, in complete absence of a gravitational pull, no pile forms as the grains are simply not attracted downwards: the difference between the area where powder is present (the outwards disc) and where it is not yet deposited (in the centre of the printing bed, radius around 4 particles diameters) is delimited by a steeper boundary in Figure 6.8b.

In Move 5, the outer tube, equipped with a screw conveyor, rotates to transport the powder downwards. The difference in powder deposition due to the gravitational environment becomes drastic at the end of this move: under $1g$, the layer is already homogeneously distributed at a packing fraction around 0.6, while in μg the centre of the layer is still at a low powder density (packing fraction approx. of 0.2). There again, the movement is helped by the presence of gravity, because in microgravity no force pushes the powder to move horizontally towards the most centred diameter of the printing volume.

The homogenisation by shaking that occurs next (moves 6 and 7) completely erases the difference due to different gravity levels, as the powder at the end of this step is evenly distributed throughout the printing volume, reaching a packing fraction around 0.6 on the entire layer, regardless of the gravitational environment.

The packing fraction is then doubled by the last step, move 8: the compression of the newly deposited layer. If this doubling of the packing fraction gives unrealistic values, it is, as discussed in the previous section, a simulation artefact that represents a high powder density and slight compression of the newly deposited layer.

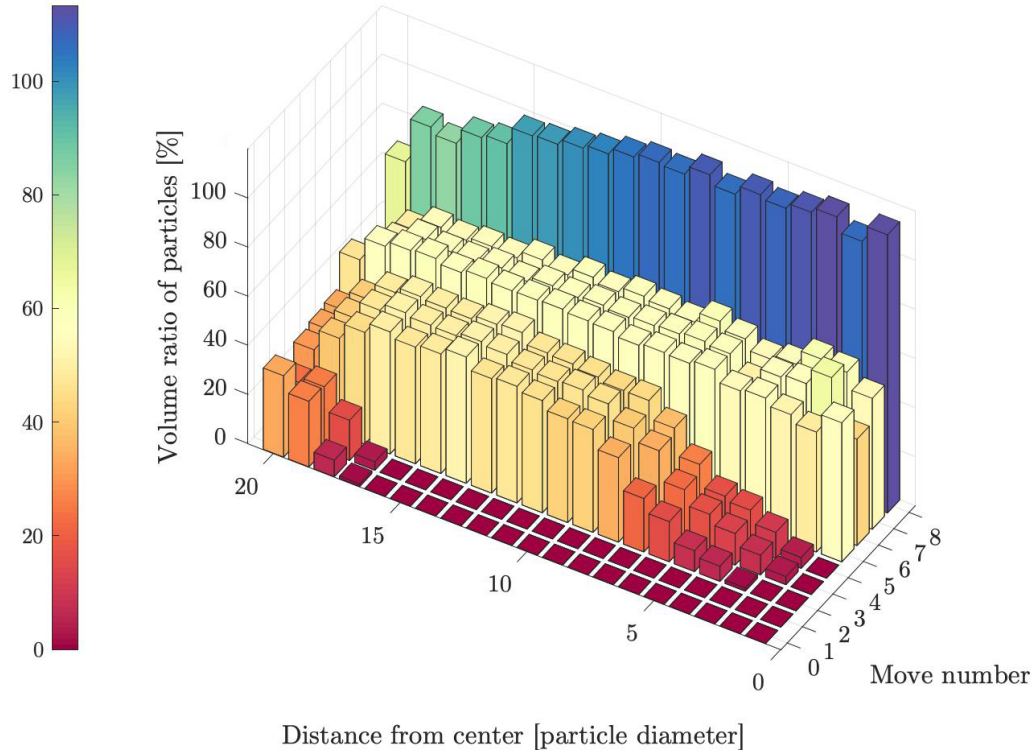

(a) Under $1g$

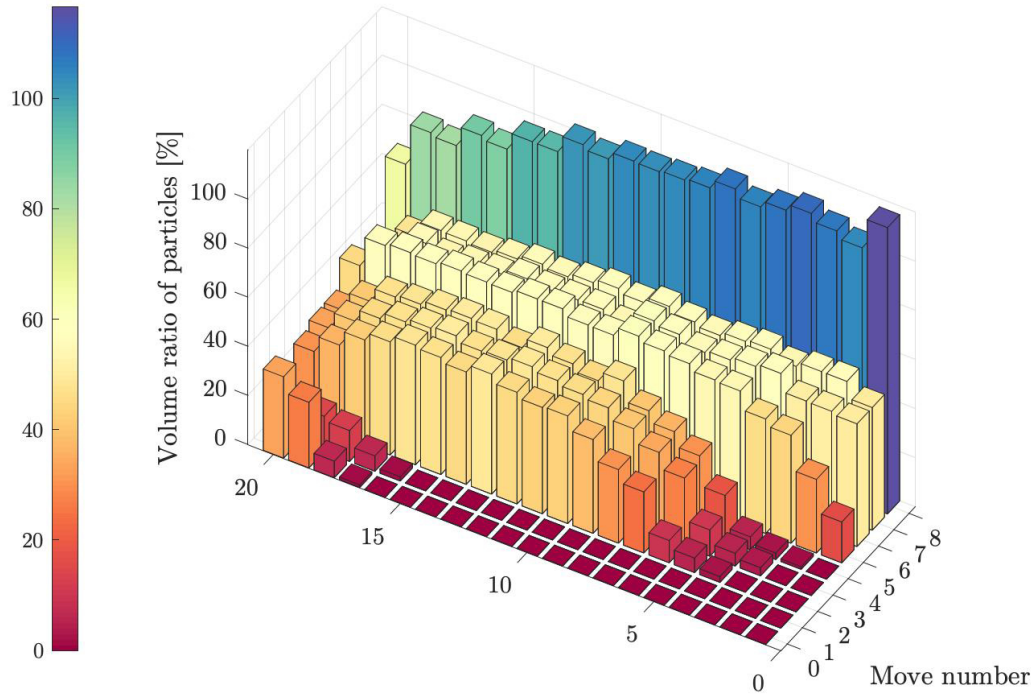

(b) Under $0g$

Figure 6.8: 3D-graph representing the evolution of the percent of volume occupied by the particles (illustrated by the height and colour of the bars) as a function of the distance from the centre of the printing volume (along x-axis) and of the step of the process (along y-axis). The volume ratio calculation is done at the end of each step. The simulation is run for highly cohesive particles ($\kappa = 10^5$ J m^{-3}), under (a) $1g$ and (b) μg.

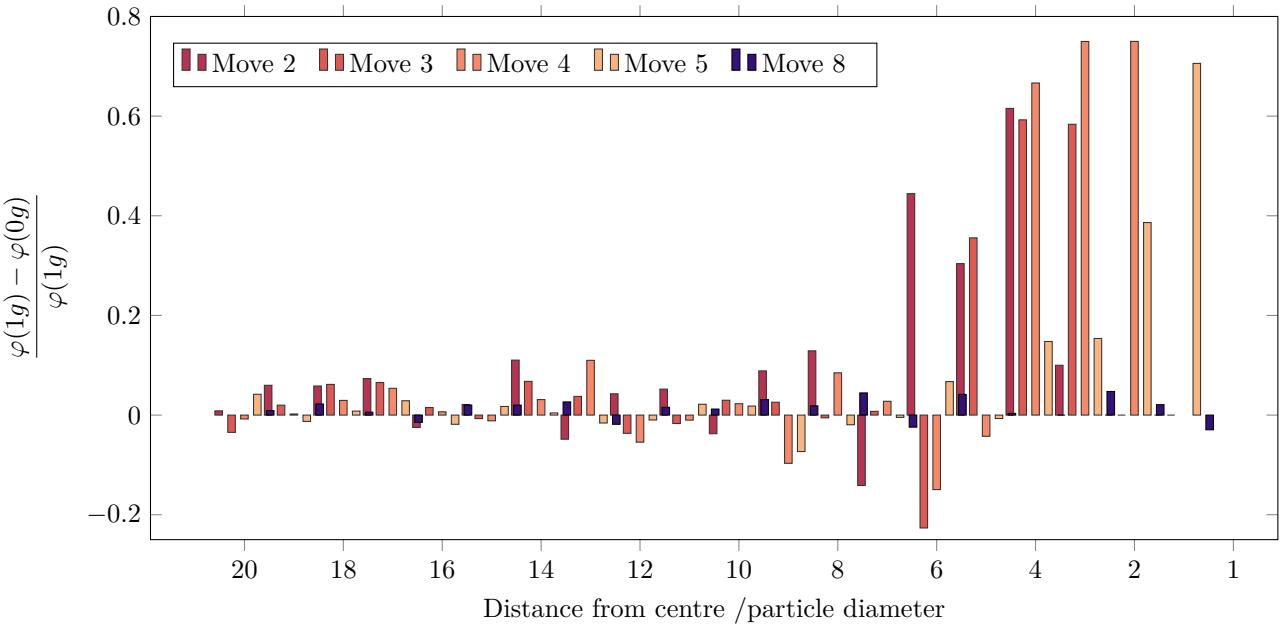

Figure 6.9: Evolution of the normalised difference in powder density between $1g$ and μg, as a function of the distance from the centre of the printing volume (along x-axis) for different steps of the process: at the end of moves 2 to 5 (powder transport) and after move 8, at the final stage. The volume ratio calculation is done at the end of each step. The simulation is run for highly cohesive particles ($\kappa = 10^5$ J m^{-3}).

All-in-all, one can observe in Figure 6.9 and by comparing Figures 6.8a and 6.8b that the presence or absence of gravity modifies the packing fraction in the printing volume during the powder transport (moves 3, 4, 5), but that after the homogenisation (moves 6 and 7) and compression (move 8), the level of gravity but has no impact on the final powder density repartition. Under Earth gravity as well as in microgravity, the simulation gives very positive results as at the end of the powder deposition the entire layer is filled with powder at high density and no obvious heterogeneity appears.

The same simulation is repeated under $-1g$, to confirm the independence of the 3D printing process to gravity by creating an unrealistic (in terms of useful applications) yet very challenging environment. Figure 6.10 shows the powder packing fraction at the end of the full deposition procedure under $-1g$, μg and $+1g$ on the bottom surface of the printer container. Under those three gravity conditions, the process gives almost perfectly similar results: if taking the entire process into account instead of comparing the moves one-by-one, the level of gravity is shown not to have any influence on the powder deposition process.

6.3.4 Impact of cohesive forces between grains

The other pertinent parameter for the process is dependence on the flowability of the powder used as raw material. In order to test it, our variable of choice is the cohesion energy κ (in J m^{-3}). This parameter gives a magnitude to the force of attraction that appears at each contact between particles. Following a series of tests previously explained, the values of the parameter κ varies from $1 \cdot 10^{-4}$ J m^{-3} (for a very low cohesion, hence a highly flowable material) to $1 \cdot 10^5$ J m^{-3} (for a highly cohesive packing). The simulation was run for those two extreme values, as well as for multiple in-between values, to assess the effect of powder cohesion of the

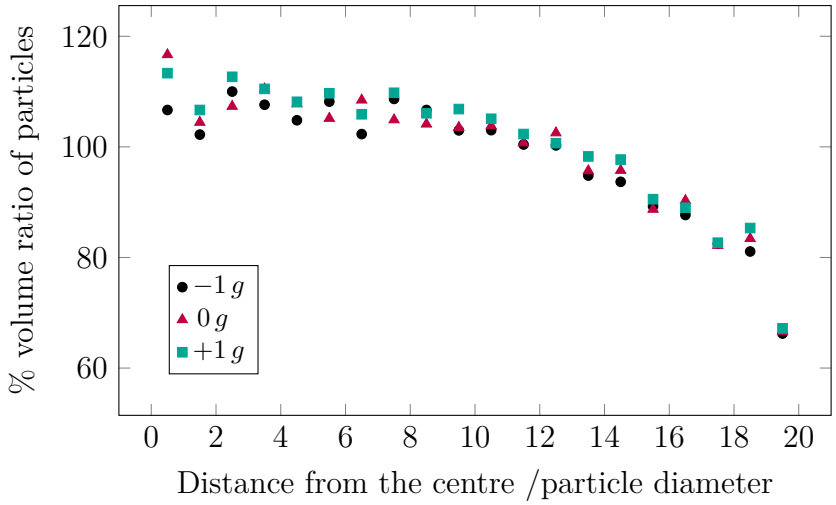

Figure 6.10: Volume ratio occupied by particles after the last step of the deposition process, for simulations run under $-1g$, $0g$ and $+1g$.

RheoPrint process.

Figure 6.11 shows the evolution of the volume ratio occupied by powder after each movement, along the radii of the divided printing volume. For the highly flowable particles (Figure 6.11a), after the first movements following the rise of the printing platform the powder is already homogeneously distributed, while this state of homogeneity is only reached after the moves 6 and 7 – corresponding to planar shaking – for the highly cohesive packing (Figure 6.11b).

Nevertheless, once again, the planar shaking followed by compression allows the packing fraction to first reach an homogeneous state around 0.6, and then to end up increasing up to over 1, showing a high density and compressed packing in the printing area at the end of the powder deposition, regardless of the cohesion of the powder.

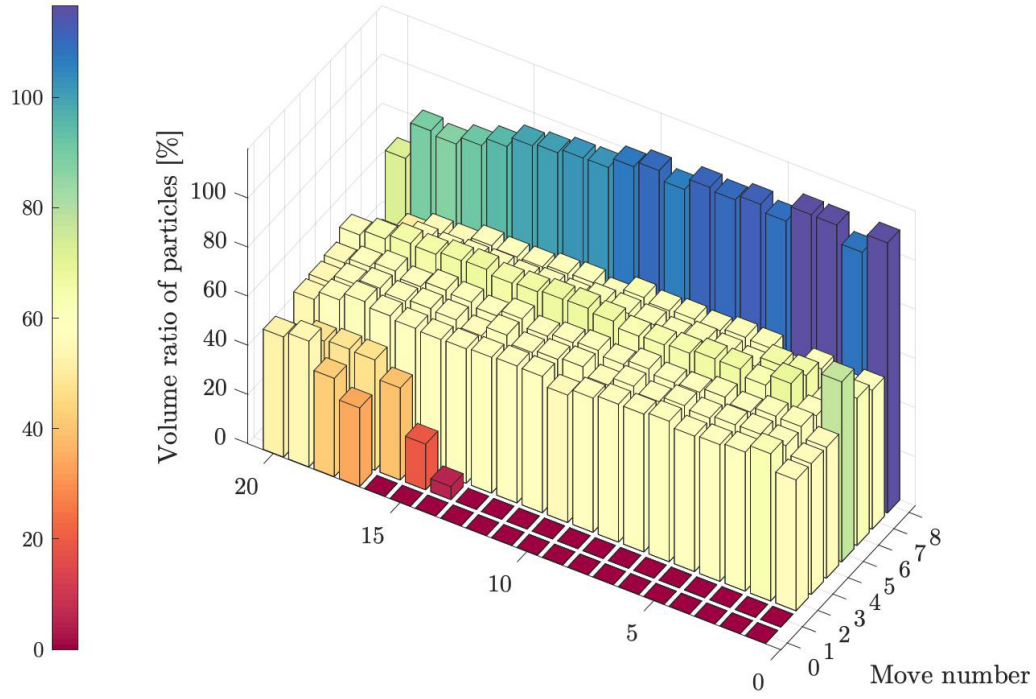

(a) Low cohesion particles $\kappa = 1 \cdot 10^{-4}$ J m^{-3}

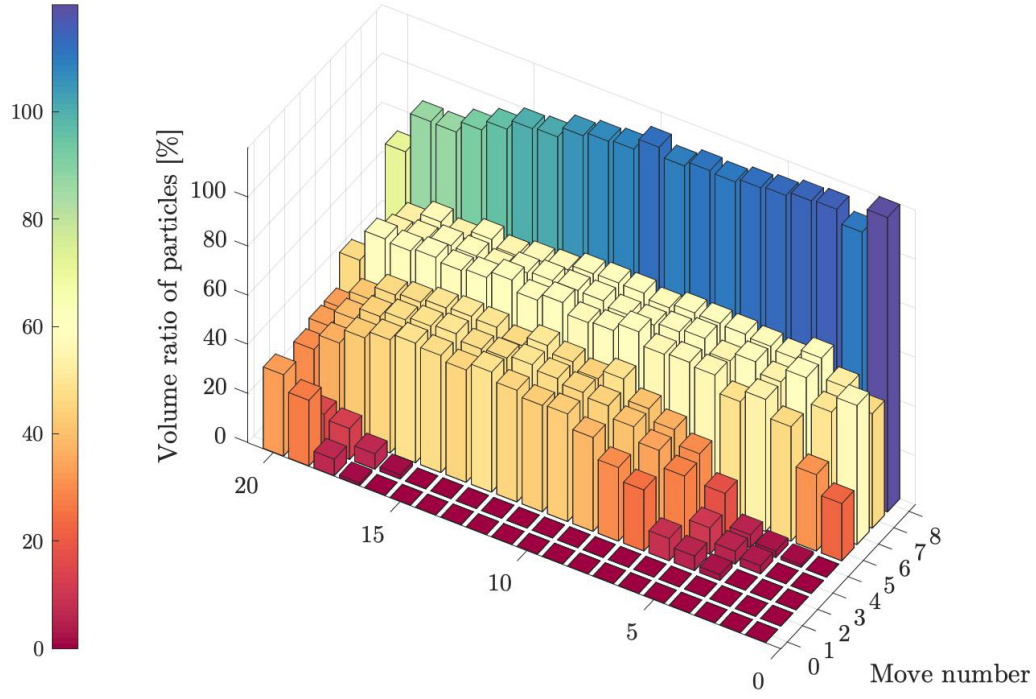

(b) Highly cohesive particles $\kappa = 1 \cdot 10^{5}$ J m^{-3}

Figure 6.11: 3D-graph representing the evolution of the percent of volume occupied by the particles (illustrated by the height and colour of the bars) as a function of the distance from the centre of the printing volume (along x-axis) and of the step of the process (along y-axis). The volume ratio calculation is done at the end of each step. The simulation is run under μg, for (a) particles of low cohesion and (b) highly cohesive particles.

Figure 6.12 compares the evolution of the packing fraction throughout the process for attractive particle interactions tweaked to go from low (highly flowable powder) to high (highly cohesive powder, prone to clustering). After Move 1, the increment of the inner tube, the lines diverge, which reflects the fact that non-cohesive powders are very sensitive to any collisions and tend to move freely within the container, while the highly cohesive particles tend to stay together, and do not explore the rest of the volume unless forced to do so. This is particularly visible on Moves 2 to 5, before the homogenisation, where the average packing fraction is much lower and more heterogeneous for cohesive samples. However, we also see that regardless of the cohesion of the packing, the homogenisation by shaking is indeed efficient, and the following compression of the layer completes the deposition process by fixing the particles in a state of high density, independently of their cohesive interactions.

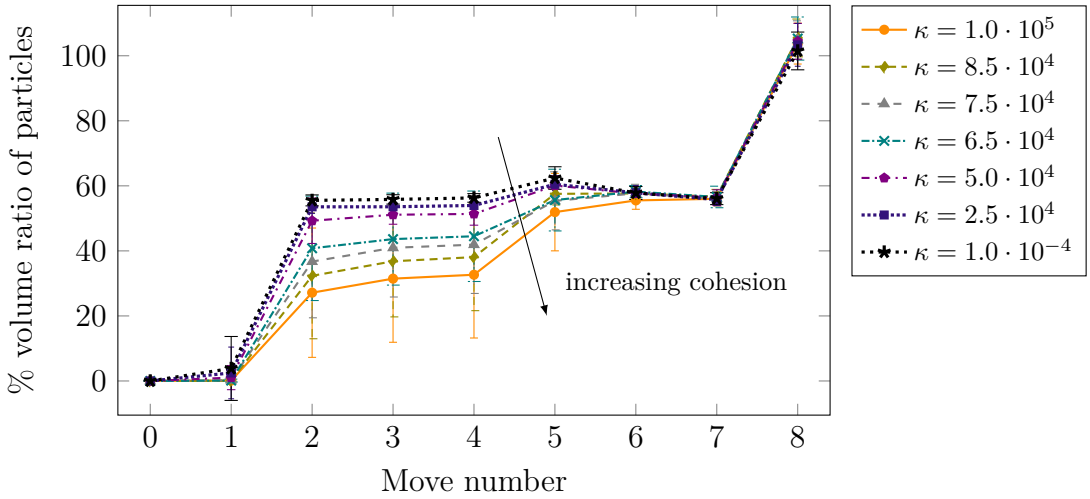

Figure 6.12: Volume ratio of particles per 3D bar chart showing the volume ratio of cohesive particles after each movement. The cohesion parameter κ is given in the legend in $\mathrm{J\,m^{-3}}$.

Once again, our simulations give very positive results for the process: whereas increased powder cohesion modifies the behaviour of the powder flow at each step of the powder transport taken separately, the general deposition seems to function extremely well independently of the raw material's flowability.

6.4 Conclusion

The 3D printing process at the heart of our study was designed to be independent of the flowability of the granular material it is fed, and of the gravitational environment under which it is used. This is achieved by a powder deposition relying on well-understood properties of granular materials independent of their rheological properties as well as using boundary forces to create a powder flow and constrain the powder to the desired location.

The entire powder deposition strategy was implemented in a DEM simulation, with the goal to provide a study of the process preliminary to experimental testing campaign. The results obtained through simulation show:

- Independence of each step of the process from the intensity and direction of the gravitational field.

- The influence of the cohesion of the powder on each singular steps, that is erased by

applying the complete process: the combined steps provide a "flowability-independent" powder deposition process.

- This study also raised the need to be aware of the risk that the deposition quality might not have a constant quality throughout the consecutive deposition steps.

Those results give a positive first assessment of the powder deposition process, as it fulfills the requirements set for the process to be relevant for ISM. However, some intrinsic limitations due to the simulation technique must be pointed out.

The need to model particles much larger in simulations than in reality begs the question of finite-size effects affecting the simulation, because the ratio between particle size and machine size is wrongly reproduced, and this could have *a priori* uncontrollable effects on the force chain distribution and jamming phenomena

As evoked in the previous chapters, one important risk in powder-based processes is the appearance of a jammed region within the packing during the transport phase, which could block the movements of some mechanical parts and therein the process. Jammed zones in the packing wouldn't have been made apparent by this DEM simulation.

The next step of this study is to verify the results exposed in this chapter to propose an experimental proof of concept of the RheoPrint AM method, by building a prototype applying this process for powder deposition and solidification (Chapter 7) and testing it, on-ground and in microgravity (Chapter 8).

Chapter 7

Design & construction of RheoPrint prototypes

7.1 Motivations & scientific objectives

The RheoPrint additive manufacturing process was developed as a response to the need for a powder-based process adapted to space environment, and in particular to microgravity. Therefore, the valid experimental proof of concept for this process is to function in microgravity. In this chapter, the following questions are addressed:

- What microgravity experimental platform is best adapted to prove the proper functioning of this process under low gravity?
- How is the process implemented into a machine: for each technical decision, what are the design requirements, and how is the chosen implementation selected over concurrent possibilities?
- How is the experimental campaign planned to provide a proof of concept of the powder-based technology as well as sufficient data to analyse the results?

To qualify as "functioning in microgravity", the powder deposition and solidification shall be realised entirely in microgravity. The objectives of this experimental campaign are defined as follows:

Objective 1: Optimise process parameters for microgravity.
The optimal set of printing parameters for microgravity must first be obtained by tweaking the following settings:

- Duration of the deposition mechanism per layer of material deposited.
- Height of the new layer deposited.
- Horizontal shaking parameters (amplitude, frequency, duration of the shaking step) for optimal homogenisation of the new layer deposited.

Objective 2: Print an object in microgravity as proof of concept.
Once a suitable set of printing parameters is found, an object should be manufactured entirely in microgravity, including the deposition and the solidification steps.

Objective 3: Obtain material for characterisation of microgravity-printed samples. In order to obtain enough material for drawing statistically valid conclusions and probe the reproducibility of the printing process, multiple samples should be 3D printed in microgravity. Those samples can serve as a base for comparing the analysis obtained through *in-situ* probing implemented within the process and post-characterisation to detect defects due to the powder deposition process (e.g. porosities and regions of heterogeneous density).

Objective 4: Test the process with raw materials of variable flowability. The robustness of the AM method to powders of different flowabilities in microgravity can be tested by using two powders of similar physical and mechanical properties but with different rheological properties, namely the two PS powders characterised in Chapter 2.

Objective 5: Record gravity-triggered changes in powder flow behaviour. Changes in powder behaviour as a function of the gravitational environment will be observed through the *in-situ* probing measures comprised in the process and implemented as user-controlled loops:

- The torque needed by the motors to move each specific rotating piece in regard to the others will be collected, giving an indication on the *ease to make the powder flow* in the process as a function of the type of powder used and gravitational environment.
- The powder deposition step, and more particularly the homogenisation, is recorded through the *in-situ* probing by image capture, observed through the bottom window.

Analysing this data will draw a description of the rheological behaviour of the powder tested, to be compared to the same data obtained on-ground.

7.2 Microgravity platform

7.2.1 Existing experimental microgravity platforms

The platforms available today for scientists to conduct experiments in low- and microgravity environment are summarised in Table 7.1. Ideally, only scientifically relevant parameters like the ones presented should be taken into account when deciding for a platform. In reality, many other criteria come into play when selecting the experimental microgravity platform for an experiment; in particular: cost, accessibility, preparation means available (among which time, engineering and construction resources, costs) or waiting time until the chosen platform can be accessed with a new experiment.

7.2.2 Technology demonstration

Which platform is best suited for technology demonstration? In developing new technologies for space applications, during the first tests in low gravity it can be essential that parameters be adjusted on the spot depending on the behaviour of the technology when activated in such new environment. Because it offers direct access to the scientists developing the technology and short but repeated periods of microgravity over multiple days of campaign, parabolic flights are a good technology demonstration platform. In particular, powder-based technologies can show little reproducibility, especially in down-scaled systems; a first technology demonstration mission on parabolic flights can save development time and costs by offering

Table 7.1: Experimental microgravity platforms available for scientific purpose today [251].

Platform	Microgravity duration	Quality of microgravity	*In-situ* access to experiment
International Space Station	> months or years	Rather good ($\sim 10^{-4}$)	Remote and indirect
Orbital spacecraft (recoverable satellites)	> months or years	Very good ($\sim 10^{-5}$)	Remote or no access
Suborbital spacecraft (sounding rockets)	5 to 13 minutes	Good $\sim 10^{-4}$ to 10^{-5}	Remote or no access
Stratospheric balloon	Up to 55 seconds	Unstable, $\sim 10^{-3}$	Remote or no access
Parabolic flight	22 seconds	Unstable, $\sim 10^{-2}$ to 10^{-3}	Direct
Drop tower	2 to 9 seconds	10^{-6}	Remote or no access
Random positioning machine	Unlimited	$1g$ in no preferred direction	Direct

direct access to the scientists developing the technique, hence enabling prompt modifications of the set-up (under strict safety regulation) and of the variable parameters. If the technology passes this first test, it should later on be flown on platforms offering longer and more stable microgravity periods.

Parabolic flight campaigns. The principle of parabolic flight consists in flying an airplane describing parabolic trajectories. As illustrated in Figure 7.1, during the parabola everything inside the airplane first undergoes an hypergravity phase as the nose of the aircraft is rising; follows a period of free fall as the plane is changing orientation until its nose is pointing down. This period is perceived inside the plane as a phase of microgravity. It is during those 22 seconds that the absence of felt gravitational pull makes possible the realisation of microgravity experiments. Follows another period of hypergravity, and finally minutes of steady flight before the next parabola. This manoeuvre is typically repeated thirty-one times per flight day, and a campaign consists of three to four days of flight.

As a proof of concept for the powder deposition and solidification process described, two identical prototypes were fully developed and built. They were tested in microgravity during two parabolic flight campaigns.

7.3 Prototypes development

The final assembly of one of the RheoPrint prototype 3D printers is presented in Figure 7.2. The prototypes built can 3D print small objects of maximum diameter 65 mm and height 50 mm, from powder feedstock. The powder container is equipped with venting holes protected by sintered metal filters that regulate the pressure difference inside and outside of the container; those filters allow to use as raw material any particles with diameter larger than 40 µm. The type of energy source used to solidify the powder also determines the maximum temperature allowed, hence the type of raw material that can be used. In the demonstration experiment presented here, polymer powders will be used.

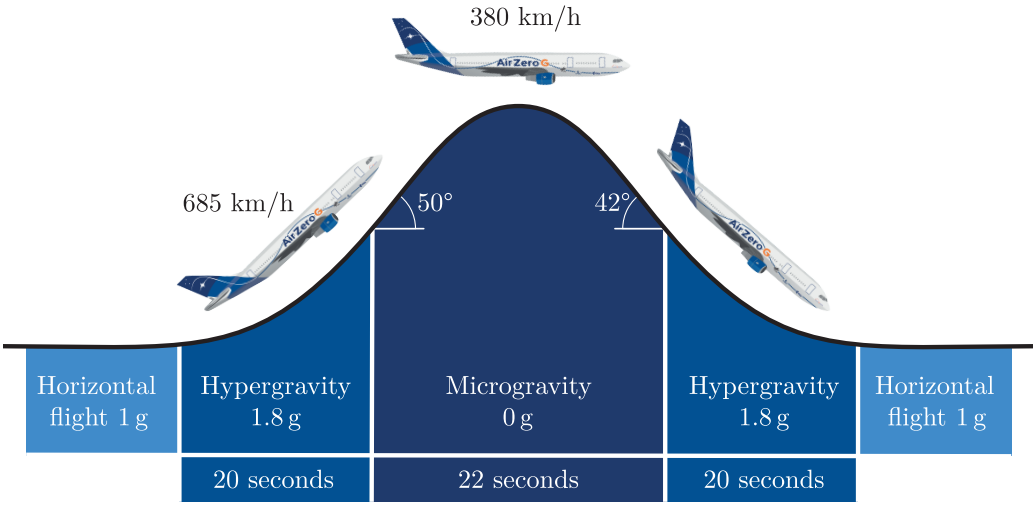

Figure 7.1: Parabolic trajectory executed by the Air Zero-G Airbus A310 aircraft of Novespace. The aircraft image is courtesy of Novespace, and all the information given is this figure are from [252].

7.3.1 Hardware

The powder container is composed of two coaxial cylinders: (A) the inner tube and (C) the outer tube, respectively of diameter 65 mm and 120 mm. On the bottom, it is closed by (D) the vibrating disc, which contains a "window" through which the raw material can be solidified by (E) the energy source, which in this prototype is an infrared lamp, placed underneath the transparent bottom window. From above, it is enclosed by (B) the closing disc, filling the space between the two cylinders and moving down to control the volume of the powder bed. The general structure is formed by 30×30 mm^2 aluminium profiles on which the individual parts are mounted.

A container in motion. The powder bed consists of the entire enclosed volume between the inner tube and the closing disc. The flow of powder is triggered through boundary forces by the movements of the different parts of the container in regard to each other. Therefore, the precise and reliable implementation of those movements is essential for the process performance.

The movements of the different mechanical parts with respect to each other are listed in detail in Table 7.2 and represented in Figure 7.3. First, the inner tube translates vertically to make space for each new layer. At the end of the powder deposition phase, it moves vertically downward to compress the powder underneath. To maintain a constant volume inside the powder containment, the closing disc translates down to counteract the motion of the inner tube; meanwhile, it rotates in alternating direction to probe the packing and keep it from jamming. In order to transport and guide the powder towards the bottom of the container, the inside wall of the outer tube is equipped with a screw conveyor rotating to push the powder down. The shell of the inner tube also rotates, independently of the translation motion, in order to probe the powder flow from within the container.

For the reader looking for technical precision of the implementation of those movements on the RheoPrint prototypes, the exact models and specifications of the motors chosen for each position in the machine are given in Appendix C.

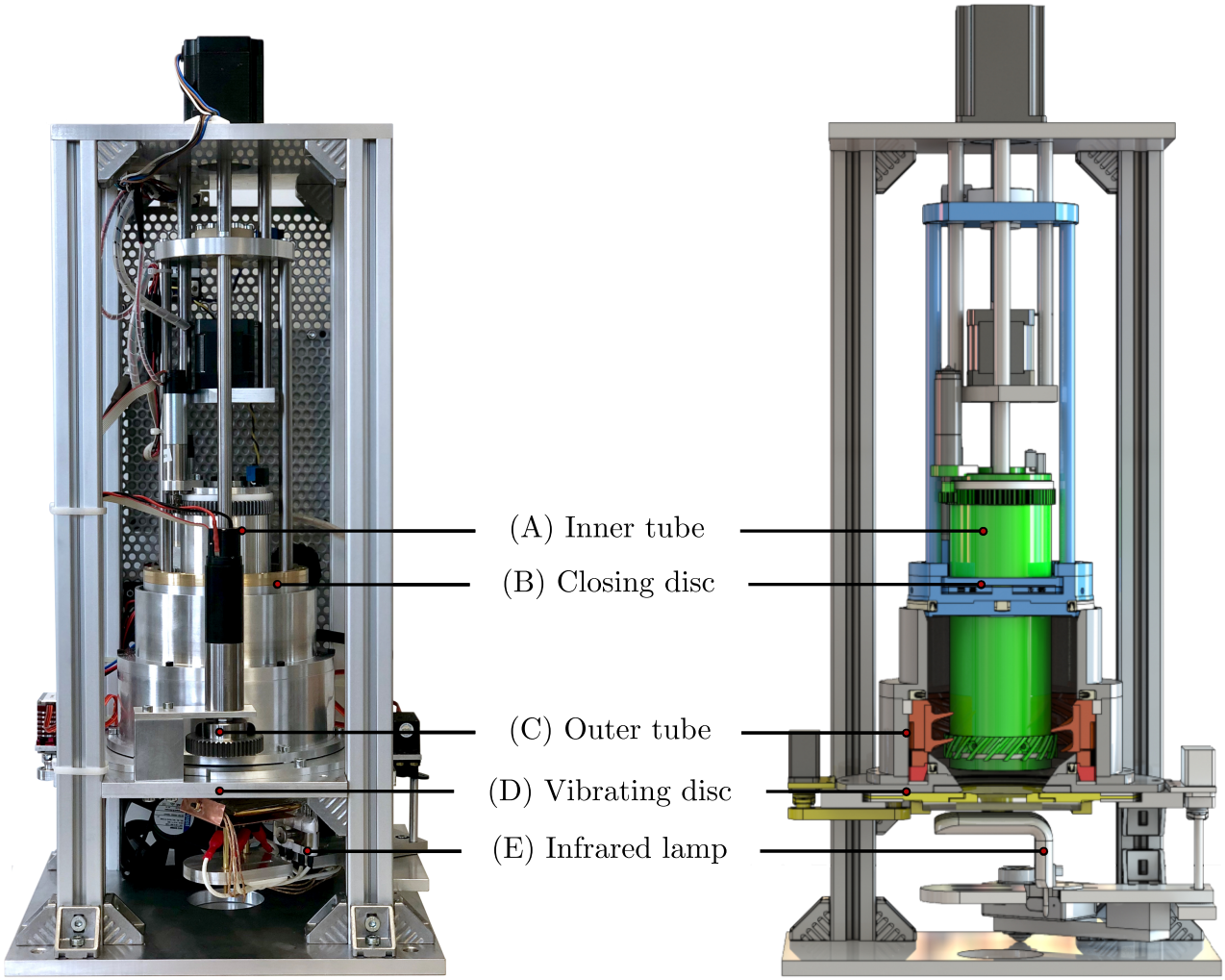

Figure 7.2: (Left) photography and (right) Computer Assisted Design (CAD) image of the prototype RheoPrint 3D printer. The main components of the printer are labeled. On the CAD image, the fixed structure is represented in grey while the moving parts are coloured, each colour representing a movement block.

Moving parts: linear motions. The inner tube and closing disc are the two parts in linear motion. In both cases, the vertical translations must be executed with precision in position: the minimum height of the printed layer determines the precision along the z-axis of the manufactured object, and must be regular as the powder deposition quality depends on the space available under the inner tube. In order to have precision printing, the layer height should be on the order of or lower than ten particle diameters, with a precision of one particle diameter, stable throughout the process. For particles of approximately 80 µm diameter, this amounts to a layer height of 0.5 ± 0.05 mm.

The type of motor chosen to execute the linear movements in the prototype are stepper motors [253]. The working principle of stepper motors is based on multiple toothed electromagnets placed around a gear mounted on the motor's shaft and made of a material sensitive to magnetic field, generally iron. The lateral electromagnets are successively powered to attract the central piece one after the other. But when the gear's teeth are aligned to one electromagnet, they are slightly offset from the next one. So each consecutive activation of an electromagnet

Table 7.2: Variables and parameters corresponding to each moving component of the 3D printer. Fixed variables are fixed depending on the raw material used within the available range presented.

Part of printer	Type of motion	Implementation	Type of variable	State	Operating range
(A) Inner tube	Translation	Spindle nut on threaded rod, driven by stepper motor	Position	Fixed	0 – 50 mm
	Rotation	Gear with transmission, pinion driven by DC motor	Speed	Fixed	0 – 60 rpm
			Current	Monitored and recorded	0 – 430 mA
(B) Closing disc	Translation	Spindle nut on threaded rod, driven by stepper motor	Position	Fixed	0 – 50 mm
			Speed	Fixed	5 – 20 mm s^{-1}
	Rotation	Gear with transmission, pinion driven by DC motor	Speed	Fixed	0 – 60 rpm
			Current	Monitored and recorded	0 – 430 mA
			Duration	Variable	20 — 60 s
(C) Outer tube	Rotation	Gear with transmission, pinion driven by DC motor	Speed	Fixed	0 – 60 rpm
			Current	Monitored and Recorded	0 – 2.4 A
			Duration	Variable	20 – 60 s
(D) Vibrating disc	Vibration	Two servo motors and linear connecting rod	Frequency	Fixed	0 – 15 Hz
			Amplitude	Fixed	0 – 4 mm
			Duration	Variable	20 – 60 s
(E) Infrared lamp	Holding arm: swivel	Holding arm: servo motor with connecting rod to move lamp in position	Power (lamp)	Fixed	500 W
			Temperature (lamp)	Monitored and recorded	0 – 220 °C
			Duration (lamp)	Fixed	20 s

rotates the central gear by one step, as the gear realigns its teeth with the ones of the lateral magnet. This allows very precise positioning, within the precision given by one step of the motor. Stepper motors also have a holding torque, meaning that when the motor is powered but the rotor stationary, it can hold a certain amount of torque without rotating (*cf.* Appendix C). This allows for the parts to hold their position at all times during the process, regardless of the load that might be imposed onto them due to powder movements or gravity-jitter, for example.

The stepper motor selected to control the linear movements of the inner tube, on the bottom of which the object is 3D printed, is equipped with a linear actuator that transforms one full rotation into a linear movement of 1.5 mm. This pitch of the threaded rod corresponds to 200

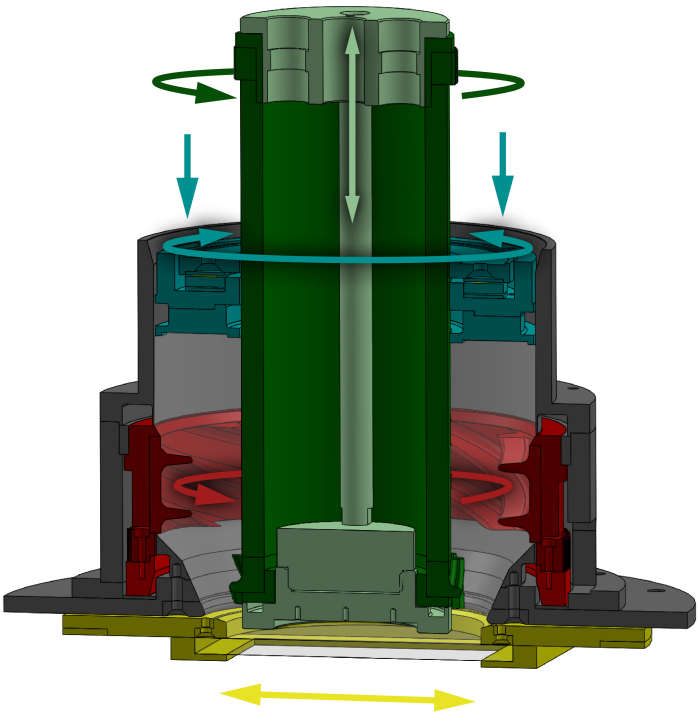

Figure 7.3: Movement of each dynamic part of the assembly (image from CAD file). The coloured parts are in motion at some point during the powder deposition process, each colour block corresponding to the motion indicated by the arrow of same colour, while the grey parts are fixed. The white shading in-between the closing disc and inner tube represents the powder bed. The screw rotation direction is determined by the transport mechanism previously described: the powder is *pushed down* by the rotation of the screw and the steric hindrance of the surrounding particles.

steps per turn, hence to 7.5 µm per step.

An open-loop control like the one implemented to control the stepper motors has a resolution of ± 2 steps, which for our set-up corresponds to ± 15 µm. The spindle nut can undergo a slight backlash at the end of each movement (∼ 20 µm), and there is a mechanical play due to tolerance in the parts manufacturing, which is on the order of 10 µm for such small parts. This gives a final resolution along the z-axis of 50 µm, which is on the order of magnitude of one particle diameter in our application.

Given the way stepper motors create rotation, they are able to achieve precise positioning without the need for a complex control loop: no feedback is needed, as no information on the present state is required to adjust the next state. They are controlled through an open loop where the number of steps to execute is fixed. Consequently, the exact position of the motor is not known at all times, whereas the number of steps (thus the path traveled since an initial position) is precisely determined. For this reason, the position of the inner tube and closing disc must be initialised at the start of each printing cycle, to have control over the starting position of the parts and therefore to know their position at all time. This is implemented through an initialisation step, run before each printing cycle and controlled by a stop-button placed on the upper section of the inner tube that is activated when it reaches its maximum position. We will come back to the initialisation step in more details further in the text.

Moving parts: rotations. In the RheoPrint process, rotations play an important role, as they not only trigger the powder flow but also probe the rheological response of the raw material

while the process is taking place. Therefore, the rotation needs to be done at constant speed for allowing comparison to be made for different materials, and the torque produced to reach this steady velocity must be recorded. This is achieved using brushless DC motors [253], controlled through a velocity-based closed-loop.

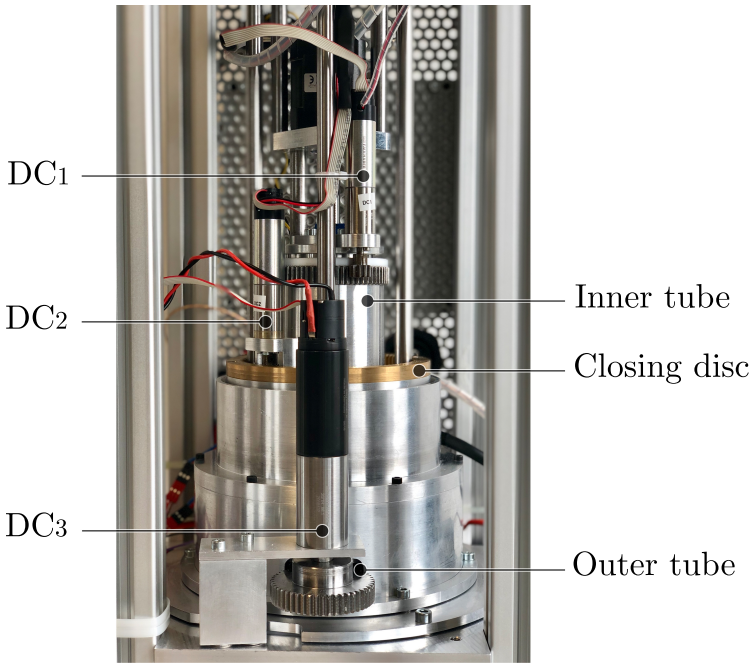

Figure 7.4: Labeled photography of the three DC motors allowing rotation of three parts of the prototype RheoPrint 3D printer: the closing disc, the inner tube and the outer tube.

DC motors convert electrical energy in the form of direct current into mechanical energy in rotation of the shaft. Basically composed of a rotating part, the rotor, and a static part, the stator, the conversion operates through electromagnets, placed circularly on one or both parts; the electromagnets are regularly provided with current in the form of pulses, creating a magnetic field that is inverted (or turned off) at every half-turn of the rotor to force it to continue its rotation instead of turning back to its previous position. Whereas in brushless DC motors the alternation of polarity of those electromagnets provides the rotary motion, in brushed motors, this polarity alternation is made possible by "brushes" in direct stationary contact with the commutator, a rotating cylinder made of many segments placed around the motor's shaft. This causes power loss through friction, deterioration with ageing and voltage drops or possible appearance of sparks. Therefore, for an application where powder is involved and to avoid all risk of powder explosion, brushless DC motors are the best option. As the input current is proportional to the magnetic field it creates, itself proportional to the force that imposes a rotation to the rotor, and hence a torque to the shaft, in the case of a velocity-controlled DC motor there is a linear relationship between the torque developed M and the current i drawn:

$$M = K_m \, i \tag{7.1}$$

where K_m the "torque constant" of the motor, a constant given by the manufacturer (values are given in Chapter 8, Table 8.1).

Each component rotates independently of the others and is therefore controlled by its specific DC motor. Optical encoders are used as time-dependent position sensors, allowing precise sensing of rotation velocity, essential for our velocity-based control. The DC motors are also

each equipped with a corresponding gear-box to allow a small motor (unavoidable in the reduced assembly space available) to reach high torque at low speed.

Moving parts: shaking system. To homogenise the powder layer under the inner tube, the vibrating disc is being shaken horizontally in the xy-plane. The requirements for this movement are the following: it needs to be done with relatively precise positioning, to be able to produce different shaking amplitudes; the maximum amplitude is fixed at 4 mm, which represents 60% of the diameter of the printing surface. Moreover, it needs to have relatively high dynamics: even if the frequency is not necessarily a relevant parameter in microgravity as no force is pushing back the particles after each impulse, the experimental microgravity platform implies limited microgravity time, and the number of "shakes" or repeated impulses is a relevant parameter. Finally, a recurrent problem for microgravity experiments also applies here: the assembly space is very limited. Most linear actuators are voracious in space as the entire space of their amplitude of movement must be freed, and obtaining fast movements yet precise amplitude can result in very expensive options.

The best fit to this description are servomotors, which basically consist of any type of motor (in our case, brushless DC motors) internally coupled to a sensor giving a position feedback to allow precise position regulation. They can travel a circular path of a given, exact angle, repeatedly and at high speed.

The principle employed is depicted in Figure 7.5. Two servomotors are placed perpendicularly on the sides of the vibrating disc. When partially rotated at small enough rotation angles, linear connecting rods transform the partial rotation of the motor's shaft into a linear movement. Alternating the movements of servo 1 and 2, placed respectively along the x- and y-axis, induces a sinusoidal movement of the vibrating disc along both axis and in the end a horizontal vibration of high amplitude. Most important, it ensures that the movement is only induced to the vibrating disc – the rest of the prototype is not affected by the vibration.

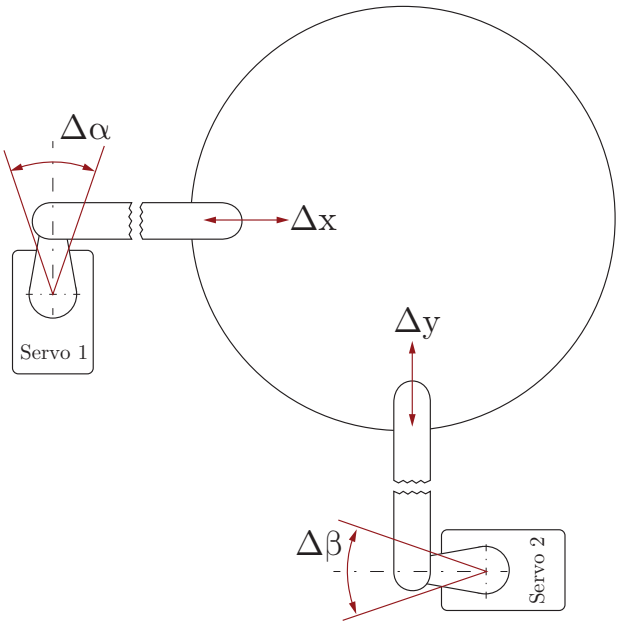

Figure 7.5: Principle of activation strategy applied to the vibrating disc.

The amplitude can be adjusted and controlled precisely within its available range ($0 <$

$A_{x/y} < 4\,\text{mm}$); it is modified by changing the angle of displacement of the servo motors, which can be done directly from code, which means without the need to access the prototype directly. The frequency of shaking is only limited by the dynamics of the servo motors. However, this solution also bears the difficulty that the alignment of the two linear connecting rods must be perfect to avoid blocking the movement.

Seals and powder-tightness. The need to contain the powder within the closed powder bed and the movements of each mechanical part in regard to the others lead to critical sealing points. All those critical points are presented in Figure 7.6. To ensure a safe containment of the powder during the whole printing process, the surfaces moving relative to each other must be sealed with dynamical seals specifically adapted to each position.

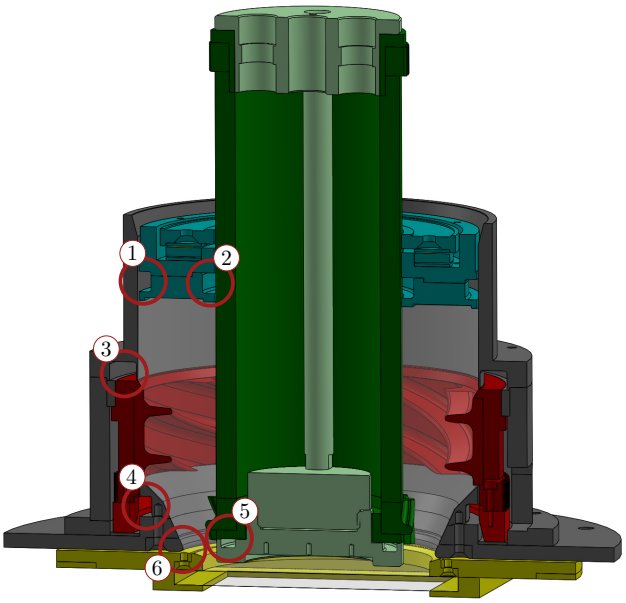

Figure 7.6: Close-up of the transverse section of the inner part of the powder container (image from CAD file) showing the space in between the coaxial cylinders where the powder is contained (clear surface on the image) and the critical sealing points.

The positions defined in Figure 7.6 as (1), (2) and (4) are sealed with a rotary shaft seal (Turcon Variseal M2S from the company Trelleborg). The working principle of rotary shaft seals is depicted in Figure 7.7b for the example of the sealing position (2), between the inner tube and the closing disc. A V-spring presses on a polymer ring, compressing it onto the surface that needs sealing and thus ensuring a lasting contact during the translation and rotation of the closing disc. The volume inside the spring is filled with silicone, to avoid powder to stagnate inside the seal. The sealing ring is made of polytetrafluoroethylene (PTFE). PTFE is a polymer with a very low friction coefficient. In particular, the coefficient of sliding friction μ_k between PTFE and aluminium, the relevant value in our case, is around 0.19 [254]. Such low friction sealing enables to create a powder-tight interface and smooth contact when parts rotate in regard to each other, as all contacts between the two rotating parts happen through the interface of this ring. It is also resistant to abrasion, as rough powders could be harmful to the sealing. Ultimately, it enables a safe dynamic seal between two rotating surfaces without lubricant.

For the sealing in position (3), a similar principle is used, but with a sealing surface axial

to the movement. (Here the sealing ring used is the Turcon Variseal HS from Trelleborg.) The polymer used for the sealing ring is also PTFE, hence it has the same characteristics as the one used for the rotary shaft seal: a low friction coefficient and good resistance to abrasion. Figure 7.7a shows the working principle of this axial flange seal, with a helical spring to keep constant contact, between the screw-conveyor part of the outer tube and the outer shell, which corresponds to the static part of the outer tube.

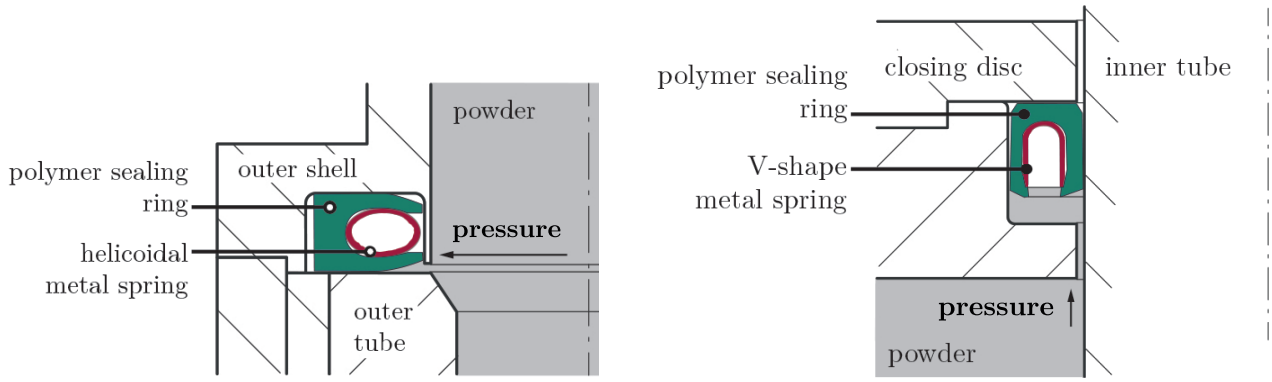

(a) Position (3) **(b)** Positions (1), (2) and (4)

Figure 7.7: Working principle of the axial flange seal, with a helical spring forcing constant pressure on the seal.

For position (5), the sealing used is a rubber O-ring coated with PTFE. The rubber ring is put under normal pressure (applied by the screw fastening between the inner tube and the printing substrate) to fill the entire volume available.

Finally, position (6) between the vibrating disc and the bottom of the powder container must be sealed as to avoid powder from penetrating between the two parts while the vibrating disc moves back and forth horizontally. A flexible silicone cloth is used to seal the gap between the fixed socket (grey in Figure 7.8) and the moving disc (yellow in Figure 7.8), clamped on the several positions. Figure 7.8 shows the maximum positions and of the vibrating disc. The flexible sealing cloth is depicted in red at the different positions of the mechanical pieces.

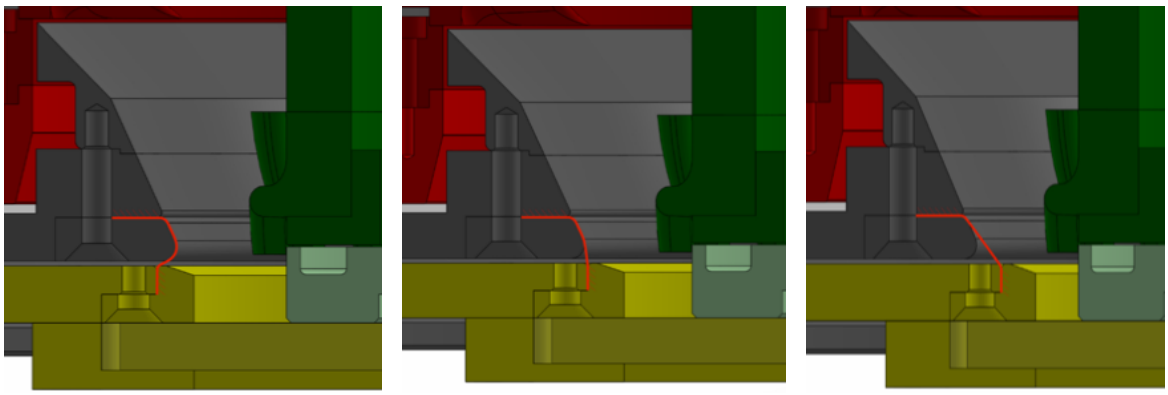

(a) Minimum position **(b)** Middle position **(c)** Maximum position

Figure 7.8: Principle of flexible sealing cloth joining the vibrating disc (represented in yellow) and the fixed outer-tube socket (in grey), in its three typical positions.

7.3.2 Printing procedure

The full printing procedure is summarised by Figure 7.9, which can be used as a reference for the reader throughout the following description.

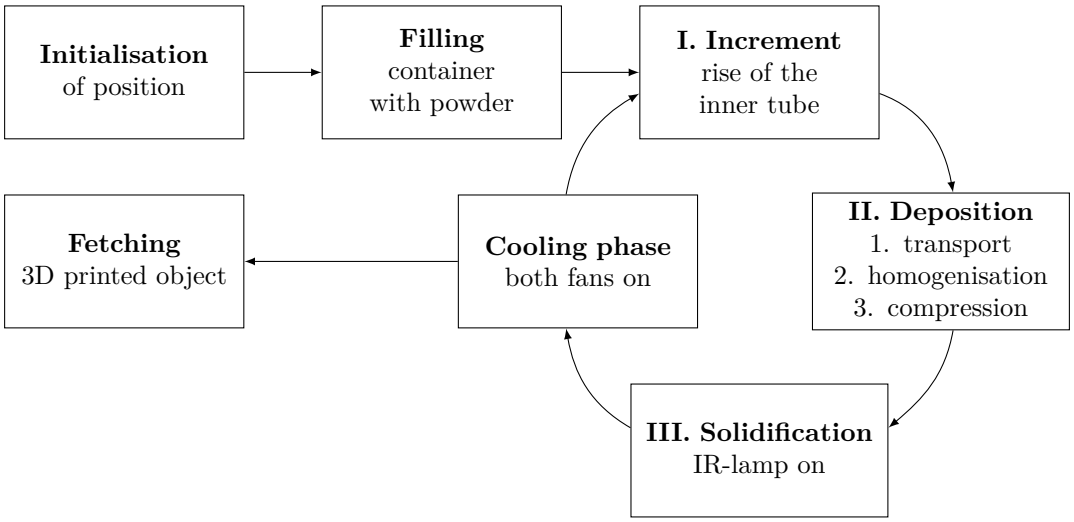

Figure 7.9: Diagram of the printing process, including steps (I) to (III) previously described, and an additional cooling phase necessary for this implementation of the process.

Initialisation. The algorithm controlling the prototype 3D printer comprises an initialisation step, that represents the necessary first step of a printing cycle. In order to describe the movement of the machine during the initialisation step, Figure 7.10 presents the different horizontal stages of the prototype, as well as the two stop-buttons used to provide a repeatable initialisation position to the machine.

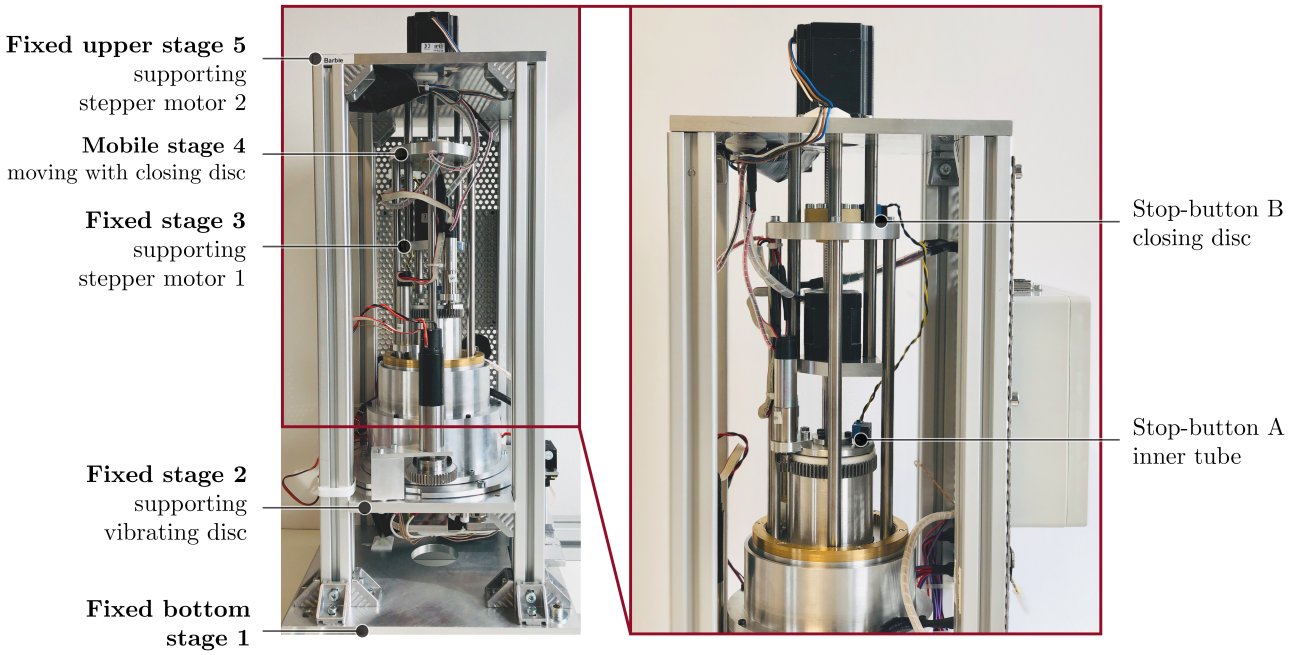

Figure 7.10: Prototype 3D printer with labeled stages and stop-buttons used for initialisation of the prototype position. The left picture is taken from the front of the prototype, while the picture on the right corresponds the side-view (projection from the right).

The initialisation step begins by the initialisation of the stepper motor 1, commanding the linear movement of the inner tube along the z-axis. It rises until reaching its maximum position, where its stop-button (labeled stop-button A in Figure 7.11) is pushed by contact against stage 3. It is then lowered by the given length for the substrate to be directly in contact with the sintering window, which is its final filling position, that it will keep until deposition of the first layer. Then starts the initialisation of stepper 2, controlling the z-axis linear movement of the closing disc. It is being raised concomitantly to the mobile stage 4, as they are permanently attached at fixed length by three metal rods. Therefore, stepper motor 2 raises both stage 4 and the closing disc by rotating the threaded rod that goes though the spindle inside stage 4. This movement takes place until the top of stage 4 reaches the bottom of stage 5. At this point, stop-button B, placed on top of stage 4, is pressed against stage 5, indicating the reference position. For this part of the set-up, the reference position corresponds to the filling position of the closing disc, so the state in which the prototype is open, ready to be filled by base-material.

Filling procedure and preparing printing substrate. On a final commercial implementation of the process, the filling procedure would be automated through a conveying fluidised bed, enabling homogeneous repartition of the powder regardless of the gravitational attraction and fully automatising the powder handling. However, on the demonstrators built, the filling is done on-ground by the operator before each printing cycle.

The exact amount of raw material needs to be introduced inside the printing bed, left accessible by the gap between the outer tube and the closing disc, visible in Figure 7.11. In order to homogenise the packing as the container is being filled, rotation of the screw conveyor and of the inner tube can be activated intermittently during the filling procedure. Once the right packing fraction is reached inside the container, it is sealed by the descent of the closing disc, rotating in alternating directions as it goes down. The rotations of the screw conveyor and inner tube also take place at the same time to keep the packing in movement and avoid jamming.

Once the filling procedure is complete, the container is full of densely packed powder, and the printing substrate directly resting against the solidification window. In this state, the container can be transported safely. Then, the printing process itself can start.

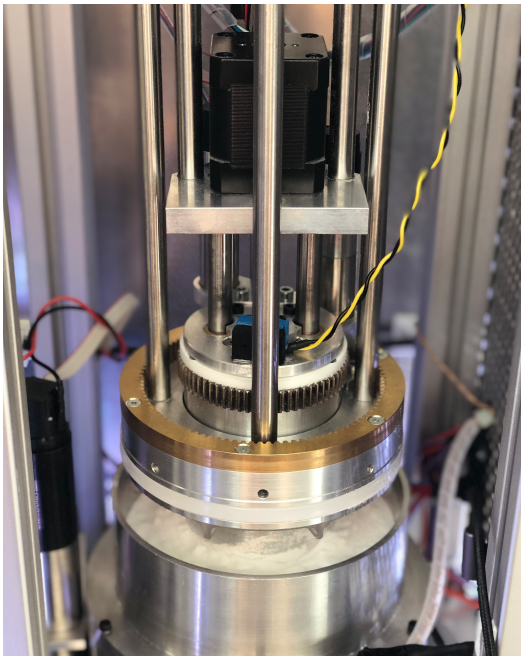

Figure 7.11: Prototype in filling position, open and filled with raw material.

Printing procedure *per se*. Without surprise, the printing procedure follows the powder deposition and solidification method described. After solidification, a cooling phase is added to cool down the window right after the power source has been turned off – in our case an infrared lamp. The glass used, as we will see below, is transparent to infrared light. However, in the prototype the heat absorbed by the powder while it is solidifying is transmitted by contact to the window; therefore the cooling phase is important to ensure that the newly solidified layer be back to a temperature at which it is solid, avoiding viscous adhesion with the glass window.

Fetching the printed object. After completion of the printing process, the prototype is opened to fetch the printed object. The entire top part of the prototype can be detached from the structure, as shown in Figure 7.12a. The printing substrate, shown virgin in Figure 7.12a, is attached to the inner tube by a M36×2 thread; it can therefore easily be disassembled from the rest of the top-structure, as shown on Figure 7.12b, and replaced by a new virgin one for the next printing cycle.

(a) **(b)**

Figure 7.12: Printing substrate of the prototype 3D printer. (a) Top part of the prototype, that can be removed from its structure to remove the printing substrate or install a virgin one. (b) The printing substrate can be simply screwed and unscrewed from the inner tube, in order for the experimenter to easily fetch the 3D printed sample.

7.3.3 Controls & electronics

Each RheoPrint prototype is composed of multiple microcontrollers and motor drivers controlling two stepper motors, three DC motors, three servo motors, an infrared-lamp as well as multiple temperature sensors and cooling fans. Powering and controlling all those devices concomitantly with the precision needed to obtain reproducible and reliable results in a relatively complex combination of hardware and coding strategies.

The octopus-control model for real time computation. As the octopus, well-endowed with nine brains – a central one controlling the global nervous system, and one small "sub-brain" per tentacle [255], controlling its specific movement and allowing each arm to move with independence yet coordination – the RheoPrint prototype 3D printer is controlled by a main microcontroller (microcontroller 1), in constant communication with multiple sub-systems. The workload can thus be divided between those different entities. The role of the main microcontroller is to go through the basic steps of the printing process, as summarised in Figure 7.9, and for each step, to send the specific command to activates the sub-system in due time. The main algorithm executed by microcontroller 1 is summarised by the diagram presented in Figure 7.13. The exact tasks executed by the main microcontroller are listed below.

This multi-stage division of the workload allows for parallel execution of multiple tasks in a reduced time, as each task, requiring a certain amount of computing power, would otherwise

block the controller for a finite amount of time – short according to human time-scale, yet tangible for the program's effective operation. This control model, devoting a determined execution duration to every routine, is required for real-time computation, which is necessary for process monitoring.

Main algorithm controlling the 3D printing process: finite-state machine. The prototype is controlled through a main algorithm, executed by the main microcontroller, consisting of the different steps summarised in Figure 7.13 and functioning following the finite-state machine (FSM) mathematical model of computation [256].

A finite state machine or automaton can by definition only be in a finite number of states. Each state has a strict definition, which in our case represents a given action or set of actions. The transition from one state to another happens in response to a specific set of inputs. Certain event or events trigger the transition from state m to state n, which means taking given actions different from the ones in the different state, until a condition be fulfilled or an event received. The FSM computational model provides a rigid structure where the sequence of actions to perform is predefined; thus, wrong inputs cannot have severe consequences as only a specific event or combination of events can enable a transition to the following state. The prototype is always in a known state, and the user knows at all times that only a given sequence of actions will trigger the transition. As the prototype 3D printer built is not a fully automatised experiment but relies on interactions with the user, it is essential that wrong inputs be ignored. Moreover, it is a computational model that can easily be modified and extended, well-fitted for prototype design.

The complete program controlling the machine is available on-demand. The different states implemented on the prototypes are presented in Figure 7.13, as well as the event E triggering the transition to the next state and actions A taken as each state starts.

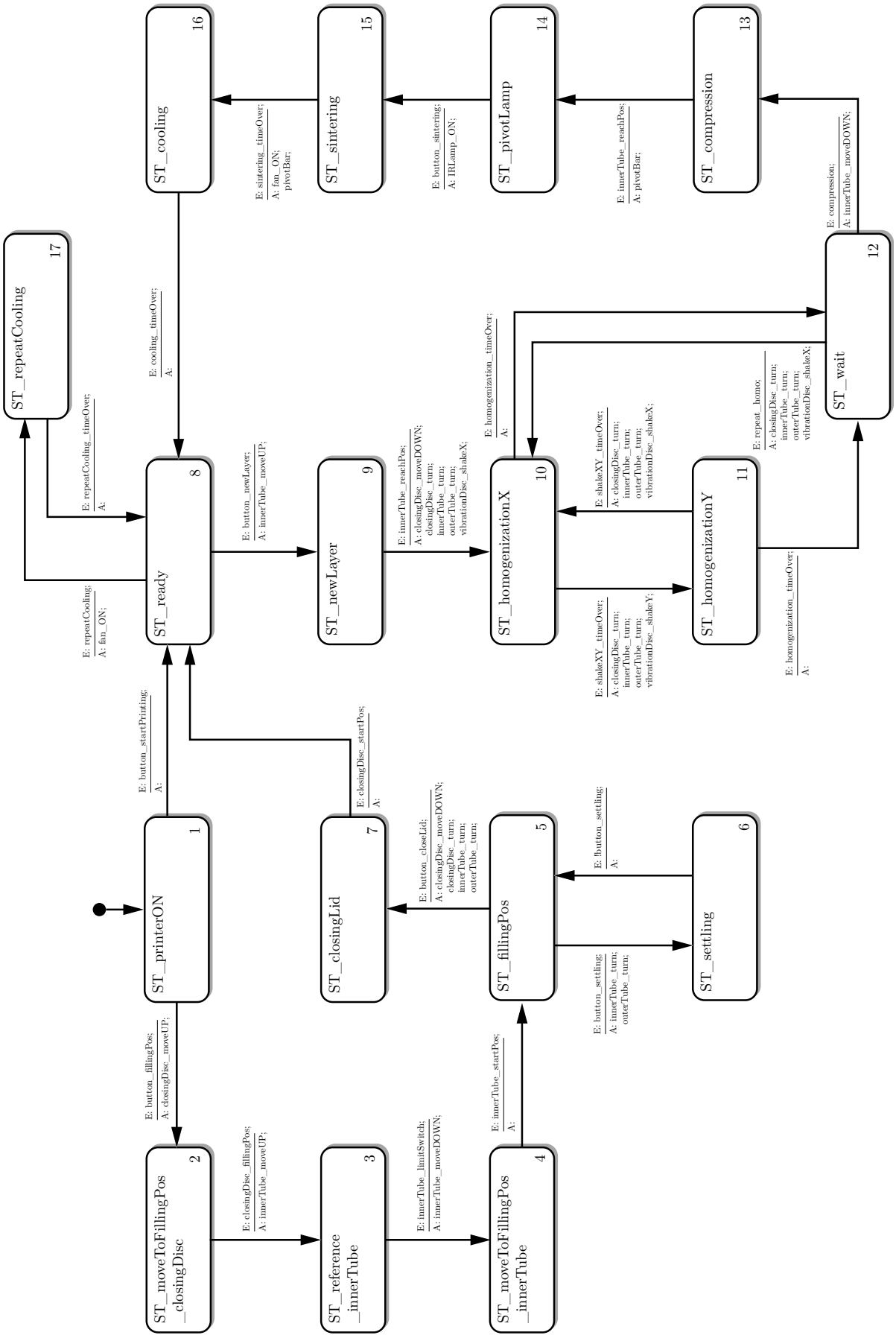

Figure 7.13: State diagram summarising the program controlling the apparatus, based on the finite-state machine mathematical model of computation.

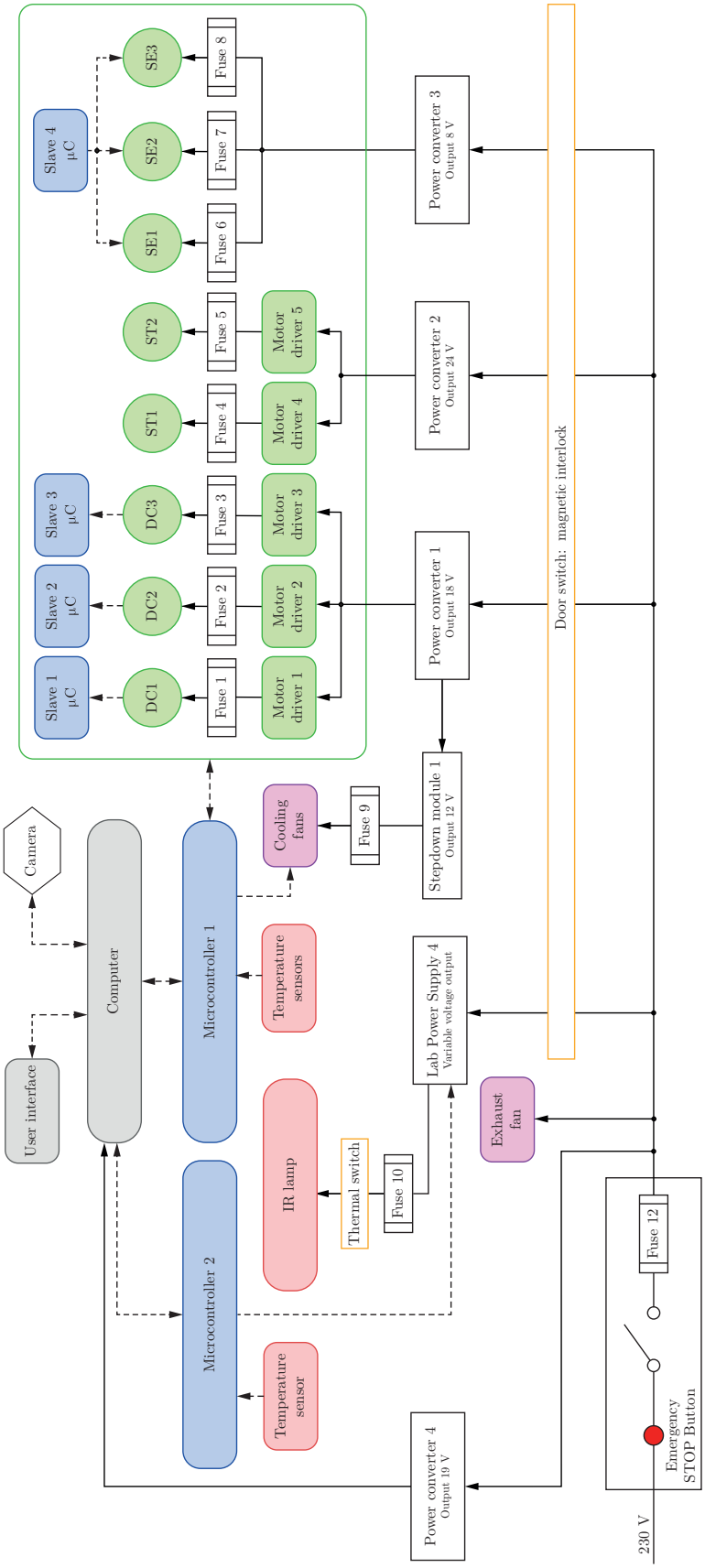

Figure 7.14: Principle block diagram of electronic components forming one RheoPrint prototype 3D printer. Dashed lines represent the exchange of information or control signal and solid lines the powering of the different devices. "SE" are servo motors, "DC" are DC motors, "ST" stepper motors and "μC" sub-microcontrollers. All microcontrollers are powered by power convecter 3.

Concrete implementation of the controls. Figure 7.14 shows a block diagram of the electronic components forming one printer. Microcontroller 1 executes the main algorithm controlling the general state of the printer. This duty involves communication with multiple devices, summarised in Figure 7.15a and consists of the following tasks:

- Communication with the three sub-microcontrollers 1, 2 and 3, corresponding to the three DC motors (the sub-microcontrollers are labelled "slave microcontrollers" in Figures 7.14 and 7.15a, as such denomination is currently used for dual systems with asymmetric control or communication). Each sub-microcontroller has the one and only task to be in constant communication with its respective encoder, that senses the position of its DC motor and sends it to the sub-microcontroller at a frequency of 30 Hz; from this information, the sub-microcontroller calculates the rotation speed and sends it to the main microcontroller.

- From the information on the current speed of each DC motor, the main microcontroller regulates their velocity in a closed control loop by modulating the signals sent to the motor drivers of DC motors 1 to 3.

- The current drawn by DC motors 1 and 2 to reach this required speed is recorded by two current sensors (labelled CS 1 and 2 in Figure 7.14), to be converted into the torque displayed by those two motors. This information is displayed on a control computer through the user interface, that we will come back to in the subsequent text.

- The last sub-microcontroller, labelled "slave microcontroller 4" in Figures 7.14 and 7.15a, controls the movements of the three servomotors used. Two are used for the the shaking system, turned on intermittently by a signal of the main microcontroller to sub-microcontroller 4; the third servomotor swivels a rotating arm bearing the energy source, swapping it from its position right under the solidification window during the solidification step to away from it during all the other steps of the printing procedure.

- To ensure a continuous air circulation and therefore heat dissipation through convection even in microgravity, two fans are constantly blowing air from the bottom side of each prototype (visible on Figure 7.19 and 7.20). To actively cool down the solidification window during the cooling phase, the two fans are turned to their maximum speed by the main microcontroller.

- The two stepper motors are controlled through an open control loop by the master microcontroller communicating with their respective motor driver.

- As will be seen in more detail when discussing the solidification system, multiple temperature safety measures are implemented, among which multiple temperature sensors on and around the infrared lamp; one of them is connected to the main microcontroller and provides the temperature of the infrared lamp at all time, to display it on the user interface.

- Another information given by the main microcontroller is the current stage of the process. It is displayed on the user interface at all time.

- Finally, some inputs are given to the microcontroller. Two stop-buttons or end-switches enable the initialisation of the position of the closing disc and inner tube. A door switch placed on the rack containing both prototypes during the parabolic flight campaigns serves as a safety measure to turn off by code all the possibly moving and heating components.

This measure is taken to avoid any health hazard to the experimenter. Finally, some steps of the process are submitted to external input to start. For example, on parabolic flight, start of the powder deposition must coincide with entry in microgravity. Such input is given by the experimenter through different buttons, redundantly implemented physically on a remote control handset and digitally on the user interface.

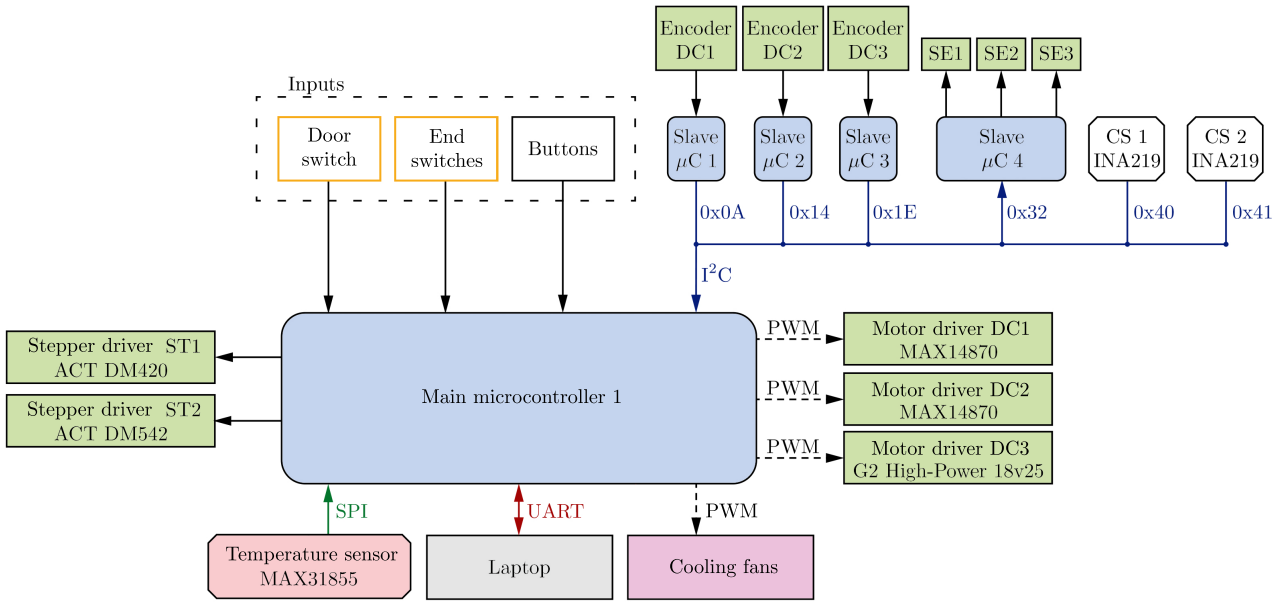

(a) Main microcontroller

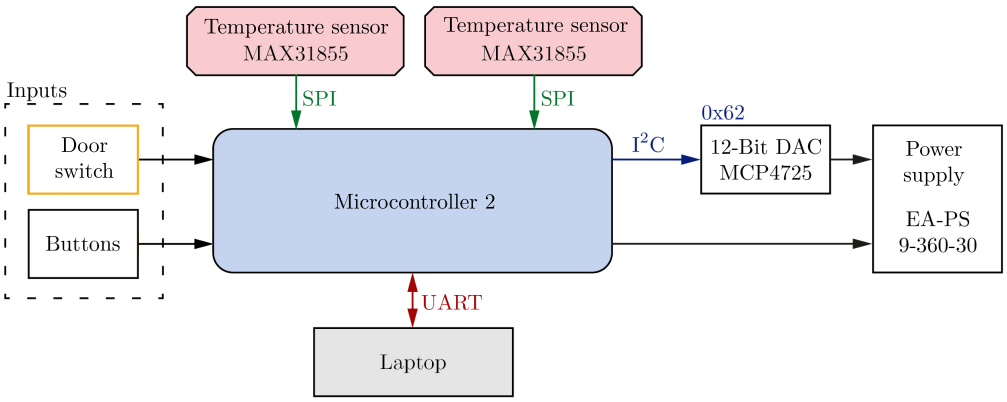

(b) Secondary microcontroller

Figure 7.15: Devices communicating with (a) the main microcontroller and (b) the secondary microcontroller, that function independently of each other. The communication channel deployed between the microcontrollers and each of their subordinated devices are also specified.

For the control of the infrared lamp, a second independent microcontroller is used. Its connections to other devices are schematised in Figure 7.15b. It is fully dedicated to the control of the infrared lamp used as an energy input to solidify the raw material. It does so by controlling directly the power supply powering the lamp, hence regulating the lamp through its input voltage. The implementation of this dedicated microcontroller 2 is a safety measure, as the controller devoted to the infrared-lamp control cannot be blocked by another task and miss critical information. Two independent temperature sensors record the temperature on the

lamp's side at all time, to give redundant information on the thermal state of the solidification system. If the temperature on the direct surrounding of the lamp reaches threshold value (fixed at 150 °C), the microcontroller provokes a system cut and the current input of the lamp is directly turned off.

Electrical control box. The digital conceptualisation of the control detailed above concretises into two electrical control boxes. Printed Circuit Boards (PCBs) were designed and printed to hold and connect the electrical components needed for driving and controlling each prototype. The base design of the PCBs is given in Appendix D.

As the main microcontroller, an Arduino Mega is used. The main PCB acts as an interface between the main microcontroller and its subordinated components; the electric box containing it is represented in Figure 7.16a. It also contains all the necessary fuses, with an easy access from the top of the box. A second PCB was printed to nest the secondary microcontroller, and the amplifiers serving as interface between the thermocouples and the microcontroller. This secondary electric box is placed directly on the prototype for the thermocouples to reach their desired position.

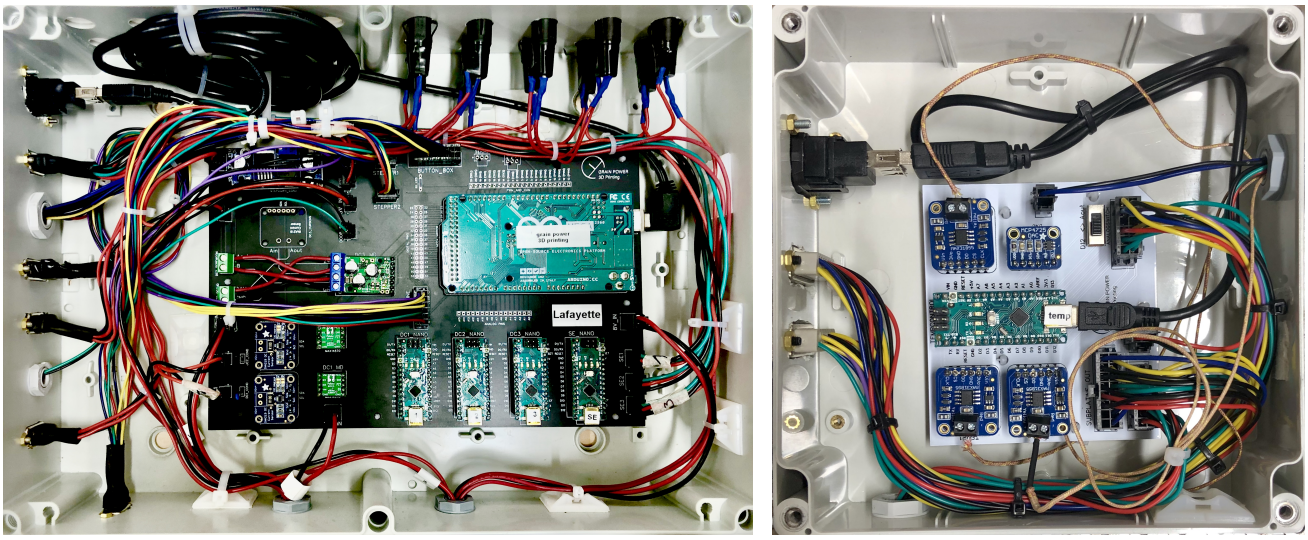

(a) Main electric box **(b)** Secondary electric box

Figure 7.16: Electric boxes containing the PCBs and electronic components controlling each Rheo-Print prototype.

7.3.4 Solidification system

The solidification step, despite not being the main focus of this work, will condition our ability to evaluate the proper functioning of the described process, as it fixes in time the state of each new powder layer at the end of the deposition step. Therefore, the design requirement for the choice of an energy source is mainly that it solidifies a large surface of powder in a short amount of time, without altering the state of deposition. In order to keep the quality of the deposited layer intact, sintering of the powder layer is preferred over melting, which would blur the state of the deposition by liquefying the entire surface.

Solidification mechanism involved in sintering. Sintering is a process that transforms a discrete solid into a coherent material, but which doesn't involve complete melting; it takes

place at a temperature lower than the bulk material's melting point. A complete description of sintering and its relevant parameters is available in [257]. In our case, the granular material used as base material is a polymer, and no binder is added, in an perspective of closed-loop recycling. The type of solidification implemented is "liquid-phase non-reaction sintering": material densification happens through a liquid phase surrounding the grains, created by surface melting of the particles. The material composition stays unchanged throughout the sintering process.

Under the heat flux emitted by the energy source, the temperature increases around the grains; once past the glass transition temperature, the the grains' outer surface softens to form a microscopic layer where the molecular mobility is high. As temperature increases, this micro-layer eventually becomes molten: its viscosity has decreased enough to facilitate material migration at the interface, now constituted of a liquid polymer phase.

Then happens the first step of liquid-phase sintering: rearrangement. Given that the diameter of the grains has decreased, and that the liquid phase acts as a lubricant, they can slide on one another to rearrange into a more compact lattice. This compaction happens through the following mechanism: to reduce their surface energy, the low-viscosity surfaces in contact merge, forming a liquid-polymer meniscus linking the solid grains together. This phenomenon is called necking; it is represented in Figure 7.17a. From this point on, the surface tension γ of the liquid neck will drive the material exchange: in order to minimise free surface, capillary forces bring the grains closer together. Unlike in Figure 7.17, in a packing every grain has multiple neighbours, hence the capillary forces tend to compact the entire packing and reorganise the grains in a closer arrangement. This phenomenon involves a reduction of volume due to the densification of the packing, hence the application of a pressure is generally beneficial to control the direction in which the shrinkage happens. Industrial processes where a specific shape and high dimensional accuracy are needed can rely on isostatic hot pressing. In our case, densification is achieved by compression of the layer between the previously deposited material and the solidification window *during* sintering.

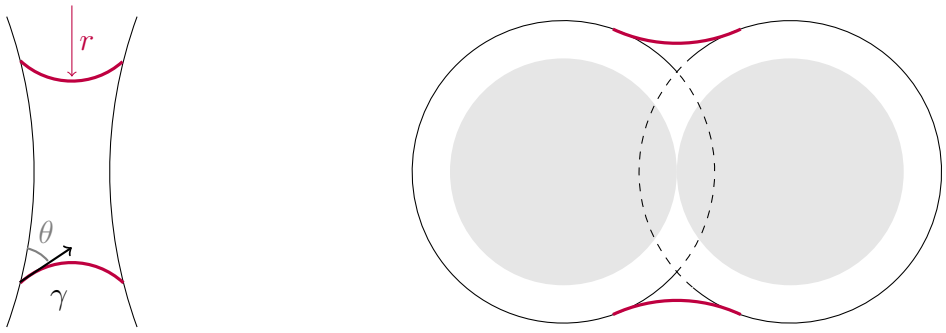

(a) (b)

Figure 7.17: Principle of liquid-phase sintering: a soft corona appears around each grain, and this molten layer forms necks between neighbouring grains to decrease their free surface. (a) A liquid phase meniscus of radius r has formed between the grains; the liquid-gas surface tension γ will bring the centres of the grains closer by capillary forces, increasing the angle θ as the ratio of molten material increases. (b) At the end of the sintering process, two grains have coalesced, but the core of the particles (in grey) stays untouched.

Subsequently, the grains' coalescence occurs: material from the solid part is dissolved and

migrates towards the interface solid-liquid-gas. This dissolution-precipitation mechanism tends to increase the quantity of material in the interface, thus increasing the curvature of the meniscus (r in Figure 7.17a) and thereby contributing to the densification of the granular bed. The grains grow by absorbing smaller grains, fully liquefied. Figure 7.17b shows two grains partially coalesced.

The sintering temperature is not a material's core-property: in order to have high material mobility, it should be higher than the glass transition temperature; to avoid complete melting, it must be lower that the melting point. Within this range, the desired state of porosity determines the sintering temperature and time. For the PS powders used in this work, the relevant melting and glass-transition temperatures can be found in Table 2.1; it is seen that the working range of the apparatus, up to 220 °C, is well within the range of sintering of the powders used.

Surface energy source. To decrease the solidification time without reducing the area solidified, the layers are sintered on their entire surface at once. To do so, a surface energy supply is needed. The energy density displayed by the source must be constant on the entire area sintered, to avoid creating a heterogeneous state of solidification, with some zones only partially sintered and some zones fully molten.

The energy source chosen is the Quattro Infrared emitter by Heraeus, shown in Figure 7.18. Its technical specifications are given in Table 7.3. It provides energy in the form of short-wave infrared (IR) light to a surface of 50×45 mm^2 at a power of 500 W. Its bottom surface is gold-coated to reflect all IR light upwards. This high power displayed homogeneously allows to sinter the full layer within 20 seconds. Besides, the heated surface is included within the substrate area, so that a rectangular object will be printed on the substrate.

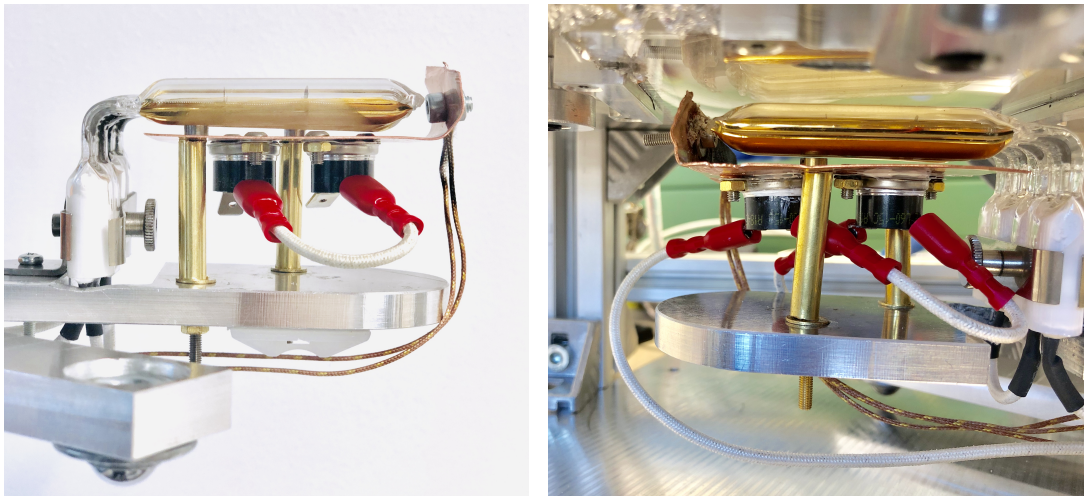

(a) **(b)**

Figure 7.18: The IR-lamp used as power source, (a) mounted on its holder and (b) inserted in the bottom area of the RheoPrint prototype 3D printer.

A holder was designed to support the IR-lamp, visible in Figure 7.18. The holder comprises a copper plate serving as a heat-sink and as a probe to attach the temperature sensors, providing information on the temperature in the direct surroundings of the infrared-lamp. Copper was used for its high thermal conductivity (400 W m^{-1} K^{-1}); the thin plate (0.5 mm) allows to monitor a temperature close to the one of the bottom of the energy source. The lamp is

Table 7.3: Technical specifications for the Heraeus Quattro IR emitter.

Maximum power	500 W
Voltage	115 V
Heated surface	$50 \times 45\,\text{mm}^2$
Infrared spectrum	Short-wave infrared (wavelength 1 to 3 µm)

also mounted on a pivoting arm in order to swivel out of its sintering position as soon as the solidification step is over, leaving the zone free for the image recording to take place.

To allow for *in-situ* monitoring of the deposition process, a camera is placed under the prototype and a hole in the base-plate allows to record the deposition step from the bottom. In order to leave this field of vision empty, the lamp, placed on its pivot arm, is pivoted away from the window at the end of each solidification step. The alternating positions are shown in Figure 7.19.

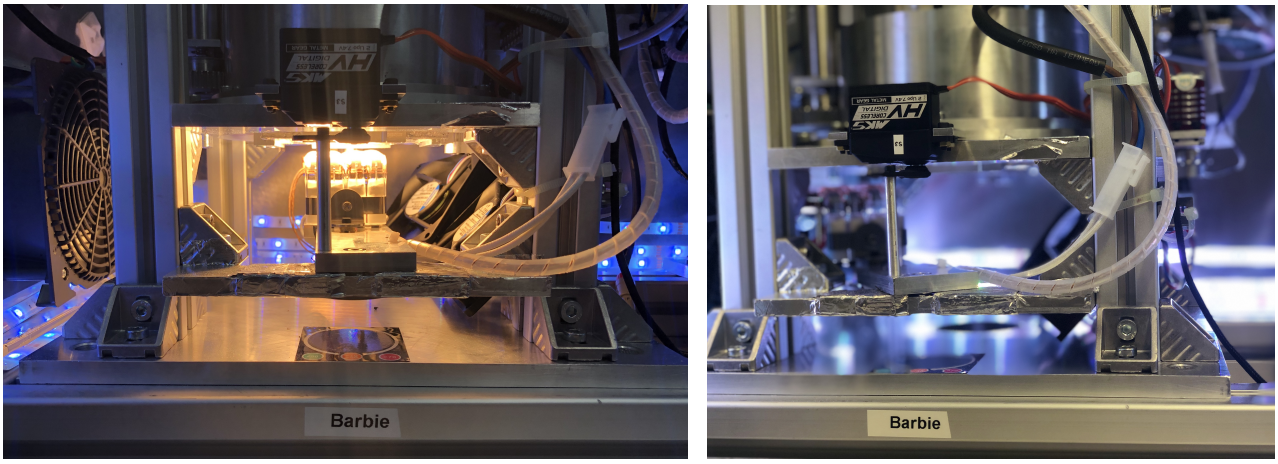

(a) IR-lamp during solidification. **(b)** IR-lamp in pivoted position.

Figure 7.19: Two positions of the IR lamp: (a) placed directly under the solidification window and (b) pivoted to allow *in-situ* monitoring of the powder deposition.

Control of the energy source. The IR-lamp is controlled through a stand-alone motherboard that commands the power supply powering the IR-lamp. The power supply is a programmable laboratory power supply of the brand Elektro-Automatic (EA-PS 9-360-30); it offers a voltage range of 0 to 360 V and current range of 0 to 30 A. The power supply is controlled by the secondary microcontroller, which constantly checks the following parameters:

- The time: an internal microcontroller timer ensures that the lamp is turned on for an interval of 20 seconds from the moment it is activated by the user triggering the solidification phase by pushing the sintering button.
- The temperature recorded by a thermal sensor placed on the upper side of the infrared-lamp.
- The voltage of 115 V and the current, at a fixed value between 0 and 4 A.
- A magnetic interlock automatically turns off the power supply if the protective cover inside

which the experiment takes place is open – this safety containment of the experiment will be discussed in more details in Section 7.4.

The components placed on the bottom of the prototype, in the vicinity of the IR-lamp, are shown in Figure 7.20. During the sintering phase, the lamp is turned on at constant power for 20 seconds. At the end of this period, the lamp is turned off and the fans double their turning rate for one minute in order to dissipate the heat and increase the cooling rate.

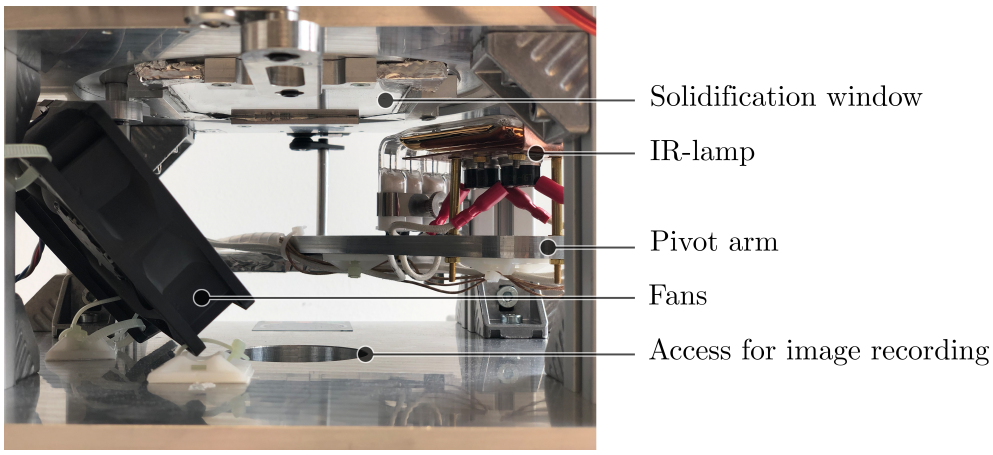

Figure 7.20: Bottom part of the prototype: at the bottom of the powder container, the solidification window creates the interface between the raw material and the energy source. The IR-lamp can pivot in and out of its solidification position by rotation of its supporting pivot arm, swivelling out of the camera field of vision. The camera is placed under the prototype and records through a circular aperture created in the bottom plate. The fans ensure a constant air flow, and increase the cooling rate after the solidification step.

Heat control systems & protection against fire hazard. Multiple heat control systems are implemented for safe use of the experimental set-up and for complying to parabolic flight safety regulation:

- The motherboard directly controlling the lamp is equipped with two temperature sensors, placed directly on the side of the lamp (position (c) in Figure 7.21), which turn off the lamp if the temperature recorded is higher than 150 °C.
- The motherboard controlling the entire process is also equipped two temperature sensors, one placed by the side of the camera (position (e) in Figure 7.21), which turns off the lamp if the temperature recorded is higher than 100 °C. The other sensors placed around the lamp give the possibility for the experimenter to monitor by hand the temperature change, as the temperatures are displayed live during the experiment on the control laptop.
- Two thermal switches are placed under the lamp, against the copper holder. They are placed under the IR-lamp (position (d) on Figure 7.21) and interrupt the circuit at 80 °C.

The thermal switches and temperature sensors are visible on Figures 7.20 and 7.18. The temperature rise during a normal heating cycle was recorded to provide "normal-use values" for choosing the safety temperatures; the result of this preliminary experiment is shown in Figure 7.21. It also shows that the cooling time necessary to reach a temperature of 40 °C is approximately 40 s.

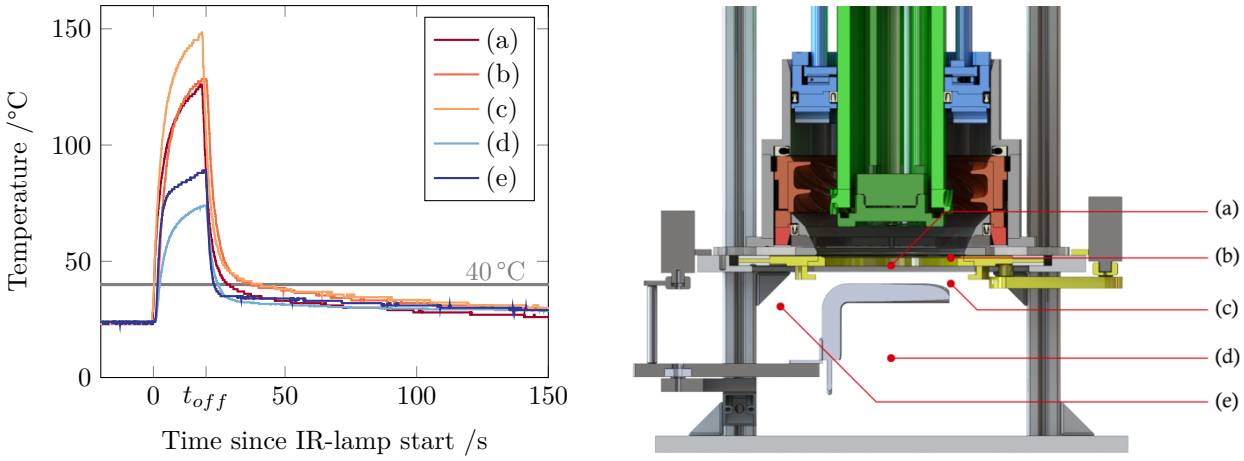

Figure 7.21: Preliminary experiment result: temperature evolution on normal-use at selected spots on the prototype. (Left) Temperature evolution recorded during a heating cycle of 20 s (started at $t_0 = 0$ s, for temperature sensors placed around the IR-lamp. (Right) Position of the different temperature sensors.

As temperature sensors, type-K thermocouples are used, which corresponds to nickel-chrome vs. nickel-aluminum systems. They have an operating range from −200 °C to 1250 °C with a resolution of 2.2 °C over the complete range, which is sufficient for this application where temperature is recorded as a safety control and not as a solidification monitoring measure.

7.3.5 Solidification window

The solidification window is a key component for the operational function of the apparatus. It is a plate of 100×100 mm^2, height 5 mm, which creates an interface between the energy source and the raw material. A top view of the prototype bottom part sectioned at the height of the solidification window is presented in Figure 7.22.

The solidification takes place *through* this window: on one side is the material to solidify, on the other side the energy source. Failure of this component would be catastrophic, as it would lead to the powder being in direct contact with the energy source, which implies a fire hazard by ignition of the powder. Therefore, the design requirements for the solidification window comprise the following points:

- It must be transparent to infrared light, and in particular short-wave infrared (wavelength $\lambda = 1$ to 3 µm) emitted by the energy source.
- It must withstand temperature up to 300 °C, which represents the maximum temperature recorded at the solidification window during preliminary testing, multiplied by a safety factor of 2.
- It must have a low coefficient of thermal expansion to avoid failure due to internal thermal stress during solidification.
- It must be transparent in the visible light spectrum (wavelength $\lambda = 0.4$ to 0.7 µm) to allow the user to observe the material deposition step as it is taking place through video recording.

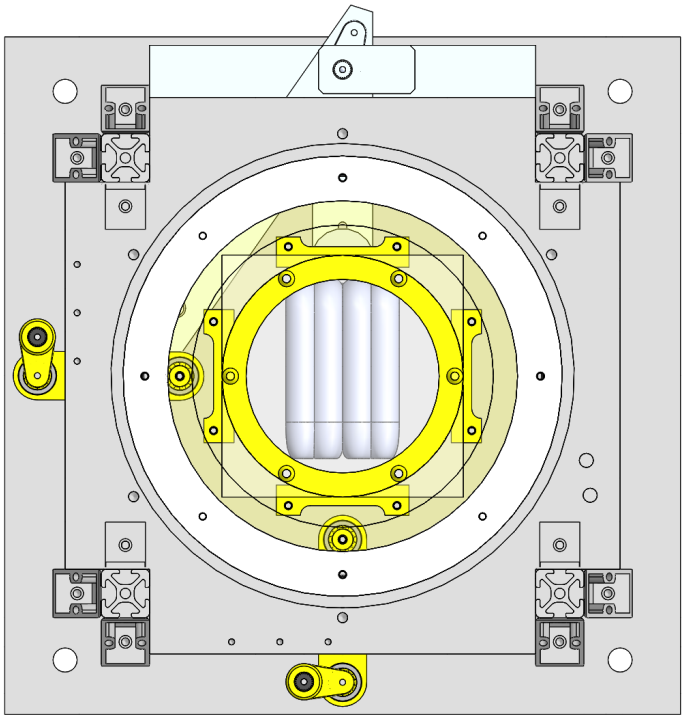

Figure 7.22: Top view of the prototype section. The solidification window is the transparent square placed in the centre of the vibrating disc, on top of the IR-lamp. It is held in place by four support brackets clamping it to the bottom of the vibrating disc. The parts in yellow are the parts in motion during the disc's vibration, while the parts in grey are the static support.

Among materials transparent in the visible and IR spectrum, a glass is better adapted to high temperature than a polymer, which could show lower melting point. The selection of the type of glass to be used is done through the optical and thermal properties of the available materials.

Figure 7.23 shows commercially available glasses with different chemical compositions, and their range of optimal transmission. The range of optimal transmission represents the range of the light spectrum on which the major part of the incoming light is transmitted, instead of being absorbed or reflected. In our case, the range of interest spans between $\lambda = 0.4\,\mu m$, the lower end of the visible spectrum, and $\lambda =$ to $3\,\mu m$, the higher wavelength emitted by the energy source (represented by red arrows in Figure 7.23). The selection of glasses presented shows a transparency of 80% or higher on all or part of the wavelength range of interest.

The second critical factor for our application is the thermal expansion coefficient. Thermal expansion is the tendency of matter to change volume (generally, increase) as temperature increases. Glasses generally show brittle failure (often related to defects in the microscopic structure), that can be triggered by thermal stresses arising from thermal dilatation. Requirements for this set-up are a low coefficient of thermal expansion, and maximum working temperature higher than 300 °C. A modification of the feedstock base-material used (notably to manufacture from a metal powder) would require a study of the interactions between the material of the solidification window and the powder.

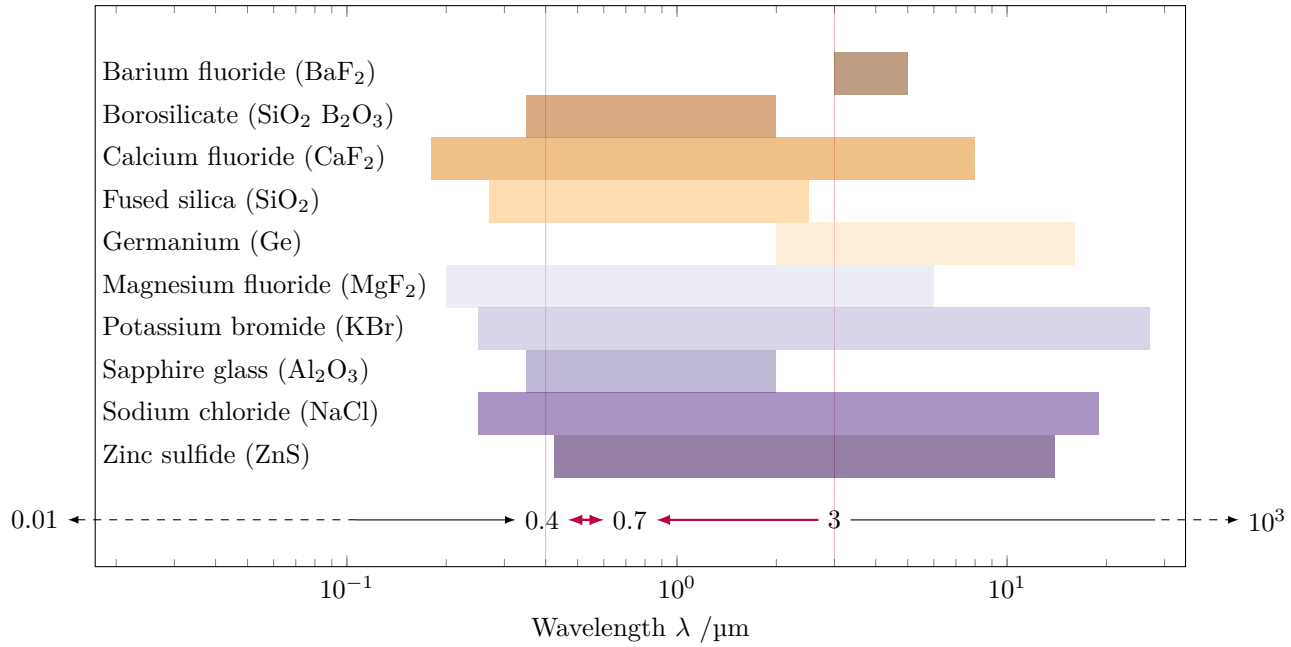

Figure 7.23: Optimal transmission range for commercially available glasses of different chemical composition. The "optimal" transmission is defined as 80% or more of the light being transmitted at a given wavelength, for measurement done in the range of 0.1 to 30 µm. The scale on the bottom of the picture represents the light spectrum: UV light ($\lambda = 0.01$ to 0.4 µm), visible light ($\lambda = 0.4$ to 0.7 µm) and IR light ($\lambda = 0.7$ to 10^3 µm). The transmission spectra were obtained from different glass manufacturers, see [258–260].

Table 7.4: Thermal properties for the list of selected glasses compositions. The information presented here correspond to the values given by the manufacturer for commercial glasses, see [258–260].

Type of glass (chemical composition)	Coef. of linear expansion α_L [10^{-6} °C^{-1}]	Softening temperature [°C]
Barium fluoride (BaF_2)	18.1	800
Borosilicate (SiO_2 B_2O_3)	3	557
Calcium fluoride (CaF_2)	18.85	800
Fused silica (SiO_2)	0.55	1000
Germanium (Ge)	6.1	937
Magnesium fluoride (MgF_2)	13.7	1255
Potassium bromide (KBr)	43	730
Sapphire glass (Al_2O_3)	5.3	2000
Sodium chloride (NaCl)	44	801
Zinc sulfide (ZnS)	7.1	1525

Among the materials showing high transparency in the range of interest, fused silica has the lowest coefficient of linear expansion, lower than that of the concurrent materials by one order of magnitude. The solidification window is therefore made of fused silica. The base material was bought from the company proQuarz GmbH, Mainz, Germany.

7.3.6 Implementation of live-monitoring

Live-monitoring of the process is an integral component of the RheoPrint powder deposition method. It splits into two *in-situ* probing strategies: the image capture and analysis during the powder deposition, recorded from underneath, and the rheological probing of the powder used as raw material.

Image capture of the deposition step. The solidification window is transparent to infrared but also to visible light. Thence, the powder deposition can be observed from below as it is taking place. A camera is positioned under each prototype to capture from a fixed point the powder deposition process. Figure 7.24b gives a typical image recorded by the camera, before processing of the image.

According to the state of the printer, the IR lamp changes position: either under the glass window during the solidification step, or swivelled aside on its rotating arm during the rest of the process to leave the field of view of the camera free. The camera used, a Brio Ultra HD Pro Webcam from Logitech, is controlled remotely from the laptop. The video it captures (at 30 to 60 frames per second (fps), resolution 1280×720 pixels) is transmitted to the user interface on the laptop, to provide live-monitoring of the deposition process to the experimenter in-flight. The processing of the images obtained is discussed in Chapter 8.

In future implementations of the process, this *in-situ* monitoring of the powder deposition can be automated to provide information on the powder layer state directly to the controlling software, without resorting to the user. The software can then process this information and by comparison with known-good, draw as a conclusion the answer to this question: Is the powder layer deposited yet, or should the deposition time be increased?

Rheological probing. In order to assess the rheological properties of the powder used as raw material, the current drawn by each DC motor is measured by current sensors connected to the main microcontroller. As the parts rotate at fixed velocity, from the current consumption converted into the torque developed, the relevant rheological parameters can be deduced, as we will see in the following chapter.

This functioning principle is the same as used in professional rheometers like the ones presented in Chapter 2. The main parameter influencing the precision of the measurement done by such machine is the mechanical friction generated by rotation of the part in motion (generally the inner cylinder); for this reason, good precision rheometers generally have air bearing between the shaft and its fixed support. In the RheoPrint process, air bearing is not conceivable at this stage of development; however we will see in Chapter 8 that the noise in torque recording is low enough to allow proper interpretation.

User interface. The user interface is used in-flight to adjust the printing parameters and observe the reaction triggered by modifying the printing parameters on the powder deposition. It was created with the software Processing [261], an open-source programming environment used for production of interactive visuals and using its own programming language, based on Java. The interface includes graphical monitoring of the current drawn by the rotation of the inner tube and closing disc and of the evolution of temperature around the IR lamp, as well as information on the current state of the algorithm controlling the printing process. A visual of the interface is presented in Figure 7.24a. Finally, the image recorded from underneath the powder container is also available to the user, as shown on Figure 7.24b.

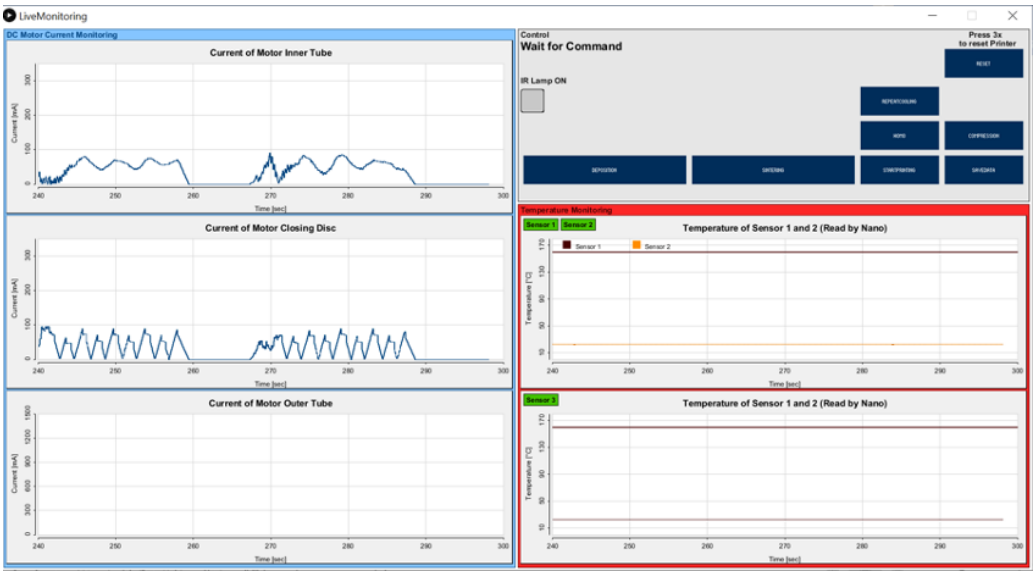

(a) User interface.

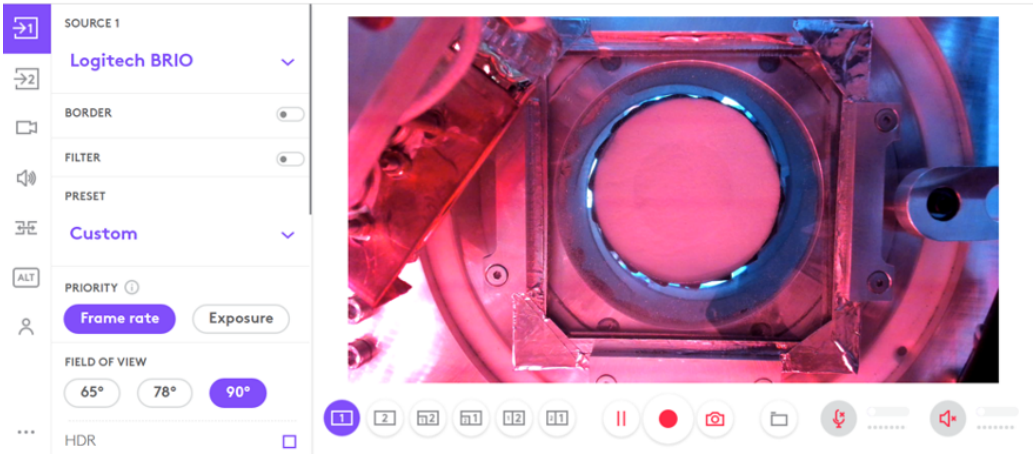

(b) Typical image recorded during live monitoring.

Figure 7.24: Screen captures of (a) the user interface designed to control the prototypes, and (b) a typical image taken during live-monitoring. In this image the prototype is empty and a virgin printing substrate is visible.

7.4 Experimental methodology

The experimental set-up, procedures and plan presented in this section correspond to the experiment carried out during the 72nd ESA three days parabolic flight campaign, in the course of the GrainPower project lead by the author.

7.4.1 Parabolic flight environment

The GrainPower rack. The rack built to nest the technology demonstration is presented in Figure 7.25 in its final form, opened from the front. It contains the two prototype 3D printers, enclosed in an aluminium containment.

The two prototypes are mounted on aluminium profiles of section $45\times45\,\mathrm{mm}^2$, forming the general rack structure. The structure measures $500\times800\times735\,\mathrm{mm}^3$, and is closed by thin

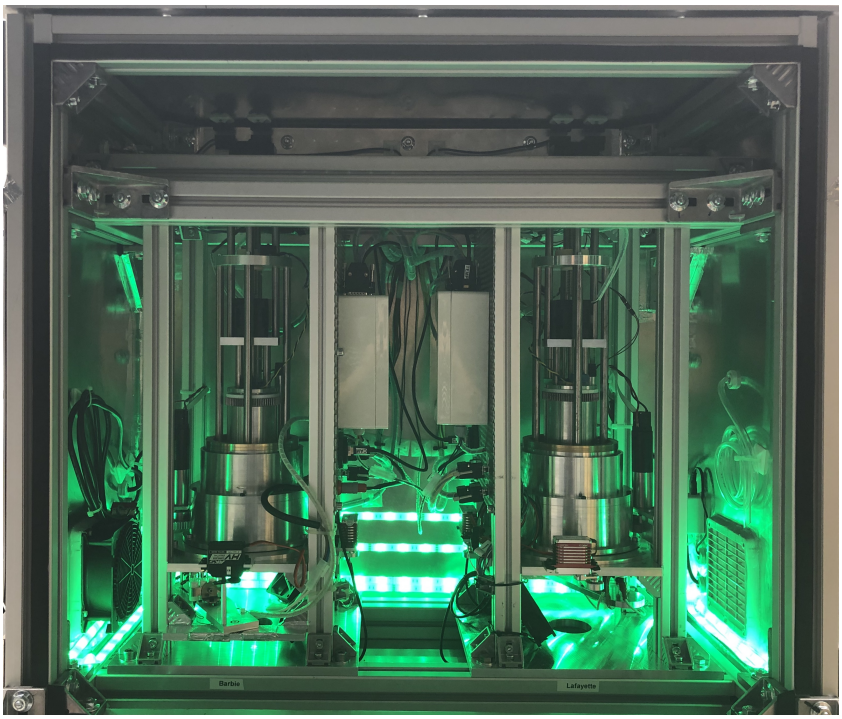

Figure 7.25: GrainPower rack open from the front with inner illumination on. The two prototypes are placed inside the rack, attached in flight configuration.

aluminium plates. To access the prototypes, the front and top plate can be easily removed with wing nuts, which is done after each flight day to fetch the printed samples and refill the powder bed with fresh powder. Closed, it is used as a table to support the two laptop computers used to control the experiment and record the data in-flight (see Figure 7.26).

Safety features. Parabolic flight campaigns offer an excellent experimental platform for microgravity experiments. This outstanding environments comes with a strict set of safety regulations. Among them is the redundancy of every safety feature. Accordingly, every thermal protection described in the previous section is implemented twice (thermal switches, temperature sensors, and optical temperature indicator). The solidification window is also modified to withstand one failure: instead of a single glass plat of thickness 5 mm as previously described, two thinner glass plates are stacked, separated on the side by a flexible silicon joint to absorb vibrations and thermal expansion. Thereby, failure of one glass plate due to thermal strain would not be catastrophic. This gives the experimenter the necessary delay for seeing the crack appearing on the glass window and stop the experiment.

The aluminium containment of the rack ensures that no powder leakage reaches the aircraft cabin, even in the event of failure of the first powder container. The closed rack is presented in Figure 7.26a. This opaque containment also allows for a safe use of the IR-lamps, as the radiations and heat are contained during operation of the lamps, and to avoid harm due to the motor movement. To ensure that heat doesn't accumulate in this closed space, an exhaust fan enables air circulation out of the containment; to provide containment of powder and possible fumes, the exhaust fan is protected by a filter that captures all particles and fumes. A commercial filter-fan combination from the company Rittal is used: the fan draws air to the inside of the containment while a filter, placed on the other side of the rack, allows warm but clean air out. To safely release the warm air into the aircraft, the outlet fan is placed pointing

towards the cabin wall and not towards the main aisle. Filters are placed on both intake and outlet, in the form of fine filter mats filtering dust smaller than 10 µm and fumes (filter class F5/M5 following DIN EN 779).

In order to ensure that the lamps and motors cannot be activated while the second containment is open, magnetic interlocks are implemented, which disable the entire system unless the containment is in place.

(a) Front view. **(b)** Back view.

Figure 7.26: Experimental rack right before being shipped to the Novespace facilities in Bordeaux, France. (a) Front with closed second containment and control-laptops attached on top, (b) seen from back, with fuses access (top), electrical control boxes (dark transparent boxes, middle) and power supply boxes (white boxes, bottom).

7.4.2 Material

The material used for this experimental campaign was described at length in Chapter 2. It consists of two PS powders sold by the Norwegian company Microbeads under the commercial name Dynoseeds. The powders, constituted of spherical grains, have a diameter of 80 µm, and they differ only by their surface state: one powder is covered in a rough, nanometric dust, while the other one has a clean, smooth surface. Their surface state is shown on Figure 2.1, and mechanical properties are given in Table 2.1. Those two materials are used as a model system to test the process described for a material of good flowability (the smooth surface powder) and a material of mediocre flowability (the rough surface powder).

Preliminary parameter adjustment: sintered height as a function of exposure time. A preliminary experiment was conducted to devise the height sintered for given exposure times, for the PS powders used. The boundary conditions are the following:

- The entire process should happen in microgravity. The duration of the $0g$ phase being 22 s, it sets the maximum sintering duration.

- The sintered height should be sufficient to sinter one layer and attach it to the previous one, ergo avoiding delamination of the sample.

The results of this experiment are presented in Figure 7.27.

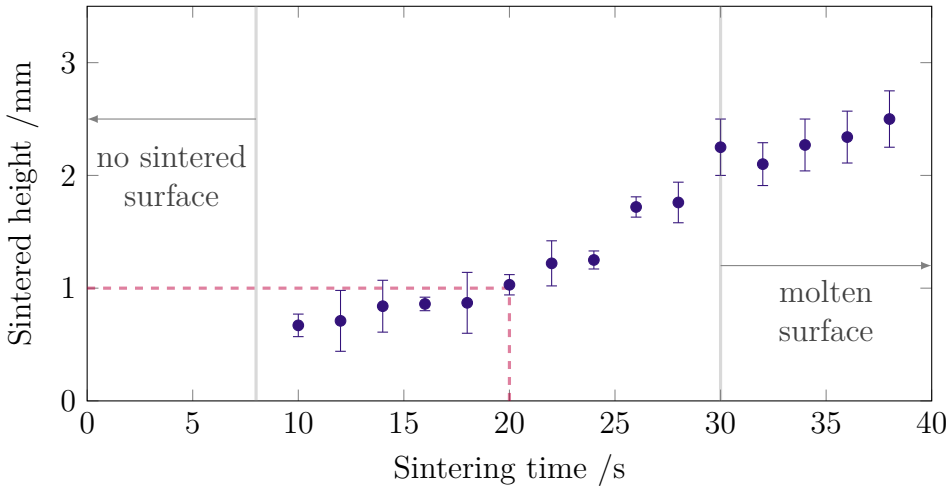

Figure 7.27: Experimental estimation of the sintered height as a function of the exposure time to IR radiation. Error bars correspond to the standard deviation for each series of measurement done on the same samples at five different spots. Red dashed lines show the chosen exposure time and layer height.

In order to sinter the equivalent of twice the layer height in 20 s, ensuring sufficient overlap between layers, the layer height is fixed at 0.5 mm (6.25 particles diameters).

7.4.3 Experimental plan & procedure

The objectives presented at the beginning of this chapter can now be translated into an experimental plan, explicitly given per day of flight in Table 7.5. In the experimental nomenclature, the two prototypes are labelled *Barbie* and *Lafayette*, abbreviated to the respective first letter; the flight-day number is appended to this letter to give the reference of each particular experiment.

Experimental procedure. The experimental procedure implemented is based on the requirement to perform the entire printing procedure in microgravity (deposition and solidification), and to enable the experimenter to observe the control variables at all time, and modify some parameters during steady flight if necessary. Apart from the obvious remark that the hypergravity phase might influence the powder deposition, the solidification relies on material exchange between grains; therefore, if the solidification is done in an environment that foster contact between the grains, zones of low density that were present in microgravity might disappear in hypergravity or in steady flight. To ensure that the results would be reproducible under longer periods of microgravity, the solidification step is conducted fully in microgravity.

The experimental procedure spans over two parabolas. Figure 7.28 provides a block diagram of the basic experimental procedure. First, one new layer is deposited, which includes incremental rise of the platform, powder downward transport, homogenisation and compression, and is realised in one parabola. During the next microgravity phase, solidification takes

Table 7.5: Experimental plan for the PFC.

Flight day – Plan and corresponding objective	**Material**
Day 1 – Optimise process parameters for microgravity (Obj. 1). This implies, in the following order: • Verify if the powder deposition functions in microgravity. • If the powder layer deposited is not homogeneous, the experimenter can modify the following parameters in-flight: - Duration of the deposition (including transport and homogenisation). - Layer height: fixed at 0.5 mm, it can be increased to ease the powder homogenisation. - Shaking amplitude: fixed at its maximum value, it could be reduced to increase the vibration frequency. • To analyse gravity-triggered changes in powder flow behaviour (Obj. 5), the data recorded and visible live as a verification mean for the experimenter are: - Direct visualisation in-flight of the deposition, through bottom window. - Live graphical visualisation of current withdrawn by each motor.	• $B1$: soft surface powder • $L1$: soft surface powder
Day 2 – Print sample(s) in microgravity for material characterisation, using best possible parameter set (Obj. 2 & 3). The experimenter can increase the material deposition time to two parabolas if they assess it necessary.	Test raw materials of variable flowability (Obj. 4). • $B2$: soft surface powder • $L2$: rough surface powder
Day 3 – Print samples in microgravity for material characterisation, using fixed printing procedure of one parabola for material deposition and one parabola for solidification and fixed printing parameters (Obj. 3 & 5).	Test raw materials of variable flowability (Obj. 4). • $B3$: soft surface powder • $L3$: rough surface powder

place. An extra parabola can be used for increasing the cooling time if the temperature remains too high; on day 1 and 2, the homogenisation was repeated for a second parabola if the powder layer deposition was showing obvious heterogeneity. The experimenter's input is required for starting the process once a stable state of microgravity is reached, and for deciding if an extra parabola is needed for material deposition and cooling.

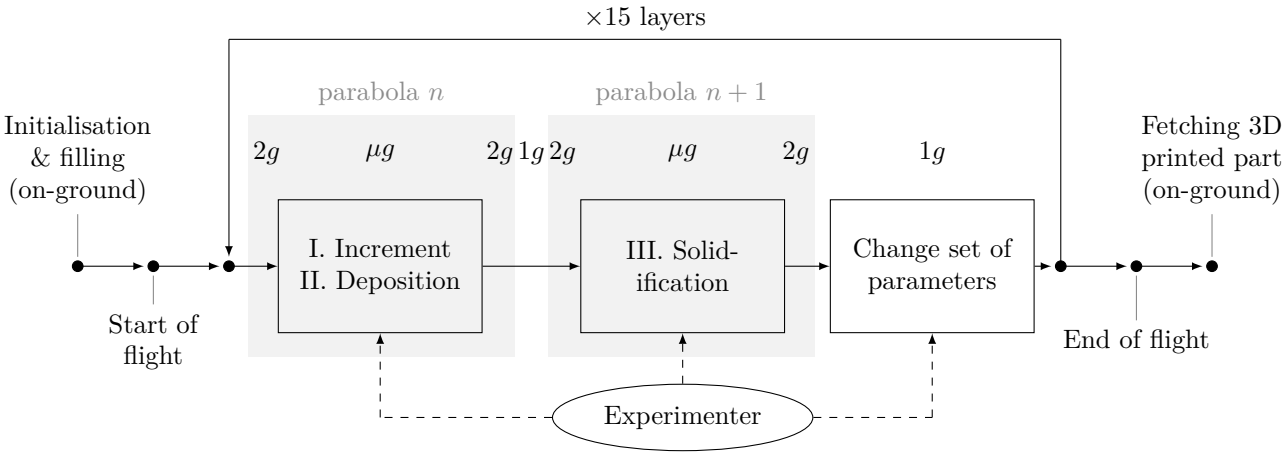

Figure 7.28: Block diagram of experimental procedure per prototype on the first day of flight.

7.5 Conclusion: obtaining a proof of concept

The working principle of the RheoPrint powder deposition and solidification process was tested in microgravity through two parabolic flight campaigns: the 34th DLR PFC in September 2019, which was used for testing the hardware under microgravity environment, and the 72nd ESA PFC, in November 2019, during which five samples were successfully manufactured fully in microgravity. This provides a proof of concept for the additive manufacturing process proposed. The printed samples and data collected during this campaign and on-ground will be analysed in Chapter 8.

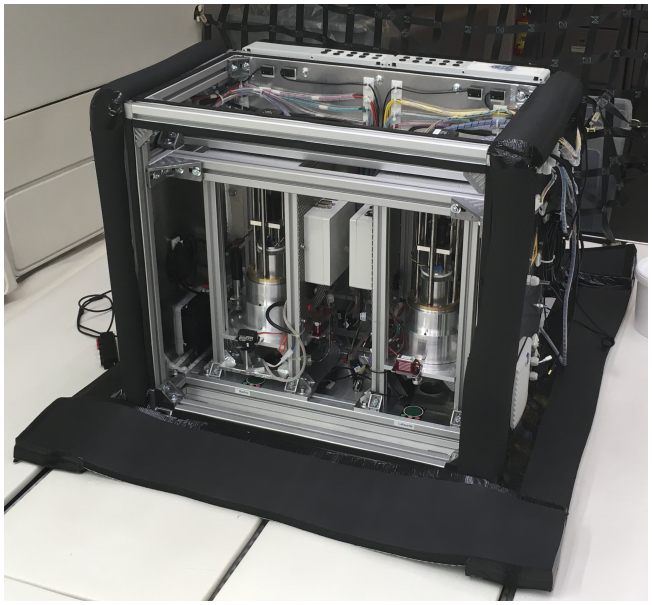

Figure 7.29: GrainPower experiment rack in the Novespace ZeroG plane, open to see the two prototype 3D printers, but the powering of the motors and lamp are disabled by the open magnetic interlocks. Black foam covers the sharp edges of the structure.

Part III

Evaluation of the RheoPrint process

Chapter 8

Results: analysis of 3D printed samples

The RheoPrint AM process shall in the following be assessed through analysis of the data recorded during manufacturing of samples using this process, and through the characterisation of the printed samples themselves. Five types of samples are used for analysis: samples manufactured on-ground from the smooth and rough surface PS powders studied in Part I; samples manufactured from those two powders, in microgravity; and finally samples manufactured from PS powder produced by closed-loop recycling of former 3D printed parts. The following questions will be addressed:

- What are the parameters asserting the proper functioning of the process, and how are they linked to the quality of the material deposition of each layer?
- How can the recorded data be linked to:
  i. The rheological properties of the raw material fed to the 3D printer.
  ii. The gravitational environment in which the powder deposition is done.
- Does the powder handling process function:
  i. Independently of the rheological properties of the raw material fed to the 3D printer, hence for powder of high flowability (smooth surface state) and powder of mediocre flowability (rough surface state).
  ii. Independently of the gravitational environment in which the powder deposition is done, hence on-ground and in microgravity.
- Can the RheoPrint 3D printing method be used with recycled powders in the perspective of closed-loop recycling?

8.1 Characterisation methods employed

8.1.1 *In-situ* monitoring of layers homogeneity

For powder-based additive manufacturing, homogeneity of the deposited layer is a critical parameter as it conditions the appearance of defects in the final printed object, which will in turn lead to stress accumulation and premature failure. Therefore, the evolution of the powder-layer homogeneity during the deposition step is meaningful to evaluate a powder-based manufactur-

ing process.

The RheoPrint process is inherently based on a closed container with an energy source placed outside of the container, facing the location where the new layers of material are deposited successively. During the solidification phase, the energy input happens through the so-called "solidification window", which is transparent to the type of energy selected – in the present case, IR-light. By selecting a material for this window that is also transparent in the visible spectrum, the powder homogenisation step can be monitored *in-situ*. After completion of each solidification step, the energy source, placed on a rotating arm, swivels away to leave the field open for image capture. A camera placed under the window records as the powder layer is deposited. A typical recorded image is presented in Figure 8.1. The powder movements are captured as the powder layer is being homogenised by horizontal shaking. The image is then analysed to extract quantitative information on the state of homogeneity of the layer.

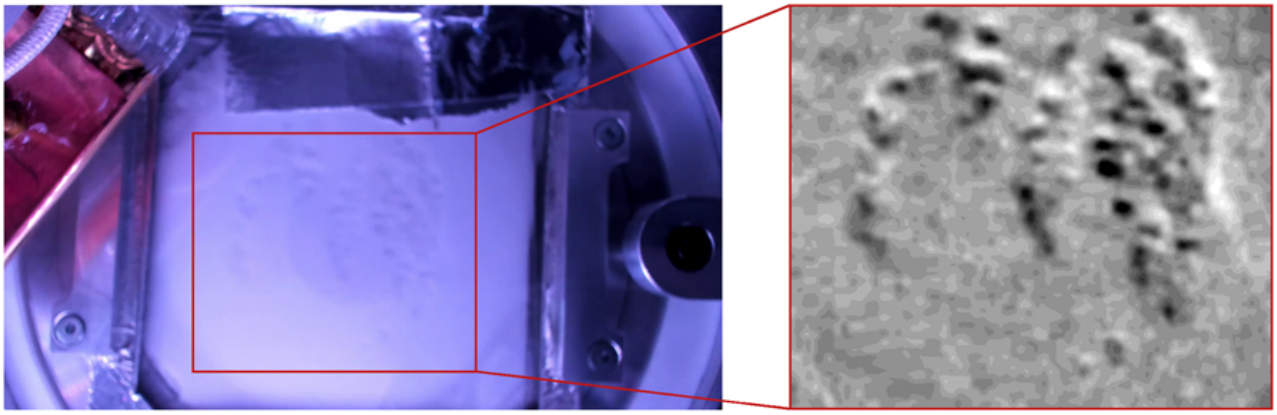

Figure 8.1: (Left) Image recorded by the *in-situ* monitoring video system, giving live indication of the evolution of the homogenisation of the newly deposited powder layer. (Right) Area of interest selected within the image, on which the image analysis procedure was applied. The post-analysis image is contrast enhanced for the reader to distinguish variations evident for a computer but difficult to perceive for the human eye.

Image analysis procedure. The image sequence obtained is analysed through the following algorithm:

- The image corresponding to the last image before starting the powder deposition procedure – hence the last image before the increment of the printing platform – is considered the image taken at t_0. It is subtracted from the rest of the stack of images in order to remove all the static impurities that might be present on the image but would pollute our analysis (e.g. dust or reflection on the solidification window).
- The image is cropped to keep only the part where the powder is under the substrate – the part where it will be solidified, hence the area of interest.
- A bandpass filter is applied to automatically remove unwanted structures from the image by decomposing it into different frequencies. This includes noise up to 5 pixels (corresponding to approx. 1 mm) and large structures over 150 pixels (approx. 60 mm), including horizontal bands that appear in the video recording.

Quarrying quantitative data. The image sequence obtained shows the formation and coalescence of "holes" or areas of lower density within the deposited layer. Those areas appear as dark or light spots on the images: the powder reflects the light that is shone upon it from the side; if there is no powder on a specific zone, the light is not reflected and a dark spot appears on the image. Besides, a bright spot appears, as the light arrives directly on the vertical side of the "hole".

The level of grey of the image represents the powder density distribution: if the layer of powder is dense and homogeneous, it reflects light homogeneously, creating a solid-colour image. If rifts create different levels of depth, the light is reflected heterogeneously, appearing as darker or lighter spots. Homogeneity of the powder layer can be summarised by the *variability* in the grey-level of the image, or the *tendency of the pixels to vary from the average grey* of the image. In statistical terms, the deviation of a variable from its mean value is the variance, σ^2; it will be used to quantify the *heterogeneity* of the powder layer deposited, as shown in Figure 8.2.

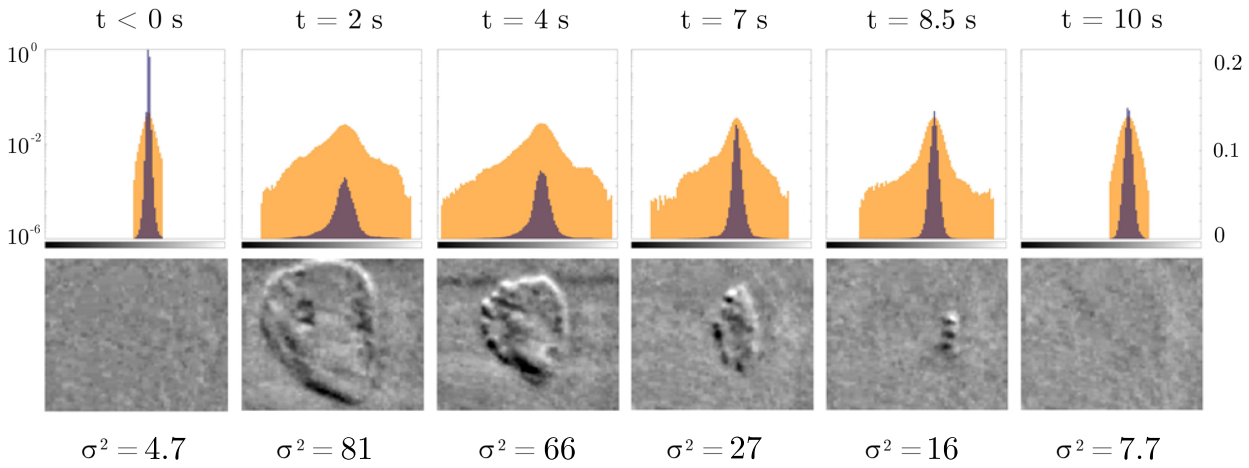

Figure 8.2: Evolution of the powder layer as it is deposited, before $t_0 = 0\,\text{s}$ and during the deposition process. Histograms of pixels grey-level distribution are presented (with grey-level as abscissa axis), as well as the corresponding variance value, highlighting the correspondence between homogeneity of the deposited layer and variance calculated on grey-level distribution. For each image, the distribution is represented in blue on the linear scale (right) and in yellow on a log-scale (left). Values given for the variance σ^2 are in pixels squared. The layer used as example here is the fifth layer of sample $B3$ (layer $B3L5$): a sample printed from smooth surface powder, in microgravity.

The variance σ^2 in distribution of pixels' grey-level synthesises the heterogeneity of the deposited layer as probed by live-imaging recorded during powder deposition. As the video recording is done at a minimum of 30 frames per seconds (and up to 50), a rate of at least one image every 0.03 s enables to follow the powder deposition at each instant of the process.

8.1.2 Live rheological probing of feedstock

To manufacture objects of constant quality from multiple raw materials, which exhibit variable rheological properties, the strategy proposed in this work to optimise material deposition is to probe the flow properties of the material in-use. During a 3D-printing cycle, the machine probes the flowability of the raw material by recording the torque needed to rotate the different parts of the container full of powder. The time devoted to the homogenisation step can be adapted accordingly automatically – a detailed explanation of the closed control loop principle is presented in Section 5.2.

Assessing flowability in-use: how to build a flying rheometer? Record of the torque produced by the different motors rotating the printer's structure is made possible by the use of DC motors. DC motors are rotary electrical motors that convert electrical energy (direct current) into mechanical energy (rotation, displayed in the form of torque). The RheoPrint 3D printer functions like a rheometer: the rotation speed of its different parts is defined prior, and an operating loop enables the motor to reach and maintain the given speed by varying its current consumption, which is recorded and transformed into a torque M. The resistance to rotation experienced by each motor is a measure of the material's *resistance to flow*. The protocol to access the relevant parameters for the material's rheological characterisation is explicitly described in Figure 8.3.

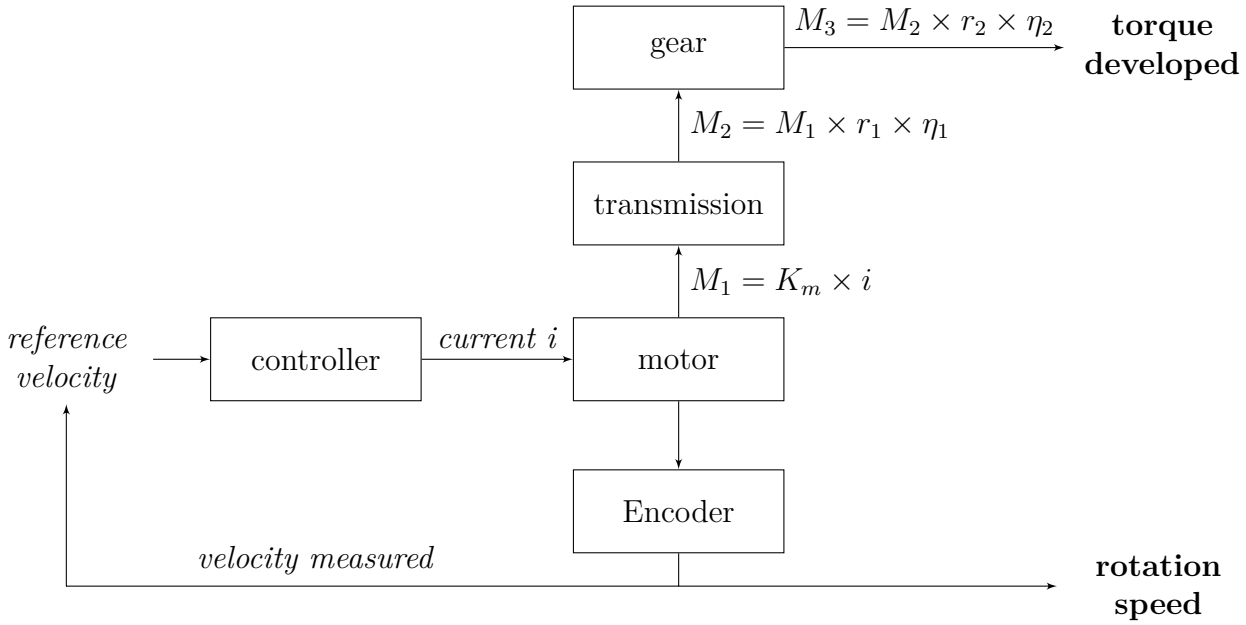

Figure 8.3: Flow chart of the conversion protocol, linking the current drawn by each DC motor to rotate at a defined velocity, to the relevant rheological parameters: the torque developed to shear the granular material at the given rotation speed. K_m is the torque constant of the specific motor, $\eta_{1,2}$ efficiency parameters of the mechanical set-up and $r_{1,2}$ gear ratios.

The current drawn by each motor is recorded and converted to the final torque M_3 developed to shear the powder, given the gear transmission system of the machine:

$$M_3 = i \; K_m \; r_1 \; \eta_1 \; r_2 \; \eta_2 \tag{8.1}$$

where M_3 is the final torque developed, i the current drawn, K_m the *torque constant* of the motor (empirical value given by the manufacturer), $\eta_{1,2}$ the efficiency ratio of the gear system and $r_{1,2}$ the gear ratio or ratio between the rotational speeds of the two connected meshing gears. $\eta_{1,2}$ represents the efficiency of an energy transmission system: the ratio between the useful work performed by the system and the total energy consumed as input. It is defined as the ratio between the output power and input power. The efficiency of the gear system (namely, losses due to friction within the force transmission gear system of the machine) is not a relevant parameter in our analysis, as the values of torque recorded will be analysed by comparison between different cases (e.g. presence or absence of gravity, raw material of different flowability). Hence, losses due to friction within the force transmission system can be considered equal for all cases, as the same machine is used; they even out in the comparison process. Therefore, the efficiency ratio $\eta_{1,2}$ is considered unity.

In the prototypes built, the torques recorded are the ones developed by rotation of the inner tube (motor DC_1) and closing disc (motor DC_2) – see Figure 8.4. The corresponding numerical parameters are given in Table 8.1.

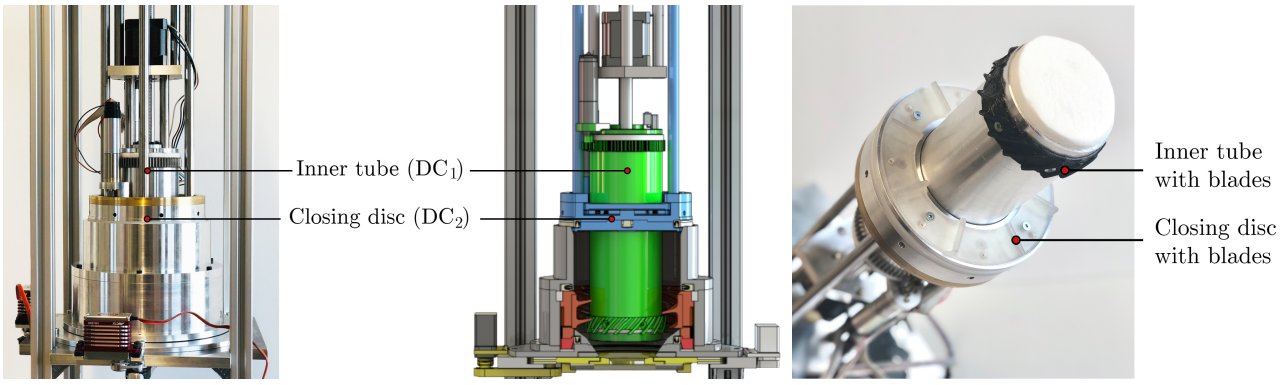

Figure 8.4: RheoPrint 3D printer picture (left) and CAD snapshot (right), with indication of its inner tube (green part of CAD snapshot) and closing disc (blue part in CAD snapshot): the two rotating parts that record the evolution of torque developed to probe the flow-behaviour of the raw feedstock material inside the closed printing bed. Blades attached to both parts can be seen on the opened apparatus.

Table 8.1: Characteristic parameters of the motors and gears used to convert the current withdrawn into the torque developed and finally into the shear stress applied to the granular material.

Parameter	**Motor DC 1 (inner tube)**	**Motor DC 2 (closing disc)**
K_m /mN m A^{-1}	22.78	22.78
r_1 for gear transmission	91	91
r_2 for gear in printer	6.8	10

Rotation of the inner tube enables to probe the material directly in the centre of the container, at the heart of the process. It rotates clockwise at an angular speed of $\omega = 0.5\pi$ rad s^{-1}, shearing the material like in a large-gap Couette-type rheometer [45, 262–264] (see Chapters 1 and 2). The bottom of the tube is equipped with paddles to enhance the particle-particle contacts over wall-particles contact by transporting a layer of particles while rotating (see Figure 8.4b).

The closing disc is alternating rotation direction every two seconds. This movement aims to break the force chains and avoid the formation of a jammed phase within the granular packing. In the meantime, it is probing the material's flow-behaviour by dynamic mechanical analysis [265, 266], with a maximum angular speed of $\pi/3$ rad s^{-1} and oscillation frequency of 0.25 Hz.

Figure 8.5 shows an exemplary evolution of the torque developed during rotation of the inner tube (Figure 8.5a) and oscillation of the closing disc (Figure 8.5b), for two consecutive deposition steps.

In Figure 8.5, as well as in all following graphs, the time $t_0 = 0$ s represents the start of the powder deposition, triggered by the user on the prototypes used experimentally. For

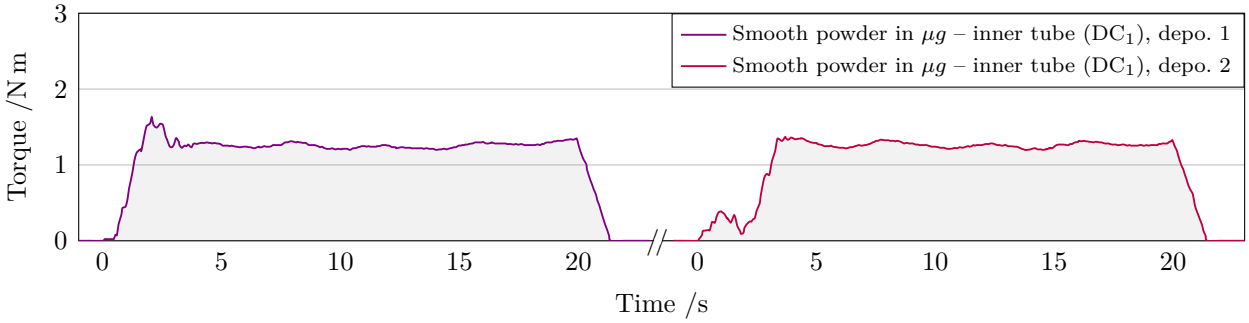

(a) Motor DC_1 (inner tube)

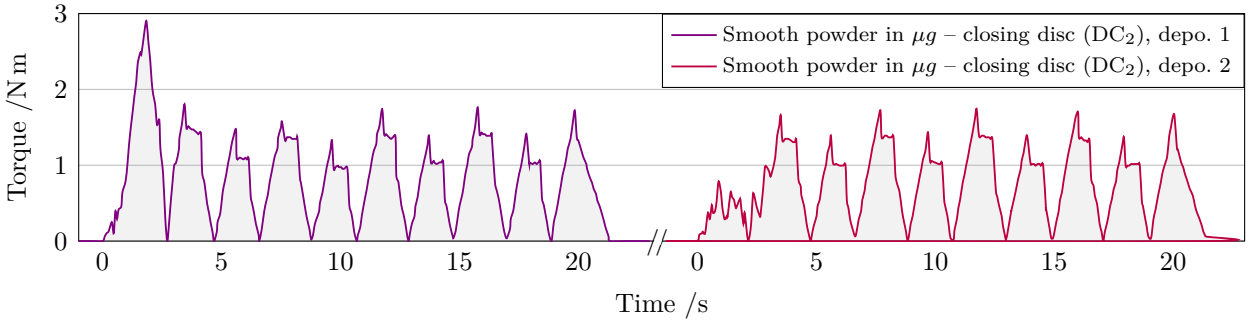

(b) Motor DC_2 (closing disc)

Figure 8.5: Evolution of the torque produced (a) by the motor DC_1 rotating the inner tube and (b) by the motor DC_2 oscillating the closing disc. For the experiments shown here, the deposition is conducted in microgravity for smooth surface powder (sample *B2L7* following the experimental nomenclature). The grey area under the curve represents the scalar quantity $\int_t M(t)dt$.

the experiment in microgravity, t_0 also represents the beginning of the microgravity period. The two different types of solicitation give different response in torque, although the order of magnitude remains the same (around 1 N m). Each deposition starts with an overshoot of torque, visible for both the simple shear (Figure 8.5a) and oscillatory motion (Figure 8.5b). The mono-directional rotation includes a short transition period over which the motor starts rotating and reaches its desired velocity, a steady rotation speed period, and finally the second transition period towards immobility. The oscillatory test also shows a slight overshoot at the beginning of each new direction turn. The angular speed must be considered as a function of time, as transition periods occupy the same amount of time as steady rotation; the steady-state angular velocity of all rotating parts are given in Table 8.2.

Table 8.2: Steady-state rotation speed of all rotating parts of the prototype 3D printers and corresponding motors.

Rotating part (motor)	Inner tube (DC_1)	Closing disc (DC_2)	Outer tube (DC_3)
Angular velocity (rad s^{-1})	$\pi/2$	$\pi/3$	$3\pi/5$
Rotation speed (m s^{-1})	0.102	0.126	0.226

The shear rate to which the material is submitted during rheological probing by concomitant rotation of the inner and outer tubes can be calculated from Eq. 1.9 for such large-gap Couette geometry. Given the rotation speed of each rotating part (see Table 8.2), the shear rate thence obtained is $\dot{\gamma} = 2.25\,\mathrm{s}^{-1}$. As seen in Chapter 2, at low shear rate, found experimentally to be

approximately $\dot{\gamma} \leq 10\,\mathrm{s}^{-1}$ for the powder used here, interparticle frictional contacts dominate the rheology (Section 2.4). The difference in physical properties (in particular, surface roughness and angular particle shape triggering mechanical locking) of the material should hence be reflected in its flow-behaviour as recorded by the machine during rheological probing.

8.1.3 Calculation of the energy transferred for powder deposition

Besides the qualitative flow behaviour exhibited by the granular packing inside the 3D printer, a quantitative evaluation of the *ease to flow* of the powder within this process is necessary for our analysis. Such value should encompasses the *difficulty to make the raw material flow* for the given duration necessary to complete powder deposition. The *total energy transferred to the granular packing* to continuously trigger powder flow is selected as such quantity, as it encompasses the energy dissipated by grains to flow along each other, regardless of the physical mechanism preventing flow.

The work of a force W or "energy transferred or converted to or from an object *via* a force F [or torque M] acting on this object" [267] is, in the case of a rotational force:

$$W = \int_t M(t)\,\omega(t)\,dt, \tag{8.2}$$

where M is the torque developed to rotate the object at angular velocity ω. The energy W_t transferred to the packing to trigger flow at angular velocity ω will be used as the quantity expressing the *difficulty of the powder to flow* (in this specific set-up), by integrating $M(t)\omega(t)$ over the duration t necessary to complete a deposition step for the given type of powder.

8.1.4 Introducing a *flowability* dimensionless number

As seen in Chapter 2, the concept of *flowability* is difficult to summarise into one quantity, as it reflects the complex dependence of powder flow-behaviour on parameters internal, but also external to the powder itself. The approach proposed here is therefore to accept *powder flowability* as a fully phenomenological quantity, which includes the situation-dependence; it is hence related to the specific process in regard to which the powder should be characterised.

Let us propose a dimensionless flowability number Fl, based on the comparison between the work necessary for the process to take place while empty, *versus* the work necessary to complete this same process beginning to end for one batch of material. The duration of the empty run must be similar to the duration necessary to process a full batch of material – in the present case, to fully deposit one powder layer. The energy displayed by the setup for an empty run, W_0, is compared to the energy displayed to complete the process for a given material quantity, W_t. The energy transfer is necessarily a non-zero quantity, as even empty, the process consumes energy to function; the addition of material increases the energy required for the process to take place, implying $0 < W_0 \leq W_t$. The relative change in energy transferred due to the presence of material can hence be calculated as:

$$Fl = \frac{W_0}{W_t - W_0}. \tag{8.3}$$

Interpreting the value taken by Fl enables the classification of the material processed within typical flow-behaviours:

- If $W_t \approx W_0$, the material requires very little energy to be processed: $Fl \to \infty$ shows *high flowability* of the material.
- If the surplus in energy needed to process the material is on the same order of magnitude as W_0, which translates into $W_t \approx 2W_0$, $Fl \approx 1$ represents *mediocre flowability* of the material.
- If $W_t \gg W_0$, the material requires high energy input to be processes: $Fl \ll 1$ shows a *low flowability*.
- If the energy necessary for the process to take place W_t diverges to become infinitely larger than the baseline energy W_0, $Fl \to 0$ indicates the the material in its present state cannot be processed, which could be due to shear thickening or the appearance of a jammed phase triggering *cessation of flow*.

The flowability number Fl will be used in the present work to compare the energy transfer necessary to obtain homogeneous layers with the RheoPrint additive manufacturing process, using various types of powders, under different gravitational levels. Comparison of Fl obtained will provide a classification of the *process-ability*, or *ease to process the given material in the given environment* of those powders in their respective environments.

8.1.5 Post-manufacture characterisation: X-ray tomography

To relate the data recorded during manufacturing to the final quality of the manufactured samples, density variations in the bulk of the samples are queried. This analysis is done through X-ray computed tomography (CT) of the 3D printed samples. X-ray CT is a non-destructive technique based on the interaction between radiation and matter [268]: an incident X-ray beam crosses the sample under probing; the incident beam, as it crosses matter, is absorbed differently by the different materials. The different absorption coefficients of the material(s) crossed by the beam give the intensity transmitted through each longitudinal line going through the sample. By moving the samples in regard to the X-ray source (or vice versa), the absorption along each longitudinal crossing is obtained, corresponding to the integral of the absorption over all points in this volume. Computing the data obtained in all directions provides an absorption per voxel, which can then be transformed into two dimensional projections corresponding to successive "slices" of the sample. The grey-levels correspond to the different absorption per voxel, hence to the different materials. A typical image obtained by CT of a PS sample sintered under weight on-ground is shown in Figure 8.6, as well as the binary image extracted from each "slice". As the capture is carried out under vacuum, black, which represents zero absorption, denotes the porosities, while grey is the sintered PS. The machine and scanning parameters used to conduct experimental measurements are presented in Table 8.3.

Table 8.3: Scanning parameters used to obtain the X-ray computed tomography of sintered PS.

CT system	Source voltage	Output current	Projections per scan	Measurements per projection	Exposure time per measurement	Voxel size
CT-ALPHA (ProCon X-ray, Germany)	80 kV	70 µA	1600	10	1000 ms	8 µm

Reference "known good" sample. A sample is sintered on-ground under the best possible conditions to serve as a reference "known good" sample for comparison with 3D printed ones. It

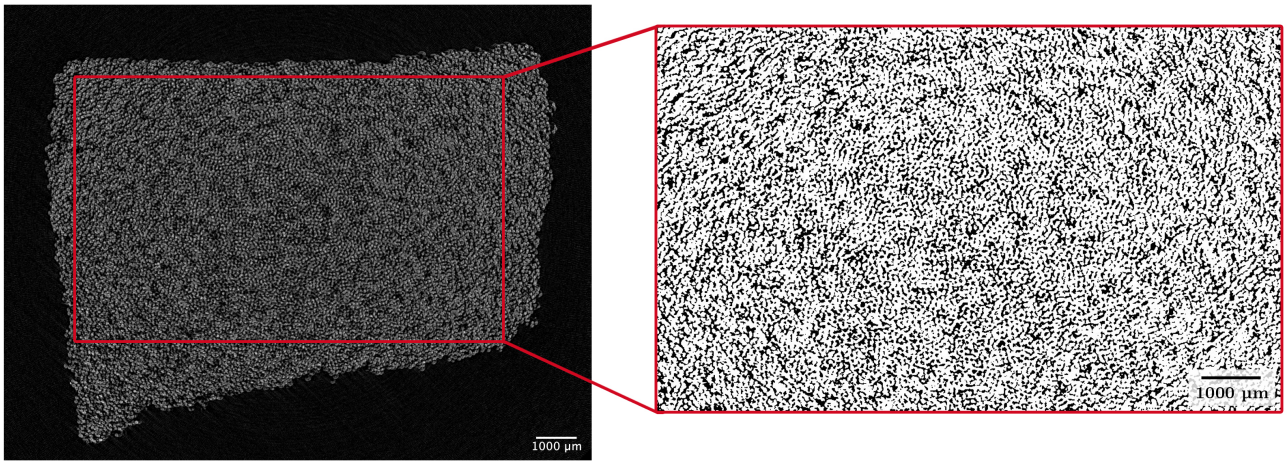

Figure 8.6: (Left) Example of X-ray computed tomography (CT) "slice" image, for a sample of PS sintered on-ground, under weight. This sample is used as for comparison of density homogeneity with the 3D printed samples. (Right) Binary image extracted from the tomography and used for analysis.

is manufactured from high flowability *SS* powder (also monodispersed, with 80 µm-diameter); the sintering takes place in an oven at 200 °C for one hour, and is realised under a weight of 3 kg to ensure continuous pressure *during* the solidification process. This aims to increase material density, as the continuous pressure enhances degassing and porosity size reduction. This "known good" exemplary sample, shown in Figure 8.6, will be used throughout the following analysis.

Samples preparation for CT. The size of sample is limited by the capacity of the machine, with a maximum sample length of approx. 10 mm along any axis. Therefore, samples are prepared with the aim to offer a faithful reflection of the powder deposition at its most challenging position: in the centre of the printing volume. As seen in Chapter 7, the solidification mechanism chosen is sintering by IR-light; the energy source is a lamp that provides an *almost* homogeneous heat-surface, enabling to solidify the entire sample-section within less than 20 s. However, the IR-lamp provides slightly stronger heating on two regions of the printing bed of approx. 10 mm by 30 mm, represented in blue in Figure 8.7. The lamp is placed accordingly to ensure that the centre of the printing bed be under one of the areas of preferred heating, as shown in the schematic representation proposed in Figure 8.7a. Each 3D printed sample is hence cut to extract a square sample of approx. 10 by 10 mm, cut out of the centre of the printing bed. This sample selection method is implemented to ensure comparability between the data-sets.

As the energy density provided by the IR-lamp is not perfectly homogeneous, in the middle of the "high heat areas" defined in Figure 8.7, a higher energy density results in a slightly higher material density in the middle of the samples selected.

Each experiment is represented by a sequence of images, "slices" of the sample in the xz-plane, as represented in Figure 8.7. The analysis techniques used to exploit the tomography imaging are described below.

8.1.6 Samples density homogeneity in bulk & pore size distribution

The homogeneity of porosity distribution in the printed samples in bulk is found by using two automatised image analysis procedures implemented in the Python PoreSpy library [269].

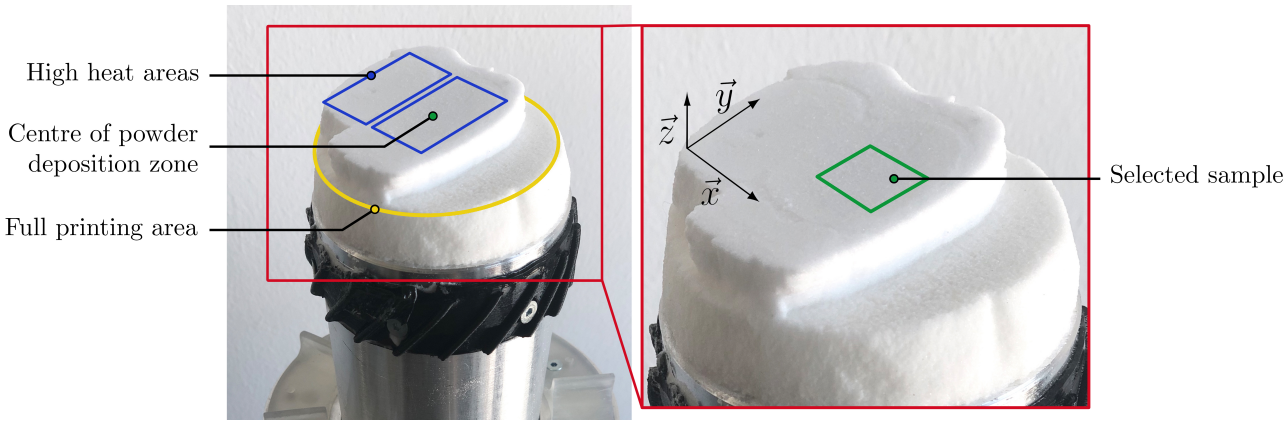

(a) Sample preparation rationale

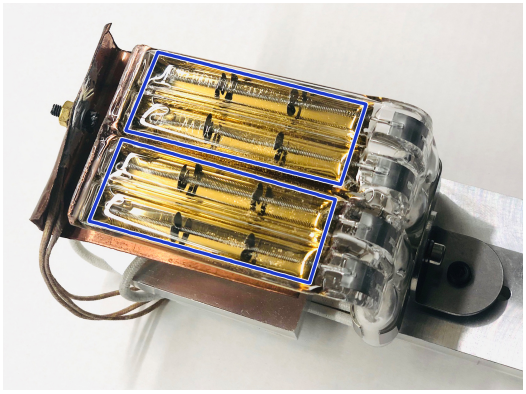

(b) IR-lamp with high heat zones

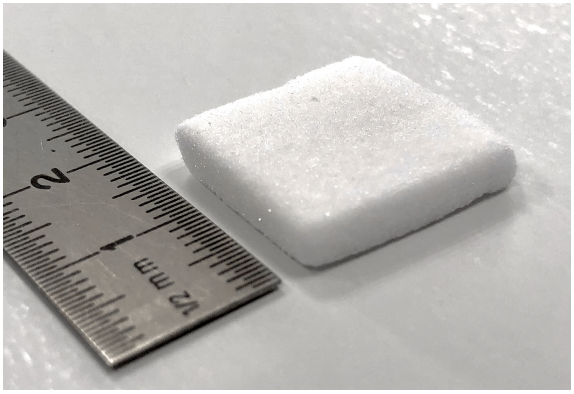

(c) Exemplary selected sample

Figure 8.7: Sample preparation rationale. (a) Superposition of high heat zones with the centre of the printing area, including delimitation of the selected sample. The sample represented here is manufactured on-ground from rough surface powder. (b) IR-lamp including schematic representation of high heat zones (in blue on the picture), corresponding to the zones marked in blue on the full sample. (c) Resulting sample after cutting (the sample represented here is sample $L3$, 3D printed in microgravity from rough surface powder).

The different functions available in PoreSpy enable to perform quantitative analysis of porous material images. Firstly, images are made binary by the automated procedure available in ImageJ [270] (the *intermodes* method is used, with dark background; the threshold is fixed for the full image sequence corresponding to one sample). Then, two strategies are employed: on one hand, the pore size distribution is estimated by filling each porosity with the radius of a sphere that overlaps it. This method is adapted for samples showing relatively spherical porosities, homogeneous in shape, which is the case for most of our 3D printed sample. A graphical representation of an image produced by this method is represented in Figure 8.8a. On the other hand, to capture the length of pores with "un-spherical" shapes and identify a possible anisotropy in pore size, the "chord length" method is employed. It consists of drawing chords that span across each pore in a given direction; the appearance frequency of each chord length can be extracted for different directions and be compared. In the present case, the chord lengths are compared in x- and z-directions, especially at longer chord length of 40 µm and higher, to detect larges defects, in the direction of the layer deposition (xy-plane) or in regard to the adhesion of layers on one another (z-direction). Finally, the density can be calculated per "slice" of depth 8 µm along the y-axis. As an example, the binary image presented in Figure 8.6 has a global density of 69.6%.

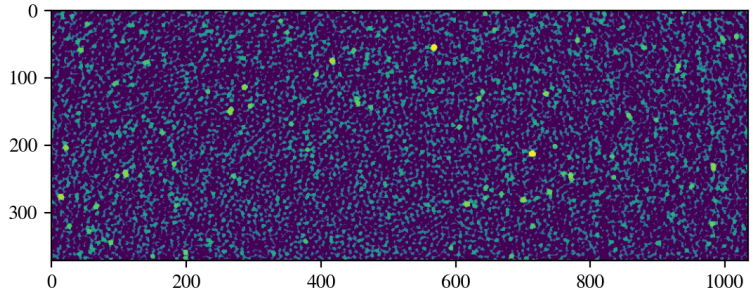

(a) Local porosity radii

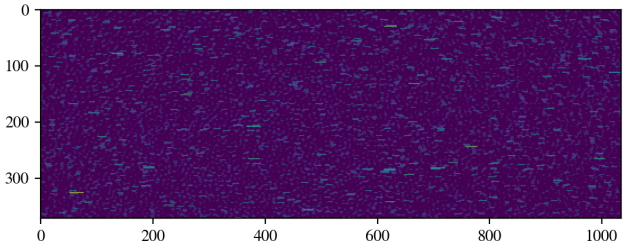

(b) Local chords length in x-direction

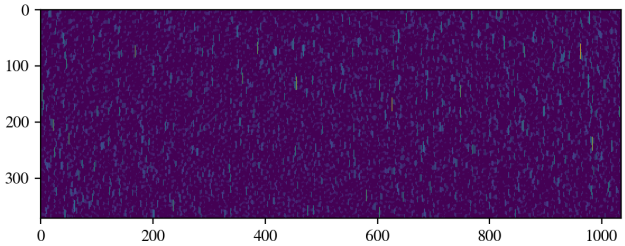

(c) Local chords length in z-direction

Figure 8.8: Graphical representations of (a) porosity radii and (b, c) chord length inside porosities, respectively along x- and z-axis (respectively horizontal and vertical directions). The sample presented as example here is sintered under weight, on-ground, from smooth surface PS powder.

8.2 Manufacturing from powders of high to mediocre flowability

The two powders used throughout this work, PS powders with smooth and rough surface state – characterised in Chapter 2 – were used as exemplary model-materials to isolate the flow-properties change due to an increase in interparticular friction. We first establish, as a baseline for comparison, the relevant observations on-ground, to verify the effect of a decrease in the feedstock material surface roughness. Results from microgravity experiments will follow in Section 8.3.

8.2.1 Reliability of torque as *in-situ* rheological characterisation

To asses wether this physical change, responsible for a different rheological response, would be recorded by the machine during the powder deposition process, the torque developed to rotate the inner tube and closing disc during material transport are observed. Torque evolution will be the first input of the process internal feedback loop (see Section 5.2), enabling to assess the quality of the feedstock material; therefore, reproducibility of the torque measurement for a given material, independence from layer number and correlation with base-material are analysed.

Evolution of torque with increasing layer number. To verify if the torque developed is qualitatively and quantitatively the same over multiple repetitions of the powder deposition process – i.e. for all layers of a sample – its temporal evolution for each layer in a sample is observed. The experiment selected is the first sample 3D printed on-ground from smooth surface powder. Torque evolution for all layers (1 to 11) is represented in Figure 8.9.

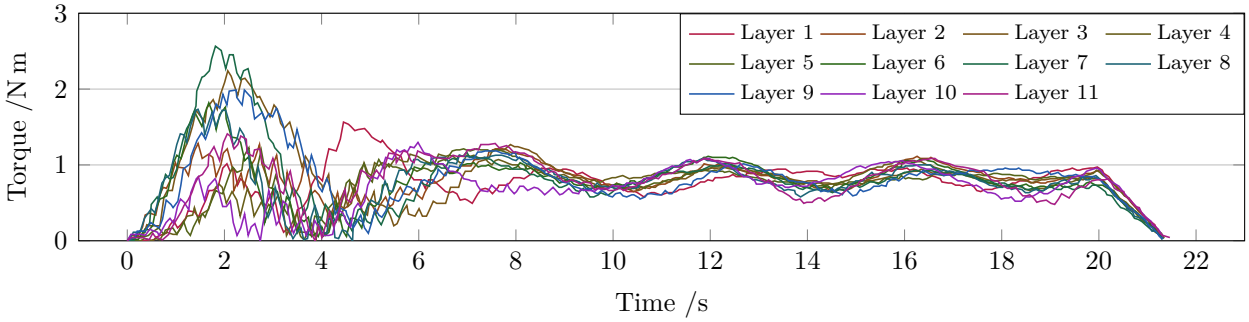

(a) Motor DC_1 (inner tube)

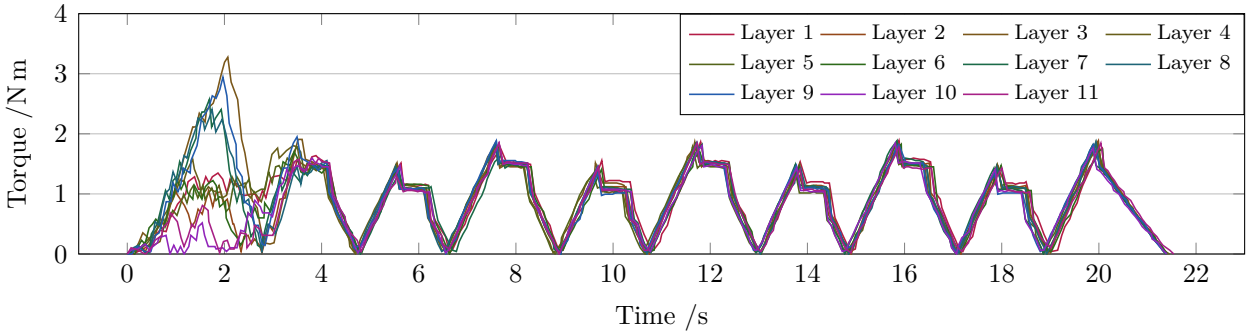

(b) Motor DC_2 (closing disc)

Figure 8.9: Temporal evolution of the torque developed for (a) the mono-directional rotation of the inner tube, and (b) the oscillatory rotation of the closing disc, for all layers of an eleven-layers sample 3D printed on-ground from smooth surface powder.

The typical curve shape shows slight oscillation of period 4 s in the mono-directional rotation (Figure 8.9a), corresponding to one full rotation of the inner tube, and therefore imputable to the apparatus itself. For oscillatory probing of the closing disc (Figure 8.9b), the rotation frequency of 0.25 Hz is clearly visible. Counterclockwise rotation seems to demand a slightly higher torque, but as this feature is observed regardless of the material fed into the process – including for empty runs (see Figure 8.10) – it is also linked to the apparatus rather than to the material.

For all repetitions of the powder deposition process, at first a transient state is observed, lasting approximately 5 s for the inner tube mono-directional rotation, and 3 s for the closing disc oscillatory motion. Then, a stationary state is reached, during which all layers show the exact same behaviour, including temporal similarity as all curves merge into a common pattern. No correlation is observed between the layer number and the torque recorded; in particular, no augmentation of torque is visible as consecutive layers are printed. Overall, the torque evolution for both types of stimuli (mono-directional rotation and oscillations) is, outside of the transition periods, practically identical for all layers constituting a sample.

Sensitivity to feedstock material flow-properties. Having shown that there is neither an evolution in pattern, nor in magnitude of the torque recorded throughout the manufacturing of one sample, sensitivity to the type of powder-feedstock can be probed. As seen in Chapter 2, the shear rate at which the material is probed in the AM set-up ($\dot{\gamma} = 2.25\,\mathrm{s}^{-1}$) should be optimal for particles' frictional interactions to dominate the rheology at high packing fraction, as is the case inside the closed container. Figure 8.10 shows a comparison between the torque

recorded for different experiments: Figures 8.10a and 8.10d, empty runs (i.e. no material is filled inside the machine). The production of a sample from smooth surface powder is shown in Figures 8.10b and 8.10e, while the production of a sample from rough surface powder is shown in Figures 8.10c and 8.10f. As all samples have a thickness of seven to fifteen layers, and as all layers per experiment show similar behaviour, one typical layer was selected as exemplary experiment for comparing qualitative torque evolution (coloured lines), but all layers are represented in light grey to show typical variability per layer within one experiment.

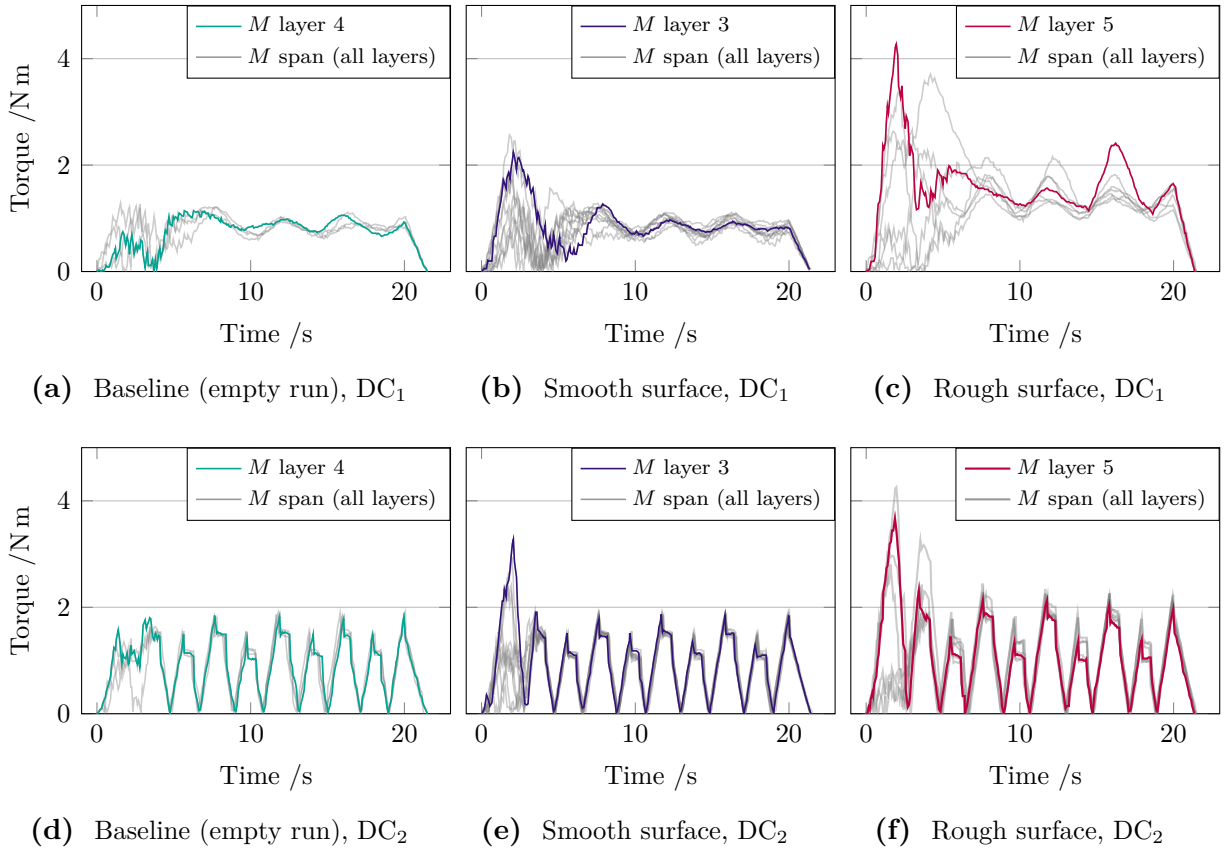

(a) Baseline (empty run), DC_1 **(b)** Smooth surface, DC_1 **(c)** Rough surface, DC_1

(d) Baseline (empty run), DC_2 **(e)** Smooth surface, DC_2 **(f)** Rough surface, DC_2

Figure 8.10: Temporal torque evolution for all layers (in light grey) and one typical layer (layer number indicated in legend), for (a) and (d) an empty run; (b) and (e) smooth surface powder, (c) and (f) rough surface powder. All data shown here was obtained on-ground in the prototype *Lafayette*.

All tests shown in Figure 8.10 show relatively similar general behaviour. The oscillation around the mean torque-value, with period $T = 4\,\mathrm{s}$, is clearly visible on all experiments run on DC_1, confirming that it is due to the apparatus. The same transient behaviour is also observed for all tests, followed by a stationary state where all layers show similar trend.

The experiment run for the smooth surface powder shows that a slightly higher torque is developed than for the empty run, which is mostly visible on peaks being higher (from 1 N m to 1.3 N m), while lows are at similar magnitude (around 0.8 N m). For rough surface powder, the peaks in torque are emphasised even more, going up to 2 N m, and the lows also become higher (1.5 N m). In particular, during the transient regime, a much higher torque is necessary to initiate powder flow, for both types of drive (mono-directional and oscillatory rotation), with an initial peak rising up to 4 N m. To observe the quantitative increase in torque developed with the two materials used, the energy transferred for each experiment is calculated for each layer (see Eq. 8.2 for work calculation). Results are displayed in Figure 8.11.

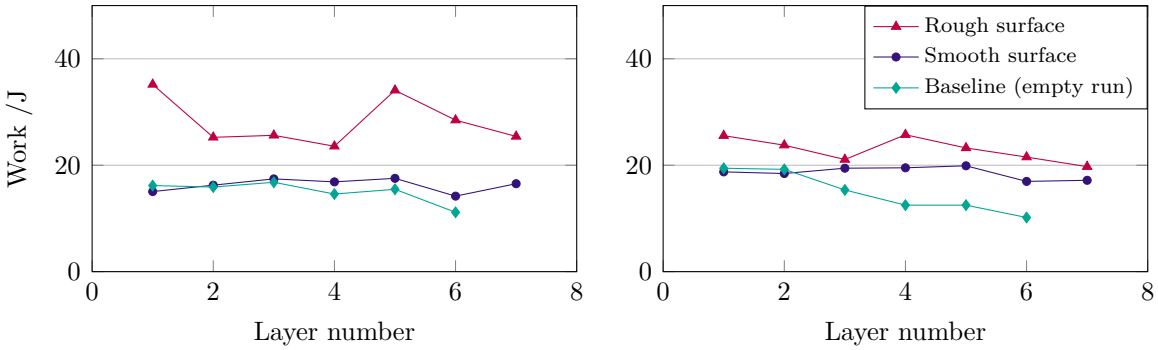

(a) Motor DC_1 (inner tube) **(b)** Motor DC_2 (closing disc)

Figure 8.11: Energy transferred through work for each powder deposition process run, for an empty machine (green diamonds), the smooth surface powder (blue circles) and the rough surface powder (red triangle), for the probing done by (a) the inner tube and (b) the closing disc.

From the torque developed by the rotation of the inner tube (Figure 8.11a), the change due to a different feedstock material is clearly recorded: for the high flowability powder with smooth surface, the torque is almost the same as for running the machine empty, which shows that the energy needed for this powder to flow is at the boundary of the apparatus' sensitivity. On the other hand, the rough surface powder, which shows mediocre flowability, requires a much higher energy input to flow: the work per layer deposition has a mean value of 28.22 J, 73% higher than for the *SS* powder, for the work displayed by the motor DC_1. This result holds true for every layer deposited. The variability in work of the series recorded by motor DC_1 is also much higher for the rough surface powder than for the smooth surface one, with respective coefficients of variations[1] of 16% for *RS* against only 7% for *SS*.

The torque recorded by the motor DC_2 shows the same trend, but much less emphasised: all records of energy transferred per layer are in average 20% higher for the rough surface powder than for the other one. The work displayed by the closing disc hence also shows a dependence on the type of powder-feedstock probed, albeit less strongly. It is hypothesised that a small empty volume at the top of the powder bed might appear after filling, resulting from the powder being drawn downward before the volume reduction induced by the descent of the closing disc. As can be seen in Figure 8.4, the blades perpendicularly attached to the closing disc only penetrate the powder bed on 10 mm: if the closing disc is not sufficiently immersed into the powder bed, the torque recorded is lower and does not fully reflect the rheological response of the feedstock material.

The *flowability number Fl* proposed in Eq. 8.3 can be calculated from the torque recorded by the rotation of the inner tube and closing disc integrated over the deposition time, as presented in Figure 8.11a; values are given in Table 8.4 for the powders of high and mediocre flowability.

Fl is one order of magnitude lower for rough surface powder than for smooth surface powder: it is around unity for the *RS* powder characterised as *low flowability* in Chapter 2, while it is superior to one (even superior to ten in the case of mono-directional probing) for the smooth surface powder *SS* characterised as *high flowability*. Based on this consequent increase of the total energy transfer necessary to process the rough surface powder, the decrease in the "ease to flow" – shown in Chapter 2 to be due to the increased surface roughness activated

[1]The coefficients of variations, given in percent, represent the variability of the data set as compared to its mean value; it is the ratio of the standard deviation by the mean value.

Table 8.4: Dimensionless number Fl proposed in Eq. 8.3 to compare the powder handling process studied, applied to different materials, and labelled *flowability number*. It is calculated from the work recorded by the inner tube mono-directional probing, on-ground, for powder with smooth surface (high flowability, SS) and rough surface (mediocre flowability, RS).

	Smooth surface powder	**Rough surface powder**
Mono-directional probing	$Fl^{1g}_{SS} = 12.0$	$Fl^{1g}_{RS} = 1.1$
Oscillatory probing	$Fl^{1g}_{SS} = 4.0$	$Fl^{1g}_{RS} = 1.8$

through interparticle friction at high packing fraction – is recorded by the RheoPrint process, and reflected in the *flowability number* Fl. The *in-situ* torque recording reliably probes the rheological properties of the feedstock material.

8.2.2 Dependence of homogenisation time on powder nature

As seen in Section 5.2 (Figure 5.7), two means can be used to monitor *in-situ* the powder deposition process: the torque recorded during deposition as seen above, and the observation from below of the new layer while it is being deposited. This direct observation offers access to the time needed before the new layer homogeneously covers the bottom: the *homogenisation time*. Dependence of the homogenisation time on powder surface state is examined in Figure 8.12, per layer. It should be noted that the material deposition step lasts 20 s for all layers deposited; the durations shown in Figure 8.12 correspond to the time necessary for the powder layer to regain the homogeneity it had before the start of deposition, indicated by the variance of the image recorded (see Section 8.1). The criterion used to determine that layer homogeneity has become optimal is the decay of variance back to 1.2 times its starting value.

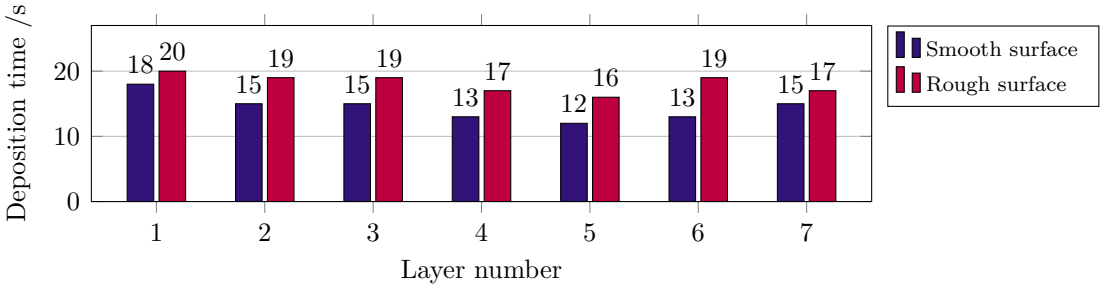

Figure 8.12: Deposition time necessary to observe homogeneous layer from the solidification window, recorded on-ground for smooth and rough surface powder.

The time needed for homogenisation of rough surface powder is always higher, in average by 4 s, than the time necessary for smooth surface powder. Besides, variability in homogenisation time is slightly higher for RS powder, with a standard deviation of 2 s *versus* 1.5 s for the SS powder: on-ground, rough surface powder requires more time to be homogeneously deposited, and is more subject to variations. This emphasises the importance of having a variable deposition time, adaptable to the type of powder fed into the process, for optimisation of process duration.

8.2.3 Density of parts manufactured on-ground & porosity size distribution

Computed tomography snapshots are presented for a "slice" of two samples 3D printed on-ground, from smooth surface powder (Figure 8.13) and rough surface powder (Figure 8.14). Both samples were obtained using exactly the same printing parameters; in particular, the same deposition time and solidification time of 20 s each, the same layer height of 500 µm and compression ratio of 50% – i.e. the printing platform rises by 1000 µm before each deposition step, then descends by 500 µm, compressing the newly deposited layer. No compression was applied during sintering to provide as much information as possible on the powder deposition. Figures 8.13 and 8.14 respectively show samples comprised of eight and seventeen layers.

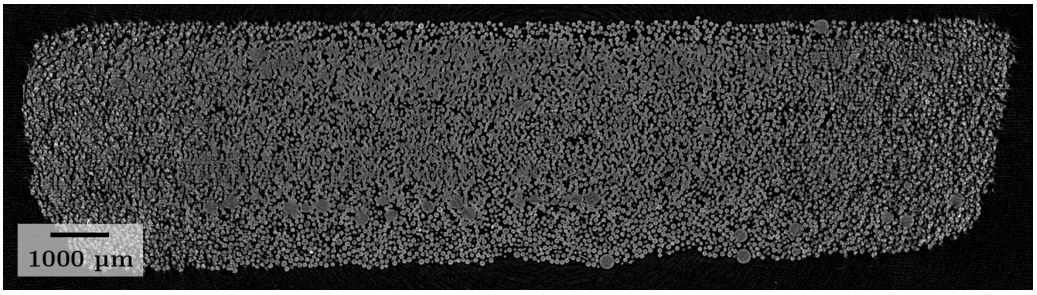

(a) "Slice" of computed tomography of sample

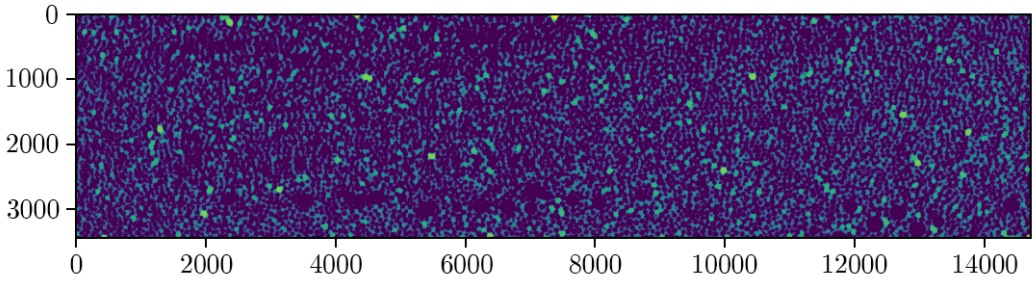

(b) Local porosity radius

Figure 8.13: Example of (a) CT "slice" of the sample 3D printed from smooth surface powder, on ground, and (b) graphical representation of the corresponding porosity size distribution.

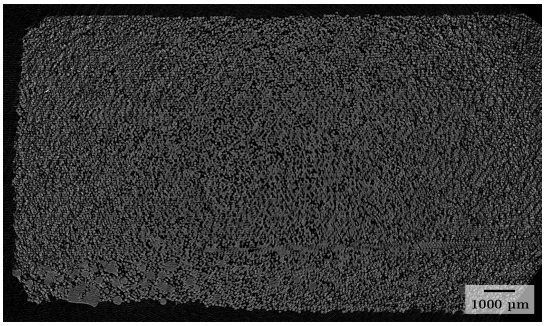

(a) "Slice" of computed tomography of sample

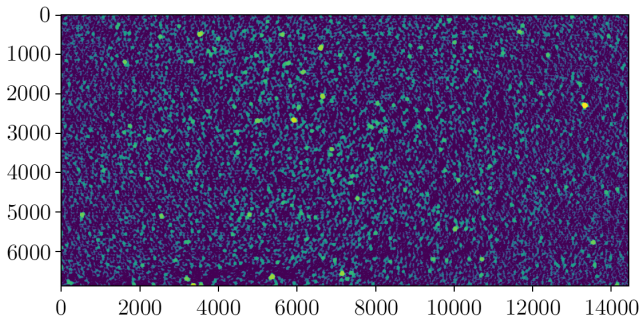

(b) Local porosity radius

Figure 8.14: Example of (a) CT "slice" of the sample 3D printed from rough surface powder, on ground, and (b) graphical representation of the corresponding porosity size distribution.

Already with the naked eye, some interesting features can be observed. In Figure 8.13, on the lower part of the image, some grains have coagulated and create no-porosity spherical

zones of diameter approx. 300 µm. Such events can also be observed on the *RS* sample in Figure 8.14. The top-part of the *SS* sample is more loosely sintered, which can be linked to the last layer deposited being sintered only once: in the process, each layer deposited is approximately 500 µm, but each sintering step heats 1 mm in order to ensure good adhesion among layers. The last layer deposited, placed here on top of the image, has been sintered only once, therefore it remains looser.

All porosities display a relatively spherical shape, and are homogeneously distributed through the sample, with neither a preferred direction nor obvious signs of delamination between layers. Notably, the 500 µm-high layers cannot be distinguished with bare eye, although the samples each comprise multiple layers. The porosity size distribution is quantified in Figure 8.15, where the probability density function is presented for the reference "known good" sample sintered on-ground under weight (Figure 8.15a), the *SS* (Figure 8.15b) and the *RS* sample (Figure 8.15c).

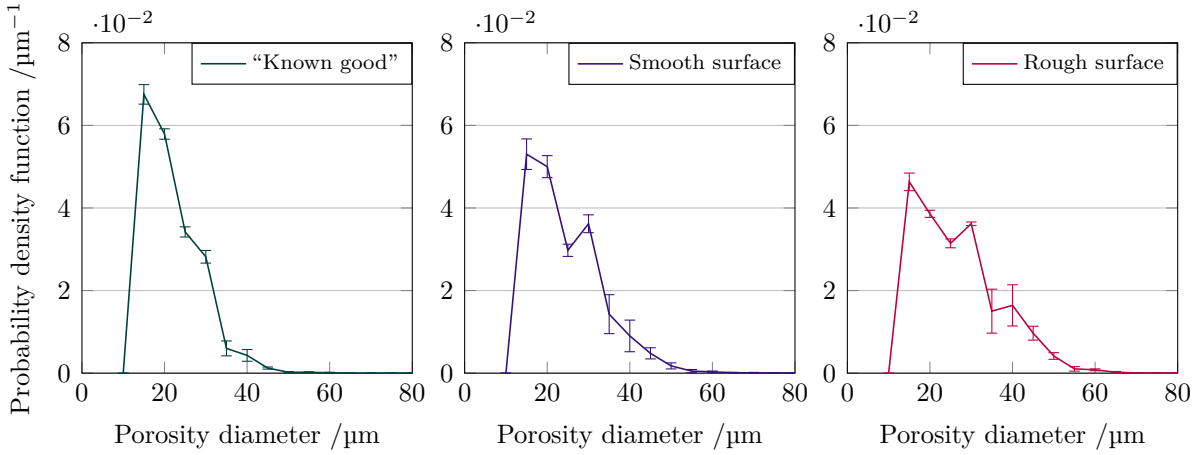

(a) Reference sample, 1*g* **(b)** Smooth surface, 1*g* **(c)** Rough surface, 1*g*

Figure 8.15: Probability density function per porosity diameter for (a) the comparative sample sintered on-ground under weight, (b) a sample 3D printed from smooth surface powder on-ground and (c) a sample 3D printed from rough surface powder on-ground. The analysis is run for one image every 80 µm, along the y-axis, and the average over the full sample is shown here; error bars represent the standard deviation in density probability per diameter for the full sample.

Comparison between the three samples shows many similarities: all have most porosities in the range of 10 µm to 20 µm, which is coherent with voids remaining among a dense randomly packed assembly of mono-dispersed particles of diameter 80 µm. The sample sintered under weight has the largest amount of small porosities (10 µm to 20 µm diameter), which shows best powder repartition, confirming its use as a comparative sample for "known good" powder repartition. The 3D printed samples also show the highest peak in porosity probability density for small porosities; however for both material-qualities, a second peak appears at 25 µm. Most importantly, large porosities of 40 µm to 60 µm have a low probability of appearance in the "known good" sample, which doubles in the *SS* sample, and triple in the *RS* sample. Besides, larger variability in this range, represented by the error bars in Figure 8.15, shows that some of such porosities are scattered throughout the sample.

The *RS* sample has generally larger porosities than the *SS* sample; to verify the impact of porosity size distribution on the overall density of the samples, the average density is calculated for the three experiments, as shown in Figure 8.16.

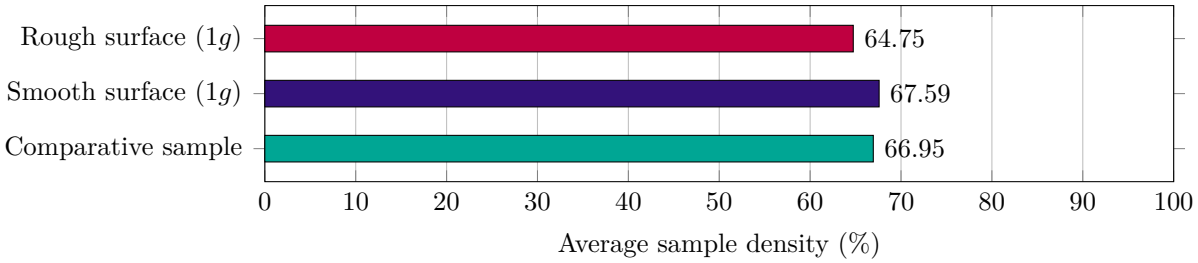

Figure 8.16: Average density of the three samples manufactured on-ground: the sample sintered under weight to obtain high powder density as a comparative for "known good", the sample 3D printed from smooth surface powder under $1g$, and the sample 3D printed from rough surface powder under $1g$.

As the samples are sintered and not melted, the average density value of a high quality 3D printed samples is expected around random close packing for mono-dispersed packing, i.e. slightly higher than 64%, the theoretical highest density value for a sample that is not crystallised [150, 153]. The average densities obtained by 3D printing samples on-ground are higher than 64%, showing almost the same for the "known good" sample sintered during compaction under weight and for the SS sample, reaching 68% density, and only 3% lower for the RS sample. Regardless of the large difference in torque developed during material deposition, and of the fact that the same printing parameters are deployed for both types of feedstock material, the average density is very similar for samples SS and RS. Although the higher porosity density is reflected in the lower average density of the RS sample, those results are very promising, as they show that powder of mediocre flowability *can* be used as base-material for additive manufacturing without resulting in heterogenous layer deposition and that by adapting the process to such type of material, similar results can be obtained as for high flowability powder.

8.3 A gravity-independent process?

Beyond theoretical considerations (see Chapter 5) and proof of concept by simulation (see Chapter 6), a demonstration of the RheoPrint principle for handling and 3D printing powder in microgravity was obtained on parabolic flight. Five samples were printed in microgravity on a three-days campaign of parabolic flights, using two prototype 3D printers (see Chapter 7). Figure 8.17 shows the PFC experimental plan, as well as the resulting samples for the first and third campaign days.

The statistical analysis that can be made from Figure 8.17a leads to a positive assessment of the process: only one sample failed to be correctly manufactured – sample $L1$, printed from rough surface powder on the first day of campaign, shown as Figure 8.17c. This failure was due to a technical problem within the temperature control system, alternating periods of over-heating leading to melting of the powder layer, and periods of lack of solidification energy. The sample picture shows a cavity in the middle of the sample, where the powder was molten. Although the powder deposition functioned well, the resulting sample shows a highly heterogeneous density and delamination. It will be used for comparative analysis in the following investigation as a "known bad" sample. The failure of the solidification control loop was corrected on the second day of campaign, and all remaining experiments were successful. The first sample 3D printed in microgravity is shown in Figure 8.17b, as directly extracted from the machine post-flight; both samples printed on the third campaign day are presented in Figures 8.17d and 8.17e: they show perfectly homogeneous surface and no obvious defects

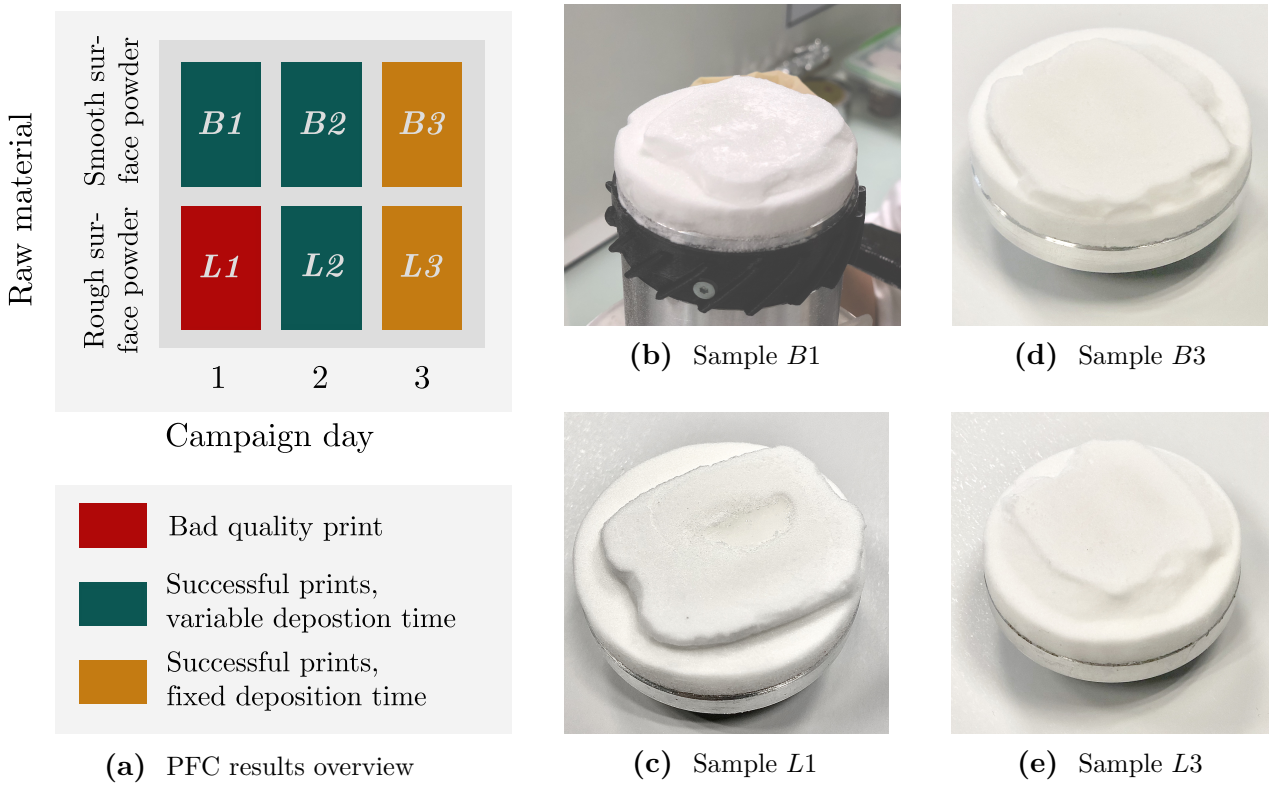

(a) PFC results overview

(b) Sample $B1$

(c) Sample $L1$

(d) Sample $B3$

(e) Sample $L3$

Figure 8.17: Overview of PFC results, including (a) experimental planning and results overview, and (b) to (e) samples fully manufactured in microgravity. In (b), sample $B1$ is shown directly as extracted from the 3D printer.

in the powder repartition (e.g. holes or molten areas). The variable printing parameters per flight day (i.e. duration of the material deposition and solidification steps) are summarised in Table 8.5.

Table 8.5: Printing parameters used during PFC to 3D print samples in microgravity from smooth and rough surface PS powders. All other printing parameters remain constant. Given the specificities of parabolic flights as microgravity platform (see Section 7.2), each step of the process must be done within 20 or 40 s.

	Day 1	**Day 2**	**Day 3**
Deposition time	40 s	40 s	20 s
Solidification time	20 to 40 s	20 s	20 s

Samples printed in microgravity as well as information recorded in-flight on powder deposition are analysed to gain better understanding of the successes and failures of the 3D printing process. Firstly, the rheological data recorded in-flight enables to assess the feasibility of parameters adaptation through *in-situ* probing.

8.3.1 Torque recorded in-flight during material deposition

The qualitative evolution of the torque recorded is observed for all layers for samples 3D printed in microgravity from smooth and rough surface powders, respectively Figures 8.18a, 8.18c and

Figures 8.18b, 8.18d (corresponding to the data collected from the inner tube and the closing disc motion).

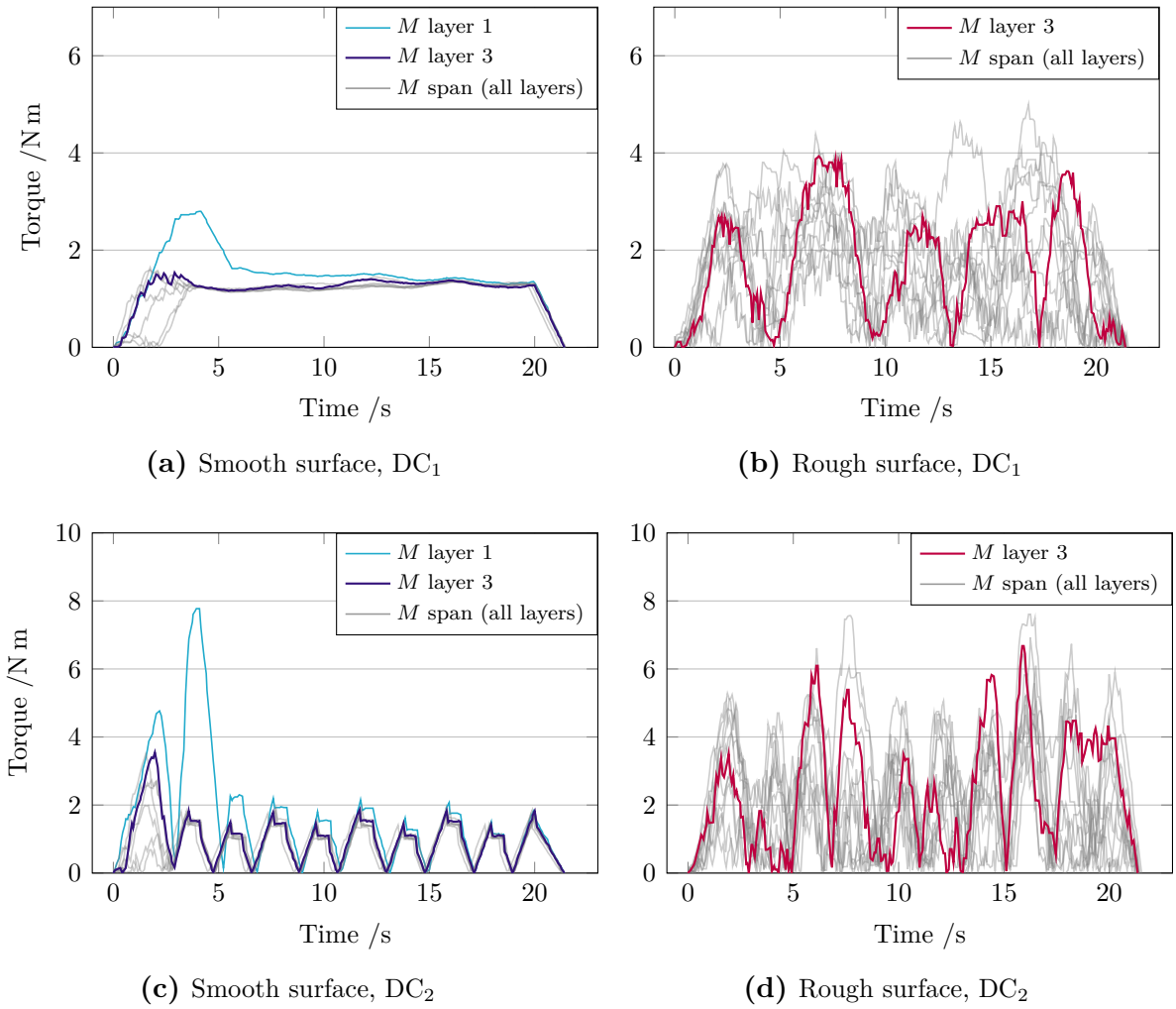

(a) Smooth surface, DC_1 **(b)** Rough surface, DC_1

(c) Smooth surface, DC_2 **(d)** Rough surface, DC_2

Figure 8.18: Temporal torque evolution for all layers (in light grey) and one hand-picked typical layer (coloured, layer number indicated in legend), for (a) and (c) smooth surface powder, (b) and (d) rough surface powder. The first layer for the *SS* sample is represented in dark grey. Powder deposition (followed by solidification) was realised fully in microgravity. The experiments shown here are, in the experimental nomenclature, experiments $B3$ and $L3$, hence manufactured with a fixed powder deposition time of 20 s.

Comparing the torque recorded by the same motors, on the same flight-day, for both powders (i.e. comparison between Figures 8.18a and 8.18b or between 8.18c and 8.18d), an unambiguous difference is observed. The smooth surface powder produces extremely well defined torque, with very small transient period at the start of motion, and extremely high reproducibility: all layers presented in Figures 8.18a and 8.18c fall almost perfectly on top of each other, merging into one line. (One outlier remains: the first printed layer, represented in dark grey, which requires a higher torque to set the packing into motion for the first time.) Samples printed from rough surface powder show another extreme. Firstly, the torque recorded using rough surface PS powder as base-material is generally higher for the same deposition time. Moreover, variability from one layer to the next is very high; the span is always similar (0 to 4 N m), but with large oscillations, observed similarly for inner tube and closing disc probing. More specifically, two frequencies of fluctuations add-up in the rough surface powder experiment: on one hand, a low-

frequency oscillation appears, on the order of 0.25 Hz, hence with similar frequency as the slight oscillation observed on-ground and linked to the apparatus (see Figure 8.10 in previous section). On the other hand, high-frequency torque fluctuations appear in addition, at a frequency on the order of 2 Hz, which is directly linked to the base-material probed. As this is not observed for the same material on-ground, it emerges as a specificity of the microgravity environment.

The high-frequency fluctuations in torque for shearing the rough surface powder relate to the appearance of stick-slip phenomena [75, 271]: we observe an alternation of phases of stress build-up as the powder is under mechanical drive, but friction between particles surfaces sets a yield stress, under which the present configuration remains stable. It is the stress increase phase; it is followed by a yield phase, once the stress becomes high enough to trigger powder flow. The packing is forced into a new configuration, hence the stress drops. Then, this configuration becomes the new stable one and the same phenomenon is repeated, leading to a sequence of peaks and drops in the stress displayed. Figure 8.19 exhibits a zoom-in on the torque fluctuations recorded by the motor DC_1 to find the length-scale at which this stick-slip phenomenon occurs in our system.

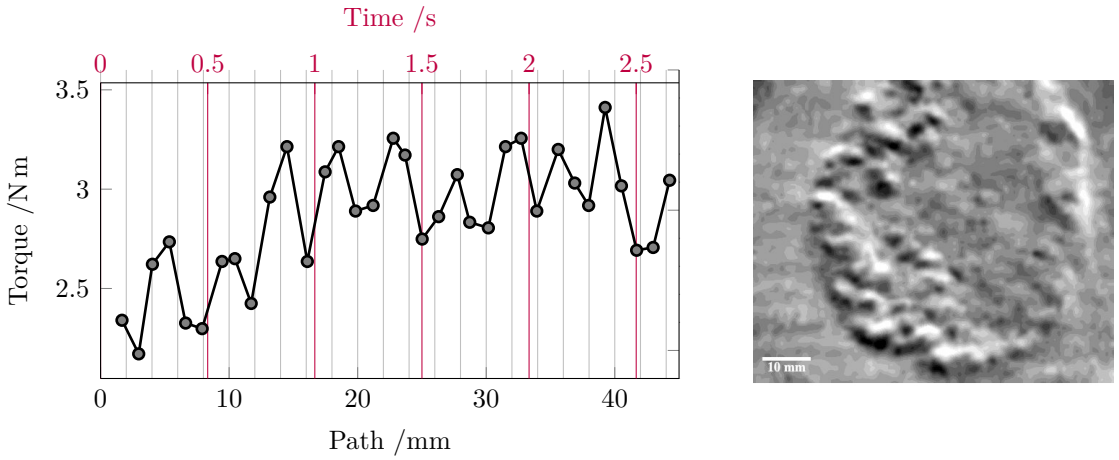

Figure 8.19: (a) Close-up of the high-frequency torque fluctuation observed when shearing rough surface powder, as a function of time (top scale, red) and equivalent path traveled at the surface of the inner tube rotating (bottom scale, black). (b) Image capture of the powder layer homogenisation, corresponding to the moment at which the torque is recorded. The specific experiment shown here is the powder deposition $L2L2$, i.e. rough surface powder deposition, on second flight-day, for the second layer of the sample. However, all experiments show qualitatively the same trend.

The torque is displayed in Figure 8.19 as a function of time (in red) but also of "path" (in black): the length travelled by one point rotating on the surface of the inner tube. Consequently, the frequency of the stick-slip motion can be linked to the length-scale at which the alternating formation and destruction of material aggregates happens: during stress build-up, the inner tube covers a path of 2 to 3 mm at its surface. The image recored during powder homogenisation in microgravity, reproduced in Figure 8.19b for the layer corresponding to the torque record in Figure 8.19a, shows the formation of powder clusters, advancing in a wave-like manner towards the centre of the printing area during shaking. The size of those clusters, observed from the bottom of the container during homogenisation step, was verified for all layers of the samples $L2$ and $L3$, during the first 15 s of the powder deposition (after, they coalesce into a more

homogeneous layer). Their average diameter is 4.7 mm^2, which is on the same length-scale as the distance covered by rotation of the inner tube during one period of the torque oscillation. Sub-divisions of a granular assembly into clusters moving as rigid blocks has been previously reported in sheared granular samples (in 2D) [19]. The interpretation proposed to explain those observations is that in microgravity, the rough surface powder under drive forms clusters in the millimetre length-scale which are then deformed and broken under shear, producing stick-slip behaviour identified through torque oscillations. The increased surface friction of the particles in a dense packing results in the high stability of grain configurations, as motion of particles among each other requires much higher stress compared to the smooth surface case.

A quantitative analysis of the torque developed is also conducted; Figure 8.20 summarises the work developed per powder deposition step, for both powders, in microgravity. The work is calculated following Eq. 8.2 for the experiments conducted in the third flight day ($B3$ and $L3$): the powder deposition is fully done in one parabola, i.e. within 21 s, for both powder, to enable comparison.

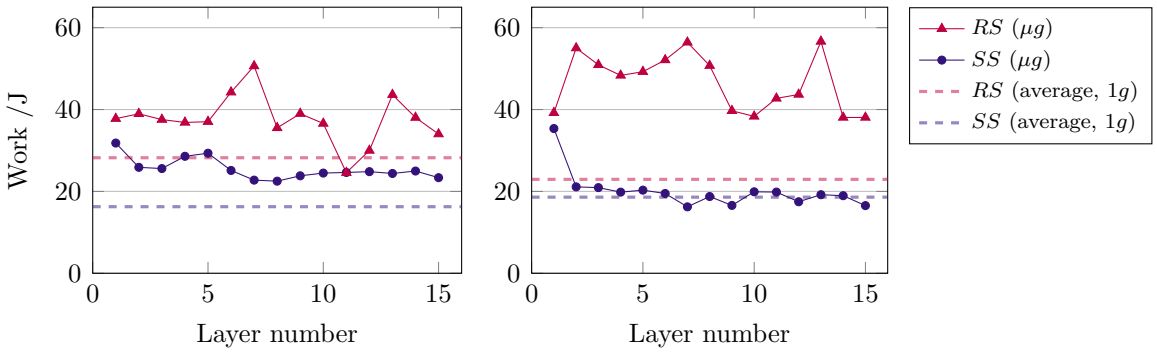

(a) Motor DC_1 (inner tube) **(b)** Motor DC_2 (closing disc)

Figure 8.20: Energy transferred through work for each powder deposition process, in microgravity, for the smooth surface powder (blue circles) and the rough surface powder (red triangles); the probing is done by (a) the inner tube and (b) the closing disc. Average values are given for the work recorded on-ground, as a reminder, for the same powders.

As with the measurements done on-ground (from which the average value per probing mechanism is reproduced here from Figure 8.20), the work developed in microgravity to shear the rough surface powder is higher than for the smooth surface powder: the work developed to rotate the inner tube is in average 38 J for RS, 48% higher than for SS. This difference is even stronger in the results obtained with the closing disc, with an average value more than twice higher for RS. Results obtained with rough surface powder also show slightly higher variability: the coefficient of variation for RS is 16%, against 10% for SS, for the torque recorded by DC_1. In the data set obtained with DC_2, the first layer of the SS sample is an outlier as it requires almost double work to be deposited; removing it, the standard deviation falls from 14 J for RS to 5.3 J for SS. Peaks happen on the same layer for both probing mechanisms, showing that a general difficulty to flow is encountered for some layers, and firmly linking those variations to specific events happening in the powder bed and not random experimental variations or motor malfunctions in microgravity.

[2]The diameter of powder aggregates observed during powder homogenisation is calculated for samples $L2$ and $L3$ using the fully automatised procedure proposed by the software ImageJ, consisting of setting a threshold in grey-level to make the image sequence binary, and running the *Analyse Particles* macro to measure the diameter of each particle per image, which is then averaged.

Generally, microgravity seems to deteriorate the flow properties of both materials: the torque recorded for processing RS powder is not only higher, but also showing erratic behaviour and large variability. The response recorded by the machines show precisely the same trend as observed through rheological testing of the two powders on-ground (see Section 2.4): in a dense granular packing, the increase in surface roughness results in higher torque necessary to overcome surface friction, and in flow heterogeneities.

How can the same material, showing the same chemical composition, grain size and shape, and surface roughness, show such different properties on-ground *versus* in microgravity? As seen in Chapter 3, the absence of a secondary force field (in our case, gravity) lowers the ability of the packing to reorganise into new configurations. This hold true for the rough surface powder, but also for the smooth surface one. Without the alternative direction it produces, force chains within the ensemble of particles are solely due to the forces impelling flow in one direction. This leads to a decrease in flexibility of the grains reconfiguration, which in turn is exhibited by an increased stiffness of the packing as a network of contacts between particles.

8.3.2 In-flight data: powder layer homogenisation time

The influence of powder flowability on the powder deposition step in microgravity is also assessed by comparing the time necessary to complete the powder deposition step in two full microgravity experiments: $B3$ and $L3$, respectively done for smooth surface powder and rough surface powder. It is noteworthy to remind the reader that the deposition time is fixed (20 s per layer); what is observed here is the time necessary for the variance in the image recorded to decay back to its starting value. Figure 8.21a and 8.21b represent the variance in the image recorded of the powder layer deposition, normalised by its average value before t_0 (start of the deposition procedure, which coincides with the beginning of the microgravity phase – see Section 8.1).

The *type* of deposition observed is different: for the more flowable powder, the variance becomes very high (increases by up to an order of magnitude) and then decays steeply to its starting value. For rough surface powder, the layer homogenisation happens through formation of the clusters described above (see Figure 8.19). They remain for a long time (up to 19 s) before coalescing. The average time for powder homogenisation, calculated for samples $B3$ and $L3$, is 11 s for RS *versus* 10 s for SS. From the $1g$-data presented in Figure 8.12, deposition time is in average one third lower in microgravity than on-ground. This reduction of the deposition time can be explained by a reduction of the friction between the newly deposited layer and its surrounding container during layer homogenisation by shaking, herein reducing the energy loss by friction.

8.3.3 Density & pore size distribution for parts manufactured in microgravity

In the following analysis, three samples will be compared: the samples $B3$ and $L3$, respectively manufactured in microgravity from smooth and rough surface powder, on the third day of campaign, with the same fixed deposition and solidification time of 20 s, and the sample $L1$, the worst quality sample 3D printed in microgravity, used as exemplary model for "known bad" sample quality. Snapshots of CT slices are given in Figure 8.22 for the three samples.

The SS sample presented in Figure 8.22a shows a very dense and homogeneous general

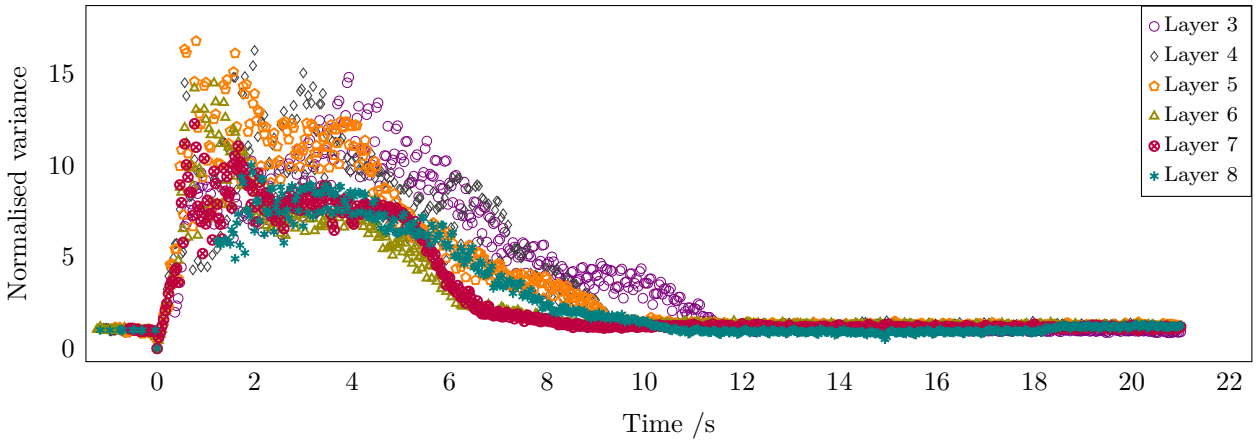

(a) Smooth surface powder

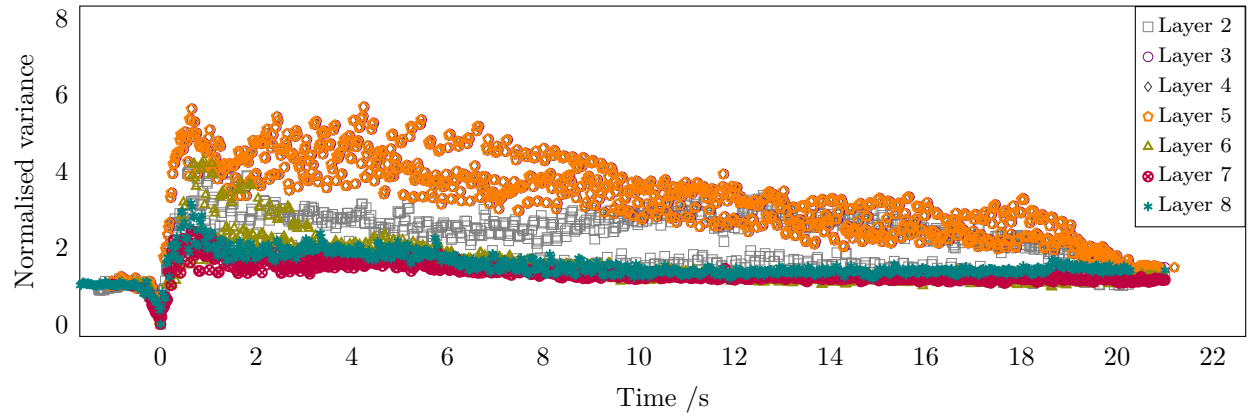

(b) Rough surface powder

Figure 8.21: Deposition time necessary to produce a new powder layer in microgravity, (a) from smooth surface powder and (b) from rough surface powder. The ordinate range is shorter on the bottom graph. The experiments shown here are, following the nomenclature explained above, samples $B3$ and $L3$. For both samples, the first layers are missing because they were not recorded.

appearance, very similar to the SS sample 3D printed on-ground. Figure 8.22b, featuring the RS sample manufactured on the first campaign day, is visibly less dense; however porosities are homogeneously distributed in the sample, with no outstanding defects. Finally, sample $L1$ in Figure 8.22c clearly shows the result of wrongly tailored solidification parameters. Instead of being sintered into homogeneous powder layers, overheating resulted in partial melting. As the empty space between grains becomes trapped into molten material, the volume loss is not counteracted by reduction of the printing bed volume – which could be realised in the present set-up by descending the inner tube. Therefore, the supplementary volume transforms into large porosities scattered along the sample. At the bottom of the sample, a fully molten layer of 1000 µm height shows that the solidification energy input was too high.

The general powder density of each sample can be compared for the three samples, hence verifying the quantity of material effectively deposited. The sample's volume-fraction of material (i.e. fraction of each slice occupied by material) along the y-axis presented in Figure 8.23 is calculated for the three samples presented in Figure 8.22, but also three samples sintered on-ground: the comparative sample sintered under weight, and samples 3D printed on-ground from rough and smooth surface powders. To ease comparison between the different gravita-

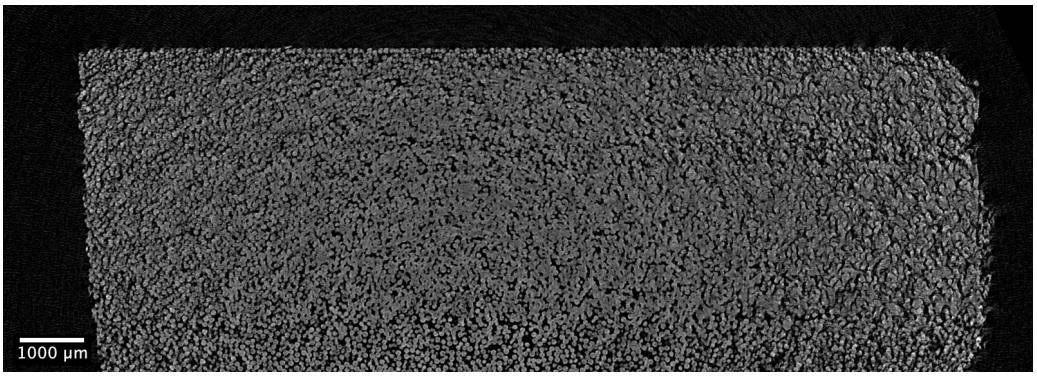

(a) Sample $B3$: smooth surface, μg

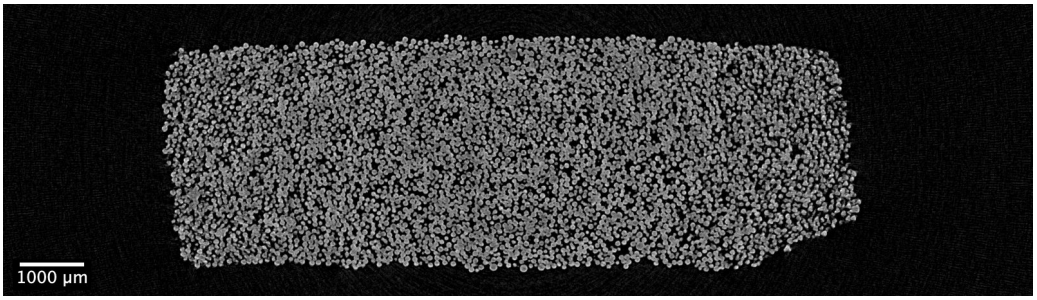

(b) Sample $L3$: rough surface, μg

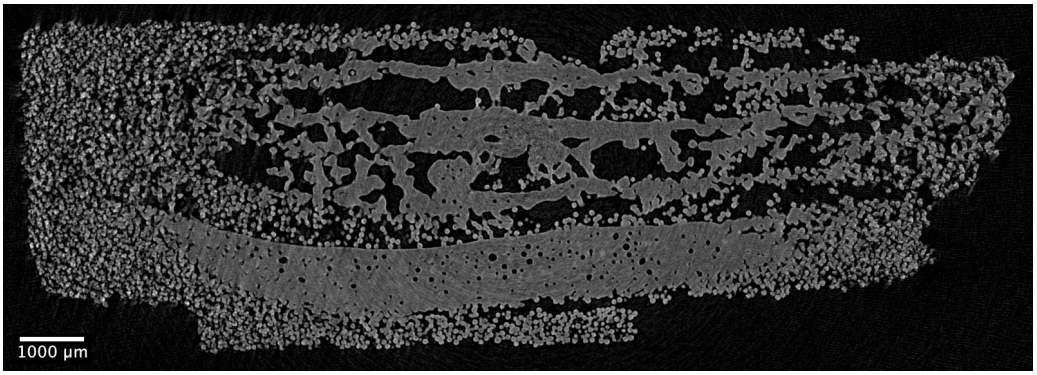

(c) Sample $L1$: rough surface, μg

Figure 8.22: Slice of CT of samples (a) $B3$, (b) $L3$ and (c) $L1$ of samples tomographies.

tional environments, samples analysed in Figure 8.23 are grouped by fabrication base-material. As volume-fraction calculations are obtained by analysis of the CT images, the density of material is given per xz-plane, along the y-axis. At y-length inferior to 0.5 mm and superior to 12 mm, reaching the extremity of the samples results in density drops.

Figure 8.23a shows that the two samples manufactured from smooth surface powder on-ground and in microgravity exhibit almost the same sample density, the microgravity manufactured one being higher by less than 2% on average. The "known good" sample analysed has a steady density level around 67%, making it in average as dense as the samples sintered from smooth surface powder. For rough surface powder, Figure 8.23b shows similar result: the density throughout the sample is very similar, with the ground-printed sample being in average 2% denser than the microgravity sample. The "known bad" RS sample shown in Figure 8.22c is also analysed. It shows surprisingly high powder content, with an average of 72% density, but also very high variability, as from one "slice" to the next the large porosities observed

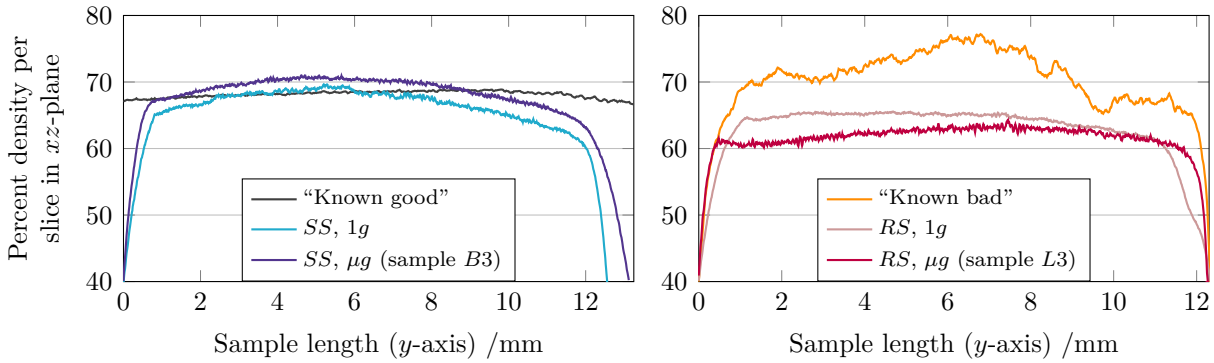

(a) Smooth surface powder

(b) Rough surface powder

Figure 8.23: Density of the 3D printed samples over their full length along the y-axis.

overtake most of the sample or are reduced to a minimal volume. This shows that regardless of the sample quality – unquestionably bad because of heterogeneous, large porosities – the amount of powder deposited is sufficient: although the solidification energy was overestimated, producing a highly uneven sample, the powder deposition procedure functioned and brought the necessary quantity of material to the printing bed.

Comparison between the two base-materials shows that the rough surface powder indeed packs less densely, may it be under Earth gravitational field or not: the RS samples are always approximately 5% less dense than the SS samples. It should be remembered in this regard that all samples are manufactured with the exact same printing parameters, regardless of their base-material, which allows to expect that this difference could be erased by a thorough experimental study to find the optimal parameters per base-material, and by implementing such optimal parameters set to be automatically picked through the control-loop described in Section 5.2.

For both types of base materials, slight variations exist throughout the sample; a slight drop in density at the extremities of samples can also be observed for all 3D printed samples, which lose 1 to 4 percent-density from the centre of the sample to its extremities along y-axis. This can be linked to the energy source used for solidification and to the sample selection procedure: as explained in Section 8.1, the samples are extracted from the centre of the printing volume, and if the middle of the sample is perfectly exposed to heat, the extremities in y fall outside of the high heat zone, and therefore are less exposed to sintering heat, hence less densely sintered.

Generally, we see that the density remains the same throughout the sample tested for each powder, regardless of the gravitational level in which it was deposited. The similarity between results on-ground and in-flight regarding density are very promising for the powder handling process. To verify if the porosity size distributions show essential differences between the samples printed on-ground and in microgravity, and if a preferred direction appears in one of those environments, the chord length analysis described in Section 8.1 is applied to the samples produced in μg and in $1g$, as shown in Figure 8.24.

The chord lengths are compared for porosity sizes along the x- and z-axis, to provide indication on the samples' anisotropy. To allow precise comparison of the different samples, each data set is fitted with a log-normal distribution, whose probability density function follows:

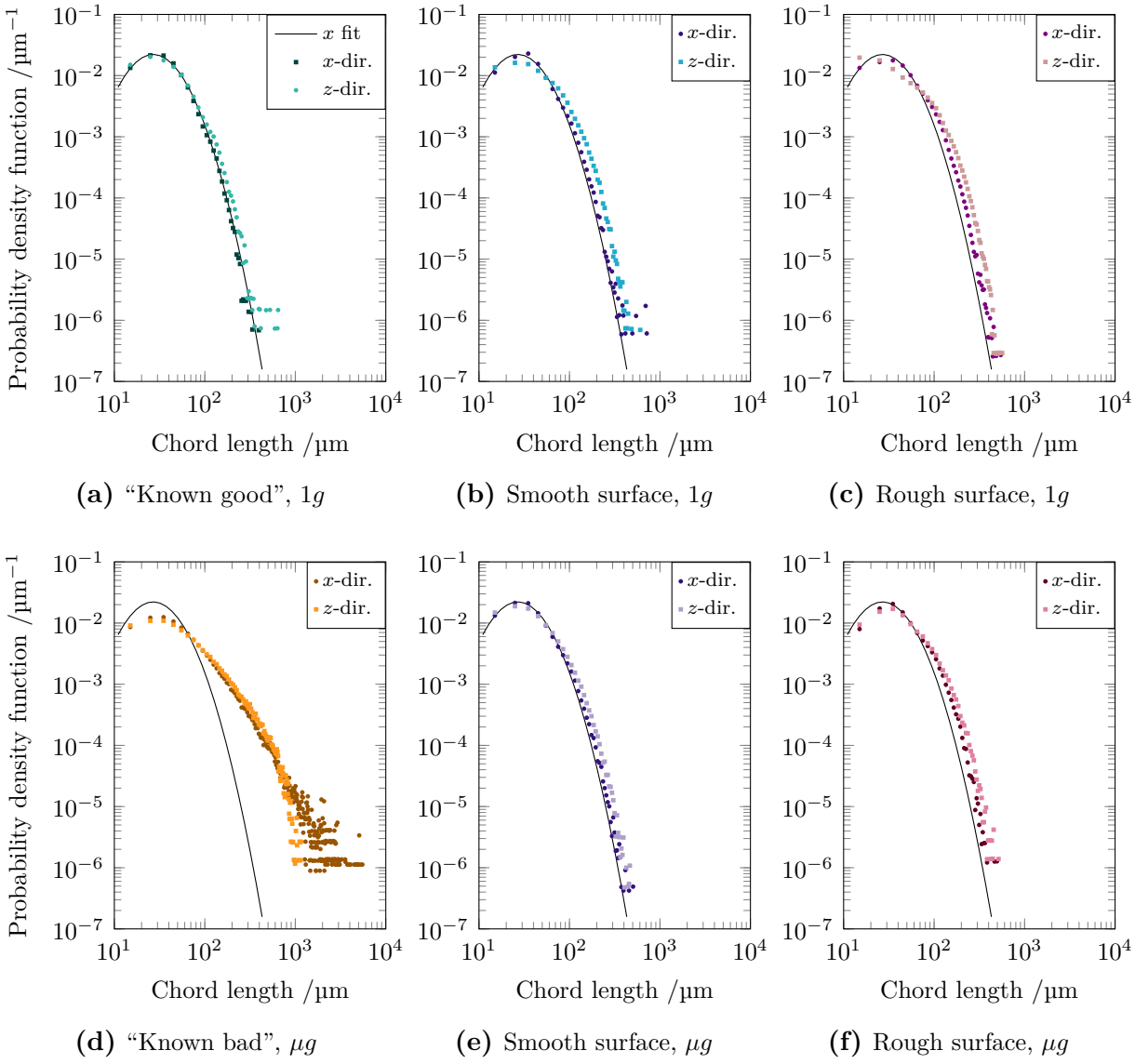

(a) "Known good", $1g$ **(b)** Smooth surface, $1g$ **(c)** Rough surface, $1g$

(d) "Known bad", μg **(e)** Smooth surface, μg **(f)** Rough surface, μg

Figure 8.24: Relative frequency of chord spanning porosities per chord length, for all samples studied, with chords extension done along x- and z-direction for each sample. The data sample for the comparative "known good" sample along the x-axis is fitted to a log-normal distribution (solid line), reproduced on all graphs for comparison.

$$p(x) = \frac{1}{x\,\sigma\sqrt{2\pi}} \exp\left(-\frac{(\ln x - \mu)^2}{2\,\sigma^2}\right). \tag{8.4}$$

The fitting parameters μ and σ, corresponding to the mean and standard deviation of the logarithm of the data, are presented for each sample in x- and z-direction in Table 8.6. The mean chord length $\langle l_{x,\,z}\rangle = \exp\left(\mu + {}^{\sigma^2}/_2\right)$ corresponding to each fit is also given to ease interpretation. The physical explanation behind the use of a log-normal distribution is as follows: if the pore size are randomly distributed in space, each large porosity will give rise to one longest chord spanning it, but also twice the amount of smaller chords around the longest one; hence each addition of a long chord also slightly rescales the distribution. The amount of small chords is therefore not fully independent from the amount of long chords. In the log-space, multiple consecutive rescaling add so that the *logarithm* of the chord lengths is expected to be normally distributed. Previous work involving the distribution of geometrical shapes enclosed within

randomly distributed voids also use the log-normal distribution [272].

Table 8.6: Fitting parameters used to fit the chord length probability density obtained for each sample in x- y-directions to the log-normal distribution, $\mu_{x,z}$ and $\sigma_{x,z}$, and mean chord length $\langle l_{x,z} \rangle$. $\langle l \rangle$ is given in µm.

Sample reference	μ_x	σ_x	$\langle l_x \rangle$	μ_z	σ_z	$\langle l_z \rangle$
Comp. "known good"	3.6	0.57	44	3.7	0.63	48
Smooth surface, $1g$	3.7	0.57	48	3.8	0.65	57
Rough surface, $1g$	3.9	0.54	56	3.9	0.67	60
Comp. "known bad"	3.9	1.1	92	4.1	1.1	110
Smooth surface, μg	3.7	0.58	47	3.7	0.64	51
Rough surface, μg	3.8	0.59	56	3.9	0.67	60

For the "known good" sample (Figure 8.24a), showing highest packing density, without surprise the mean chord lengths are the lowest of all experiments. They are also very close in size, with $\langle l_z \rangle$ being larger than $\langle l_x \rangle$ by only 4 µm. This confirms the use of this sample as exemplary for high density and homogeneous repartition of the powder, linked to its manufacturing procedure: the sample was densified by tapping and sintered under weight to allow for compaction of the packing during sintering. The solid line representing the log-normal fit for the data series in x is represented in Figure 8.24a and reproduced on all panels of Figure 8.24 to offer a baseline, easing comparison between samples.

Comparison of the 3D printed samples to this baseline shows that they all undergo a mild but notable increase in porosity size. This is due to the fact that the comparative sample is sintered continuously under weight, applying a constant pressure to allow porosities to close during solidification, while the 3D printed samples are all put under a fixed amount of compression (i.e. compressed to a fixed height z, but not under fixed pressure) and then sintered. In other words, the compression is not maintained constant during solidification. This is necessary for providing an assessment of the process by observing the powder repartition, but a constant compression pressure could be maintained during the solidification step in further manufacturing campaigns to decrease porosity size and thereby increase sample quality.

The sample 3D printed from SS under $1g$ shows a shift in chord length along the z-axis, stronger than for the sample manufactured in μg; the ratio $\langle l_z \rangle / \langle l_x \rangle$ is equal to 1.2 for the $1g$ sample, against 1.1 for the μg sample, which is the sample showing highest isotropy of all samples. Visible in the graphs by comparing Figures 8.24b and 8.24e, the presence of gravity leads to a small anisotropy by having pores slightly elongated in the z-direction. Comparison between Figures 8.24c and 8.24f also reveals that for the RS samples, the porosities seems to also show a slight z-elongation, however not captured by the fit, which gives similar mean chord lengths $\langle l_x \rangle$ and $\langle l_z \rangle$ for the $1g$ and μg samples.

Among the two powders used as base manufacturing material, the two SS samples (Figures 8.24b and 8.24e) have generally smaller porosities than the RS samples (Figures 8.24c and 8.24f), whose distribution is shifted by approx. 10 µm towards larger chord lengths. This can be related to the general porosity of the different samples shown in Figure 8.23: regardless of the environment in which the samples were manufactured, the good quality RS samples are slightly less dense than the SS samples. As stated previously, this is due to the lower ability

of the rough surface powder to pack densely: higher surface friction leads to lower grain mobility, which results in a less dense packing. We observe this phenomena in both gravitational environments and orientations.

Finally, an interesting observation lies in the "known bad" sample's chord length probability (Figure 8.24d). The distribution shows a long tail at large chord lengths $l_{x,y} \geq 10^3$ µm in x-direction, which does not appear along z-direction, indicating the long horizontal porosities due to delamination between layers, clearly visible in Figure 8.22c. This shows an exemplary anisotropic sample with preferential direction of porosity growth along the x-direction. Comparison with the log-normal fit from the "known good" sample also shows that at small chord length $l_{x,y} \leq 10^2$ µm, the probability density is smaller for the heterogeneous sample, populated mostly by larger porosities. The porosities are hence larger in general in most of the sample, as well as largely isotropic with a strong x-direction elongation.

The main conclusion from this analysis of the samples' anisotropy is that apart from a minute elongation of porosities along the z-axis in the ground-manufactured samples, the porosity chord length distributions are very similar to the comparative "known good", and show high isotropy for all samples printed. The decrease in density of the RS samples is linked to an increase in porosity size, but not accompanied by the appearance of defects in the deposition. The quantity of material brought to the printing area, as well as the homogenisation time (representing the amount of material brought down and then to the printing-bed centre), are sufficient. Having shown that the porosity shapes are isotropic (for all samples except the "known bad"), they are approximated by spheres to compare the probability density per porosity diameter in the different samples in Figure 8.25.

An obvious difference in pores size for the "known bad sample" can first be remarked. The pore size distribution of this sample is reproduced in the inset of Figure 8.25b in a more adapted scale, as its porosity diameter distribution has a much longer tail than all other samples, with a low density probability of small pores under 50 µm-diameter and some very large pores up to 700 µm-diameter.

Apart from this outlier experiment, from the probability density per porosity diameter we draw the same conclusions as from previous analysis strategies. It confirms that a clear difference between base materials can be made: even if the distribution is relatively close, with two peaks at porosity diameters 15 µm and 30 µm, for the smooth-surface samples the smaller porosity size is almost twice more likely to appear while for the RS, the two porosity-diameters are almost as likely to appear. This clearly shows that the lower average sample density encountered on the RS samples is due to a higher amount of larger porosities of diameter 25 µm to 45 µm, albeit those porosities being distributed evenly throughout the samples. Besides, it confirms that the samples printed on-ground and in microgravity from their respective base-materials show very similar porosity distribution: within experimental error, the gravitational environment in which the samples have been manufactured does not play a role in the quality of the powder deposition in the RheoPrint process.

This analysis of samples 3D printed under gravity and in absence thereof shows that the powder deposition is realised as efficiently, on-ground as in microgravity, for both powder-types used as demonstrators. High reproducibility is found between samples manufactured from the same base-material in both gravitational environments, with a very homogeneous pore size distribution and isotropy of the samples. The ground-printed samples show slightly higher anisotropy. A difference between samples realised with each base materials persists, which is

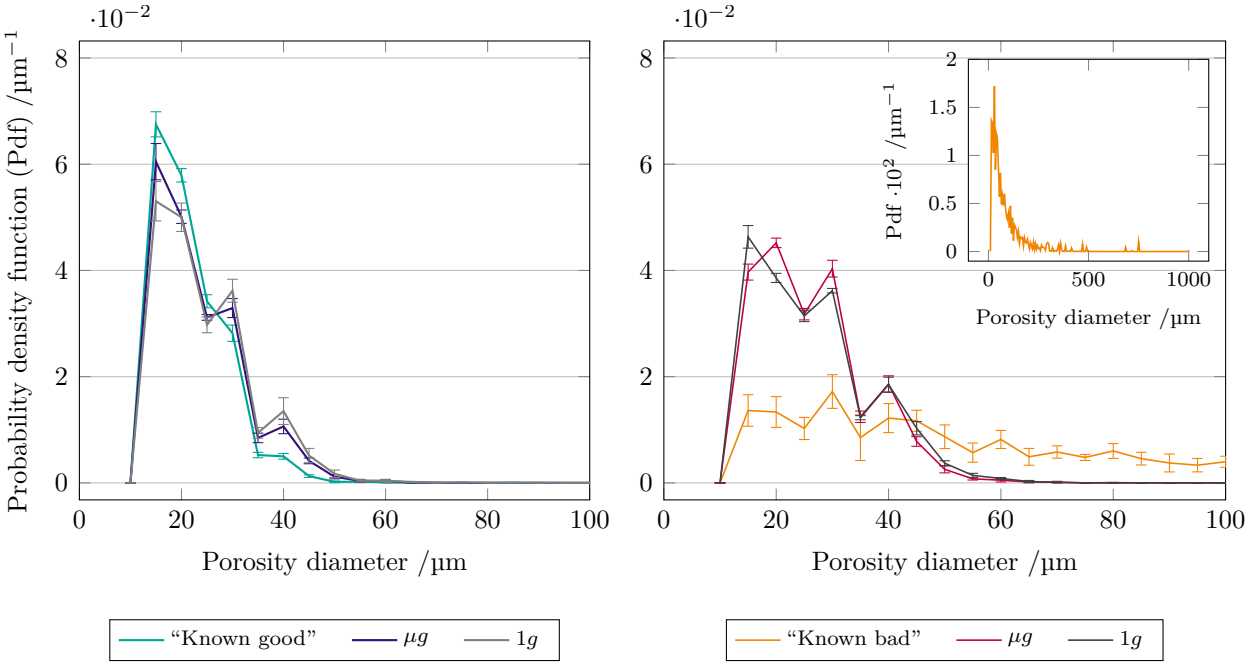

(a) Smooth surface **(b)** Rough surface

Figure 8.25: Probability density function per porosity diameter for (a) the comparative sample sintered on-ground under weight, and samples 3D printed from smooth surface powder on-ground and in microgravity. (b) Sample 3D printed from rough surface powder, on-ground and in microgravity, including the "known good" and "known bad" samples for comparison. The analysis is run for one image every 80 µm, along the y-axis, and the average over the full sample is shown here; error bars represent the standard deviation in density probability per diameter for the full sample. The inset in (b) shows the "known bad" data over the full range.

attributed to the lower ability to pack densely for rough surface powder (see Chapter 2). It is also noteworthy that printing parameters used were exactly the same for both materials, on-ground and in microgravity, rising the expectation that the rough surface powder could be more densely packed by finding the optimal printing parameters, in particular increasing compression before and during solidification. Within experimental variations, all powders are handled by the process with precision and efficiency, regardless of the gravitational field.

8.4 3D printing recycled material

8.4.1 Recycled powder: physical & rheological characterisation

The possibility to use as base-material powder produced from direct recycling, would be a strong asset for a manufacturing process for space applications. This represents an important challenge for a powder-handling process, as such materials show very high variability in flow-properties, emphasised by the multiplicity of recycling methods available and the absence of normalised recycling procedures for additively manufactured components. To conclude the testing campaign presented here to assess the possibilities and limitations of the RheoPrint process, samples were manufactured directly from powder obtained by closed-loop recycling.

Former samples manufactured on-ground using the studied process, from PS powders with both smooth and rough surface state (similar to the samples examined in Section 8.2), were ground to a particle size in the range of 50 µm to 500 µm. The machine used to produce the recycled material is a commercial grinder from the manufacturer WMF (Germany, formerly *Württembergische Metallwarenfabrik*), model Skyline, equipped with metal grinding burr; the printed material is processed by going through the two conical burr grinding wheels while they are describing a counter-rotation. The new feedstock powder hence produced is constituted of grains with highly variable geometry, surface state and size. Microscopies of the resulting powder are shown in Figure 8.27; the material is partially constituted of 80 µm PS grains that have already gone through deposition and sintering once, yet retain their mostly spherical shape, although showing deformed spherical shape and altered surface state. Those particles often remain sintered together (Figure 8.27b) or agglomerate into larger clusters. Larger chunk of molten PS with angular geometry also constitute a part of the recycled material (Figure 8.27a, 8.27c and 8.27d). Impurities are also found in the material (e.g. dark particles in Figure 8.27a). The material is purposely left in this rough, heterogeneous state, without undergoing sieving nor a second grinding, to challenge the process and find its limit capabilities.

Figure 8.26: Picture of the grinding apparatus used to transform the former 3D-printed parts into new feedstock material.

Rheological characterisation of recycled powder: tensile strength measurement. To compare the powder obtained by recycling former 3D printed objects, to the PS powders used throughout the present work (80 µm diameter powder with smooth and rough surface state), the rheological characterisation method proposed by Valverde *et al.* [70, 105] under the name of powder tensile strength measurement was used. This testing method was described in detail and applied to the two previously described powders in Section 2.3. Testing of the recycled material is reported in Figure 8.28; in the inset, a comparison of the tensile strengths of the three powders is given to ease comparison.

The three powders compared here, all made from PS of the same chemical composition, show distinct rheological behaviour. The recycled powder *Rec* has the highest tensile strength, although its larger average grain size could have resulted in a decrease in van der Waals cohesive interactions. Tensile strength of the two other powders is lower: by 12% for RS, which itself decreases by 14% to reach 77.5 Pa for SS. The high value found for the *Rec* powder may be explained by the fact that particles are subject to enhanced surface friction and mechanical locking due to their angular, irregular shape, making the collective motion more difficult – in particular for this particular test the expansion of the packing, which involves separation of the particles. For the RS powder, surface friction remains, but mechanical locking on the scale of particles becomes less strong due to their spherical shapes. Finally, the SS samples is subject to the lesser amount of surface friction, and having also spherical grains, shows the lowest amount of stress needed to set the grains apart.

This experiment reflects the essential link between physical and rheological characteristic of

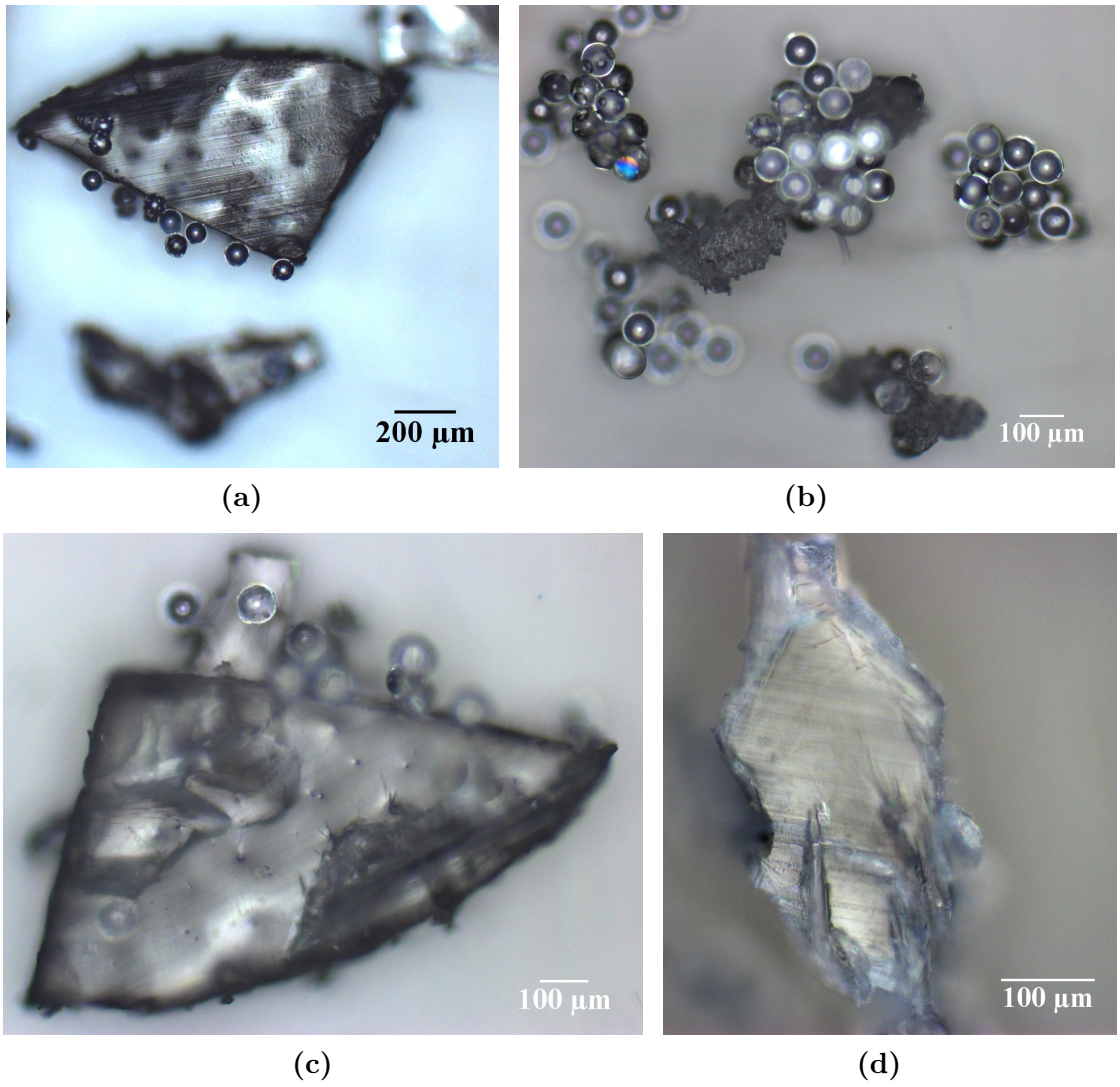

Figure 8.27: Microscopies of the PS recycled material obtained by grinding former 3D printed parts.

the powder, as three powders of grains of the same chemical composition show flow-behaviours at the opposite ends of the spectrum: the *SS* powder shows high flowability, the *RS* powder mediocre flowability, and the *Rec* powder low flowability.

8.4.2 Samples 3D printed from closed-loop recycling

The material produced from this simplistic closed-loop recycling procedure is used to 3D print new samples. One sample is shown in Figure 8.29. The printing parameters are kept the same, in particular the deposition time, to ease comparison of the values recorded during the *in-situ* rheological probing; however the layer height is doubled to 1 mm to allow the deposition of larger grains. Because the energy source is not adapted to this layer height, the samples printed show two molten areas in the regions of higher heat input (*cf.* Figure 8.7 for the geometry imposed by the heat source).

The sample printed, which includes residual dust (dark spots in Figure 8.29), also shows a less homogeneous section than all samples manufactured from virgin powder: the edge is marked by the succession of layers, showing that the material density in-between layers is smaller than within each layer triggering easier delamination. However, in bulk, the samples

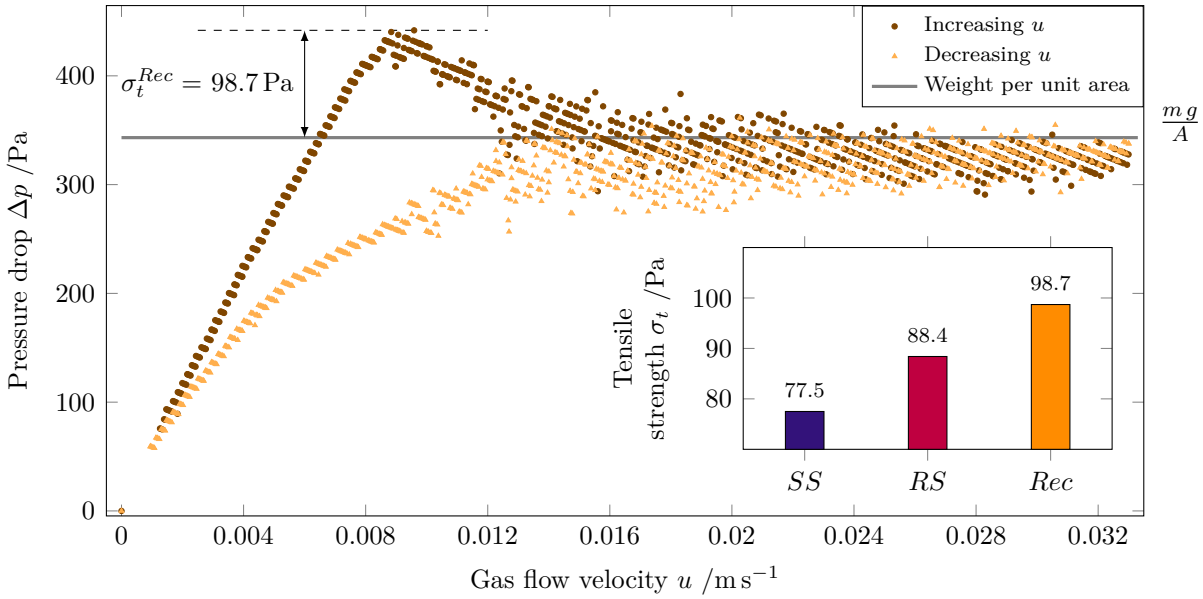

Figure 8.28: Tensile strength measurement applied to the recycled powder *Rec*. The sample tested has a mass 70 g, to allow comparison between this experiment and the ones presented in Figure 2.8. In the inset, tensile strength of the three PS powders are given: the smooth surface one (SS), the rough surface one (RS) and the recycled material (Rec).

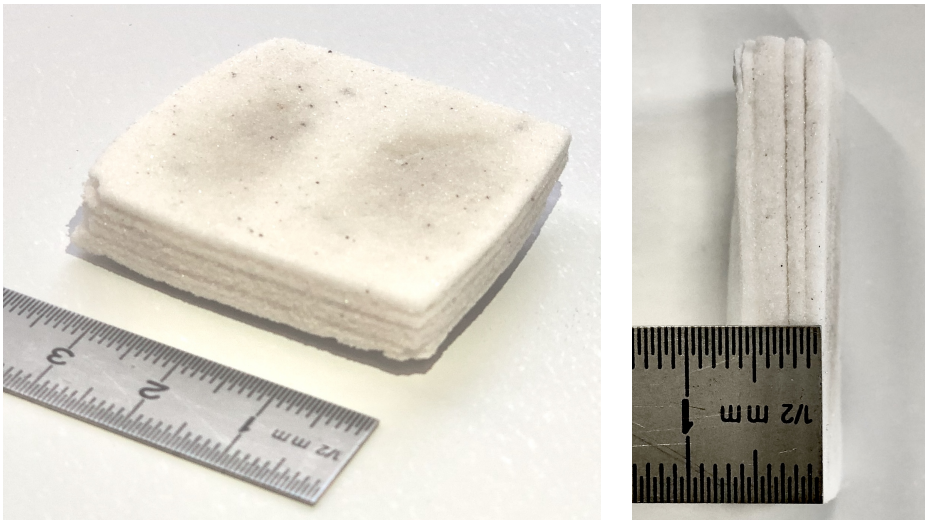

(a) Full sample **(b)** Section cut

Figure 8.29: Picture of the sample 3D printed from material obtained by closed-loop recycling.

are fully solidified and show no hole nor obvious low powder density zone. The deposition process functioned, as samples manufactured from recycled powder have a perfectly smooth sample surface and no bubble-like defects appear in the centre of the sample as they would due to missing material.

8.4.3 *In-situ* probing of recycled material during manufacturing

In-situ rheological probing provided by the RheoPrint AM process provides a characterisation of the material in regard to the SS and RS powders used previously. The torque recorded by the inner tube and closing disc during material deposition are given in Figure 8.30.

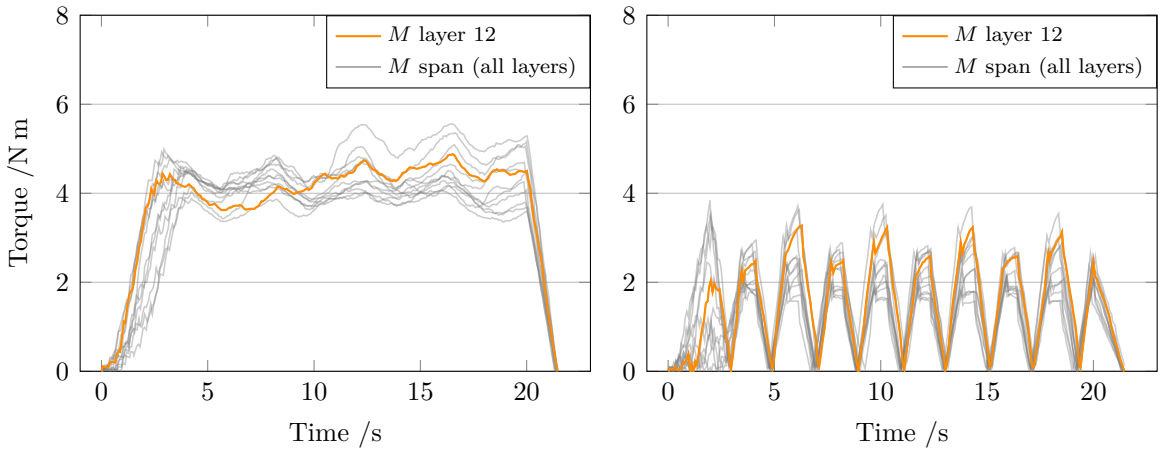

(a) Inner tube (DC_1) **(b)** Closing disc (DC_2)

Figure 8.30: Temporal torque evolution for all layers (in light grey) and one hand-picked typical layer (layer number indicated in legend), for granular material produced by closed-loop recycling.

The torque recorded shows relatively high variability from one layer to the next – although much lower than for the *RS* powder in μg – with a span of 2 N m around values averaging at 4 N m. The low frequency oscillations in phase with the rotation rate are also observed; when compared to the empty run presented in Figures 8.10a and 8.10d, they are here again strengthened by the presence of material. High frequency oscillations like the ones associated to stick-slip in the *RS* microgravity experiment (Figures 8.18d and 8.18d) are not visible. The difference in grain shape triggered by using recycled material does not imply strengthening of the stick-slip phenomena during manufacturing on-ground. While for previous experiments, both on-ground and in microgravity, the torque was generally showing the same order of magnitude for both probing systems, for the recycled powder the torque recorded by the inner tube is half as large as the one recorded by the closing disc. Again, as in previous ground experiments, it can be linked to the samples' mass being the same but not the sample volume: the angular grains can pack at higher density than spherical particles, hence, pulled by gravity, the blades of the closing disc might not be fully in contact with the powder bed.

For quantitative comparison, we can turn to Figure 8.31, in which the work produced by each motor during each material deposition is given, for all experiments presented above. Although results obtained by both probing systems are shown, the emphasis is put on the ones obtained from motor DC_1 with the inner tube rotation, as the low torque recorded by the closing disc is thought to be linked to its blades not fully penetrating the granular material, especially under $1g$ and with non-spherical material.

Containing results obtained for every situation tested, Figure 8.31 provides an overview of the full testing campaign completed for the RheoPrint process. While good-quality samples were successfully produced in all situations tested, the different materials also exhibited distinct behaviours, recorded by the machine. The torque recorded during material deposition is very high for the *Rec* powder; regarding the mono-directional probing of the inner tube (Fig. 8.31a), it is higher than for any other material, with a mean value of 81 J, doubled compared to the *RS* powder in microgravity. In terms of variability of the *Rec* samples, the torque recorded is relatively stable, with a coefficient of variation is of 6.4% (10% lower than for *RS* in μg). The *flowability number* calculated for the *Rec* powder (still from the data set recoded by DC_1) gives $Fl = 0.23$: the lowest of all materials tested.

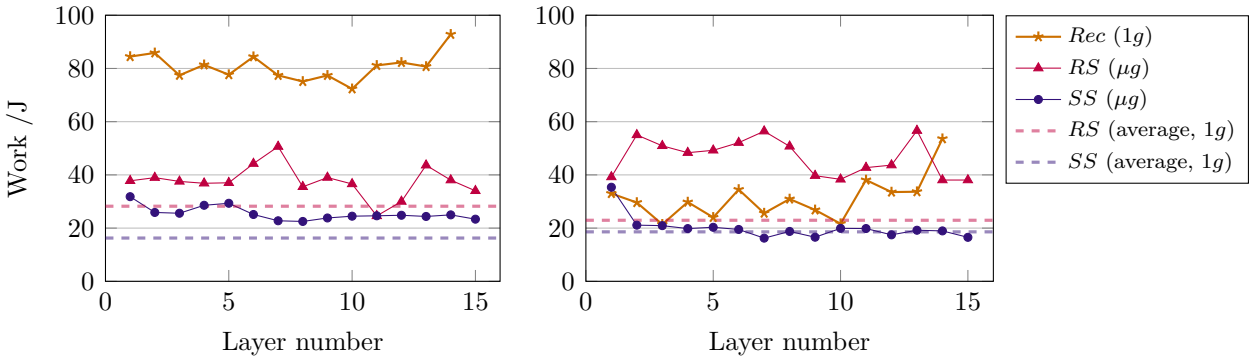

(a) Motor DC_1 (inner tube) **(b)** Motor DC_2 (closing disc)

Figure 8.31: Energy transferred through work for each powder layer deposited, for recycled material; the probing is done by (a) the inner tube and (b) the closing disc.

This increased surface roughness, then lowered sphericity of the grains, causes the greater difficulty they experience in moving along each other, increasing locking between particles and stress necessary to allow such motion to take place (i.e. to overcome frictional interactions). It generally lowers the *ease to flow*, which is expressed in higher stress recorded for the same motion to happen within the packing, and rise of inhomogeneities in this stress record. This behaviour is generally expected [94, 95, 97]. A quantitative measure of the magnitude of stress increase due to those two successive physical changes enables insightful comparison with the change recorded for the same powder, but tested with and without gravity. The change in gravitational environments seems to have a powerful, detrimental influence on powder flowability. The increase in energy necessary to make powder flow is of the same magnitude for a given powder tested on-ground *versus* in microgravity, as for the change from a material composed of spherical, rough surface grains to one formed by angular grains of irregular shape and size, much more prone to hooking and resisting motion: the average shear stress triples. The effects proposed to conclude Section 8.3, namely lower mobility of the grains in regard to each other in absence of a gravitational secondary force field triggering a decrease in the ability of the packing to reorganise into a new configuration, hence to flow, are responsible for an increase in shear stress of the same magnitude as this intrinsic change in the powder nature.

8.5 Conclusion: a process tailored for space applications

To be used as a fixed technology for in-space applications, additive manufacturing methods will need to evolve into more versatile technologies with increased reliability [10, 161]. The process developed in the course of this work was tested in five distinct situations:

- On-ground, using as feedstock material a 80 µm-diameter PS powder with smooth surface showing high flowability.
- On-ground, using as feedstock material the same PS powder, whose surface was roughened by dry-coating of a nano-metric angular powder showing mediocre flowability.
- In microgravity, using as feedstock material the same high flowability PS powder.
- In microgravity, using as feedstock material the same mediocre flowability PS powder.
- On-ground, using as feedstock material powder produced by closed-loop recycling of pre-

viously 3D printed parts, the PS powder was obtained by grinding former samples in a simplistic commercial burr-grinder, excluding any selective purification of the material (i.e. sieving, repeated grindings or density-based material selection). Rheological characterisation of the resulting powder reveals it as low flowability.

The primary result to report for assessing the AM process, is the successful manufacturing of samples in all situations mentioned. The resulting parts maintain their shape, show homogeneous external appearance and smooth surfaces, without obvious defects, holes, nor heterogeneous powder repartition. Samples were put through further analysis to verify if this macroscopic assessment could be extended to the microscopic scale.

Cross-influence of gravity and feedstock-material's flowability. Samples manufactured on-ground and in microgravity from rough and smooth surface powder were analysed in-bulk by X-ray computed tomography. Hardly any variation is visible between the "known good", perfectly sintered sample, and the 3D printed sample manufactured from the best flowability powder, SS, in microgravity (respectively Figures 8.24a and 8.24e). The average density of this μg SS sample is of 69.5%, 2.5% higher than the density of the "known good" ground-sintered comparative sample. More generally, for samples manufactured both from SS and RS, a homogeneous powder repartition is reached for both powders. The porosities are relatively spherical. The samples 3D printed on-ground have minute anisotropy with a slight z-elongation, but high isotropy is obtained for the samples manufactured in microgravity, regardless of the base-material used (Figure 8.24). For all sintered samples, porosities are also homogeneously distributed throughout the samples. The porosities in the RS samples tend to be larger than on the SS samples, with an increased density of porosities around 35 µm-diameter. However, the reparation, size and shape of those porosities remains homogeneous within the samples manufactured under $1g$ as well as in μg. Comparison between the RS samples printed on-ground and in microgravity show extremely promising results, with no difference in porosity size distribution (Figures 8.24c – 8.24f and 8.25b, Table 8.6). The larger porosities result in an average decrease of approx. 5% in the overall density of the samples manufactured from rough surface powder as compared to the ones manufactured from smooth surface powder (Figure 8.23). Larger porosities in RS samples are linked to the decreased packing efficiency undergone by materials showing increasing surface roughness (see Chapter 2). This tends to show that the maximum packing density for each specific type of powder is reached, in absence of other means implemented to increase material density. In order to erase this difference, compression should be applied *during* the material solidification, as it is also done during hot isostatic pressing [273], but using mono-directional normal compression. Implementing this simple amelioration could allow to drastically decrease samples porosities, and in turn to obtain perfect control over the porosity of the printed parts, including to allow density gradients throughout parts additively manufactured.

To the best knowledge of the author, no other powder-based additive manufacturing process commercially available to this day allows to 3D print homogeneous parts from material directly as produced by recycling former 3D printed parts – may it be on-ground or under low-gravity. For space exploration missions, self-sustainability being of paramount importance, the possibility to recycle former objects into new manufacturing material is essential [173, 203].

It should be noted that all the samples analysed in-bulk (SS and RS in $1g$ and μg) were manufactured using the same printing parameters. The mild differences obtained in material deposition, show that the use of different material is reflected in the process; yet all powders

could be packed at the maximum packing density they allow. The compression pressure applied before and during solidification should hence be adapted to the nature of the feedstock material. Similarly, all experiments were done for a fixed mass of powder, as control over the exact packing fraction locally cannot be obtained for such quantities of powder. However, the rough surface powder tends to occupy more space, as the grains pack less closely. The volume left to the material could be adapted to the feedback torque recorded by the closing disc as it descends to close the printing volume, in order to ensure contact between the top of the container and the material. Finally, homogenisation time could be optimised through the image analysis procedure proposed, to minimise fabrication time. A detailed study of printing parameters adjustment, and use of different base-materials for manufacturing, will be the next step for the RheoPrint AM process.

Control loop and dimensionless flowability index. To function efficiently in the various conditions described above, with as feedstock powder spanning through the entire range of typical flow-behaviours, the method proposed is the implementation of an automated control loop to adapt the process parameters to the base-material flowability. As seen in Chapter 2, the working definition of *flowability* used throughout the present work is a phenomenological description of the *ease* of grains to move in regard to each other, this motion becoming powder flow when happening collectively. The physical mechanisms behind a decrease in this collective mobility can be any phenomena decreasing grains' motion freedom, may it relate to a change in the gravitational environment (Chapter 3), an increase in surface roughness (Chapter 2), or yet another increase in the collective stiffness of the packing as an ensemble. In order to install a control loop to modify the printing parameters accordingly, probing mechanisms must be implemented to provide direct, reliable information on the flow-behaviour of the feedstock material. The two probing mechanisms proposed here (described in detail in Chapter 5) are based on two different driving mechanisms: mono-directional shear realised by the inner tube, and oscillatory shear provided through the closing disc of the AM apparatus. They were tested in the different situations above-mentioned and shown to give reliable, accurate description of the material's flow-behaviour, in full accordance with the known rheological response of those materials tested in Chapter 2 on-ground and in Chapter 3 in microgravity.

Based on the definition of *flowability* given above, and on the *in-situ* rheological probing provided by the two driving mechanisms, a dimensionless number is proposed to serve as *flowability indicator*. Fl is used in this work to provide a classification of the five above-mentioned situations, taking into account not only the material itself, but also the environment in which the powder is put into motion. As flowability is not an intrinsic material characteristic, the statement made through this dimensionless number is that the nature of the powder should be as important as the environment in which the experiments are conducted to determine and quantify powder flowability. Hence, any external factors influencing the process well-function should also enter. The Fl indexes are shown in Figure 8.32, calculated for the five situations mentioned above.

Both probing mechanisms record the expected behaviour: increasing particles' surface roughness is reflected in an increased stress necessary to impel flow within the process, with the SS powder under $1g$ being largely more *flowable* than the RS powder in the same gravitational environment: $Fl^{1g}_{SS} > Fl^{1g}_{RS}$. The heterogeneous, angular grain shape of recycled materials emphasise this flowability decrease, with $0.1 \sim Fl^{1g}_{Rec} \ll Fl^{1g}_{SS,\,RS}$. Regardless of the g-level, for both probing systems, flowability decreases largely with increasing surface roughness, Fl_{RS} being half or less of Fl_{SS}. For the RS and SS powders, the change in gravitational environment

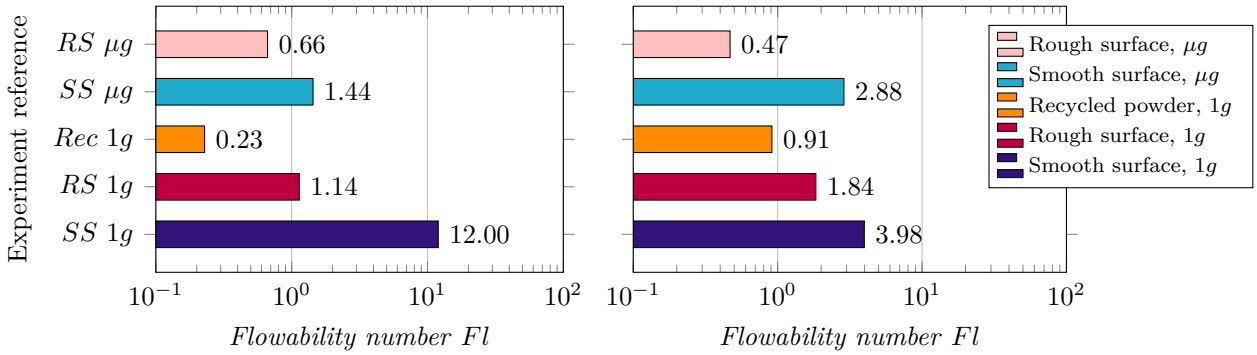

(a) Motor DC_1 (inner tube) **(b)** Motor DC_2 (closing disc)

Figure 8.32: *Flowability number* proposed in Eq. 8.3, calculated for all 3D printing experiments realised, i.e. for the five situations in which the RheoPrint additive manufacturing process was tested.

further decreases flowability, lowering by one order of magnitude the flowability indicators with $Fl^{\mu g}_{RS} \sim 0.1$ and $Fl^{\mu g}_{SS} \sim 1$. The SS powder looses flowability much more than the RS powder when Earth gravitational field is removed: the most drastic decrease in Fl is recorded by DC_1 for SS, going from $Fl^{1g}_{SS} = 12$ to $Fl^{\mu g}_{SS} = 1.4$.

Those results are coherent among each other and with previous characterisation obtained in the course of this work (Chapter 2 and Chapter 3); they remain for every layer 3D printed, underlining that a profound characteristic of the different granular systems is recorded. Notably, the decrease in powder flowability remarked in Chapter 3 is once again underlined by those results.

Having shown the sufficient sensitivity of the probing mechanisms proposed and implemented in the RheoPrint prototypes built, the next step in the development of this AM process is the optimisation of its printing parameters to maximise efficiency, particularly in terms of reproducibility, low porosity, and manufacturing time. It was shown that this could be done by the live automated adaptation of the process, through a feedback loop based on the information given by the flowability number proposed.

Handling granular materials independently of the gravitational environment. As seen in Chapter 3, microgravity environment lowers powder flowability: at the exact same chemical and physical characteristics, and using the same manufacturing method, microgravity-processed material exhibits higher stress and higher variability in energy input needed to be handled; flow inhomogeneities like stick-slip behaviour and clustering are enhanced in this environment, and the material generally packs at lower packing fraction. Those observations lead to the conclusion that the microgravity environment lowers a powder's ability to reorganise into new configurations; a physical explanation behind this phenomena is proposed in subsequent text.

Gravity provides a secondary force field. The resulting forces acting among grains in a powder are multi-directional, as forces spanning the grains assembly are scattered simply by the geometrical effects due to force transmission among discrete constituents of the granular ensemble (see Chapter 1). Therefore, albeit the gravitational attraction being in one direction, gravity applied to granular media provides forces in multiple directions, including, for a dense powder in motion, in directions different to the flow direction. Hence, it provides a supplementary force pointing in a different direction, that disrupts the strong force chains created in

the flow direction by the forces impelling granular flow in this particular direction. Similarly as the RheoPrint process avoids the appearance of a jammed phase by superposing multiple flow directions, the presence of gravity plays this role in processes where the magnitude of flow-impelling forces is comparable to the magnitude of forces resurgent from gravity.

The use of flowability indicators like the *flowability number* Fl proposed in Eq. 8.3, encompassing the change in flow-properties due to a change in physical state of the material, but also changes due to external, environmental conditions, are essential to describe the flow-behaviour of granular materials in environments where no empirical knowledge can be built upon. Planetary surfaces, like Lunar or Martian grounds, are examples of such environment, where previous knowledge is faint. The development of technologies for handling powders in such environments will have to rely on faithful indicators and demonstrators, which are yet to be invented. It is the opinion of the author that a step in this direction is to unequivocally accept the concept of powder flowability as a process-related, environment-dependent physical quantity. Experiments like the ones reported in this chapter show the possibility to link materials' rheological behaviour, their *process-ability*, and the environment in which they are processed, through a common dimensionless indicator.

Conclusion

Technological challenges offer the possibility to rethink the way we imagine and design the technologies of tomorrow. The approach of the work presented here has been to create an additive manufacturing process adapted – or rather, *adaptable* – to a wider set of constraints than any other existing process (Chapter 4). Particularly, as future exploratory space missions will necessitate long endurance and rely on self-sufficiency, more versatile and robust solutions will be crucial to augment autonomy, making strict restrictions on feedstock quality obsolete for in-space applications. In this perspective, a 3D printing process was developed, which enables to additively manufacture parts from granular material feedstock, independently of the gravitational level and of the flow-behaviour of the base material (Chapter 5). The powder handling method, implemented under the name "RheoPrint", was first tested by DEM simulation (Chapter 6); then evaluated though experiments on-ground and in microgravity. To obtain a proof of concept, two prototypes were built as demonstrators (Chapter 7). As exemplary feedstock materials, PS powder was used, first in its virgin state (smooth surface), then after dry-coating with nanometer-scale angular powder (rough surface): taken through multiple rheological characterisation methods, those two powders were employed to isolate the effect of increased surface friction on powder flow-properties, questioning the concept of *powder flowability* (Chapter 2). In parallel, they were used in microgravity experiments to link powder rheological response to the presence or absence of gravitational field (Chapter 3). Both powders were finally used to 3D print multiple samples in microgravity. The experimental campaign was continued on-ground, notably by manufacturing samples from material obtained from grinding previously printed parts, thence proving the workability of the process in a closed-loop recycling approach. Analysis of the printed parts offered the possibility to asses the AM process developed (Chapter 8), supporting further improvement in methods for quantifying flow-behaviour accurately, and ultimately optimising powder handling methods' efficiency under varying gravitational levels. To the knowledge of the author, no other parts have been manufactured from low-flowability powder in microgravity to this day.

Powder rheology in microgravity. Development of the AM process mentioned above relied on previous microgravity experiments (Sections 3.2 and 3.3), which showed that in the piston-probing set-up used, in absence of the secondary force field created by gravity, compression fatally leads to the appearance of a jammed phase (Figures 3.3 and 3.6). The onset of jamming was found to appear at lower packing fraction in absence on gravity than on-ground (Figure 3.4). The author hopes that those results will spur interest in further investigation on the influence of gravity on the packing fraction at jamming in granular media.

Factors determining rheological regimes. Theoretical prediction on the rheological response of granular fluids under shear were used to gain understanding of the parameters influencing the rheological response of granular materials under external drive. Obtaining the

first experimental confirmation of theoretical predictions from Kranz *et al.* [14, 86], made by adapting MCT to granular materials, three distinct rheological regimes (Newtonian, shear-thinning, and Bagnold regime) were found to appear in fluidised granular media (Section 1.4, Figure 1.10).

In granular materials with no external energy input, the feature of the different rheological regimes was found to depend on physical properties of the granular particles. The two PS powders used throughout this work to study the effect of increasing surface roughness, were first characterise by their physical surface state (Section 2.1), then by their flow-behaviour through three different rheological tests:

- The *flow energy* phenomenological flowability test proposed by Freeman Technology on the FT4 rheometer (Section 2.2).
- The *tensile strength* test proposed by Valverde *et al.* [70, 105] to characterise the cohesion strength of a granular medium, i.e. the pressure necessary to break cohesive bonds among grains and fluidise the powder bed (Section 2.3).
- High precision rheometry, on the MCR 102 from Anton Paar, used to obtain *flow start-up curves* from which are calculated *elastic shear moduli* for both materials, and finally trace full steady-state *flow curves* (Section 2.4).

Interparticular friction in granular materials is an intriguing parameter: depending on other characteristics of the system [132, 134], its impact on powder rheology can be essential or irrelevant. In particular, the effect of local packing fraction is a key factor to assess the rheological response of a powder, as interparticle friction is activated when the particles are pushed together by an external force. The effect of boundary pressure (i.e. confined or unconfined granular medium) and of packing density is hence emphasised (Figure 2.6). Flow curves of the two powders studied (Figure 2.13) show that at low shear rate $5 \cdot 10^{-3}\ \mathrm{s}^{-1} \leq \dot{\gamma} \leq 20\ \mathrm{s}^{-1}$, surface friction has a strong influence on powder rheology: the macroscopic stress needed to handle rough surface granular materials is higher, increasing by up to one third in excess of the value for smooth surface powder. In this range of shear rates, increased surface roughness also triggers the appearance of flow inhomogeneities, notably shear-banding (visible through the appearance of a non-monotonic flow curve). At high shear rates $\dot{\gamma} > 30\,\mathrm{s}^{-1}$, both materials are found to shear-thicken, slowly entering a Bagnold regime, at which point their macroscopic response becomes independent of their surface state. This study thus enabled to identify the regime in which the microscopic features of the grains composing a granular material are most reflected in its rheological properties.

The RheoPrint additive manufacturing process. 3D printing processes can be summerised as the alternation of material deposition and a material solidification. The deposition of granular materials, independently of their physical properties and of the gravitational level, has been the main challenge addressed in this work. The process developed for handling and additively manufacturing granulates relies solely on driving mechanisms that function regardless of the gravitational environment, and of the flow properties of the feedstock material. The powder deposition, summarised in Figure 5.3, consists of transporting the right amount of material to the printing area, creating a homogeneous powder layer, and finally putting this layer under compression to reduce the amount of porosities in the final 3D printed part. As it was shown that powder transport cannot be implemented by direct normal pressure on the granular material, as this would increase the risk to jam the material and prevent any further collective grain

motion, powder transport is solely realised through shear, using a screw-conveyor mechanism to trigger large-scale movements in the packing. The superposition of a driving mechanism in a second direction, to continuously build and disrupt force chains, defuses the appearance of a jammed phase. Powder is then homogenised into a thin layer of constant density by horizontal shaking. Ultimately, the material deposition happens through the coordinated motion of the different parts of its container (Figure 5.2).

Proof of concept. The proposed powder handling method (Chapter 5) was tested through DEM simulation (Chapter 6). Simulations confirm that each step of the process functions independently of gravity, and that the combination of all the steps provides a powder handling method that is independent of the magnitude of interparticle cohesive forces (Figure 6.12). At the end of the sequence of steps, the powder packing fraction on the bottom surface of the printer container is almost identical, whether the process was simulated under $-1g$, μg, or $+1g$ (Figure 6.10).

Experimental validation of the whole process was performed both on ground and in microgravity conditions, utilising parabolic flights as a microgravity platform to assess the gravity-(in)dependence of the process (Section 8.3), using three different powders to assess the independence of the process on powder flowability. In particular, the two powders mentioned above, composed of 80 µm-diameter particles with smooth and roughened surface served as feedstock material, demonstrating respectively high and mediocre flowability (Section 8.2). Finally, closed-loop recycling of printed parts was demonstrated under $1g$ by using as feedstock material a powder obtained from grinding former samples, resulting in a low-flowability powder (Section 8.4).

In all these combinations, parts could be successfully manufactured; the resulting 3D printed samples are macroscopically homogeneous and without obvious defects or inhomogeneities (Figure 8.17 and 8.29). In particular, the RheoPrint process allows to 3D print homogeneous parts from material directly obtained by recycling former 3D printed parts, something that no commercially available additive manufacturing process to date can achieve, and that will be a critical asset for increasing the self-sustainability space exploration missions.

Microscopic analysis of the samples printed from the rough and smooth surface powders was performed to confirm the process performences. X-ray computed tomography shows no qualitative variation between the samples manufactured from high flowability powder on-ground and in weightlessness, and a "known good" perfectly sintered reference sample (Figure 8.25). Samples manufactured on-ground show a slight elongation of porosities along z-direction in the Cartesian space, diminished when manufacturing happens in microgravity (Figure 8.24). More generally, the μg and $1g$ samples show similar pore size distribution (Table 8.6). In all manufactured samples, the powder repartition is homogeneous down to the microscopic level, with a near-perfect high density and isotropic porosities. There is no detectable systematic change in porosity between the samples manufactured under different gravitational environments, and minimal change correlated to the base-material flow-properties (Figure 8.24), due to a decreased packing efficiency for materials with increased particle-surface roughness, as was already established from their rheology (Chapter 2).

***In-situ* probing "powder flowability".** The rheological properties of granular materials show complex, multi-factorial evolution; they notably strongly vary with environmental conditions. Versatility in powder handling processes hence implies adaptability to the material's

flowability. Behind this ill-defined concept of *powder flowability* lies a description of the *ease* with which the particles move along each other, in the specific environment in which they happen to be: it is not an intrinsic powder property, but a phenomenological characteristic. To allow optimal functioning without renouncing efficiency, the strategy employed here is to adapt the manufacturing parameters to the rheological properties probed at a given instant, in order to achieve powder handling regardless of flowability, i.e. in various environments and notwithstanding the nature of the granular feedstock.

The powder flow-response is therefore probed *in-situ* during material transport, inside the powder bed, by two probing systems, providing respectively mono-directional and oscillatory shearing. Knowing the regime in which the physical properties of the material are most reflected in their rheological response (Chapter 2), the rotation rate of the probing systems are set accordingly. Through the information obtained on the flow-behaviour of the feedstock material, the printing parameters (in present case, deposition time and compression ratio) can be optimised to achieve the best possible print quality from the material fed to the process, *in its given state* – encompassing all external factors influencing the granular behaviour, among which gravitational environment. The implementation of this control-loop is described in Figure 5.7; it was demonstrated in Chapter 8 that the *in-situ* probing mechanisms proposed are sufficiently sensitive and reliable to capture difference in flow-behaviour between the different base-materials used, as well as a change in gravitational environment (Figures 8.10, 8.18 and 8.30, as well as a global summary in Figure 8.32).

Next steps for the additive manufacturing process developed. The essential next step for a manufacturing process tailored for space applications will be to adapt it – and in particular the solidification step – to other materials than polymers. The PS powders used as demonstrators offered perfect property variations for a proof of concept; however the important candidates for the targeted applications are metal and ceramic powders, which will require to adapt the solidification energy source, as well as the material constituting the solidification window (see Figure 7.2 and 7.20 for illustration of the indicated parts).

Besides, this process can in principle be applied to any fluid (for example, a polymeric resin) or particulate solid (powders or colloids); a resign-based [274] or colloids-based [275, 276] AM process tailored for microgravity is also desirable for opening new possibilities for in-space manufacturing.

Furthermore, the powder handling method proposed could be combined with other powder-based additive manufacturing processes developed for microgravity applications (in particular, methods described in Ref. [141] or [182]), increasing the robustness of the powder manipulation surrounding the manufacturing process itself.

Space rheology to foster sustainable manufacturing on-ground. The application to space missions poses as a need the possibility to reuse and recycle feedstock material; but more generally, for common applications on-ground, such capabilities will be more and more valued. In a world where the amount of waste produced will have to be drastically lowered in the future, the possibility to use low flowability materials, in particular material produced from closed-loop recycling, would also qualify additive manufacturing as a tool adapted to future terrestrial needs.

The need to gain a better understanding of phenomena happening in environments where our empirical knowledge does not hold true also triggers the necessity to unify certain concepts

and precise their definition. Specifically, it is the case for the notion of *powder flowability*, which has been at the centre of the present work. Following the definition of granular flowability given above, an indicator has been proposed (Eq. 8.3); it is meant to assert the fact that flowability is not an intrinsic material characteristic but depends as much on the material itself as on the environment in which it evolves. Such a flowability indicator is proposed in the hope to prompt further interest in proposing a clearer definition of granular flowability, associated with normalised testing procedure and a given SI-unit (or absence thereof, as in the case of a dimensionless number proposed here).

A long way lies ahead before additive manufacturing of human shelter on a planetary surface; but far from being a utopian vision, the scientific and technical grounds that will be the stepping stones for humans to make their way to space are now being developed. In this work, ideas have been proposed to further mature powder handling and additive manufacturing technologies, for the purpose of space-based activities. To fulfil human curiosity, leading the way to explore and discover further and further into space, the technical and technological advancement will go hand-in-hand with understanding physical mechanisms behind the phenomena observed under Earth atmosphere, as well as outside of it – to the Moon, Mars, and beyond.

Bibliography

[1] A. C. Owens, O. L. de Weck, C. Stromgren, W. Cirillo, and K. Goodliff, *Supportability Challenges, Metrics, and Key Decisions for Human Spaceflight*, tech. rep. (American Institute of Aeronautics and Astronautics, 2017).

[2] H. W. Jones, "The Recent Large Reduction in Space Launch Cost", in 48$^{\text{th}}$ International Conference on Environmental Systems, ICES-2018-81 (2018).

[3] National Research Council of the National Academies, *3D Printing in Space* (The National Academies Press, Washington, DC, 2014).

[4] T. Prater, C. Hill, F. Ledbetter, M. Fiske, J. Edmunsson, M. Meyyappan, P. Hall, C. Roberts, L. D. Huebner, and N. Werkheiser, "NASA's In-Space Manufacturing Project: Update on Manufacturing Technologies and Materials to Enable More Sustainable and Safer Exploration", in 70$^{\text{th}}$ International Astronautical Congress (IAC) (2019), IAC–19.D3.2B.5.

[5] R. S. Skomorohov, C. Welch, and A. M. Hein, "In-orbit Spacecraft Manufacturing: Near-term Business Cases", in 67$^{\text{th}}$ International Astronautical Congress (IAC) (2016).

[6] T. Prater and N. Werkheiser, *The Multimaterial Fabrication Laboratory: In-Space Manufacturing as an Enabling Technology for Long Endurance Human Spaceflight*, 5$^{\text{th}}$ Tennessee Valley Interstellar Workshop, Huntsville (AL) United States of America (USA), 2017.

[7] M. Gaskill and M. Johnson, *Solving the Challenges of Long Duration Space Flight with 3D Printing*, (2019) `https://www.nasa.gov/mission_pages/station/research/news/3d-printing-in-space-long-duration-spaceflight-applications` (visited on Apr. 1, 2019).

[8] T. Prater, Q. Bean, R. Beshears, T. Rolin, N. Werkheiser, E. Ordonez, R. Ryan, and F. Ledbetter III, *Summary Report on Phase I and Phase II Results From the 3D Printing in Zero-G Technology Demonstration Mission, Volume I*, tech. rep. (Marshall Space Flight Center, Huntsville, Alabama, 2016).

[9] T. Prater, N. Werkheiser, F. Ledbetter, D. Timucin, K. Wheeler, and M. Snyder, "3D Printing in Zero G Technology Demonstration Mission: complete experimental results and summary of related material modeling efforts", International Journal of Advanced Manufacturing Technology **101**, 391–417 (2018).

[10] T. DebRoy, H. L. Wei, J. S. Zuback, T. Mukherjee, J. W. Elmer, J. O. Milewski, A. M. Beese, A. Wilson-Heid, A. De, and W. Zhang, "Additive manufacturing of metallic components – Process, structure and properties", Progress in Materials Science **92**, 112–224 (2018).

[11] A. F. Hepp, B. A. Palaszewski, A. J. Colozza, G. A. Landis, D. A. Jaworske, and M. J. Kulis, "In-Situ Resource Utilization for Space Exploration: Resource Processing, Mission-Enabling Technologies, and Lessons for Sustainability on Earth and Beyond", in 12th International Energy Conversion Engineering Conference (2014), p. 3761.

[12] A. Sack and T. Pöschel, "Dissipation of Energy by Dry Granular Matter in a Rotating Cylinder", Scientific Reports **6**, 26833 (2016).

[13] H. M. Jaeger, S. R. Nagel, and R. P. Behringer, "Granular solids, liquids, and gases", Reviews of Modern Physics **68**, 1259–1273 (1996).

[14] W. T. Kranz, F. Frahsa, A. Zippelius, M. Fuchs, and M. Sperl, "Rheology of Inelastic Hard Spheres at Finite Density and Shear Rate", Physical Review Letters **121**, 148002 (2018).

[15] D. Frenkel, "Soft condensed matter", Physica A **313**, 1–31 (2002).

[16] P. G. de Gennes, "Granular matter: a tentative view", Reviews of Modern Physics **71**, S374–S382 (1999).

[17] C. H. Liu, S. R. Nagel, D. A. Schecter, S. N. Coppersmith, S. Majumdar, O. Narayan, and T. A. Witten, "Force fluctuations in bead packs", Science **269**, 513–515 (1995).

[18] R. P. Behringer, K. E. Daniels, T. S. Majmudar, and M. Sperl, "Fluctuations, correlations and transitions in granular materials: Statistical mechanics for a non-conventional system", Philosophical Transactions of the Royal Society A **366**, 493–504 (2008).

[19] A. Drescher and G. de Jong de Josselin, "Photoelastic verification of a mechanical model for the flow of a granular material", Journal of the Mechanics and Physics of Solids **20**, 337–351 (1972).

[20] T. S. Majmudar and R. P. Behringer, "Contact force measurements and stress-induced anisotropy in granular materials", Nature **435**, 1079–1082 (2005).

[21] A. Tordesillas, "Force chain buckling, unjamming transitions and shear banding in dense granular assemblies", Philosophical Magazine **87**, 4987–5016 (2007).

[22] B. Miller, C. O'Hern, and R. P. Behringer, "Stress fluctuations for continuously sheared granular materials", Physical Review Letters **77**, 3110–3113 (1996).

[23] S. N. Coppersmith, C. H. Liu, S. Majumdar, O. Narayan, and T. A. Witten, "Model for force fluctuations in bead packs", Physical Review E **53**, 4673–4685 (1996).

[24] A. Abed Zadeh, J. Barés, T. A. Brzinski, K. E. Daniels, J. Dijksman, N. Docquier, H. O. Everitt, J. E. Kollmer, O. Lantsoght, D. Wang, M. Workamp, Y. Zhao, and H. Zheng, "Enlightening force chains: a review of photoelasticimetry in granular matter", Granular Matter **21**, 83 (2019).

[25] T. Wakabayashi, "Photo-elastic method for determination of stress in powdered mass", Journal of the Physical Society of Japan **5**, 383–385 (1950).

[26] P. Dantu, "Contribution a l'etude mecanique et geometrique des milieux pulverulents", in Proceedings of the 4$^{\text{th}}$ International Conference on Soil Mechanics and Foundations Engineering (1957), pp. 144–148.

[27] D. Howell, R. P. Behringer, and C. Veje, "Stress Fluctuations in a 2D Granular Couette Experiment: A Continuous Transition", Physical Review Letters **82**, 5241–5244 (1999).

[28] L. Sanfratello, J. Zhang, S. C. Cartee, and E. Fukushima, "Exponential distribution of force chain lengths: a useful statistic that characterizes granular assemblies", Granular Matter **13**, 511 (2011).

[29] S. F. Edwards and C. C. Mounfield, "A theoretical model for the stress distribution in granular matter. I. Basic equations", Physica A **226**, 1–11 (1996).

[30] C. C. Mounfield and S. F. Edwards, "A theoretical model for the stress distribution in granular matter. II. Forces in pipes", Physica A **226**, 12–24 (1996).

[31] S. F. Edwards and C. C. Mounfield, "A theoretical model for the stress distribution in granular matter. III. Forces in sandpiles", Physica A **226**, 25–33 (1996).

[32] D. M. Mueth, H. M. Jaeger, and S. R. Nagel, "Force distribution in a granular medium", Physical Review E **57**, 3164–3169 (1998).

[33] F. H. Hummel and E. J. Finnan, "The Distribution of Pressure on Surfaces Supporting a Mass of Granular Material", Minutes of Proceedings of the Institution of Civil Engineers **212**, 369–392 (1921).

[34] S. Savage, "Modeling and Granular Material Boundary Value Problems", in *Physics of Dry Granular Media*, Vol. 350, edited by H. Herrmann, J. Hovi, and S. Luding (Springer, Dordrecht, Springer, Dordrecht, 1998) Chap. Modeling and Granular Material Boundary Value Problems.

[35] N. Topić, J. A. Gallas, and T. Pöschel, "Nonuniformities in the angle of repose and packing fraction of large heaps of particles", Physical Review Letters **109**, 128001 (2012).

[36] S. S. Nadukuru and R. L. Michalowski, "Arching in Distribution of Active Load on Retaining Walls", Journal of Geotechnical and Geoenvironmental Engineering **138**, 575–584 (2012).

[37] H. A. Janssen, "Versuche über Getreidedruck in Silozellen [On Grain Pressure in Silos]", Zeitschrift des Vereins Deutscher Ingenieure **39**, 1045–1049 (1895).

[38] M. E. Cates, J. P. Wittmer, J. P. Bouchaud, and P. Claudin, "Jamming and stress propagation in particulate matter", Physica A **263**, 354–361 (1999).

[39] M. E. Cates, J. P. Wittmer, J. P. Bouchaud, and P. Claudin, "Jamming, force chains, and fragile matter", Physical Review Letters **81**, 1841–1844 (1998).

[40] A. J. Liu and S. R. Nagel, eds., *Jamming and Rheology: Constrained Dynamics on Microscopic and Macroscopic Scales* (Taylor & Francis, New York, 2001).

[41] A. J. Liu and S. R. Nagel, "Jamming is not just cool any more", Nature **396**, 21–22 (1998).

[42] E. Brown, N. Rodenberg, J. Amend, A. Mozeika, E. Steltz, M. R. Zakin, H. Lipson, and H. M. Jaeger, "Universal robotic gripper based on the jamming of granular material", Proceedings of the National Academy of Sciences **107**, 18809–18814 (2010).

[43] R. A. Bagnold, "Experiments on a Gravity-Free Dispersion of Large Solid Spheres in a Newtonian Fluid under Shear", Proceedings of the Royal Society of London Series A **225**, 49–63 (1954).

[44] P. Schall and M. van Hecke, "Shear Bands in Matter with Granularity", Annual Review of Fluid Mechanics **42**, 67–88 (2010).

[45] M. Couette, "Études sur le frottement des liquides", Annales de Chimie et de Physique **21**, 433–510 (1890).

[46] A. Mallock, "Determination of the viscosity of water", Proceedings of the Royal Society of London **45**, 273–279 (1888).

[47] G. I. Taylor, "Stability of a viscous liquid contained between two rotating cylinders", Philosophical Transactions of the Royal Society of London **223**, 289–343 (1923).

[48] D. M. Mueth, G. F. Debregeas, G. S. Karczmar, P. J. Eng, S. R. Nagel, and H. M. Jaeger, "Signatures of granular microstructure in dense shear flows", Nature **406**, 385–389 (2000).

[49] ISO Standard 3219:1999, *Plastics – Polymers/resins in the liquid state or as emulsions or dispersions – Determination of viscosity using a rotational viscometer with defined shear rate*, 1993.

[50] T. G. Metzger, *The Rheology Handbook*, 4th ed. (Vincentz Network, Hanover, 2014), p. 432.

[51] E. Daub, "Scaling Of Stick-Slip Instabilities In Granular Materials", in KITP Program – The Physics of Glasses: Relating Metallic Glasses to Molecular, Polymeric and Oxide Glasses (2010).

[52] R. G. Cain, N. W. Page, and S. Biggs, "Microscopic and macroscopic aspects of stick-slip motion in granular shear", Physical Review E **64**, 016413 (2001).

[53] T. Divoux, M. A. Fardin, S. Manneville, and S. Lerouge, "Shear Banding of Complex Fluids", Annual Review of Fluid Mechanics **48**, 81–103 (2016).

[54] T. Pöschel and S. Luding, eds., *Granular Gases* (Springer-Verlag, Berlin Heidelberg, 2001).

[55] M. Adachi, P. Yu, and M. Sperl, "Magnetic excitation of a granular gas as a bulk thermostat", npj Microgravity **5**, 19 (2019).

[56] E. Falcon, S. Aumaître, P. Évesque, F. Palencia, C. Lecoutre-Chabot, S. Fauve, D. Beysens, and Y. Garrabos, "Collision statistics in a dilute granular gas fluidized by vibrations in low gravity", Europhysics Letters **74**, 830–836 (2006).

[57] S. Tatsumi, Y. Murayama, H. Hayakawa, and M. Sano, "Experimental study on the kinetics of granular gases under microgravity", Journal of Fluid Mechanics **641**, 521–539 (2009).

[58] T. Steinpilz, G. Musiolik, M. Kruss, F. Jungmann, T. Demirci, M. Aderholz, J. E. Kollmer, J. Teiser, T. Bila, E. Guay, and G. Wurm, "ARISE: A granular matter experiment on the International Space Station", Review of Scientific Instruments **90**, 104503 (2019).

[59] P. Yu, M. Schröter, and M. Sperl, "Velocity Distribution of a Homogeneously Cooling Granular Gas", Physical Review Letters **124**, 208007 (2020).

[60] N. V. Brilliantov and T. Pöschel, *Kinetic Theory of Granular Gases* (Oxford University Press, 2004).

[61] G. Vicente, "Kinetic Theory of Inelastic Hard Spheres", in *Granular Gaseous Flows – A Kinetic Theory Approach to Granular Gaseous Flows* (Springer International Publishing, 2019) Chap. 1, pp. 1–55.

[62] T. P. C. van Noije and M. H. Ernst, "Velocity distributions in homogeneous granular fluids: the free and the heated case", Granular Matter **1**, 57–64 (1998).

[63] P. K. Haff, "Grain flow as a fluid-mechanical phenomenon", Journal of Fluid Mechanics **134**, 401–430 (1983).

[64] S. McNamara and W. Young, "Inelastic collapse in two dimensions", Physical Review E **50**, R28–R31 (1994).

[65] É. Falcon, R. Wunenburger, P. Évesque, S. Fauve, C. Chabot, Y. Garrabos, and D. Beysens, "Cluster formation in a granular medium fluidized by vibrations in low gravity", Physical Review Letters **83**, 440–443 (1999).

[66] E. Opsomer, F. Ludewig, and N. Vandewalle, "Phase transitions in vibrated granular systems in microgravity", Physical Review E **84**, 051306 (2011).

[67] E. Opsomer, F. Ludewig, and N. Vandewalle, "Dynamical clustering in driven granular gas", EPL (Europhysics Letters) **99**, 40001 (2012).

[68] M. Noirhomme, E. Opsomer, N. Vandewalle, and F. Ludewig, "Granular transport in driven granular gas", The European Physical Journal E **38**, 9 (2015).

[69] E. Opsomer, M. Noirhomme, N. Vandewalle, E. Falcon, and S. Merminod, "Segregation and pattern formation in dilute granular media under microgravity conditions", npj Microgravity **3**, 1 (2017).

[70] A. Castellanos, "The relationship between attractive interparticle forces and bulk behaviour in dry and uncharged fine powders", Advances in Physics **54**, 263–376 (2005).

[71] I. Goldhirsch, "Introduction to granular temperature", Powder Technology **182**, 130–136 (2008).

[72] D. Ren, L. M. Leslie, and D. Karoly, "Landslide Risk Analysis using a New Constitutive Relationship for Granular Flow", Earth Interactions **12**, 1–16 (2008).

[73] P. Richard, M. Nicodemi, R. Delannay, P. Ribière, and D. Bideau, "Slow relaxation and compaction of granular systems", Nature Materials **4**, 121–128 (2005).

[74] R. A. Wilkinson, R. P. Behringer, J. T. Jenkins, and M. Y. Louge, "Granular Materials and the Risks They Pose for Success on the Moon and Mars", AIP Conference Proceedings **746**, 1216–1223 (2005).

[75] F. Radjai, P. Evesque, D. Bideau, and S. Roux, "Stick-slip Dynamics of a One-dimensional Array of Particles", Physical Review E **52**, 5555–5564 (1995).

[76] I. S. Aranson and L. S. Tsimring, "Patterns and collective behavior in granular media: Theoretical concepts", Reviews of Modern Physics **78**, 641–692 (2006).

[77] I. Goldhirsch, "Rapid granular flows", Annual Review of Fluid Mechanics **35**, 267–293 (2003).

[78] GDR MiDi, "On dense granular flows", European Physical Journal E **14**, 341–365 (2004).

[79] Y. Forterre and O. Pouliquen, "Flows of Dense Granular Media", Annual Review of Fluid Mechanics **40**, 1–24 (2008).

[80] S. Luding, "Molecular Dynamics Simulations of Granular Materials", in *The Physics of Granular Media*, edited by H. Hinrichsen and D. E. Wolf (John Wiley & Sons, Ltd, 2005) Chap. 13, pp. 297–324.

[81] P. A. Cundall and O. D. L. Strack, "A discrete numerical model for granular assemblies", Géotechnique **29**, 47–65 (1979).

[82] G. Lumay and N. Vandewalle, "Compaction of anisotropic granular materials: Experiments and simulations", Physical Review E **70**, 051314 (2004).

[83] W. Kranz, M Sperl, and A Zippelius, "Glass transition for driven granular fluids.", Physical Review Letters **104**, 225701 (2010).

[84] M. Sperl, W. T. Kranz, and A. Zippelius, "Single-particle dynamics in dense granular fluids under driving", EPL (Europhysics Letters) **98**, 28001 (2012).

[85] W. T. Kranz, M. Sperl, and A. Zippelius, "Glass transition in driven granular fluids: a mode-coupling approach", Physical Review E **87**, 022207 (2013).

[86] W. T. Kranz and M. Sperl, "Kinetic theory for strong uniform shear flow of granular media at high density", EPJ Web of Conferences **140**, 03064 (2017).

[87] W. T. Kranz, F. Frahsa, A. Zippelius, M. Fuchs, and M. Sperl, "Integration through transients for inelastic hard sphere fluids", Physical Review Fluids **5**, 024305 (2020).

[88] W. Götze, *Complex dynamics of glass-forming liquids: A Mode-Coupling Theory* (Oxford University Press, Oxford, UK, 2009).

[89] U. Bengtzelius, W. Götze, and A. Sjolander, "Dynamics of supercooled liquids and the glass transition", Journal of Physics C: Solid State Physics **17**, 5915–5934 (1984).

[90] D. Tabor, "Imperfect gases", in *Gases, Liquids and Solids: And Other States of Matter*, 3rd ed. (Cambridge University Press, 1991), pp. 122–151.

[91] L. M. C. Janssen, "Mode-Coupling Theory of the Glass Transition: A Primer", Frontiers in Physics **6**, 97 (2018).

[92] L. Bocquet, W. Losert, D. Schalk, T. C. Lubensky, and J. P. Gollub, "Granular shear flow dynamics and forces: Experiment and continuum theory", Physical Revew E **65**, 011307 (2001).

[93] M. Fuchs and M. E. Cates, "Theory of Nonlinear Rheology and Yielding of Dense Colloidal Suspensions", Physical Review Letters **89**, 248304 (2002).

[94] R. V. More and A. M. Ardekania, "Effect of roughness on the rheology of concentrated non-Brownian suspensions: A numerical study", Journal of Rheology **64**, 67 (2020).

[95] N. A. Pohlman, B. L. Severson, J. M. Ottino, and R. M. Lueptow, "Surface roughness effects in granular matter: Influence on angle of repose and the absence of segregation", Physical Review E **73**, 031304 (2006).

[96] A. A. Maradudin and P. Mazur, "Effects of surface roughness on the van der Waals force between macroscopic bodies", Physical Review B **22**, 1677–1686 (1980).

[97] P. Mazur and A. A. Maradudin, "Effects of surface roughness on the van der Waals force between macroscopic bodies: II. Two rough surfaces", Physical Review B **23**, 695–705 (1981).

[98] M. Capece, R. Ho, J. Strong, and P. Gao, "Prediction of powder flow performance using a multi-component granular Bond number", Powder Technology **286**, 561–571 (2015).

[99] I. Zimmermann, M. Eber, and K. Meyer, "Nanomaterials as Flow Regulators in Dry Powders", Zeitschrift fur Physikalische Chemie **218**, 51–102 (2004).

[100] H. Rumpf, "Die Wissenschaft des Agglomerierens", Chemie Ingenieur Technik **46**, 1–11 (1974).

[101] J. Yang, A. Sliva, A. Banerjee, R. N. Dave, and R. Pfeffer, "Dry particle coating for improving the flowability of cohesive powders", Powder Technology **158**, 21–33 (2005).

[102] M. Leturia, B. Mohammed, S. Lagarde, I. Ronga, and K. Saleh, "Characterization of flow properties of cohesive powders: A comparative study of traditional and new testing methods", Powder Technology **253**, 406–423 (2014).

[103] H.-J. Yang, F.-Q. Wei, K.-H. Hu, G.-D. Zhou, and J. Lyu, "Comparison of rheometric devices for measuring the rheological parameters of debris flow slurry", Journal of Mountain Science **12**, 1125–1134 (2015).

[104] *Freeman Technology*, `https://www.freemantech.co.uk/powder-testing/ft4-powder-rheometer-powder-flow-tester`.

[105] J. Valverde, A. Castellanos, A. Ramos, A. T. Pérez, M. a. Morgan, and P. K. Watson, "An automated apparatus for measuring the tensile strength and compressibility of fine cohesive powders", Review of Scientific Instruments **71**, 2791–2795 (2000).

[106] *Anton Paar*, `https://www.anton-paar.com`.

[107] J. E. Mark, ed., *Polymer Data Handbook*, 2nd edition (Oxford University Press, New York, United States of America, 2009).

[108] S. Vock, B. Klöden, A. Kirchner, T. Weißgärber, and B. Kieback, "Powders for powder bed fusion: a review", **4**, 383–397 (2019).

[109] R. M. Nedderman, *Statistics and Kinematics of Granular Materials* (Cambridge University Press, 1992).

[110] A. Zocca, C. M. Gomes, T. Mühler, and J. Günster, "Powder-bed stabilization for powder-based additive manufacturing", Advances in Mechanical Engineering **2014**, 491581 (2014).

[111] H. H. Hausner, "Friction conditions in a mass of metal powder", International Journal of Powder Metallurgy **3**, 7–13 (1967).

[112] R. L. Carr, "Evaluating flow properties of solid", Chemical Engineering **72**, 163–169 (1965).

[113] D. Schulze, *Powders and Bulk Solids – Behavior, Characterization, Storage and Flow* (Springer-Verlag Berlin Heidelberg, Berlin, 2008).

[114] Y. Grasselli, H. J. Herrmann, G. Oron, and S. Zapperi, "Effect of impact energy on the shape of granular heaps", Granular Matter **2**, 97–100 (2000).

[115] M. G. Kleinhans, H. Markies, S. J. de Vet, A. C. inf Veld, and F. N. Postema, "Static and dynamic angles of repose in loose granular materials under reduced gravity", Journal of Geophysical Research **116**, E11004 (2011).

[116] B. H. Kaye, "Characterizing the Flowability of a Powder Using the Concepts of Fractal Geometry and Chaos Theory", Particle & Particle Systems Characterization **14**, 53–66 (1997).

[117] A. Brucks, T. Arndt, J. M. Ottino, and R. M. Lueptow, "Behavior of flowing granular materials under variable g", Physical Review E **75**, 032301 (2007).

[118] S. Klein and B. White, "Dynamic shear of granular material under variable gravity conditions", in 26$^{\text{th}}$ AIAA: Aerospace Sciences Meeting, Vol. 88, 0648 (1988).

[119] O. R. Walton, C. P. D. Moor, and K. S. Gill, "Effects of gravity on cohesive behavior of fine powders: implications for processing lunar regolith", Granular Matter **9**, 353–363 (2007).

[120] W. Nan, M. Ghadiri, and Y. Wang, "Analysis of powder rheometry of FT4: Effect of particle shape", Chemical Engineering Science **173**, 374–383 (2017).

[121] W. Nan, V. Vivacqua, M. Ghadiri, and Y. Wang, "Numerical analysis of air effect on the powder flow dynamics in the FT4 Powder Rheometer", EPJ Web of Conferences **140**, 03036 (2017).

[122] H. Darcy, *Les fontaines publiques de la ville de Dijon : exposition et application des principes à suivre et des formules à employer dans les questions de distribution d'eau*, edited by V. Dalmont (1856).

[123] T. Voigtmann, M. Siebenbürger, C. P. Amann, S. U. Egelhaaf, S. Fritschi, M. Krüger, M. Laurati, K. J. Mutch, and K. H. Samwer, "Rheology of colloidal and metallic glass formers", Colloid and Polymer Science **298**, 681–696 (2020).

[124] K. N. Pham, G. Petekidis, D. Vlassopoulos, S. U. Egelhaaf, W. C. K. Poon, and P. N. Pusey, "Yielding behavior of repulsion- and attraction-dominated colloidal glasses", Journal of Rheology **52**, 649 (2008).

[125] M. Laurati and S. U. Egelhaaf, "Nonlinear rheology of colloidal gels with intermediate volume fraction", Journal of Rheology **55**, 673 (2011).

[126] M. A. Fardin, T. J. Ober, C. Gay, G. Grégoire, G. H. McKinley, and S. Lerouge, "Potential ways of thinking about the shear-banding phenomenon", Soft Matter **8**, 910–922 (2012).

[127] H. Perrin, C. Clavaud, M. Wyart, B. Metzger, and Y. Forterre, "Interparticle Friction Leads to Nonmonotonic Flow Curves and Hysteresis in Viscous Suspensions", Physical Review X **9**, 031027 (2019).

[128] C. Coulomb, "Premier mémoire sur l'électricité et le magnétisme", Histoire de l'Académie Royale des Sciences, 569–577 (1785).

[129] C. Coulomb, "Second mémoire sur l'électricité et le magnétisme", Histoire de l'Académie Royale des Sciences, 578–611 (1785).

[130] O. Reynolds, "LVII. On the dilatancy of media composed of rigid particles in contact. With experimental illustrations", Philosophical Magazine and Journal of Science **20**, 469–481 (1885).

[131] D. Wang, J. Ren, J. A. Dijksman, H. Zheng, and R. P. Behringer, "Microscopic Origins of Shear Jamming for 2D Frictional Grains", Physical Review Letters **120**, 208004 (2018).

[132] R. Mari, R. Seto, J. F. Morris, and M. M. Denn, "Shear thickening, frictionless and frictional rheologies in non-Brownian suspensions", Journal of Rheology **58**, 1693 (2014).

[133] J. R. Royer, D. L. Blair, and S. D. Hudson, "Rheological Signature of Frictional Interactions in Shear Thickening Suspensions", Physical Review Letters **116**, 188301 (2016).

[134] M. Wyart and M. E. Cates, "Discontinuous Shear Thickening without Inertia in Dense Non-Brownian Suspensions", Physical Review Letters **112**, 098302 (2014).

[135] S. M. Dammer, J. Werth, and H. Hinrichsen, "Electrostatically Charged Granular Matter", in *The Physics of Granular Media*, edited by H. Hinrichsen and D. E. Wolf (Wiley, 2004) Chap. 11.

[136] J. N. Israelachvili, "Adhesion and Wetting Phenomena", in *Intermolecular and Surface Forces*, 3rd ed. (Elsevier, 2011) Chap. 17, pp. 415–467.

[137] J. S. McFarlane, D. Tabor, and F. P. Bowden, "Adhesion of solids and the effect of surface films", Proceedings of the Royal Society of London A **202**, 224–243 (1950).

[138] J. N. Israelachvili, "Van der Waals Forces between Particles and Surfaces", in *Intermolecular and Surface Forces*, 3rd ed. (Elsevier, 2011) Chap. 13, pp. 253–289.

[139] H. Hamaker, "The London–van der Waals attraction between spherical particles", Physica **4**, 1058–1072 (1937).

[140] D. S. McKay, G. Heiken, A. Basu, G. Blanford, S. Simon, R. Reedy, B. M. French, and J. Papike, "The Lunar Regolith", in *Lunar Sourcebook* (Cambridge University Press, 1991) Chap. 7, pp. 285–356.

[141] A. Zocca, J. Lüchtenborg, T. Mühler, J. Wilbig, G. Mohr, T. Villatte, F. Léonard, G. Nolze, M. Sparenberg, J. Melcher, K. Hilgenberg, and J. Günster, "Enabling the 3D Printing of Metal Components in μ-Gravity", Advanced Materials Technologies **4**, 1900506 (2019).

[142] J. Blum, G. Wurm, S. Kempf, T. Poppe, H. Klahr, T. Kozasa, M. Rott, T. Henning, J. Dorschner, R. Schräpler, H. U. Keller, W. J. Markiewicz, I. Mann, B. A. Gustafson, F. Giovane, D. Neuhaus, H. Fechtig, E. Grün, B. Feuerbacher, H. Kochan, L. Ratke, A. El Goresy, G. Morfill, S. J. Weidenschilling, G. Schwehm, K. Metzler, and W. H. Ip, "Growth and form of planetary seedlings: Results from a microgravity aggregation experiment", Physical Review Letters **85**, 2426–2429 (2000).

[143] J. Blum, "Dust agglomeration", Advances in Physics **55**, 881–947 (2006).

[144] R. Weidling, C. Güttler, and J. Blum, "Free collisions in a microgravity many-particle experiment. I. Dust aggregate sticking at low velocities", Icarus **218**, 688–700 (2012).

[145] S. G. Love, D. R. Petit, and S. R. Messenger, "Particle aggregation in microgravity: Informal experiments on the International Space Station", Meteoritics & Planetary Science **49**, 732–739 (2014).

[146] S. T. Nase, W. L. Vargas, A. A. Abatan, and J. J. McCarthy, "Discrete characterization tools for cohesive granular material", Powder Technology **116**, 214–223 (2001).

[147] W. N. Bond, "The surface tension of a moving water sheet", Proceedings of the Physical Society **47**, 549–558 (1935).

[148] P. Evesque, "Distribution of contact forces in a homogeneous granular material of identical spheres under triaxial compression", Poudres & Grains **14**, 82–95 (2004).

[149] C. S. O'Hern, L. E. Silbert, A. J. Liu, and S. R. Nagel, "Jamming at zero temperature and zero applied stress: The epitome of disorder", Physical Review E **68**, 011306 (2003).

[150] J. D. Bernal and J. Mason, "Packing of Spheres: Co-ordination of Randomly Packed Spheres", Nature **188**, 910–911 (1960).

[151] C. E. Carr, N. C. Bryan, K. N. Saboda, S. A. Bhattaru, G. Ruvkun, and M. T. Zuber, "Acceleration profiles and processing methods for parabolic flight", npj Microgravity **4**, 14 (2018).

[152] H. A. Makse, J. Brujić, and S. F. Edwards, "Statistical Mechanics of Jammed Matter", in *The Physics of Granular Media*, edited by H. Hinrichsen and D. E. Wolf (John Wiley & Sons, Ltd, 2005) Chap. 3, pp. 45–85.

[153] C. S. O'Hern, S. A. Langer, A. J. Liu, and S. R. Nagel, "Random Packings of Frictionless Particles", Physical Review Letters **88**, 075507 (2002).

[154] R. S. Farr, J. R. Melrose, and R. C. Ball, "Kinetic theory of jamming in hard-sphere startup flows", Physical Review E **55**, 7203–7211 (1997).

[155] N. Murdoch, B. Rozitis, K. Nordstrom, S. F. Green, P. Michel, T. L. De Lophem, and W. Losert, "Granular convection in microgravity", Physical Review Letters **110**, 018307 (2013).

[156] B. M. Guy, C. Ness, M. Hermes, L. J. Sawiak, J. Sun, and W. C. K. Poon, "Testing the Wyart–Cates model for non-Brownian shear thickening using bidisperse suspensions", Soft Matter **16**, 229–237 (2020).

[157] S. Sture, N. C. Costes, S. N. Batiste, M. R. Lankton, K. A. Alshibli, B. Jeremic, R. A. Swanson, and M. Frank, "Mechanics of Granular Materials at Low Effective Stresses", Journal of Aerospace Engineering **11**, 67–72 (1998).

[158] K. A. Alshibli, S. Sture, and N. C. Costes, "Constitutive and stability behavior of soils in microgravity environment", AIP Conference Proceedings **504**, 246–252 (2000).

[159] N. C. Costes, V. C. Jano, and S. Sture, "Microgravity Experiments on Granular Materials", MRS Proceedings **87**, 203–212 (1986).

[160] N. Murdoch, B. Rozitis, S. F. Green, T. L. De Lophem, P. Michel, and W. Losert, "Granular shear flow in varying gravitational environments", Granular Matter **15**, 129–137 (2013).

[161] A. E. Trujillo, M. T. Moraguez, S. I. Wald, A. C. Owens, and O. L. de Weck, "Feasibility Analysis of Commercial In-Space Manufacturing Applications", in AIAA SPACE: Space and Astronautics Forum and Exposition (2017).

[162] B. Hubscher, *Open for Business: 3-D Printer Creates First Object in Space on International Space Station*, National Aeronotics and Space Administration (NASA), (2014) `https://www.nasa.gov/content/open-for-business-3-d-printer-creates-first-object-in-space-on-international-space-station` (visited on Jan. 10, 2020).

[163] H. Kodama, "Automatic method for fabricating a three-dimensional plastic model with photo-hardening polymer", Review of Scientific Instruments **52**, 1770–1773 (1981).

[164] T. Wohlers and T. Gornet, *History of additive manufacturing* (Wohlers Associates, Inc., Fort Collins, Colorado, USA, 2014).

[165] W. K. Swainson, "Method of Producing a Three-Dimensional Figure by Holography", Great Britain Patent 1243044 (1971).

[166] W. K. Swainson, "Method, Medium and Apparatus for Producing Three-Dimensional Figure Product", United States Patent 4041476 (1977).

[167] ISO/ASTM Standard 52900-2015, *Standard Terminology for Additive Manufacturing Technologies – General Principles – Terminology*, West Conshohocken, PA, 2015.

[168] K. M. Taminger and R. A. Hafley, *Electron Beam Freeform Fabrication for Cost Effective Near-Net Shape Manufacturing*, tech. rep. (NASA Langley Research Center, Hampton, VA, USA, 2008).

[169] B. D. Foster and B. Matthews, "Laser-assisted Wire Additive Manufacturing System for the Deep Space Gateway", in Deep Space Gateway Science Workshop 2018, 2063 (2018).

[170] R. Syrovatka, *Ins and outs of 3D printing*, (2020) `https://www.esa.int/ESA_Multimedia/Images/2020/05/Ins_and_outs_of_3D_printing` (visited on Oct. 29, 2020).

[171] R Crockett, D Petersen, and K Cooper, "Fused Deposition Modeling in microgravity", in Proceedings of the 10$^{\text{th}}$ Solid Freeform Fabrication Symposium (1999), pp. 671–678.

[172] K. G. Cooper and M. R. Griffin, *Microgravity Manufacturing Via Fused Deposition*, tech. rep. 212636 (NASA, Marshall Space Flight Center, Alabama, USA, 2003).

[173] T. Prater, M. Werkheiser, F. Ledbetter, and K. Morgan, "In-Space Manufacturing at NASA Marshall Space Flight Center: A Portfolio of Fabrication and Recycling Technology Development for the International Space Station", in AIAA SPACE: Space and Astronautics Forum and Exposition (2018).

[174] ESA, *Europe 3D printer set for Space Station*, (2014) http://www.esa.int/Enabling_Support/Space_Engineering_Technology/Europe_s_3D_printer_set_for_Space_Station (visited on Oct. 29, 2020).

[175] M. Snyder, J. Dunn, M. Chen, A. Kemmer, N. Paul-Gin, M. Napoli, E. Gonzalez, and M. Pless, "Manufacturing in Microgravity and in Varying External Forces Environments", United States Patent 9656426 B2 (Made In Space, Inc., 2017).

[176] Y. Kim, C. Yoon, S. Ham, J. Park, S. Kim, O. Kwon, and P.-J. Tsai, "Emissions of Nanoparticles and Gaseous Material from 3D Printer Operation", Environmental Science & Technology **49**, 12044–12053 (2015).

[177] Michael Snyder, "Nanoparticle filtering environmental control units", United States Patent 9802355 (Made In Space, Inc., 2017).

[178] M. A. Gibson, N. M. Mykulowycz, J. Shim, R. Fontana, P. Schmitt, A. Roberts, J. Ketkaew, L. Shao, W. Chen, P. Bordeenithikasem, J. S. Myerberg, R. Fulop, M. D. Verminski, E. M. Sachs, Y. M. Chiang, C. A. Schuh, A. John Hart, and J. Schroers, "3D printing metals like thermoplastics: Fused filament fabrication of metallic glasses", Materials Today **21**, 697–702 (2018).

[179] ASTM Standard F3187-16, *Standard Guide for Directed Energy Deposition of Metals*, West Conshohocken, PA, 2016.

[180] P. Kobryn, N. Ontko, L. Perkins, and J. Tiley, "Additive Manufacturing of Aerospace Alloys for Aircraft Structures", in Cost Effective Manufacture via Net-Shape Processing, 3 (2006), pp. 1–14.

[181] M. Molitch-Hou, *Researchers 3D Print Metal in Zero G for ESA*, (2016) www.engineering.com/3DPrinting/3DPrintingArticles/ArticleID/13879/Researchers-3D-Print-Metal-in-Zero-G-for-ESA.aspx (visited on Oct. 29, 2020).

[182] P. H. Smith, J. W. Murray, D. O. Jones, J. Segal, and A. T. Clare, "Magnetically assisted directed energy deposition", Journal of Materials Processing Technology **288**, 116892 (2021).

[183] L. E. Murrab, S. M. Gaytanab, D. A. Ramirezab, E. Martinezab, J. Hernandezab, K. N. Amatoab, P. W. Shindoab, F. R. Medinaab, and R. B. Wickerab, "Metal Fabrication by Additive Manufacturing Using Laser and Electron Beam Melting Technologies", Journal of Materials Science & Technology **28**, 1–14 (2012).

[184] Society of Automotive Engineers (SAE) Standard AMS7005, *Wire-Fed Plasma Arc Directed Energy Deposition Additive Manufacturing Process*, 2019.

[185] F. Gärtner, T. Stoltenhoff, T. Schmidt, and H. Kreye, "The cold spray process and its potential for industrial applications", Journal of Thermal Spray Technology **15**, 223–232 (2006).

[186] D. M. Keicher, C. L. Atwood, D. L. Greene, M. L. Griffith, L. D. Harwell, F. P. Jeantette, J. A. Romero, L. P. Schanwald, and D. T. Schmale, "Energy-Beam-Driven Rapid Fabrication System", United States Patent 6476343 B2 (Sandia Corporation, 2002).

[187] F. P. Jeantette, D. M. Keicher, J. A. Romero, and L. P. Schanwald, "Method and System for Producing Complex-Shape Objects", United States Patent 6046426 A (Sandia Corporation, 2000).

[188] S. Watson and T. Sottak, *Optomec 3D Metal Printing Technology Chosen by Navajo Technical University for NASA Mission*, (2019) https://optomec.com/optomec-3d-metal-printing-technology-chosen-by-navajo-technical-university-for-nasa-mission (visited on Oct. 29, 2020).

[189] European Space Agency, *Method for Additive Manufacture of Metal Alloys*, (2020) http://www.esa.int/Enabling_Support/Space_Engineering_Technology/Method_for_Additive_Manufacture_of_Metal_Alloys (visited on Oct. 29, 2020).

[190] V. R. Davé, "Electron-Beam Assisted Materials Fabrication", PhD thesis (Massachusetts Institute of Technology, USA, 1995).

[191] C. R. Deckard, "Method and Apparatus for Producing Parts by Selective Sintering", United States Patent 4863538 (Board of Regents, The University of Texas System, 1989).

[192] E. M. Sachs, J. S. Haggerty, M. J. Cima, and P. A. Williams, "Three-Dimensional Printing Techniques", United States Patent 5204055 (Massachusetts Institute of Technology, 1993).

[193] M. Schmid and K. Wegener, "Additive Manufacturing: Polymers Applicable for Laser Sintering (LS)", in International Conference on Manufacturing Engineering and Materials (ICMEM), Vol. 149 (2016), pp. 457–464.

[194] C. Y. Yap, C. K. Chua, Z. L. Dong, Z. H. Liu, D. Q. Zhang, L. E. Loh, and S. L. Sing, "Review of selective laser melting: Materials and applications", Applied Physics Reviews **2**, 041101 (2015).

[195] S. L. Sing, W. Y. Yeong, F. E. Wiria, B. Y. Tay, Z. Zhao, L. Zhao, Z. Tian, and S. Yang, "Direct selective laser sintering and melting of ceramics: a review", Rapid Prototyping Journal **23**, 611–623 (2017).

[196] B. Zhang, Y. Li, and Q. Bai, "Defect Formation Mechanisms in Selective Laser Melting: A Review", Chinese Journal of Mechanical Engineering **30**, 515–527 (2017).

[197] J. Günster, A. Zocca, C. M. Gomes, and T. Muehler, "Method for Stabilizing a Powder Bed by means of Vacuum for Additive Manufacturing", United States Patent 9533452B2 (Bundesrepublik Deutschland – Bundesministerium fuer Wirtschaft und Technologie – Bundesanstalt für Materialforschung und -prüfung, 2017).

[198] Bundesanstalt für Materialforschung und -prüfung, Clausthal University of Technology, and German Aerospace Center, *BAM, CUT and DLR want to manufacture a tool for the first time in zero gravity – Research group tests innovative 3D printing process for space flight*, (2018) `https://www.bam.de/Content/EN/Press-Releases/2018/Materials/2018-03-04-3d-printing-of-mechanical-tools-in-space.html` (visited on Mar. 18, 2019).

[199] A. T. Sutton, C. S. Kriewall, M. C. Leu, and J. W. Newkirk, "Powder characterisation techniques and effects of powder characteristics on part properties in powder-bed fusion processes", Virtual and Physical Prototyping, `10.1080/17452759.2016.1250605` (2016).

[200] L. Cordova, M. Campos, and T. Tinga, "Revealing the Effects of Powder Reuse for Selective Laser Melting by Powder Characterization", JOM **71**, 1062–1072 (2019).

[201] R. L. Muhlbauer, K. Turner, F. Hiatt, R. Dyer, J. Slostad, and R. P. Hoyt, "Customizable, Recyclable ISS Packaging (CRISSP): Vibrational Energy Attenuation from 3D Printed Packaging Materials", in AIAA SPACE: Space and Astronautics Forum and Exposition, 5243 (2016).

[202] Small Business Innovative Research, *CRISSP – Custom Recyclable International Space Station Packaging*, (2017) `https://www.sbir.gov/sbirsearch/detail/1148879` (visited on Oct. 29, 2020).

[203] J. Anderson, *Full Circle: NASA to Demonstrate Refabricator to Recycle, Reuse, Repeat*, tech. rep. (Marshall Space Flight Center, Huntsville (AL) USA, 2017).

[204] G. Tapia and A. Elwany, "A Review on Process Monitoring and Control in Metal-Based Additive Manufacturing", Journal of Manufacturing Science and Engineering **136**, 060801 (2014).

[205] S. Fish, J. Beaman, A. Bryant, D. Leigh, S. Kubiak, and J. C. Booth, "Real-time Process Control for Additive Manufacturing", International Patent Application 2015/095544 A1 (Board of Regents, The University of Texas System, 2015).

[206] M. L. Griffith, W. H. Hofmeister, G. A. Knorovsky, D. O. MacCallum, M. E. Schlienger, and J. E. Smugeresky, "Direct Laser Additive Fabrication System with Image Feedback Control", United States Patent 6459951 B1 (Sandia Corporation, 2002).

[207] V. R. Dave, R. B. Madigan, M. J. Cola, and M. S. Piltch, "Method and System for Monitoring Additive Manufacturing Processes", United States Patent Application Publication 0264553 A1 (Sigma Labs, Inc., 2018).

[208] K. P. Costabile, *Interim, In Situ Additive Manufacturing Inspection*, edited by NASA Technology Transfer Program, (2017) `https://technology.nasa.gov/patent/MFS-TOPS-70` (visited on Oct. 29, 2020).

[209] S. A. Gold and T. G. Spears, "Acoustic Monitoring Method for Additive Manufacturing Processes", United States Patent 9989495 B2 (General Electric Company, 2018).

[210] "System and Method for In-situ Inspection of Additive Manufacturing Materials and Builds", International Patent Application 2018/0111192 A1 (Huntington Ingalls Incorporated, 2018).

[211] J. A. Beacham Jr. and S. A. Abitz, "System and Method for Additive Manufacturing Process Control", International Patent Application 2017/058346 Al (General Electric Company, 2017).

[212] D. Duarte Campos, M. Philip, S. Gürzing, C. Melcher, Y. Lin, J. Schöneberg, A. Blaeser, B. Theek, H. Fischer, and M. Betsch, "Synchronized Dual Bioprinting of Bioinks and Biomaterial Inks as a Translational Strategy for Cartilage Tissue Engineering", 3D Printing and Additive Manufacturing **6**, 63–71 (2019).

[213] F. L. C. Morgan, L. Moroni, and M. B. Baker, "Dynamic Bioinks to Advance Bioprinting", Advanced Healthcare Materials **9**, 1901798 (2020).

[214] J. Schöneberg, F. De Lorenzi, B. Theek, A. Blaeser, D. Rommel, A. Kuehne, F. Kießling, and H. Fischer, "Engineering biofunctional in vitro vessel models using a multilayer bioprinting technique", Scientific Reports **8**, 10430 (2018).

[215] M. Johnson and B. Dunbar, *Three-dimensional Bioprinting in Space*, (2019) `https://www.nasa.gov/mission_pages/station/research/news/b4h-3rd/it-3d-bioprinting-in-space/` (visited on May 19, 2020).

[216] TechShot, Inc., *3D BioFabrication Facility*, (2020) `https://techshot.com/bioprinter` (visited on Oct. 29, 2020).

[217] S. Litkenhous and B. Dunbar, *In-Space Manufacturing*, (2019) `https://www.nasa.gov/oem/inspacemanufacturing` (visited on May 18, 2020).

[218] R. Hoyt, J. Cushing, and J. Slostad, *SpiderFab: Process for On-Orbit Construction of Kilometer-Scale Apertures*, tech. rep. NNX12AR13G (Tethers Unlimited Inc., Bothell, 98011 WA, USA, 2013).

[219] Robert Hoyt, "Methods and Apparatus for Manufacturing and In-Space Assembly of Antennas", United States Patent Application Publication 2019/0027835 (Tethers Unlimited Inc., 2019).

[220] T. Master, *Phoenix*, (2020) `https://www.darpa.mil/program/phoenix` (visited on Mar. 6, 2020).

[221] A. Kemmer, M. Snyder, M. Chen, and J. Dunn, "Additive manufacturing of extended structures", United States Patent 10052820 (Made In Space, Inc., 2018).

[222] M. Snyder, "In-Space Manufacturing and Assembly of Spacecraft Device and Techniques", United States Patent Application Publication 2017/0036783 (Made In Space, Inc., 2017).

[223] A. Janda, D. Maza, A. Garcimartín, E. Kolb, J. Lanuza, and E. Clément, "Unjamming a granular hopper by vibration", EPL (Europhysics Letters) **87**, 24002 (2009).

[224] S. M. Khefif, A. Valance, and F. Ould-Kaddour, "Spreading of a granular droplet under horizontal vibrations", Physical Review E **97**, 062903 (2018).

[225] S. Nadler, O. Bonnefoy, J. M. Chaix, G. Thomas, and J. L. Gelet, "Parametric study of horizontally vibrated grain packings", The European Physical Journal E **34**, 66 (2011).

[226] K. Mair and J. F. Hazzard, "Nature of stress accommodation in sheared granular material: Insights from 3D numerical modeling", Earth and Planetary Science Letters **259**, 469–485 (2007).

[227] S. F. Edwards and R. B. Oakeshott, "Theory of powders", Physica A **157**, 1080–1090 (1989).

[228] R. Niu, M. Ramaswamy, C. Ness, A. Shetty, and I. Cohen, "Tunable solidification of cornstarch under impact: How to make someone walking on cornstarch sink", Science Advances **6**, 19 (2020).

[229] Y. Yu, "Theoretical modelling and experimental investigation of the performance of screw feeders", PhD thesis (Wollongong, China, 1997).

[230] A. Kudrolli, M. Wolpert, and J. P. Gollub, "Cluster Formation due to Collisions in Granular Material", Physical Review Letters **78**, 1383–1386 (1997).

[231] M. Grasso and B. M. Colosimo, "Process defects andin situmonitoring methods in metal powder bed fusion: a review", Measurement Science and Technology **28**, 044005 (2017).

[232] S. K. Everton, M. Hirsch, P. I. Stavroulakis, R. K. Leach, and A. T. Clare, "Review of in-situ process monitoring and in-situ metrology for metal additive manufacturing", Materials and Design **95**, 431–445 (2016).

[233] K. R. Momber A.W., "Classification and Characterization of Abrasive Materials", in *Principles of Abrasive Water Jet Machining* (Springer, London, 1998) Chap. 2, pp. 5–19.

[234] K. Oguri and T. Arai, "Two different low friction mechanisms of diamond-like carbon with silicon coatings formed by plasma-assisted chemical vapor deposition", Journal of Materials Research **7**, 1313–1316 (1992).

[235] Z. Rena, H. Qinb, Y. Donga, G. Doll, and C. Ye, "A boron-doped diamond like carbon coating with high hardness and low friction coefficient", Wear **436–437**, 203031 (2019).

[236] X. Li and N. Tan, "Calculation model of the equivalent spiral shear stress of conditioned sand", Public Library of Science (POS) One **14**, 1–20 (2019).

[237] R. A. Figueroa-Díaz, A. d. J. Balvantín-García, J. Á. Diosdado de la Peña, P. Cruz-Alcantar, I. Murillo-Verduzco, and P. A. Pérez-Olivas, "Stress analysis in a screw conveyor axis under a specific fault condition", Ingeniería, investigación y tecnología **20**, 1–11 (2019).

[238] Y. Z. Bejua and J. Mandal, "Expanded polystyrene (EPS) geofoam: preliminary characteristic evaluation", in International conference on Transportation Geotechnics and Geoecology, Vol. 189, 239–246 (2017).

[239] C. Kloss, C. Goniva, A. Hager, S. Amberger, and S. Pirker, "Models, algorithms and validation for opensource DEM and CFD-DEM", Progress in Computational Fluid Dynamics **12**, 140–152 (2012).

[240] J. Shäfer, S. Dippel, and D. Wolf, "Force Schemes in Simulations of Granular Materials", Journal de Physique I **6**, 5–20 (1996).

[241] S. Luding, "Cohesive, frictional powders: contact models for tension", Granular matter **10**, 235 (2008).

[242] H. Hertz, "Über die Berührung fester elastischer Körper", Journal für die Reine und Angewandte Mathematik **92**, 156–171 (1882).

[243] R. Mindlin, "Compliance of Elastic Bodies in Contact", Journal of Applied Mechanics Trans. ASME **16**, 259–268 (1949).

[244] R. Mindlin and H. Deresiewicz, "Elastic spheres in contact under varying oblique forces", Journal of Applied Mechanics Trans. ASME **20**, 327–344 (1953).

[245] J. Ai, J.-F. Chen, J. M. Rotter, and J. Y. Ooi, "Assessment of rolling resistance models in discrete element simulations", Powder Technology **206**, 269–282 (2011).

[246] K. L. Johnson, K. Kendall, A. D. Roberts, and D. Tabor, "Surface energy and the contact of elastic solids", Proceedings of the Royal Society of London A **324**, 301–313 (1971).

[247] G. Wypych, "Polystyrene (PS)", in *Handbook of Polymers*, edited by G. Wypych (Elsevier, Oxford, 2012), pp. 541–547.

[248] A. Handbook, *Properties and Selection of Aluminum Alloys*, edited by K. Anderson, J. Weritz, and J. G. Kaufman, Vol. 2B (2019).

[249] K. F. Malone and B. H. Xu, "Determination of contact parameters for discrete element method simulations of granular systems", Particuology **6**, 521–528 (2008).

[250] S. Lommen, D. Schott, and G. Lodewijks, "DEM speedup: Stiffness effects on behavior of bulk material", Particuology **12**, 107–112 (2014).

[251] N. Sentse, M. Sabbatini, G. D. Chiara, D. Ducros, and K. Oldenburg, *ESA User Guide to Low Gravity Platforms*, 3rd ed., HSO-K/MS/01/14 (ESA – Directorate of Human Spaceflight and Operations, 2014).

[252] Novespace, *Scientific research flights*, (2019) `https://www.airzerog.com/scientific-research-services/` (visited on Apr. 27, 2020).

[253] C. J. Fraser, "Electrical and electronics principles", in *Mechanical Engineer's Reference Book (Twelfth Edition)*, edited by E. H. Smith, Twelfth Edition (Butterworth-Heinemann, 1994) Chap. 2, pp. 2–57.

[254] G. K. Nikas, in *Friction, Lubrication, and Wear Technology*, Vol. 18, edited by G. E. Totten (ASM Handbook, 2017) Chap. Friction and Wear of Seals, pp. 957–968.

[255] G. Levy, T. Flash, and B. Hochner, "Arm Coordination in Octopus Crawling Involves Unique Motor Control Strategies", Current Biology **25**, 1195–1200 (2015).

[256] V. A. Pedroni, *Finite State Machines in Hardware – Theory and Design (with VHDL and SystemVerilog)* (The MIT Press, 2013).

[257] D. Bernache-Assollant and J.-P. Bonnet, "Frittage : aspects physico-chimiques – Partie 1 : frittage en phase solide", Techniques de l'ingénieur, AF6620 (2005).

[258] Edmund Optics, *Understanding Optical Windows*, (2020) `https://www.edmundoptics.com/knowledge-center/application-notes/optics/understanding-optical-windows/` (visited on Oct. 29, 2020).

[259] Thorlabs, Inc., *Flat Windows*, (2020) `https://www.thorlabs.de/navigation.cfm?guide_id=2367` (visited on Oct. 29, 2020).

[260] Sydor Optics, *Products description*, (2020) `http://shopsydor.com` (visited on Oct. 29, 2020).

[261] C. Reas and B. Fry, *Processing: A Programming Handbook for Visual Designers and Artists*, 2nd ed. (The MIT Press, Cambridge, Massachusetts, USA, 2014), p. 664.

[262] M. Couette, "Oscillations tournantes d'un solide de révolution en contact avec un fluide visqueux", Comptes Rendus de l'Académie des Sciences de Paris **105**, 1064–1067 (1887).

[263] M. Couette, "Sur un nouvel appareil pour l'étude du frottement des fluides", Comptes Rendus de l'Académie des Sciences de Paris **107**, 388–390 (1888).

[264] P. Dontula, C. W. Macosko, and L. E. Scriven, "Origins of concentric cylinders viscometry", Journal of Rheology **49**, 807–818 (2005).

[265] M. Otsuki and H. Hayakawa, "Shear jamming, discontinuous shear thickening, and fragile states in dry granular materials under oscillatory shear", Physical Review E **101**, 032905 (2020).

[266] B. P. Tighe, "Relaxations and rheology near jamming", Physical Review Letters **107**, 158303 (2011).

[267] J. Walker, D. Halliday, and R. Resnick, "Kinetic Energy and Work", in *Fundamentals of Physics*, edited by S. Johnson, A. Rentrop, J. Atkins, and E. Swain, 10th ed. (Wiley, 2014) Chap. 7, pp. 149–176.

[268] C. Thiery, *Tomography à rayons X*, tech. rep. P950-V3 (Technique de l'Ingénieur, 2013).

[269] J. T. Gostick, Z. A. Khan, T. G. Tranter, M. D. Kok, M. Agnaou, M. Sadeghi, and R. Jervis, "PoreSpy: A Python Toolkit for Quantitative Analysis of Porous Media Images", Journal of Open Source Software **4**, 1296 (2019).

[270] C. A. Schneider, W. S. Rasband, and K. W. Eliceiri, "NIH Image to ImageJ: 25 years of image analysis", Nature Methods **9**, 671–675 (2012).

[271] G. Reiter, A. L. Demirel, J. Peanasky, L. L. Cai, and S. Granick, "Stick to slip transition and adhesion of lubricated surfaces in moving contact", The Journal of Chemical Physics **101**, 2606–2615 (1994).

[272] E. Marakis, M. C. Velsink, L. J. Corbijn van Willenswaard, R. Uppu, and P. W. H. Pinkse, "Uniform line fillings", Physical Review E **99**, 043309 (2019).

[273] H. V. Atkinson and S. Davies, "Fundamental aspects of hot isostatic pressing: An overview", Metallurgical and Materials Transactions A **31**, 2981–3000 (2000).

[274] R. Felzmann, S. Gruber, G. Mitteramskogler, P. Tesavibul, A. R. Boccaccini, R. Liska, and J. Stampfl, "Lithography-Based Additive Manufacturing of Cellular Ceramic Structures", Advanced Engineering Materials **14**, 1052–1058 (2012).

[275] C. M. Larson, J. J. Choi, P. A. Gallardo, S. W. Henderson, M. D. Niemack, G. Rajagopalan, and R. F. Shepherd, "Direct Ink Writing of Silicon Carbide for Microwave Optics", Advanced Engineering Materials **18**, 39–45 (2016).

[276] C. Zhu, A. J. Pascall, N. Dudukovic, M. A. Worsley, J. D. Kuntz, E. B. Duoss, and C. M. Spadaccini, "Colloidal Materials for 3D Printing", Annual Review of Chemical and Biomolecular Engineering **10**, 17–42 (2019).

[277] H. M. Collins, *Gravity's Ghost: Scientific Discovery in the Twenty-First Century* (The University of Chicago Press, Chicago, 2011).

List of acronyms

$1g$	gravity on-ground
μg	microgravity
2D	two dimensional
3D	three dimensional
ABS	acrylonitrile butadiene styrene
AM	Additive Manufacturing
AMF	Additive Manufacturing Facility
Athena	Advanced Telescope for High-ENergy Astrophysics
BFF	BioFabrication Facility
BMGs	Bulk Metallic Glasses
CAD	Computer Assisted Design
CNC	Computer Numerical Control
CRISSP	Customisable Recyclable International Space Station Packaging
CT	computed tomography
DC	direct-current
DED	Directed Energy Deposition
DEM	Discrete Element Method
DLR	German Aerospace Center, abbreviated from German *Deutsches Zentrum fü Luft- und Raumfahrt e.V.*
EB	Electron Beam
EBF^3	Electron Beam Free-Form Fabrication
ESA	European Space Agency
ESAMM	Extended Structure Additive Manufacturing Machine
EVA	Extra-Vehicular Activity
FDM	Fused Deposition Modeling
fps	frames per second
FSM	finite-state machine
FT4	Freeman Technology 4 Powder Rheometer
HPDE	high density polyethylene
IR	infrared

ISM	In-Space Manufacturing
ISS	International Space Station
ITT	Integration Through Transients
LAMMPS	Large-scale Atomic/Molecular Massively Parallel Simulator
LBM	Laser Beam Melting
LENS	Laser Engineered Net Shaping
LEO	Low Earth Orbit
LIGGGHTS	LAMMPS Improved for General Granular and Granular Heat Transfer Simulations
MCR	Modular Compact Rheometer
MCT	Mode Coupling Theory
MD	Molecular Dynamics
MFC	Mass Flow Controller
NASA	National Aeronautics and Space Administration
OSP	Orthogonal Superimposed Perturbation
PBF	Powder Bed Fusion
PC	polycarbonate
PCB	Printed Circuit Board
PCBs	Printed Circuit Boards
PEI	polyetherimide
PFC	Parabolic Flight Campaign
PI	principal investigator
PMMA	polymethylmethacrylate
PS	polystyrene
PTFE	polytetrafluoroethylene
rpm	revolutions per minute
SEM	Scanning Electron Microscopy
SI	International System of Units, abbreviated from French *Système International (d'unités)*
SJKR	Simplified Johnson-Kendall-Roberts
SLM	Selective Laser Melting
SLS	Selective Laser Sintering
USA	United States of America
UV	ultraviolet

List of Figures

1.1 Force chains appearing (a) during shear and (b) in isotropic compression, made visible using stress-birefringent photo-elastic 2D particles. Images from Ref. [28], reproduced with permission of Springer. 8
1.2 On a large pile of granular material under its own weight, the force chains arch, inducing an heterogeneous repartition of the weight of the heap. Image reproduced from Ref. [36] with permission from ASCE. This material may be downloaded for personal use only. Any other use requires prior permission of the American Society of Civil Engineers. This material may be found at `https://doi.org/10.1061/(ASCE)GT.1943-5606.0000617`. 9
1.3 Different configurations of the granular packing imply different reorientation and redistribution of the force. 10
1.4 Schematic of a cylindrical container full of granular material considered a continuum material. 11
1.5 Graphical representation of the solution proposed by Janssen, presented in Equation 1.5 11
1.6 Schematic representation of a Taylor-Couette shear-cell seen from above. 14
1.7 Diagram of the control loop of a stress-controlled system. Such system can be deployed even if the variable fixed by the user is the rotation speed of the rotating part of the rheometer, leading to an indirect stress controlled system. 15
1.8 The type of fluidisation observed in the granular bed shifts as the gas velocity u (or flow rate Q) is increased, from (a) no fluidisation to (e) turbulent fluidisation, for the same powder sample. 17
1.9 Theoretical state diagram of the driven granular fluid under shear. Image from Ref. [14], licensed under the Creative Commons Attribution 4.0 International . . 20
1.10 Comparison between theoretical prediction proposed by Kranz *et al.* [14, 86] based on the Mode Coupling Theory applied to agitated granular fluids and experimental data produced. 22
1.11 Evolution of fitting parameters (a) ω_c and (b) $n\,T_{gr}^0$ as a function of packing fraction φ_{th} used in calculating all theoretical flow curves presented above. . . . 23

2.1 Scanning Electron Microscopy (SEM) images of the PS powder used as raw material (the microscopies are done for particles of diameter 250 µm), (a) for powder with smooth surface state, at the scale of a particle and (b) at the scale of its surface; (c) for powder with rough surface state, at the scale of a particle and (d) at the scale if its surface. The imaging was done using low voltage (1 keV) SEM. 26
2.2 SEM images of the rough surface PS powder used as raw material (a) before and (b) after a 20 hours long shear test with 2 minutes of fluidisation before and after at flow rate of $5\,\mathrm{L\,min^{-1}}$. The imaging was done using low voltage (1 keV) SEM. 27

2.3 (a) Freeman Technology 4 Powder Rheometer (FT4). (b) Schematic of the flowability measurement method proposed by the FT4 rheometer. Images (a) and (b) from [104], reproduced with authorisation from Freeman Technology. (c) Helix used as measuring system in the FT4 rheometer *flow energy* measurement, of radius $r = 24\,\text{mm}$. 32
2.4 (a) Sequence of measurements proposed by the preset FT4 dynamic test. The first sequence (in blue) corresponds to the stability test, and the second sequence (in green) is the "variable rotation rate" test. (b) Sequence of measurements proposed in the present work to test the influence of the helix penetrating the sample. 33
2.5 Five measurements, for samples of varying mass (thence varying filling height), plotted (a) as the *total flow energy* E and (b) as the *specific flow energy* E^*, at four increasing penetration speeds. The experimental procedure follows the measurements sequence presented in Figure 2.4b (fluidisation as conditioning). The measurements were conducted on samples of PS powder of diameter 40 µm; the error bars correspond to the maximum and minimum values out of five repetition of each measurement. 34
2.6 Dimensionless *specific flow energy* E^* as a function of the helix penetration speed, for PS powder of diameters 40, 80, 140, 250 µm. 35
2.7 Dimensionless *specific flow energy* E^* as a function of the helix penetration rate, for the two PS powder RS (rough surface state) and SS (smooth surface state). 36
2.8 Pressure drop across the powder bed for (a) smooth surface PS powder, and (b) rough surface PS powder. The powder bed has a diameter $d_b = 50.5\,\text{mm}$ and the sample mass is $m = 70\,\text{g}$. The insets are the measured pressure drop across the powder bed before removing the baseline (dotted line in the insets) due to the pressure drop across the porous substrate. 38
2.9 Rheometry experimental set-up. 39
2.10 Image capture from live-monitoring of the sample's volume. 39
2.11 Diagram illustrating the experimental procedure used to obtain the rheological measurements presented below. 40
2.12 Startup curves for PS powder of grain diameter 80 µm, at shear rates $\dot{\gamma} \in [10^{-2}, 8 \cdot 10^{1}]$, for (a) smooth and (b) rough surface state. Samples' mass is 80 g. The first one hundred full rotations of the inner cylinder are presented, corresponding to a shear strain up to $\gamma \approx 550$, in order to show the transition between transient and stationary flow; however, each experiment was run for up to approx. 5000 turns. 41
2.13 Flow curves for shear experiments performed in a Couette-type shear-cell on the PS powder of diameter 80 µm, for powder with (a) smooth and (b) rough surface state. 43

3.1 Evolution of the relevant interaction forces on the microscopic scale between two particles (a) as a function of length l separating the particles' surfaces, for particles of 80 µm diameter, and (b) as a function particles radius r for spheres separated by 0.01 µm. 52
3.2 Piston-probing principle: experimental setup. 55

3.3 (Top graph) Piston position in height as a function of time. Error bars represent the experimental precision in optical measurement. (Bottom graph) Pressure recorded by the top sensor during the first step up of the piston, on-ground (blue dots, labelled $1g$) and in microgravity (red triangles, labelled μg). The critical jamming time are marked, as well as five points of interest that correspond to images (a) to (e): (a) and (b) are images from the bottom of the experiment cell looking up in microgravity, and (c), (d) and (e) on-ground; the piston's platform is black and the PS powder white. 57
3.4 Critical packing fraction at jamming, estimated from the height at which the piston is driven to a halt by the resistance of the jammed packing, (left) on-ground and (right) in microgravity. 58
3.5 Typical pressure evolution per step up of the piston, (a) on-ground and (b), (c) in microgravity. 59
3.6 Pressure recorded by the top sensor inside the powder container, (a) on-ground and (b) in microgravity, for a longer duration after the initial densification step leading to a jamming transition. 61
3.7 Torque developed for one step up of the piston, (a) on-ground and (b) in microgravity. 62
3.8 Maximum torque developed at each upward step of the piston, and corresponding rise of the piston along z-axis. 62
3.9 Schematic representation of the regions appearing in the experimental cell where material is confined during piston-probing, (a) in microgravity and (b) on-ground, where the powder forms a slope at its angle of repose α with the horizontal. 63
3.10 Relative viscosity η_r as a function of the packing density φ, for $\dot{\gamma} \to 0$ and $\dot{\gamma} \to \infty$. Reprinted with permission from [132]. Copyright 2014, The Society of Rheology. 65

4.1 Principle schematic of extrusion-based manufacturing technique. 73
4.2 (a) First AM apparatus launched to space: the Zero-G 3D printer of Made In Space Inc. installed in the glove-box of the ISS. Image credit Made In Space Inc. (b) AMF, 3D printer currently on-board the ISS. Image credit Made In Space Inc. & Lowe's. (c) CubeSat rails structure, fully 3D printed on board the ISS in the AMF. Images reproduced with permission, © Made In Space Inc./NASA. . 75
4.3 Principle schematic of the DED additive manufacturing technique (here, the wire-based method is represented; however the material feedstock can also be in the form of powder). 77
4.4 A collaboration between ESA, RHP Technology GmbH (Austria) and the Fraunhofer Institute for Material and Beam Technology (Germany) produced a 3 m diameter optic bench for the Athena mission, using the hybrid technique combining plasma metal deposition and CNC milling. The size of the machines gives an idea of the complexity to adapt such mechanism to the ISS environment. Images reproduced with permission, © RHP/SBI R. Syrovatka, from Ref. [170]. 78
4.5 Principle schematic of the SLS or SLM additive manufacturing technique: a powder-bed is created by successive recoating, from which an object is selectively solidified section-by-section. 79

4.6 (a) Schematic of the gas flow assisted powder deposition technique for powder-bed based additive manufacturing of powder in low- and microgravity. (b) The two 12 mm wrenches presented are the first ever metal parts that were 3D printed by LBM in microgravity on parabolic flight. Images from Ref. [141], reproduced under CC BY-NC-ND 4.0 License. 81
4.7 (a) 3D printed packaging ensuring the stability of hardware shipped to the ISS. (b) The so-called Refabricator: a small unit for transforming plastic trash into feedstock filament for FDM manufacturing. (c) Refabricator payload in its final form, as shipped to the ISS in 2019. Images reproduced with permission, © Tethers Unlimited, Inc./NASA. 83
4.8 ESAMM projects are producing a great number of artists' rendering, as the ones presented here, but no hardware has – yet – found its way to space. (a) The principle idea of the SpiderFab. Image reproduced with permission, © NASA/Tethers Unlimited, Inc. and (b) the Archinaut One creating in-orbit an antenna in three stages of evolution. Image reproduced with permission, © Made In Space, Inc./NASA. 85

5.1 Principle of the additive manufacturing method proposed. 90
5.2 Schematic representation of the movements of the different parts composing the RheoPrint powder deposition process. 91
5.3 Schematic representation of the different stages of the RheoPrint additive manufacturing process, including the corresponding step of the process. 92
5.4 Illustration of the superimposition of force chains. 93
5.5 Transport mechanism using screw conveyor blades. 94
5.6 Overview of the step-wise additive manufacturing method proposed: one iteration of the process consists in this sequence of actions, repeated n times until the object is fully manufactured. 95
5.7 Principle of the double control loop implemented on the RheoPrint process: the raw material flow properties is probed upstream 97
5.8 A jammed force chain (left) will break if the load varies from its straight angle of application to a transverse load, unless soft particles change shape to adapt to the new angle of application of the force (right). Reprinted from Ref. [38] with permission from Elsevier. 98
5.9 Evolution of the vertical pressure inside a cylindrical container as as a function of the height of this container 101

6.1 Principle diagram of DEM simulation with contact detection. 104
6.2 Schematic representation of (a) the overlap distance δ between two particles - in this case, the normal overlap δ_N is represented; and (b) the contact area between two spherical particles when they collide, defined as the disc of surface A_{ij}. The particles are in three dimensions, hence the area A_{ij} is the projection of the "double-lens shape" on the tangential plane. 106
6.3 Section view of the assembled model used as mesh, labeled with names of the parts. Coloured parts are the moving parts. The movements of each part at each step of the powder deposition are given in Table 6.5. 109
6.4 Division of the bottom layer of the powder bed used to visualise the simulation results. 111

6.5 Diagram showing a possible packing of the particles. Both layers have similar packing fractions, but the number of particles counted within each region is different. . . . 112
6.6 Evolution of the average volume ratio occupied by the particles on the entire bottom volume, as the process is taking place, at the end of movements 0 to 8. . 114
6.7 Evolution of volume occupied by particles for the simulated deposition of three consecutive layers, including solidification steps in between each powder deposition. The deposition time is constant for all layers in (a) and increased for each new layer in (b). . . . 115
6.8 3D-graph representing the evolution of the percent of volume occupied by the particles as a function of the distance from the centre of the printing volume and of the step of the process (along y-axis), under (a) $1g$ and (b) μg. . . . 117
6.9 Evolution of the normalised difference in powder density between $1g$ and μg, as a function of the distance from the centre of the printing volume (along x-axis) for different steps of the process: at the end of moves 2 to 5 (powder transport) and after move 8, at the final stage. . . . 118
6.10 Volume ratio occupied by particles after the last step of the deposition process, for simulations run under $-1g$, $0g$ and $+1g$. . . . 119
6.11 3D-graph representing the evolution of the percent of volume occupied by the particles as a function of the distance from the centre of the printing volume and of the step of the process (along y-axis), (a) for particles of low cohesion and (b) for highly cohesive particles.. . . . 120
6.12 Volume ratio of particles per 3D bar chart showing the volume ratio of cohesive particles after each movement. . . . 121

7.1 Parabolic trajectory executed by the Air Zero-G Airbus A310 aircraft of Novespace. The aircraft image is courtesy of Novespace, and all the information given is this figure are from [252]. . . . 126
7.2 (Left) photography and (right) CAD image of the prototype RheoPrint 3D printer. The main components of the printer are labeled. On the CAD image, the fixed structure is represented in grey while the moving parts are coloured, each colour representing a movement block. . . . 127
7.3 Movement of each dynamic part of the assembly (image from CAD file). . . . 129
7.4 Labeled photography of the three DC motors allowing rotation of three parts of the prototype RheoPrint 3D printer: the closing disc, the inner tube and the outer tube. . . . 130
7.5 Principle of activation strategy applied to the vibrating disc. . . . 131
7.6 Close-up of the transverse section of the inner part of the powder container (image from CAD file) showing the space in between the coaxial cylinders where the powder is contained (clear surface on the image) and the critical sealing points. 132
7.7 Working principle of the axial flange seal, with a helical spring forcing constant pressure on the seal. . . . 133
7.8 Principle of flexible sealing cloth joining the vibrating disc (represented in yellow) and the fixed outer-tube socket (in grey), in its three typical positions. . . . 133
7.9 Diagram of the printing process, including steps (I) to (III) previously described, and an additional cooling phase necessary for this implementation of the process. 134

7.10 Prototype 3D printer with labeled stages and stop-buttons used for initialisation of the prototype position. The left picture is taken from the front of the prototype, while the picture on the right corresponds the side-view (projection from the right). . . . 134
7.11 Prototype in filling position, open and filled with raw material. . . . 135
7.12 Printing substrate of the prototype 3D printer. (a) Top part of the prototype, that can be removed from its structure to remove the printing substrate or install a virgin one. (b) The printing substrate can be simply screwed and unscrewed from the inner tube, in order for the experimenter to easily fetch the 3D printed sample. . . . 136
7.13 State diagram summarising the program controlling the apparatus, based on the finite-state machine mathematical model of computation. . . . 138
7.14 Principle block diagram of electronic components forming one RheoPrint prototype 3D printer. Dashed lines represent the exchange of information or control signal and solid lines the powering of the different devices. "SE" are servo motors, "DC" are DC motors, "ST" stepper motors and "μC" sub-microcontrollers. All microcontrollers are powered by power convecter 3. . . . 139
7.15 Devices communicating with (a) the main microcontroller and (b) the secondary microcontroller, that function independently of each other. The communication channel deployed between the microcontrollers and each of their subordinated devices are also specified. . . . 141
7.16 Electric boxes containing the PCBs and electronic components controlling each RheoPrint prototype. . . . 142
7.17 Principle of liquid-phase sintering: a soft corona appears around each grain, and this molten layer forms necks between neighbouring grains to decrease their free surface. . . . 143
7.18 The IR-lamp used as power source, (a) mounted on its holder and (b) inserted in the bottom area of the RheoPrint prototype 3D printer. . . . 144
7.19 Two positions of the IR lamp: (a) placed directly under the solidification window and (b) pivoted to allow *in-situ* monitoring of the powder deposition. . . . 145
7.20 Bottom part of the prototype: at the bottom of the powder container, the solidification window creates the interface between the raw material and the energy source. . . . 146
7.21 Preliminary experiment result: temperature evolution on normal-use at selected spots on the prototype. . . . 147
7.22 Top view of the prototype section. The solidification window is the transparent square placed in the centre of the vibrating disc, on top of the IR-lamp. It is held in place by four support brackets clamping it to the bottom of the vibrating disc. The parts in yellow are the parts in motion during the disc's vibration, while the parts in grey are the static support. . . . 148
7.23 Optimal transmission range for commercially available glasses of different chemical composition. . . . 149
7.24 Screen captures of (a) the user interface designed to control the prototypes, and (b) a typical image taken during live-monitoring. In this image the prototype is empty and a virgin printing substrate is visible. . . . 151
7.25 GrainPower rack open from the front with inner illumination on. The two prototypes are placed inside the rack, attached in flight configuration. . . . 152

7.26 Experimental rack right before being shipped to the Novespace facilities in Bordeaux, France. (a) Front with closed second containment and control-laptops attached on top, (b) seen from back, with fuses access (top), electrical control boxes (dark transparent boxes, middle) and power supply boxes (white boxes, bottom). 153
7.27 Experimental estimation of the sintered height as a function of the exposure time to IR radiation. 154
7.28 Block diagram of experimental procedure per prototype on the first day of flight. 155
7.29 GrainPower experiment rack in the Novespace ZeroG plane, open to see the two prototype 3D printers, but the powering of the motors and lamp are disabled by the open magnetic interlocks. Black foam covers the sharp edges of the structure. 156

8.1 Image of the new layer being deposited recorded by the *in-situ* monitoring video system. 160
8.2 Evolution of the powder layer as it is deposited, including the histograms of pixels grey-level distribution and corresponding variance value, for layer $B3L5$. . 161
8.3 Flow chart of the conversion protocol, linking the current drawn by each DC motor to rotate at a defined velocity, to the relevant rheological parameters: the torque developed to shear the granular material at the given rotation speed. K_m is the torque constant of the specific motor, $\eta_{1,2}$ efficiency parameters of the mechanical set-up and $r_{1,2}$ gear ratios. 162
8.4 RheoPrint 3D printer picture and CAD snapshot, with indication of its inner tube and closing disc. 163
8.5 Evolution of the torque produced for two consecutive deposition steps (a) by the motor DC_1 rotating the inner tube and (b) by the motor DC_2 oscillating the closing disc. The area under the curve represents the scalar quantity $\int_t M(t)dt$. . 164
8.6 (Left) Example of X-ray computed tomography (CT) "slice" image, for a sample of PS sintered on-ground, under weight. This sample is used as for comparison of density homogeneity with the 3D printed samples. (Right) Binary image extracted from the tomography and used for analysis. 167
8.7 Sample preparation rationale. 168
8.8 Graphical representations of (a) porosity radii and (b, c) chord length inside porosities, respectively along x- and z-axis (respectively horizontal and vertical directions). The sample presented as example here is sintered under weight, on-ground, from smooth surface PS powder. 169
8.9 Temporal evolution of the torque developed for (a) the mono-directional rotation of the inner tube, and (b) the oscillatory rotation of the closing disc, for all layers of an eleven-layers sample 3D printed on-ground from smooth surface powder. . 170
8.10 Temporal torque evolution for all layers (in light grey) and one typical layer (layer number indicated in legend), for (a) and (d) an empty run; (b) and (e) smooth surface powder, (c) and (f) rough surface powder. All data shown here was obtained on-ground in the prototype $Lafayette$. 171
8.11 Energy transferred through work for each powder deposition process run, for an empty machine (green diamonds), the smooth surface powder (blue circles) and the rough surface powder (red triangle), for the probing done by (a) the inner tube and (b) the closing disc. 172
8.12 Deposition time necessary to observe homogeneous layer from the solidification window, recorded on-ground for smooth and rough surface powder. 173

8.13 Example of (a) CT "slice" of the sample 3D printed from smooth surface powder, on ground, and (b) graphical representation of the corresponding porosity size distribution. . . . 174
8.14 Example of (a) CT "slice" of the sample 3D printed from rough surface powder, on ground, and (b) graphical representation of the corresponding porosity size distribution. . . . 174
8.15 Probability density function per porosity diameter for (a) the comparative sample sintered on-ground under weight, (b) a sample 3D printed from smooth surface powder on-ground and (c) a sample 3D printed from rough surface powder on-ground. The analysis is run for one image every 80 µm, along the y-axis, and the average over the full sample is shown here; error bars represent the standard deviation in density probability per diameter for the full sample. . . . 175
8.16 Average density of the three samples manufactured on-ground: the sample sintered under weight to obtain high powder density as a comparative for "known good", the sample 3D printed from smooth surface powder under $1g$, and the sample 3D printed from rough surface powder under $1g$. . . . 176
8.17 Overview of PFC results, including (a) experimental planning and results overview, and (b) to (e) samples fully manufactured in microgravity. In (b), sample $B1$ is shown directly as extracted from the 3D printer. . . . 177
8.18 Temporal torque evolution for all layers (in light grey) and for a typical layer (layer number indicated in legend), for (a) and (c) smooth surface powder, (b) and (d) rough surface powder, for powder deposition experiments realised fully in microgravity. . . . 178
8.19 (a) Close-up of the high-frequency torque fluctuation observed when shearing rough surface powder, as a function of time and equivalent path traveled at the surface of the inner tube rotating. (b) Image capture of the powder layer homogenisation, corresponding to the moment at which the torque is recorded. . 179
8.20 Energy transferred through work for each powder deposition process, in microgravity, for the smooth surface powder (blue circles) and the rough surface powder (red triangles); the probing is done by (a) the inner tube and (b) the closing disc. Average values are given for the work recorded on-ground, as a reminder, for the same powders. . . . 180
8.21 Deposition time necessary to produce a new powder layer in microgravity, (a) from smooth surface powder and (b) from rough surface powder. The ordinate range is shorter on the bottom graph. The experiments shown here are, following the nomenclature explained above, samples $B3$ and $L3$. For both samples, the first layers are missing because they were not recorded. . . . 182
8.22 Slice of CT of samples (a) $B3$, (b) $L3$ and (c) $L1$ of samples tomographies. . . . 183
8.23 Density of the 3D printed samples over their full length along the y-axis. . . . 184
8.24 Relative frequency of chord spanning porosities per chord length, for all samples studied, with chords extension done along x- and z-direction for each sample. The data sample for the comparative "known good" sample along the x-axis is fitted to a log-normal distribution (solid line), reproduced on all graphs for comparison. . . . 185

8.25 Probability density function per porosity diameter for (a) the comparative sample sintered on-ground under weight, and samples 3D printed from smooth surface powder on-ground and in microgravity. (b) Sample 3D printed from rough surface powder, on-ground and in microgravity, including the "known good" and "known bad" samples for comparison. The analysis is run for one image every 80 µm, along the y-axis, and the average over the full sample is shown here; error bars represent the standard deviation in density probability per diameter for the full sample. The inset in (b) shows the "known bad" data over the full range. . 188
8.26 Picture of the grinding apparatus used to transform the former 3D-printed parts into new feedstock material. 189
8.27 Microscopies of the PS recycled material obtained by grinding former 3D printed parts. 190
8.28 Tensile strength measurement applied to the recycled powder *Rec.* 191
8.29 Picture of the sample 3D printed from material obtained by closed-loop recycling. 191
8.30 Temporal torque evolution for all layers (in light grey) and one hand-picked typical layer (layer number indicated in legend), for recycled PS powder. Experiments are realised on-ground. 192
8.31 Energy transferred through work for each powder layer deposited, for recycled material; the probing is done by (a) the inner tube and (b) the closing disc. . . 193
8.32 *Flowability number* proposed in Eq. 8.3, calculated for all 3D printing experiments realised, i.e. for the five situations in which the RheoPrint additive manufacturing process was tested. 196

A.1 Reproduction of piston-probing experiment discussed in Sections 3.2 and 3.3 in 2D using birefringent particles to observe the formation of force chains as the granular sample is out under compression by the rise of the piston, (a) with the presence of a secondary force field reproducing Earth gravity, and (b) without, reproducing microgravity. xviii

D.1 Design of the Printed Circuit Board (PCB) used as an interface for the secondary microcontroller and its different sub-systems. xxxiv
D.2 Design of the Printed Circuit Board (PCB) used as an interface for the main microcontroller and its different sub-systems. xxxv

List of Tables

2.1 Physical properties of the bulk-polymer composing the grains of the powder used as raw material. The mechanical and physical properties are given by the manufacturer; the glass transition temperature is from Ref. [107]. 28
2.2 Comparative assessment of the possibilities offered by the rheometers MCR from Anton Paar (Austria) and FT4 from Freeman Technology (United Kingdom). The specifications listed here are only valid for the powder-testing version of the rheometers. 29
2.3 Shear moduli G at low shear rate $\dot{\gamma} < 1$ for smooth and rough surface state powder. G is the average slope of the linear part ($\gamma < 40$) of the stress-strain curves, for shear rates $\dot{\gamma} \in [10^{-2}, 1]$. 42

3.1 References for hardware used on the piston-probing experimental setup. 56

4.1 Overview of the different additive manufacturing technologies commercially available today, as well as the type of materials they can print from. Further information on the different AM techniques can be found in the current ISO/ASTM norm on AM terminology [167]. 74

5.1 Numerical parameters corresponding to our system simplified as a horizontal cylinder: a PS powder in an aluminium container. 100

6.1 Notation used for the variables δ and v in the Hertz-Mindlin contact model. . . 105
6.2 Notation used for the coefficients $k_{N,T}$ and $\gamma_{N,T}$ in the Hertz-Mindlin contact model. The coefficients are specific to this model, i.e. $k_{N,T}$ are not Hooke's elastic constants. 106
6.3 Material properties of polystyrene [247] and aluminium [248]. 108
6.4 Simulation parameters $k_{N,T}$ and $\gamma_{N,T}$ for the two type of interactions present in our model: PS-PS and PS-aluminium. 109
6.5 Description of the movements of the different parts of the mesh as the simulation progresses through an entire powder deposition step. 110
6.6 Description of boundary movements in the simulation. 113

7.1 Experimental microgravity platforms available for scientific purpose today [251]. 125
7.2 Variables and parameters corresponding to each moving component of the 3D printer. Fixed variables are fixed depending on the raw material used within the available range presented. 128
7.3 Technical specifications for the Heraeus Quattro IR emitter. 145
7.4 Thermal properties for the list of selected glasses compositions. The information presented here correspond to the values given by the manufacturer for commercial glasses, see [258–260]. 149
7.5 Experimental plan for the PFC. 155

8.1 Characteristic parameters of the motors and gears used to convert the current withdrawn into the torque developed and finally into the shear stress applied to the granular material. . . . 163
8.2 Steady-state rotation speed of all rotating parts of the prototype 3D printers and corresponding motors. . . . 164
8.3 Scanning parameters used to obtain the X-ray computed tomography of sintered PS. . . . 166
8.4 Dimensionless number Fl proposed in Eq. 8.3 to compare the powder handling process studied, applied to different materials, and labelled *flowability number*. It is calculated from the work recorded by the inner tube mono-directional probing, on-ground, for powder with smooth surface (high flowability, SS) and rough surface (mediocre flowability, RS). . . . 173
8.5 Printing parameters used during PFC to 3D print samples in microgravity from smooth and rough surface PS powders. . . . 177
8.6 Fitting parameters used to fit the chord length probability density obtained for each sample in x- z-directions to the log-normal distribution, $\mu_{x,z}$ and $\sigma_{x,z}$, and mean chord length $\langle l_{x,z} \rangle$. . . . 186

C.1 Precise description of the inner tube movements and their technical implementation. . . . xxx
C.2 Precise description of the closing disc movements and their technical implementation. . . . xxxi
C.3 Precise description of the outer tube movements and their technical implementation. . . . xxxi
C.4 Precise description of the vibrating disc movements and their technical implementation. . . . xxxii
C.5 Precise description of the movements of the IR holder on its swiveling arm and their technical implementation. . . . xxxii

Appendices

Appendix A

Observing force chains formation

Using birefringent particles, force chains become apparent in granular media in 2D (see Chapter 1, and Ref. [24]). To gain a better understanding of the mechanisms at stake in the piston-probing experiment presented in Chapter 3 (see Sections 3.2 and 3.3), this experiment was reproduced in 2D using birefringent particles, hence enabling direct observation of the differences in force chains formation due to the present or absence of a secondary force field – Earth gravity.

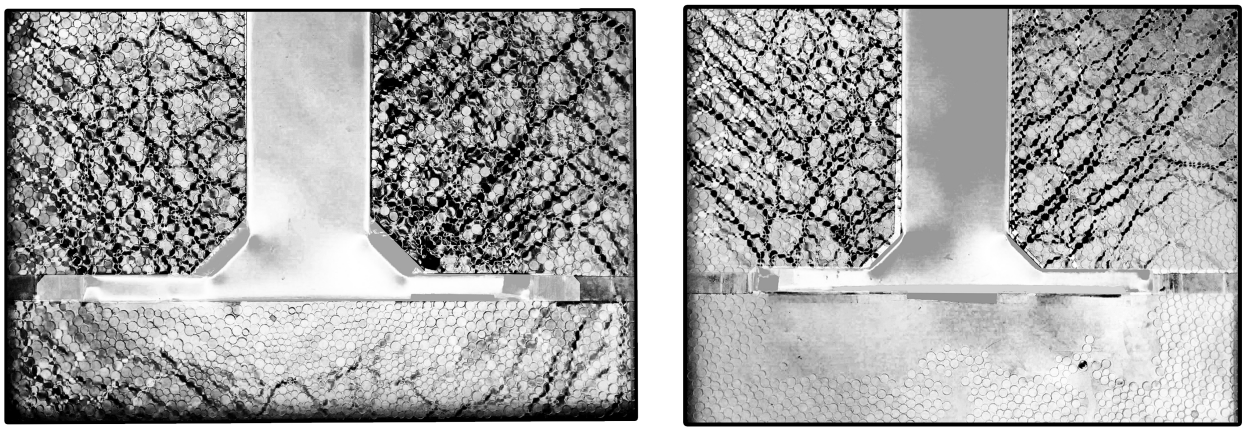

(a) $1g$ **(b)** μg

Figure A.1: Reproduction of piston-probing experiment discussed in Sections 3.2 and 3.3 in 2D using birefringent particles to observe the formation of force chains as the granular sample is out under compression by the rise of the piston, (a) with the presence of a secondary force field reproducing Earth gravity, and (b) without, reproducing microgravity.

Images resulting from this 2D reproduction of piston-probing are presented in Figure A.1. The gravitational forces were reproduced by tilting the experimental box perpendicular to the ground for Figure A.1a, hence using gravity to draw all particles downward vertically; for reproduction of the microgravity experiment (Figure A.1b), the experimental box remained horizontal to the ground, thence no force is bringing the particles towards the bottom of the box. Comparison of the two images, the "regions" proposed in Figure 3.9, becomes visible, as well as the effect of the secondary force field for the particles under the piston's platform. For both images, above the platform a large number of force chains appear under compression of the rising piston. Under the platform however, in $1g$ (Figure A.1a) force chains are visible close to the container wall, where the weight of the granular packing placed on the upper part of the

container is passed down onto the bottom particles. Under this pressure, as well as the weight of the particles themselves, the packing crumbles under the platform and the volume emptied by the piston rise is filled intermittently. On the other hand, in μg (Figure A.1b), under the piston's platform no force chain is visible, and the space created by the piston rise is left empty.

This result, produced by a small hands-on experiment with little control of the external parameters, fully supports the conclusions of the piston-probing experiment presented in Section 3.3.

Appendix B

Simulation

The DEM simulation presented in Chapter 6 is run on the software LAMMPS Improved for General Granular and Granular Heat Transfer Simulations (LIGGGHTS); the command script used is reproduced as Appendix B.1. Snapshots of the results' visualisation are given as Appendix B.2.

B.1 Command script

```
echo    both
atom_style  granular
atom_modify     map array
communicate single vel yes
processors  2 2 2
boundary  f f f
newton    off
units   si
region    calcul_domain block -0.08 0.08 -0.08 0.08 -0.001 0.26 units box
create_box  2 calcul_domain


# Specify neighbour cutoff distance
neighbor  0.001 bin
neigh_modify  delay 0


# Specify material properties and interactions
fix   m_kn    all property/global kn peratomtypepair 2    1.52e6 4.10e6 4.10e6
    4.63e7
fix   m_kt    all property/global   kt peratomtypepair 2    2.04e5 5.51e5 5.51e5
     2.04e6
fix   m_gamman  all property/global   gamman peratomtypepair 2  4.56e8 8.92e8
    8.92e8 3.31e15
fix   m_gammat  all property/global   gammat peratomtypepair 2  4.10e8 8.01e8
    8.01e8 2.95e15

fix   m4  all property/global   coefficientFriction peratomtypepair 2     0.5
    0.3 0.3 1.05
fix   m5  all property/global   coefficientRollingFriction peratomtypepair 2
    0.005 0.005 0.005 0.005
```

```
fix             m6  all property/global   cohesionEnergyDensity peratomtypepair
    2   1.0e5 1.0e-4 1.0e-4 1.0e-4
27
29 # Specify contact model
pair_style      gran model hertz/stiffness tangential history cohesion sjkr
    rolling_friction epsd2
31 pair_coeff      * *
33
# Specify time step and gravitational acceleration
35 timestep  5.0e-7
fix   gravi all gravity 9.81 vector 0.0 0.0 -1.0
37
39 # Specify how to import mesh from CAD
fix   CAD1 all mesh/surface file vibratingDisc_0.stl type 2 scale 1 curvature 1e
    -5
41 fix   CAD2 all mesh/surface file outerTube_socket_0.stl type 2 scale 1 move 0 0
    0.011 curvature 1e-5
fix   CAD3 all mesh/surface/stress file outerTube_low_1.stl type 2 scale 1 move
    0 0 0.0366 curvature 1e-5
43 fix   CAD4a all mesh/surface/stress file innerTube_bottom_0.stl type 2 scale 1
    move 0 0 0.005 curvature 1e-5
fix   CAD4b all mesh/surface/stress file innerTube_pipe_paddles_1.stl type 2
    scale 1 move 0 0 0.024 curvature 1e-5
45 fix   CAD4c all mesh/surface/stress file innerTube_pipe_1.stl type 2 scale 1
    move 0 0 0.024 curvature 1e-5
fix   CAD5 all mesh/surface file outerTube_top_2.stl type 2 scale 1 move 0 0
    0.0698 curvature 1e-5
47 fix   CAD6 all mesh/surface/stress file closingDisc_paddles.stl type 2 scale 1
    move 0 0 0.2077 curvature 1e-5

49 fix   geometry all wall/gran model hertz/stiffness tangential history cohesion
    sjkr rolling_friction epsd2 mesh n_meshes 8 meshes CAD1 CAD2 CAD3 CAD4a CAD4b
     CAD4c CAD5 CAD6


51
# Specific regions
53 region          Inner_cylinder cylinder z 0.0 0.0 0.0325 0.0698 0.2007 side out
    units box
region          Outer_cylinder cylinder z 0.0 0.0 0.06 0.0698 0.2007 side in
    units box
55
57 # Specific region where particles will be inserted
region          Deposition_area intersect 2 Outer_cylinder Inner_cylinder
59
61 # Specify particle number, size
fix   particles1 all particletemplate/sphere 15485863 atom_type 1 density
    constant 1050 radius constant 1e-3 volume_limit 1e-15
63 fix   particles1_distrib all particledistribution/discrete 32452843 1 particles1
     1.0
fix   particles1_insertion all insert/pack seed 49979687 distributiontemplate
    particles1_distrib insert_every once overlapcheck yes all_in yes maxattempt
    10000 particles_in_region 76000 region Deposition_area ntry_mc 100000
65
```

```
# Update position, velocity and angular velocity at each time-step
fix   integr all nve/sphere


# Specify screen information showing during calculation
thermo_style  custom step time cpu cpuremain atoms ke
thermo    1000
thermo_modify lost ignore norm no


# Setting is finished: run simulation and specify which property is dumped
# 1) Create the particles
run   1
# 2) Create the walls (geometry) and specify measurement variables
dump          dmp all custom/vtk 1000 post/particles_*.vtk type id radius x y z
   vx vy vz fx fy fz omegax omegay omegaz tqx tqy tqz
dump          dmp1 all mesh/vtk 1000 post/mesh1_*.vtk id CAD1
dump          dmp2 all mesh/vtk 1000 post/mesh2_*.vtk id CAD2
dump          dmp3 all mesh/vtk 1000 post/mesh3_*.vtk id CAD3
dump          dmp4a all mesh/vtk 1000 post/mesh4a_*.vtk id CAD4a
dump          dmp4b all mesh/vtk 1000 post/mesh4b_*.vtk id CAD4b
dump          dmp4c all mesh/vtk 1000 post/mesh4c_*.vtk id CAD4c
dump          dmp5 all mesh/vtk 1000 post/mesh5_*.vtk id CAD5
dump          dmp6 all mesh/vtk 1000 post/mesh6_*.vtk id CAD6

variable  time equal step*dt

variable  Fx3 equal f_CAD3[1]
variable  Fy3 equal f_CAD3[2]
variable  Fz3 equal f_CAD3[3]
variable  Mx3 equal f_CAD3[4]
variable  My3 equal f_CAD3[5]
variable  Mz3 equal f_CAD3[6]
fix   dmp7 all print 1000 "${time} ${Fx3} ${Fy3} ${Fz3} ${Mx3} ${My3} ${Mz3}"
   file post/OuterTube.csv title "t,Fx,Fy,Fz,Mx,My,Mz" screen no

variable  Fx4a equal f_CAD4a[1]
variable  Fy4a equal f_CAD4a[2]
variable  Fz4a equal f_CAD4a[3]
variable  Mx4a equal f_CAD4a[4]
variable  My4a equal f_CAD4a[5]
variable  Mz4a equal f_CAD4a[6]
fix   dmp8a all print 1000 "${time} ${Fx4a} ${Fy4a} ${Fz4a} ${Mx4a} ${My4a} ${
   Mz4a}" file post/InnerTube1.csv title "t,Fx,Fy,Fz,Mx,My,Mz" screen no

variable  Fx4b equal f_CAD4b[1]
variable  Fy4b equal f_CAD4b[2]
variable  Fz4b equal f_CAD4b[3]
variable  Mx4b equal f_CAD4b[4]
variable  My4b equal f_CAD4b[5]
variable  Mz4b equal f_CAD4b[6]
fix   dmp8b all print 1000 "${time} ${Fx4b} ${Fy4b} ${Fz4b} ${Mx4b} ${My4b} ${
   Mz4b}" file post/InnerTube2.csv title "t,Fx,Fy,Fz,Mx,My,Mz" screen no

variable  Fx4c equal f_CAD4c[1]
variable  Fy4c equal f_CAD4c[2]
variable  Fz4c equal f_CAD4c[3]
```

```
variable  Mx4c equal f_CAD4c[4]
variable  My4c equal f_CAD4c[5]
variable  Mz4c equal f_CAD4c[6]
fix   dmp8c all print 1000 "${time} ${Fx4c} ${Fy4c} ${Fz4c} ${Mx4c} ${My4c} ${Mz4c}" file post/InnerTube3.csv title "t,Fx,Fy,Fz,Mx,My,Mz" screen no

variable  Fx6 equal f_CAD6[1]
variable  Fy6 equal f_CAD6[2]
variable  Fz6 equal f_CAD6[3]
variable  Mx6 equal f_CAD6[4]
variable  My6 equal f_CAD6[5]
variable  Mz6 equal f_CAD6[6]
fix   dmp9 all print 1000 "${time} ${Fx6} ${Fy6} ${Fz6} ${Mx6} ${My6} ${Mz6}" file post/ClosingDisc.csv title "t,Fx,Fy,Fz,Mx,My,Mz" screen no


# 3) Process movements displayed

# Step 0: Movement of closing disk
fix   move_0 all move/mesh mesh CAD6 linear 0 0 -0.23
run   1000000
unfix   move_0

run   200000

unfix   gravi
fix   gravi_0 all gravity 9.81 vector 0.0 0.0 1.0


# Step 1: Incremental rise of the inner tube
fix   move_1a all move/mesh mesh CAD4a linear 0 0 2.0e-1
fix   move_1b all move/mesh mesh CAD4b linear 0 0 2.0e-1
fix   move_1c all move/mesh mesh CAD4c linear 0 0 2.0e-1
run         200000
unfix   move_1a
unfix   move_1b
unfix   move_1c


# Step 2: Powder transport
fix   move_2a all move/mesh mesh CAD4a rotate origin 0 0 0 axis 0 0 -1 period 0.025
fix   move_2b all move/mesh mesh CAD4b rotate origin 0 0 0 axis 0 0 -1 period 0.025
fix   move_2c all move/mesh mesh CAD4c rotate origin 0 0 0 axis 0 0 -1 period 0.025
fix     move_3 all move/mesh mesh CAD6 linear 0 0 -0.5e-1
run         200000
unfix   move_2a
unfix   move_2b
unfix   move_2c
unfix   move_3
fix   move_4 all move/mesh mesh CAD6 rotate origin 0 0 0 axis 0 0 1 period 0.05
run         200000
unfix   move_4

fix   move_5 all move/mesh mesh CAD6 rotate origin 0 0 0 axis 0 0 -1 period 0.05
run         200000
```

```
unfix   move_5

fix   move_6 all move/mesh mesh CAD3 rotate origin 0 0 0 axis 0 0 -1 period
   0.025
run         200000
unfix   move_6


# Step3: Layer homogenisation
fix   move_7 all move/mesh mesh CAD1 wiggle amplitude 10e-3 0 0 period 0.05
run         400000
unfix   move_7
fix   move_8 all move/mesh mesh CAD1 wiggle amplitude 0 10e-3 0 period 0.05
run         400000
unfix   move_8


# Step 4: Compression
fix   move_9a all move/mesh mesh CAD4a linear 0 0 -1.0e-1
fix   move_9b all move/mesh mesh CAD4b linear 0 0 -1.0e-1
fix   move_9c all move/mesh mesh CAD4c linear 0 0 -1.0e-1
run   200000
```

Listing B.1: Commands script for LIGGGHTS simulation.

B.2 Snapshots of simulation results

Snapshots are shown in chronological order, for the entire deposition process of one layer, as described in Chapter 6. Each image is taken at the end of the respective move, unless specified otherwise. The external container is not shown for the granulate to be visible. The simulation is run for a gravitational acceleration $g = 0$, with 76000 particles of diameter $d = 2\,\text{mm}$. The colour scale represents the magnitude of the speed at which the particles are moving, hence highlighting the particles in motion *versus* the static particles for each step fo the deposition process.

Move 0 – Particles are inserted and dropped down into the container using artificially high gravity.

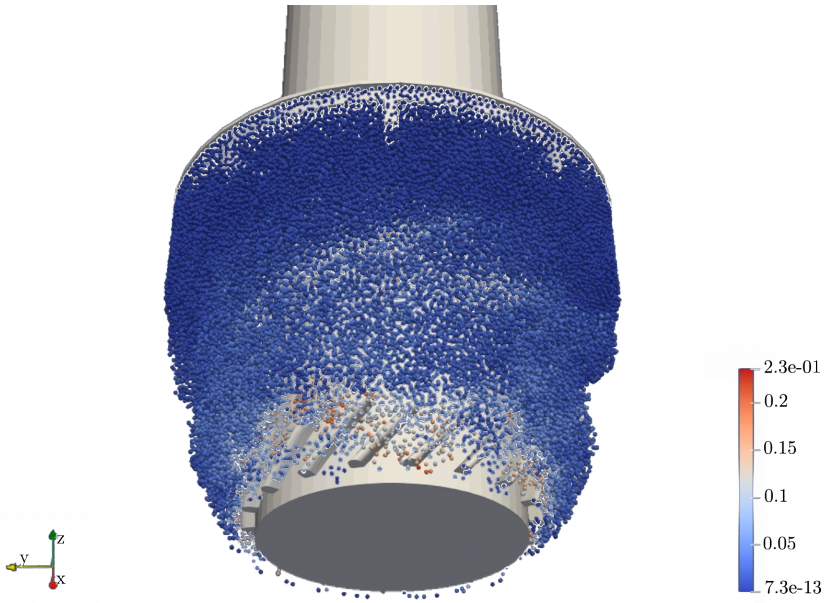

Move 1 – Inner tube rises by two increments.

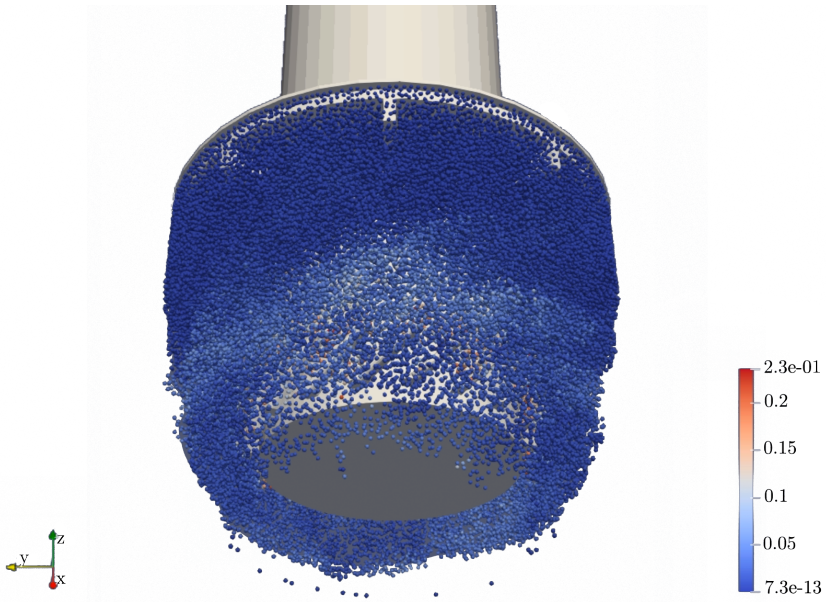

Move 2.1 – Inner tube rotation.

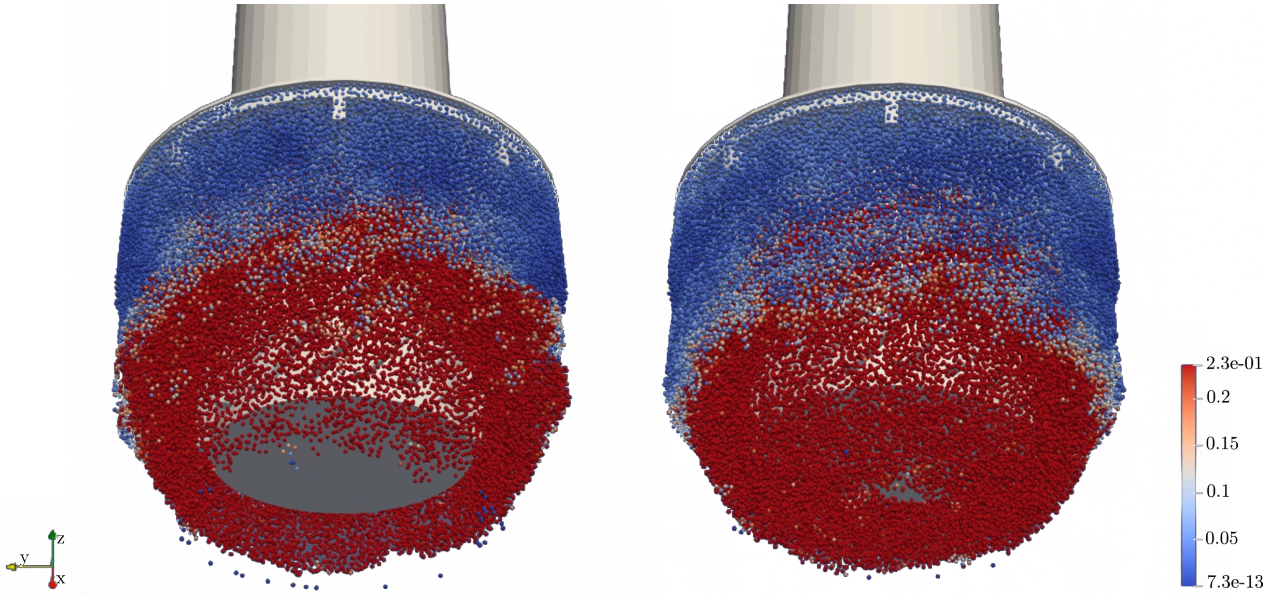

Start of move End of move

Move 2.2 – Closing disc compression.

Move 3 & 4 – Closing disc rotation (counterclockwise and clockwise).

Move 5 – Outer tube screw-conveyor rotation.

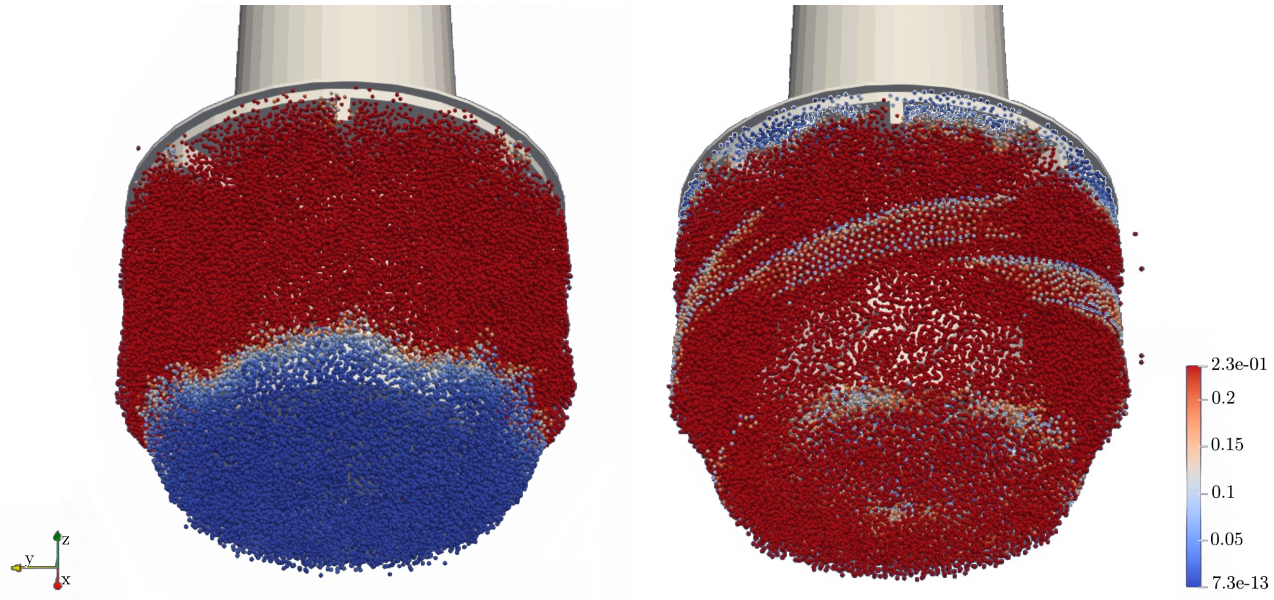

Start of move

End of move

Move 6 & 7 – Vibrating disc shaking in x- and y-direction.

Move 8 – Inner tube compression downwards by one increment.

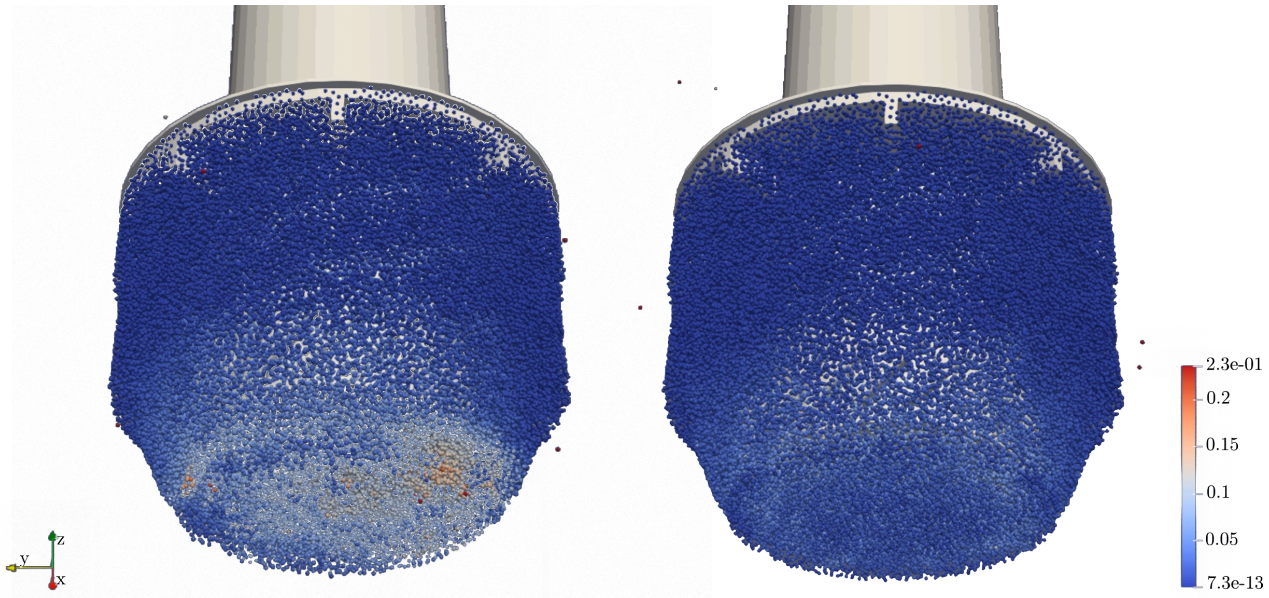

Start of move End of move

Appendix C

Electronic hardware specifications

Movements of the different parts of the RheoPrint prototype 3D printers are implemented by various motors, adapted to the design requirements for each desired movement. Tables C.1 to C.5 give the motors specifications for the final version of the prototypes for each part in motion. For parts describing multiple movements (generally rotation and linear movement), the sub-classification is done as a function of the type of motion.

C.1 Inner tube

Table C.1: Precise description of the inner tube movements and their technical implementation.

Type of movement	**Technical realisation**	**Type of motor**	**Characteristics of the components**	
Linear	Spindle nut on threaded rod, driven by stepper motor **SM1**	Bipolar stepper motor with lead screw NEMA 17	**Motor characteristics**	
			Nominal voltage	24 V
			Current per Phase	1.5 A / Phase
			Max. thrust force	111 N
			Linear step size	5.08 µm
			Steps per revolution	400-25600
			Electrical input	
			Input current	$\leq$ 1.5 A
			Input voltage	24 V
			Operating speed range	$\leq$ 20 mm s^{-1}
Rotation	Gear with transmission, pinion driven by DC motor **DC1**	DC motor Faulhaber-1741U018CXR Gearhead 17/1 11:1	**Motor characteristics**	
			Nominal voltage	18 V
			Maximum current	1.2 A
			Torque constant	22.71 mN m A^{-1}
			Stall torque	26.1 mN m
			No load maximal speed	7300 rpm
			Speed constant	420 min /V
			Electrical input	
			Input current	$\leq$ 1.5 A
			Input voltage	18 V
			Operating speed range	$\leq$ 60 rpm

C.2 Closing disc

Table C.2: Precise description of the closing disc movements and their technical implementation.

Type of movement	**Technical realisation**	**Type of motor**	**Characteristics of the components**	
Linear	Spindle nut on threaded rod, driven by stepper motor **SM2**	Bipolar stepper motor with lead screw NEMA 23	**Motor characteristics**	
			Nominal voltage	24 V
			Current per Phase	1.9 A / Phase
			Max. thrust force	267 N
			Linear step size	9.906 µm
			Steps per revolution	400-25600
			Electrical input	
			Input current	$\leq$ 2 A
			Input voltage	24 V
			Operating speed range	$\leq$ 20 mm s^{-1}
Rotation	Gear with transmission, pinion driven by DC motor **DC2**	DC motor Faulhaber-1741U018CXR Gearhead 17/1 20:1	**Motor characteristics**	
			Nominal voltage	18 V
			Maximum current	1.2 A
			Torque constant	22.71 mN m A^{-1}
			Stall torque	26.1 mN m
			No load maximal speed	7300 rpm
			Speed constant	420 min /V
			Electrical input	
			Input current	1.5 A
			Input voltage	18 V
			Operating speed range	$\leq$ 60 rpm

C.3 Outer tube

Table C.3: Precise description of the outer tube movements and their technical implementation.

Type of movement	**Technical realisation**	**Type of motor**	**Characteristics of the components**	
Rotation	Gear with transmission, pinion driven by DC motor **DC3**	DC motor Faulhaber-2668W024CR Gearhead 26/1R 23:1	**Motor characteristics**	
			Nominal voltage	24 V
			Maximum current	23 A
			Torque constant	28.9 mN m A^{-1}
			Stall torque	656 mN m
			No load maximal speed	7800 rpm
			Speed constant	331 min /V
			Electrical input	
			Input current	$\leq$ 24 A
			Input voltage	24 V
			Operating speed range	$\leq$ 60 rpm

C.4 Vibrating disc

Table C.4: Precise description of the vibrating disc movements and their technical implementation.

Type of movement	Technical realisation	Type of motor	Characteristics of the components	
			Motor characteristics	
Vibration	Servo motors **SE1** and **SE2** with connecting rod transforming the rotation of the motor's shaft into a linear movement in the x-axis and in the y-axis	Two MKS Standard servo: HBL880 Digital-Servo	Nominal voltage	6 V to 8.4 V
			Stall current	6.0 A (8.2 V) 5.4 A (7.4 V) 4.4 A (6.0 V)
			Torque constant	-
			Stall torque	11.2 kg/cm (8.2 V) 10.1 kg/cm (7.4 V) 8.2 kg/cm (6.0 V)
			No load maximal speed	0.032 s (8.2 V) 0.036 s (7.4 V) 0.044 s (6.0 V)
			Speed constant	-
			Electrical input	
			Input current	$\leq$ 6.2 A
			Input voltage	-
			Operating speed range	-

C.5 Infrared lamp

Table C.5: Precise description of the movements of the IR holder on its swiveling arm and their technical implementation.

Type of movement	Technical realisation	Type of motor	Characteristics of the components	
			Motor characteristics	
Swivel	Servo motor **SE3** with connecting rod	HITEC HS7954 SH High Voltage Super Torque	Nominal voltage	6 V to 8.4 V
			Stall current	-
			Torque constant	-
			Stall torque	3.0 N m (7.4 V) 2.5 N m (6.0 V)
			No load maximal speed	0.12 s (7.4 V) 0.15 s (6.0 V)
			Speed constant	-
			Electrical input	
			Input current	-
			Input voltage	-
			Operating speed range	-

Appendix D

Printed circuit boards

The Printed Circuit Boards (PCBs) designed serve as interface between the different components controlling the prototype 3D printers. The main microcontroller is placed on the main PCB, and serves to control the principal algorithm, going through the different steps of the printing process and sending the adequate commands to the multiple sub-systems. Its two faces are presented in Figure D.2. The secondary microcontroller PCB, which is dedicated to the control of the infrared-lamp, is presented in Figure D.1.

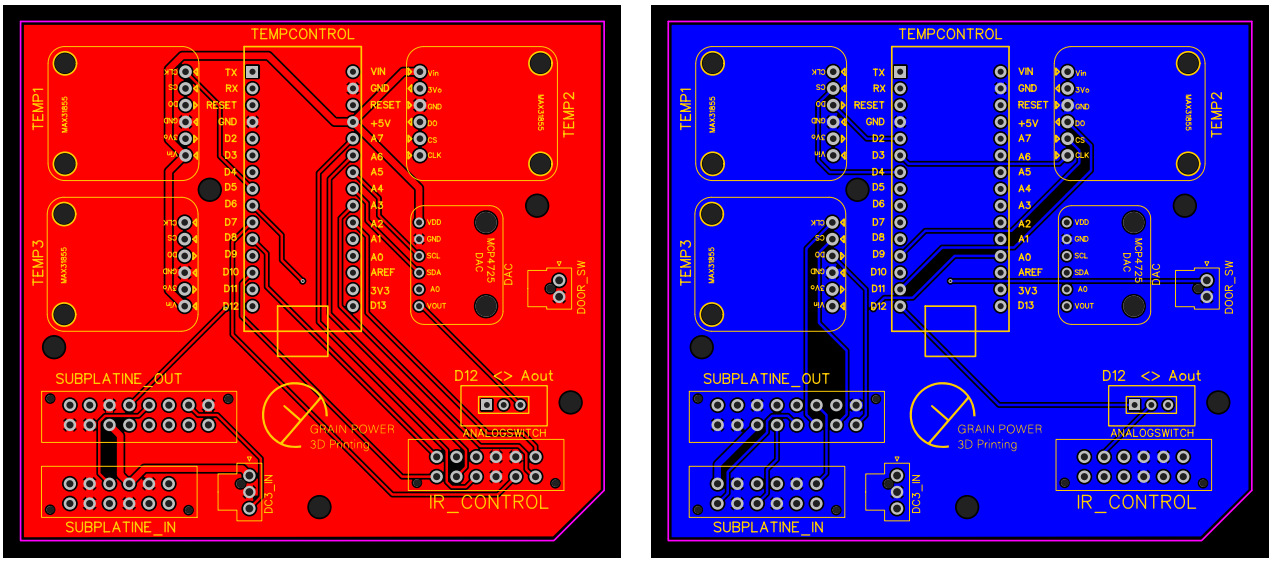

(a) Front **(b)** Back

Figure D.1: Design of the Printed Circuit Board (PCB) used as an interface for the secondary microcontroller and its different sub-systems.

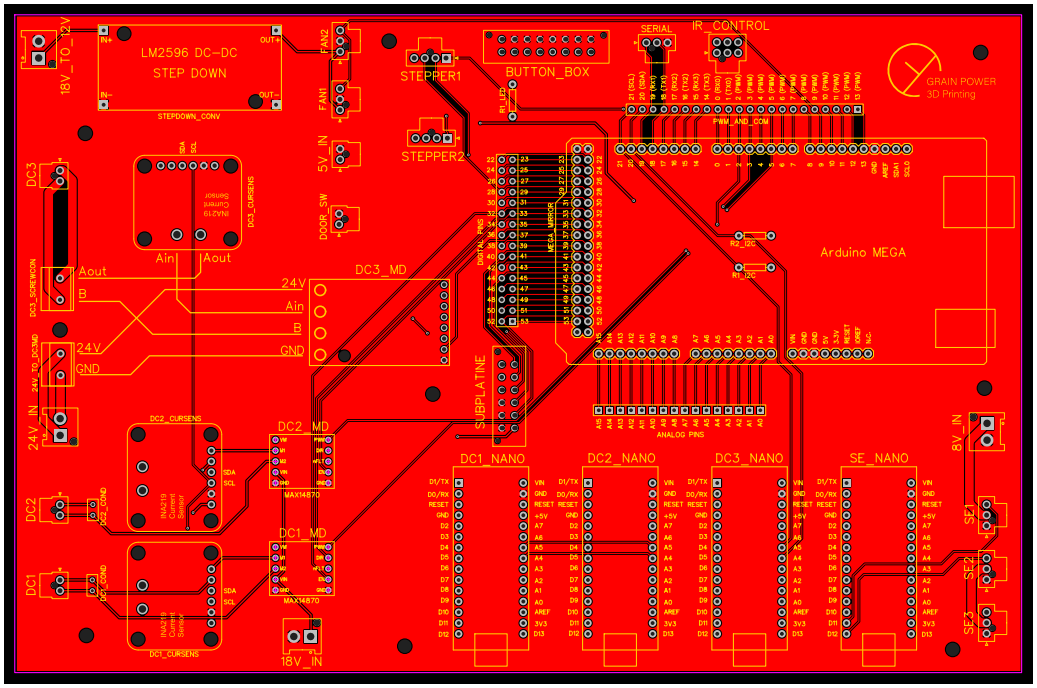

(a) Front

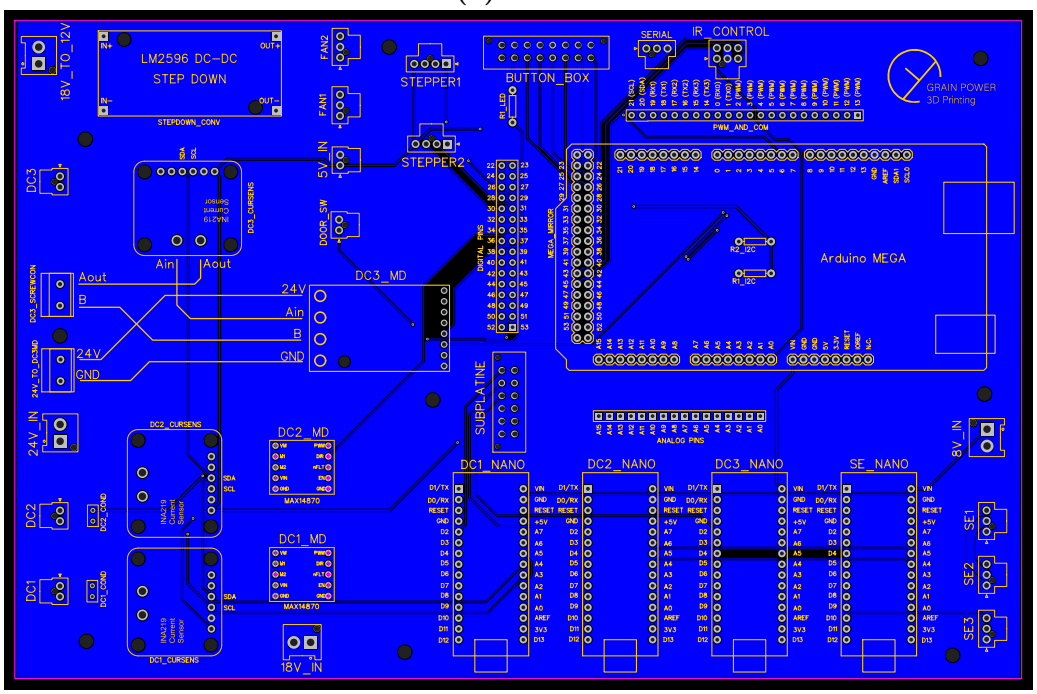

(b) Back

Figure D.2: Design of the Printed Circuit Board (PCB) used as an interface for the main microcontroller and its different sub-systems.

Appendix E

Cognitive science project

As science is a social activity and scientific knowledge does not emerge independently of the social, cultural, historical, political and economic context within which it is embedded, science must always keep a critical look on itself, to conserve credibility and improve its means of research and thus its results. Nonetheless, sociological factors merely feature in scientific experiments or in our understanding of scientific knowledge. Even though the scientist individuality plays a central role in determining which questions to ask (and which to ignore, by default), how to frame them, what data to collect, and how to analyse and interpret it; they remain invisible.

As principal investigator (PI) of the GrainPower project, selected to take part in the ESA Education Fly Your Thesis! 2019 program, the author sought the involvement of a cognitive scientist. It was meant to allow diversity in background in the team and to propose a different perspective on the development of a scientific, technological experiment. This project was conducted in collaboration with Abeba Birhane `[https://abebabirhane.wordpress.com]`; she is co-author of the following text and carried out the actual research independently. She is an Irish citizen, former physics student and now doing her PhD in Cognitive Science at the University College of Dublin in the School of Computer Science. Although Abeba Birhane's work is categorised under the broad umbrella of cognitive science, at the core of her project is an attempt to explore the often discarded concepts such as history, context, language, political and other factors, which play a role behind what we see as base knowledge and objective scientific practices. Therefore, her work is fitting best within the broader Science and Technology Studies domain.

The main purpose of this project was to study the development of a scientific experiment from the point of view of the human interactions, as was done among others by Collins [277], a pioneer of the sociology of scientific knowledge. It aims to give another resonance to the work done, also by involving new actors and therefore interest from other fields of research.

Concretely, the work of the team during the preparation of the experiment was observed, Abeba Birhane took part in in all the steps of the Fly Your Thesis! program to examine, record and interview *in-situ* the other team members as well as other scientists and the entire "fauna" surrounding such experimental platform. Getting onboard with a multidisciplinary team of scientists and observing the development of a 3D-printing experiment in microgravity has been an opportunity to study the intertwined and reciprocal nature of sociological factors and scientific practices. It has further allowed situating the realisation of a technological proof of concept and

the evolution of groups' dynamics, language and discourse in the wider sociological, political and historical context. As far as her PhD research goes, This collaborative engagement provided the material for a worked-out example where a unique experimental practice and knowledge production can be situated and analysed in the broader social and societal environment.

Sociologists often theorise with little exposure to actual scientific practices, and similarly scientists are to a large extent unaware of the philosophical assumptions they base their work on, underestimating the role of language, and the sociological and political forces that operate behind ones work. We aim to propose an alternative way of working, by increasing awareness of scientists to their surroundings and to the work of their colleagues. From this project, we hope to produce a publication underlining certain complex factors that define scientific projects and yet often stay unnoticed. It is also hoped that such successful collaboration will spur interest for multidisciplinary team work in other projects, working to close existing gaps between *hard* and *social* sciences.

Appendix F

Curriculum vitae

Olfa D'Angelo

August 19th 1992

Résidence des Tilleuls – Bât. C
55 rue des Arcs Saint Cyprien
31 300 Toulouse, France

+33 24 34 49 64

olfa.dangelo@mail.com

Languages

French – Native speaker

English – Fluent

Spanish – Fluent

German – Good global level

Language scale from 0 (Basics) to 6 (Native Speaker).

Software skills

Simulation	DEM simulation (LIGGGHTS) FEA simulation (ABAQUS)
Programming languages	C++ Java (Processing, imageJ) Matlab Mathematica Python
3D design	CATIA SolidWorks AutoCAD
Design	Photoshop Illustrator

Research topics

Powder rheology • Granular media • Additive manufacturing • In-space manufacturing • Process monitoring • DEM simulation • *In-situ* resource utilisation • Microgravity research

Education

2017-2021 **Ph.D. in Engineering Science** — Germany
Institute for Materials Physics in Space (DLR)
RWTH University Aachen
Powder-based additive manufacturing for space

2013-2017 **Master in Material Science and Engineering** — France/Sweden
Multi-national diploma
University of Lorraine & Luleå University of Technology

2015-2017 **Master in Management & Business Administration (MBA)** — France
High Institute of Management and Business Administration
ISAM-IAE, University of Lorraine

2011-2013 **Bachelor in Science** — France
European School of Material Engineering (EEIGM)

2007-2011 **High school, grad. with highest honours** — France/USA

Publications

Scientific publication

O. D'Angelo et al., *A gravity-independent powder-based additive manufacturing process tailored for space applications*, submitted to Additive Manufacturing (2021). `arXiv:2102.09815 [cond-mat.mtrl-sci]`.

Scientific publications (in preparation)

O. D'Angelo, A. Horb, A. Cowley, M. Sperl, W. T. Kranz, *Granular piston-probing in microgravity: powder compression, from densification to jamming*, in preparation (2021).

O. D'Angelo, M. Sperl, W. T. Kranz, *Constitutive equations for dense agitated granular flows: from theoretical description to rheology experiment*, in preparation (2021).

L. Heitmeier, O. D'Angelo, Th. Voigtmann, *Rheological response of granular materials under varying gravitational conditions: a comparative study of Discrete Element Method simulation and experiment*, in preparation (2021).

O. D'Angelo, Th. Voigtmann, *Granular rheology in microgravity: a review*, in preparation (2021).

O. D'Angelo, A. Meyer, *Handling powders of any flowability through rheological in-situ monitoring towards in-space recycling*, in preparation (2021).

Patents

O. Lopez-D'Angelo, A. Meyer, *Apparatus and Method for Additive Manufacturing of Components in Environments with Various Gravitation-levels and with Materials of Different Flowability*, German Patent Application DE 10 2020 123 753.7, (2020).

M. Fateri, M. Sperl, O. Lopez-D'Angelo, *Method and apparatus for additive manufacturing*, German Patent Application DE 10 2017 207 769 A1, (2018).

Other publications

O. Lopez-D'Angelo, "The means to our ambitions: 3D printing as a stepping stone for humanity on its way to space", *SELGRA Newsletter* (2019) `https://mailchi.mp/44af5d628425/selgranewsletter_june2019`.

B. Imhof et al., "Advancing Solar Sintering for Building A Base On The Moon", 69th International Astronautical Congress, Adelaide, Australia (2017).

Awards & Fellowships

2021 — **ELGRA Research Prize** — Cologne, Germany & Amsterdam, Netherlands
VIP-DROP^2 – Visco-plastic fluids droplets in microgravity

2020 — **Student Travel Grant** — Rio de Janeiro, Brazil
International Congress on Rheology 2020

2018-2020 — ***Fly Your Thesis! 2019*** — Leiden, Netherlands
ESA Education competitive program (ESA/ESTEC)

2017-2020 — ***Networking/Partnering Initiative* Fellowship** — Cologne, Germany
Co-funding of doctorate research (30 k€/year) (ESA/EAC)

2017-2020 — ***DLR/DAAD* Fellowship** — Cologne, Germany
German Academic Exchange Service, doctorate funding

2016 — ***Entreprendre 2016*** — Nancy, France
National entrepreneurship contest, 1st place

2016 — ***Generation Sustainable Development*** — Nancy, France
National sustainable development project contest, 1st place

2016 — ***Creativ'Est*** — Nancy, France
Regional creative project contest, 2nd place

2016 — ***Entreprendre en Lorraine*** — Nancy, France
Regional entrepreneurship contest, 1st place

Talks & conferences

2021 — **United Nations Office for Outer Space Affairs** — Cyberspace
Invited speaker – Webinar Series on Hypergravity/Microgravity

2021 — **Annual European Rheology Conference** — Cyberspace
Podium talk – Chair for session *Powder rheology, granular flows and rheology of solids*

2020 — **International Congress on Rheology** — Rio de Janeiro, Brazil
Podium talk – Chair for session *Colloids, suspensions & granular media*

2020 — **Physical Poetics #4** — Brussels, Belgium
Micro Gravities – Invited speaker, 1 hour evening lecture (video recorded)

2019 — **International Conference on Advanced Material Research** — Moscow, Russia
Podium talk

2019 — **1st Sino-German Workshop on 3D printing in Space** — Beijing, China
Invited speaker

2018 — **Annual European Rheology Conference** — Sorento, Italy
Poster presentation on experimental rheology

Projects & experience

Teaching experience

2020 — **ESA/ELGRA Gravity-Related Research Summer School** — Transinne, Belgium
On parabolic flight campaign preparation

2020 — **Erg Saint-Luc – School of Graphic Research** — Brussels, Belgium
3 weeks workshop for 30 students on *The Concept of Representation – between Art and Science*

Projects

2016 — **Master Thesis – Spaceship EAC (ESA)** — Cologne, Germany
Additive manufacturing technologies for in-space manufacturing
European Astronaut Centre – Supervisors: Aidan Cowely & Samantha Cristoforetti

2016 — **Laboratory research internship – CETELOR** — Epinal, France
Development of structural composite material for extrusion-based AM

2015 — **Start-up Project *Infility*** — Nancy, France
Entrepreneurship project – Development of new, sustainable materials for 3D printing

Cologne, May 2021

Olfa D'Angelo